A Microscopy Study of PVD Grown Cu: Sample preparation, optimisation and *in-situ* analysis

By

Megan Canavan

Supervisor: Prof. Valeria Nicolosi

A thesis submitted in fulfilment of the requirements of the degree of

Doctor in Philosophy

In the

School of Physics

Trinity College Dublin

January 2019

Declaration

I declare that this thesis has not been submitted as an exercise for a degree at this or any other university and it is entirely my own work, except for unpublished collaborative work and assistance acknowledged herein.

I agree to deposit this thesis in the University's open access institutional repository or allow the Library to do so on my behalf, subject to Irish Copyright Legislation and Trinity College Library conditions of use and acknowledgement.

Elements of this work that have been carried out jointly with others or by collaborators have been duly acknowledged.

I have read and I understand the plagiarism provisions in the General Regulations of the University Calendar for the current year, found at: http://www.tcd.ie/calendar.

I have also completed the Online Tutorial on avoiding plagiarism 'Ready, Steady, Write', located at http://tcd-ie.libguides.com/plagiarism/ready-steady-write

_____

Megan Canavan, January 2019

To Jean Murphy and Timothy Canavan

Summary

Continuous downscaling of transistor feature size in integration circuits has been needed in order to produce faster circuit speed, higher chip functionality and lower production cost. Device speed increases with shortening of the channel length but this leads to issues with interconnect resistive-capacitive (RC) delay. Interconnects have evolved from being aluminium (Al) based to copper (Cu) due to the reduced resistivity in bulk Cu. However, due to the continual decrease in the feature size of Cu interconnects, the physical limitation of the size effect, there is a significant increase in resistivity.

The aim of this industry-led project was to understand which factors contribute to this resistivity increase. The project was a collaborative effort between our group, and both Prof. Boland's group (most particularly Dr. Xiaopu Zhang) and the Intel researcher-in-residence Mr. Peter Gleeson, who focused on analysing the surface through Scanning Tunneling Microscopy (STM) and measuring the resistivity of Cu nanowires through Conductive-Atomic Force Microscopy (C-AFM), respectively. My work focused on the in-depth analysis of the grain boundaries and interfaces of the Cu film using Transmission Electron Microscopy (TEM) and Scanning TEM (STEM) characterization to correlate the structure of the Cu interconnects to the physical behavior, more specifically to find the link between size and resistivity increase. These objectives shifted due to the demands of the industry partner, Intel, as it became more important and challenging to achieve high-resolution data analysis of the Cu films and nanowire (NW) grain boundaries and interfaces. The focus shifted to optimising the lamella preparation technique to provide the best possible S/TEM imaging for complementary data to the STM and C-AFM. This project work was primarily focused on lamella preparation techniques for TEM imaging and analysis.

This thesis discusses a variety of sample preparation techniques for the TEM of physical vapour deposition (PVD) grown Cu films and nanowires (NWs). The overall aim of this work was to create and develop lamella preparation techniques, which enable high-resolution S/TEM imaging and analysis of Cu films and NW microstructure.

Focused ion beam (FIB) milling was used to prepare lamellae of a 40 nm Cu film on silicon dioxide (SiO_2), a 50 nm Cu film on a tantalum (Ta) barrier layer and 100 nm Cu NWs on a proprietary barrier layer. All are deposited on a silicon (Si) substrate.

Cross-sectional lamellae were prepared and the technique optimised for the 40 nm Cu film on SiO_2. These lamellae were prepared using an established wedge technique combined with low kV beam milling. S/TEM imaging was used to highlight the quality of the lamellae prepared by obtaining high-resolution images of the sample. The grains, grain boundaries and film interface were analysed using Energy Dispersive X-Ray (EDX) spectroscopy. Damage was experienced by the lamellae due to the electron beam at 300 kV accelerating voltage. A damage study of the Cu film was recorded at both 300 kV and 80 kV. This damage was a reflection of the quality of the evaporated Cu film.

Cross-sectional lamellae of 50 nm Cu on 7 nm Ta were also prepared using low kV FIB milling. Due to the high quality sample preparation, the lamellae were imaged using aberration-corrected STEM imaging. Through this imaging the Cu grains and complex grain boundaries were detected. Electron energy loss spectroscopy (EELS) analysis of the lamellae was used to calculate the absolute thickness of the lamellae with an approximate value of 30 nm. Twin boundaries running parallel to the Cu film were identified and the slight misalignment of 1 – 2° causing the incoherency between the grains was potentially linked to the out-of-plane rotation at the surface observed by STM analysis.

Various plan-view lamella preparation methods were executed using predominantly low kV FIB milling of the 50 nm Cu film on 7 nm Ta. These varied from side-view mounted with low kV milling, hydrofluoric (HF) acid etched Cu film and *in-situ* xenon-fluoride (XeF_2) etched Cu film accompanied by a final low kV FIB polish. From this, grain size, grain boundary misorientation and texture of the film surface could be identified through Transmission Kikuchi Diffraction (TKD) of the plan-view lamellae. High-resolution S/TEM imaging of these plan-view lamellae confirmed the high quality, low amorphisation and minimal damage achieved by these preparation methods. Analysis of the plan-view lamella led to a potential correlation between the “zipper” like grain boundary structure characterised by STM analysis.

Site-specific cross-sectional lamellae of 100 nm Cu NWs were prepared by low kV FIB milling. High-resolution S/TEM imaging of these Cu NWs was achieved. Similar grain boundary features were discovered within these NWs including twin boundaries. Grains rarely ran the depth of the film with a mixture of grain size and shape evident throughout.

Micron-sized mounds formed on the surface of annealed Cu films were observed after exposure to temperatures of 300 – 400°C. These mounds were successfully cross-sectioned using FIB milling and it was observed that the internal structure, a trapezoidal shape bounded by the Si (111) and Si (100) planes, was similar to that reported in the literature. To confirm whether the mounds formed were an intermixing of Cu and Si forming Cu_3Si, a lamella cross-section for TEM was successfully prepared. HRTEM imaging and EDX analysis were performed, confirming the intermixing of the film and substrate along with the migration of the barrier layer to the mound surface.

In order to achieve real-time observation of these mound formations, an alternative *in-situ* lift-out procedure using FIB milling was developed and optimised for the preparation of lamellae for *in-situ* annealing in the TEM. This technique combined for the first time the use of rotating microgrippers for lift-out and thinning, and a unique adhesive substance, SEMGlu, during the lift-out procedure, instead of the traditional micromanipulator needle and platinum (Pt) weld. Lamellae were successfully mounted onto a MEMS device for *in-situ* TEM annealing experiments without damage to the MEMS. HRTEM imaging of the polished lamella verified that this method can produce high quality lamellae comparable with regular *in-situ* lift-out procedures.

Abstract

A variety of sample preparation techniques have been developed and optimised for PVD grown Cu films and Cu NWs. These techniques include traditional cross-sectional preparation, plan-view preparation, site-specific cross-sectional preparation and *in-situ* lamella fabrication technique for *in-situ* annealing within the TEM. These techniques have been developed to obtain high-resolution S/TEM imaging and analysis of Cu film and NW microstructure.

Cross-sectional lamellae of 40 nm Cu film on SiO_2 were successfully prepared through low kV FIB milling and the employment of an established wedge technique. HRTEM and STEM imaging of these lamellae determined the various grain and grain boundaries present within the Cu film. TEM imaging was performed at both 300 and 80 kV due to the damage experienced by the Cu film at higher accelerating voltages. This was determined to be due to the fact that the evaporated Cu film was of poorer quality to the sputtered 50 nm Cu film on 7 nm Ta later analysed.

Cross-sectional lamellae of 50 nm Cu on 7 nm Ta were successfully prepared to a very high quality with minimal damage, uniform crystallinity and little amorphisation. From this high-resolution aberration-corrected STEM imaging and analysis was achieved. Atomic resolution imaging of the Cu film revealed a complex grain boundary mixture of tilt and twist and twin boundaries running at an angle and also parallel to the film surface. Slight misalignments of 1 - 2° within these parallel twin boundaries could potentially be contributing to the out-of-plane rotation of grain boundaries on the film surface detected by STM analysis and simulations. EELS obtained were used to determine the absolute thickness of lamellae with approximate values of 30 nm.

Plan-view lamellae of 50 nm Cu film on 7 nm Ta were successfully prepared through various alternative techniques including side-mounted low kV milling, HF etching of the Si substrate to remove the Cu film and *in-situ* XeF_2 etch with the FIB to remove the Si substrate. HRTEM imaging of these lamellae was obtained and the grain size, misorientation angle and texture was analysed through TKD. This confirmed the predominant surface grain orientation being [111] corroborating STM analysis.

Site-specific lamellae of Cu NWs were prepared using low kV FIB milling. High-resolution S/TEM imaging of these Cu NWs was achieved. Similar grain boundary features were discovered within these NWs including twin boundaries.

Finally, in order to achieve real-time observation of Cu_3Si mounds formed during annealing of the 50 nm Cu film on 7 nm Ta, an alternative *in-situ* lift-out procedure using FIB milling was developed and optimised for the preparation of lamellae for *in-situ* annealing in the TEM. This technique combined for the first time the use of rotating microgrippers for lift-out and thinning, and a unique adhesive substance, SEMGlu, during the lift-out procedure, instead of the traditional micromanipulator needle and Pt weld. Lamellae were successfully mounted onto a MEMS device for *in-situ* TEM annealing experiments without damage to the MEMS. HRTEM imaging of the polished lamella verified that this method can produce high quality lamellae comparable with regular *in-situ* lift-out procedures.

Acknowledgements

I would like to sincerely thank my supervisor, **Prof. Valeria Nicolosi** for all the guidance and support she has given me throughout my time in the Nicolosi group both during my PhD and my final year undergraduate project. I would also like to thank her for awarding me this opportunity to work as part of her group for the past 6 years. It has been a pleasure to work in such a friendly, exciting and innovative team.

A special thanks to the entire Nicolosi group past and present for all their support and friendship over the course of my PhD including: Dr. Joao Coelho, Dr. Anuj Pokle, Carol McCaffrey, Chris Hobbs, Dr. Henrik Petterrson, Dr. Eva McGuire and Dr. Edmund Long for being the best desk buddy a microscopist could ask for.

I would also like to thank **Mr. Peter Gleeson**, Intel researcher-in-residence, my mentor as part of my Enterprise Partnership Scheme. Peter has provided great support and guidance throughout my project and has become a great friend over the course of my PhD.

A huge thanks to all the staff members of the Advanced Microscopy Laboratory (AML), Trinity College Dublin; **Mr. Cathal McAuley**, **Mr. Dermot Daly**, **Mr. Clive Downing** and **Dr. Eoin McCarthy** for their absolute unwavering support and generosity with their time throughout my PhD. Also, a special thanks to all AML staff and students past and present for making it a great place to work over the years.

Many thanks to **Mr. Dermot Daly**, who taught me everything I know about lamella preparation; the good, the bad and the ugly and who really is the best storyteller I know.

Thanks to **Mr. Clive Downing** for all the training and assistance with regards TEM imaging and analysis and also for all data acquired on the NION UltraSTEM**.**

A special thanks to **Dr. Eoin McCarthy** for his training, guidance and support with regards all of my *in-situ* TEM annealing experiments and the proofing and correcting of our fabrication technique publication.

Thanks to **Mr. Andreas Rummel** and **Mr. Cathal McAuley** for the contribution towards the fabrication technique publication.

Many thanks to **Prof. Quentin Ramasse** and **Dr. Patricia Abellan** for all aberration-corrected STEM data acquired at SuperSTEM Daresbury.

A massive thank you to **Dr. Hannah Nerl** for proof reading this thesis and for all the tea, chats and cake and for being a great friend.

I would like to thank the **Irish Research Council**, **Intel Ireland**, **PIYRA** and **SFI** for their funding and the opportunity to pursue this PhD work.

Finally I would like to thank my family; my parents and my sister for always being there for me and their unconditional love and support in everything I do.

And of course, to my love, Colm, this thesis is dedicated to you, for putting up with me over all these years, for being my proof reader and for not murdering me during those writing days. I would not have done this without you. I love you and thank you.

List of Publications

Timothy J. Pennycook, Lewys Jones, Henrik Pettersson, Joao Coelho, Megan Canavan, Beatriz Mendoza-Sanchez, Valeria Nicolosi & Peter D. Nellist, "*Atomic scale dynamics of a solid state chemical reaction directly determined by annular dark-field electron microscopy*" - *Sci Reports*, **4**, pp. 1-4 (2014)

Francis Oliver Vinay Gomes, Anuj Pokle, Marko Marinkovic, Torsten Balster, Megan Canavan, Karsten Fleischer, Ralf Anselmann and Valeria Nicolosi, Veit Wagner "*Influence of temperature on morphological and optical properties of MoS_2 layers as grown based on solution process precursor*." – *Thin Solid Films,* **645**, pp. 38-44 (2018)

Megan Canavan, Dermot Daly, Andreas Rummel, Eoin K. McCarthy, Cathal McAuley and Valeria Nicolosi, "*Novel in-situ lamella fabrication technique for in-situ TEM*" – *Ultramicroscopy*, **190**, pp. 21-29 (2018)

Table of Contents

1. Introduction

Gordon Moore, one of the founders of Intel, predicted in a paper published in 1965 that the number of components in an integrated circuit (IC) would double every two years. [1] This is a law, which has been the touchstone of the semiconductor industry to this day, with the law holding true for much longer than originally hypothesized. As can be seen from the transistor count graph in Figure 1.1, this trend has continued successfully, with a reported 19.7 billion transistors per commercially available single-chip processor in 2017.[2]

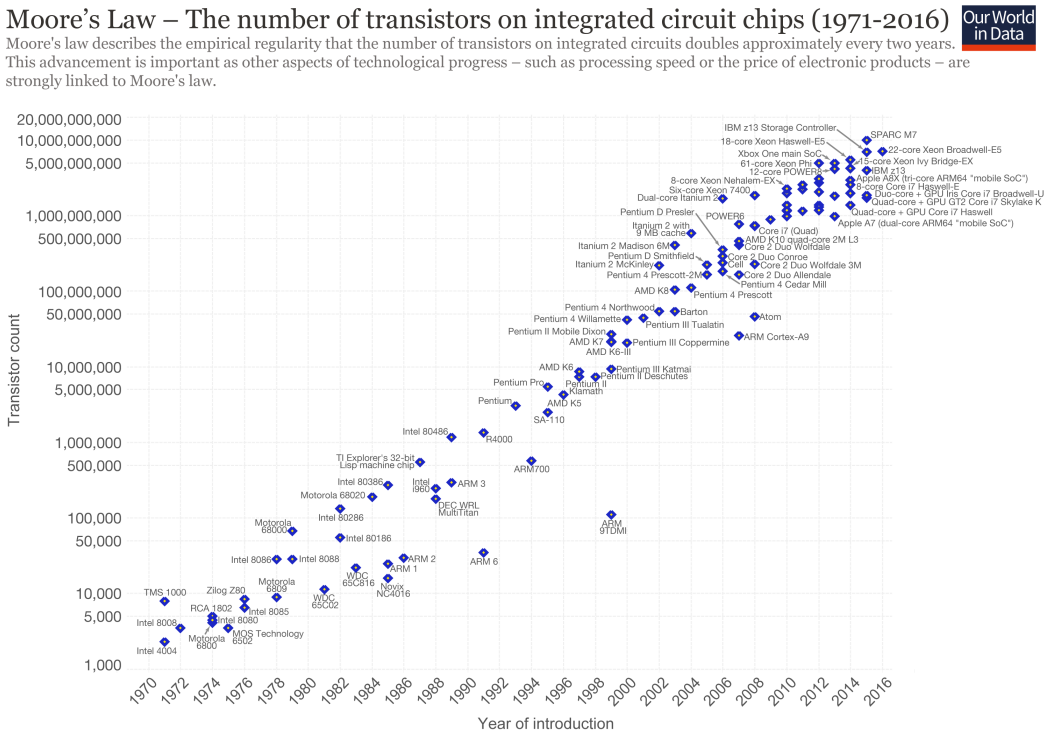

Figure 1-1: Displaying transistor on integrated circuit chips from 1971 – 2016.[2]

Transistors are classified into 3 main components based on the manufacturing process; front-end-of-line (FEOL), middle-of-line (MOL) and back-end-of-line (BEOL). The first step FEOL is the transistor fabrication into the silicon wafer. MOL consists of source/drain contacts and metal one layer with tungsten (W) interconnects (plugs). BEOL is for the upper levels of copper (Cu) metallization, which are separated by a dielectric material. Silicon dioxide (SiO_2) is usually used as the interlayer dielectric material (ILD).[3] A contact forms an interconnection between metal and active-/poly-silicon. A via connects to metal layers. They are formed by overlapping the two interconnecting layers and providing a contact hole filled with metal, between the two.[4]

Cu interconnects are produced using the dual damascene process. Cu is patterned by chemical mechanical polishing (CMP) as it is not easily patterned using a dry etching process.[5] By using the dual damascene process the trench and via are formed prior to the deposition of the metal barrier/Cu seed layer/Cu fill. This means there is only one metal fill and one CMP step required for each level of interconnection. This leads to a lower process cost than the single damascene process.[6]

Continuous downscaling of transistor feature size in integrated circuits has been needed in order to produce faster circuit speed, higher chip functionality and lower production cost.
Device speed increases as device dimensions are reduced, but the resulting increase in interconnect resistance, as the cross sectional area decreases, leads to increasing resistive-capacitive (RC) delay. Other interconnect issues include cross-talk and noise which seems to be of particular concern for local and intermediate levels and also power dissipation and distribution. Cross-talk effects include noise on non-switching wires and increased delay on switching wires.[6]

Interconnects have evolved from being aluminium (Al) based to Cu due to the reduced resistivity in bulk Cu. However, due to the continual decrease in the feature size of Cu interconnects and the physical limitation of the size effect, there is a significant increase in resistivity.[7]-[9]

The aim of this industry-led project was to understand which factors contribute to this resistivity increase. The samples analysed are Cu films deposited on tantalum (Ta)/SiO_2 on a Si substrate. The project was a collaborative effort between our group, and both Prof. Boland's group (most particularly Dr. Xiaopu Zhang) and the Intel researcher-in-residence Mr. Peter Gleeson, who focused on analysing the surface through Scanning Tunneling Microscopy (STM) and measuring the resistivity of Cu nanowires (NWs) through Conductive-Atomic Force Microscopy (C-AFM), respectively. My work focused on the in-depth analysis of the grain boundaries and interfaces of the Cu film using Transmission Electron Microscopy (TEM) and Scanning TEM (STEM) characterization to correlate the structure of the Cu interconnects to the physical behavior, more specifically to find the link between size and resistivity increase. These objectives shifted due to the demands of the industry partner, Intel, as it became more important and difficult to achieve high-resolution data analysis of the Cu films and NW grain

boundaries and interfaces. The focus shifted to optimising the lamella preparation technique to provide the best possible S/TEM imaging for complementary data to the STM and C-AFM. This project work was primarily focused on lamella preparation techniques for TEM imaging and analysis.

1.1 Cu Interconnects

1.1.1 What is an Interconnect?

Interconnects are the wiring within integrated circuits which connect one transistor to another and to external connections. They have now become the dominant factor in determining system performance and power dissipation. Interconnects have evolved from Al to Cu over the last 20 years. This is due to the lower bulk resistivity of Cu (1.68 μΩ.cm compared with 2.7 μΩ.cm for Al), which helps reduce the resistive-capacitive (RC) delay.[10] Just by changing to a Cu interconnect, as opposed to Al, the RC delay can be reduced by up to 40%. Combining this with a dielectric material with a low capacitance (low κ material) can reduce the RC by up to 50%. By using Cu in combination with low ε dielectrics, the speed can be doubled and the power halved. Cu can also withstand high current densities.[4][11]

There are 3 types of interconnects: local, intermediate and global, see Figure 1-2. Local interconnects are the lowest level of interconnects. They connect gates, drains, and sources in Metal Oxide Semiconductor (MOS) technology. Local interconnects can afford to have a larger resistivity than intermediate or global interconnects as they don't travel long distances. This can be seen from the formula below for resistance, showing the dependence on interconnect length and its resistivity:

$$R = \frac{\rho L}{A} \qquad (1.1)$$

where R is the resistance, ρ is the resistivity, L is the length and A is the cross-sectional area. Intermediate interconnects connect devices within a block. They are larger and wider than local interconnects, to provide the lower resistance. Global interconnects are the longest, and are used to distribute power and clock signals around the circuit.[4][12]

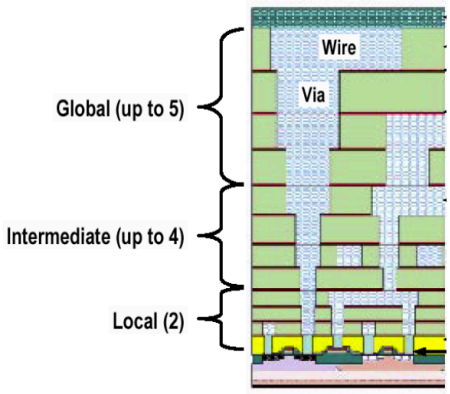

Figure 1-2: Diagram of range of interconnects.[13]

1.2 Diffusion Barrier

Although Cu is a welcome alternative to Al for interconnect material, it has its own set of drawbacks. One of these is the diffusion of Cu into surrounding interlayer materials which causes device degradation. For Cu interconnects the activation energy for bulk diffusion is 2.3 eV, for grain boundary diffusion is 1.2 eV and for interface diffusion is 0.7 – 1 eV. This is why the main diffusion path for Cu is the interface, due to its lower activation energy. Due to this interface diffusion, a diffusion barrier/liner is essential between Cu and the dielectric material. This barrier also acts as a good adhesion layer for the Cu when the correct barrier material is selected.[14] Not only that but the barrier can also reduce the electromigration performance. Refractory metals such as titanium (Ti), Ta, W and their respective nitrides are usually the preferred choice of barrier liners due to their high thermal stability.[15] Ta is an effective barrier due to its thermal stability and resistance to electromigration. Ta provides good adhesion and it can typically be used as a bilayer with tantalum nitride (TaN), which acts as a good diffusion barrier.[16], [17]

1.3 Electromigration

Electromigration is the self-diffusion of metal ions due to the application of an electric field. This net flux of atoms is caused by the electron wind force moving the ions in the direction of the electron flow and a back stress, which pushes the ions in the opposite direction.[18]
The flux (J) can be described by the following formula:

$$J = -\frac{DC}{kT}(Z^* eE - \Omega\frac{\delta\sigma}{\delta x}) \qquad (1.2)$$

where D is the diffusivity, C is the concentration of atoms, k is Boltzmann's constant, T is temperature, Z* is the effective charge number, e is the electric charge, E is the electric field, Ω is the atomic volume and δσ/δx is the stress gradient along the line.[18]

It was first described by James Black in 1967 as "cracked stripes" appearing in the aluminium. His paper demonstrated how voids/openings appeared in the metal due to the movement of Al when a high current was applied to the material.[19], [20] Although resistance to electromigration in Cu is an order of magnitude higher than that of Al it still provides reliability concerns with regards interconnects.[21] This movement of metal ions leads to the formation of voids causing open circuits and hillocks causing short circuits. As a result of this the electromigration lifetime of Cu interconnects is constantly under investigation. It has been discovered that the resistance to electromigration can be improved by replacing the cap layer with Ta/TaN as opposed to SiN_x.[15]

1.4 The Issue – Size Effect

The classical size effect refers to the increase in resistivity of metal films and wires as their critical dimensions (thickness of film, width and height of wires) approach or become less than the electron mean free path, λ. For example, the resistivity of a Cu 40 nm wide wire is reported to be 2.5 times higher than that of bulk Cu. This resistivity has been attributed to scattering of the conducting electrons at the grain boundaries and surfaces/interfaces. Also, the increasing fraction of refractory metal liner in the trench can also be a contributor to the resistivity.[5], [8], [22]-[25]

1.5 Sample Preparation for Transmission Electron Microscopy

In order to try and analyse this size effect issue on the nanoscale, Cu films on Si substrate with a barrier layer of <10 nm needed to be investigated within a TEM. In order to be able to achieve this, microscale specimens need to be prepared from bulk macroscale samples. This is what directed this thesis work to TEM sample preparation. Detailed in this section is a variety of sample preparation techniques to create electron transparent specimens for TEM analysis,

from mechanical preparation to state-of-the-art Focused Ion Beam (FIB) preparation techniques.

The first question to answer when preparing a sample for the TEM is whether to use a sample placed on a TEM grid or to create a self-supported sample where no grid is needed and the whole sample acts as a grid itself. The type of specimen depends on what type of information you want to obtain from your sample. Typically whether self-supporting or a grid, it will 3 mm in diameter.[26]

A 3 mm diameter disk is cut using a coring process. If it is ductile, a mechanical punch can be used. For conducting materials, spark erosion also known as electrical discharge machining can also be used. A desired shape is achieved by using electrical discharges (sparks). Material is removed by a series of rapid recurring current discharges between two electrodes, separated by a dielectric liquid and subject to an electric voltage.[27] There are many other types of method including; abrasive slurry disk cutting, which uses a rotary motion of the coring tube to drill round the disk and ultrasonic cutting, which involves an ultrasonic drill vibrating in water.[26]

The final disk must be thicker than the mechanical damage depth potentially caused by the disk cutting or else the final specimen will contain damage that will not be able to be removed.

1.5.1 Dimpling

After the 3 mm diameter disk has been formed, a pre-thinning stage has to be achieved before the final thinning. This is typically called the dimpling or dimple grinding stage. A small radius tool is used to grind and polish the disk to a fixed radius of curvature in the centre.[26]

For the polishing procedure a suspension of diamond particles in oil or water is used. The sample can be ground from just one-side or both. This depends on the brittleness of the sample. Dimple grinding from both sides reduces deformation of the surface.[28] Dimple grinding is performed until the sample reaches a thickness between 10 – 30 μm. This again depends on brittle nature of the sample.

1.5.2 Tripod Polishing

An alternative to dimple grinding for the pre-thinning stage is tripod polishing. Tripod polishing is more beneficial than dimple grinding as it allows the disk to be thinned much further, as low as 1 µm, meaning less time spent on ion polishing.[26]

The tripod polishing method was developed to prepare site-specific TEM samples of Si semiconductor devices with large transparent areas.[29] A tripod polisher is a device to hold/mount the sample, which has three feet, while it is being mechanically thinned on a polishing wheel.[26]

For some materials, such as Si, this tripod polishing method can be used right up to the point of electron transparency with no need for ion polishing. Tripod polishing can be used for both cross-sectional and plan-view sample preparation.[29]

Tripod polishing has two alternative methods; flat polishing and wedge polishing. Flat polishing is typically performed when a final ion polish will be performed after. Wedge polishing tends to be used as the final polishing of the sample for TEM.

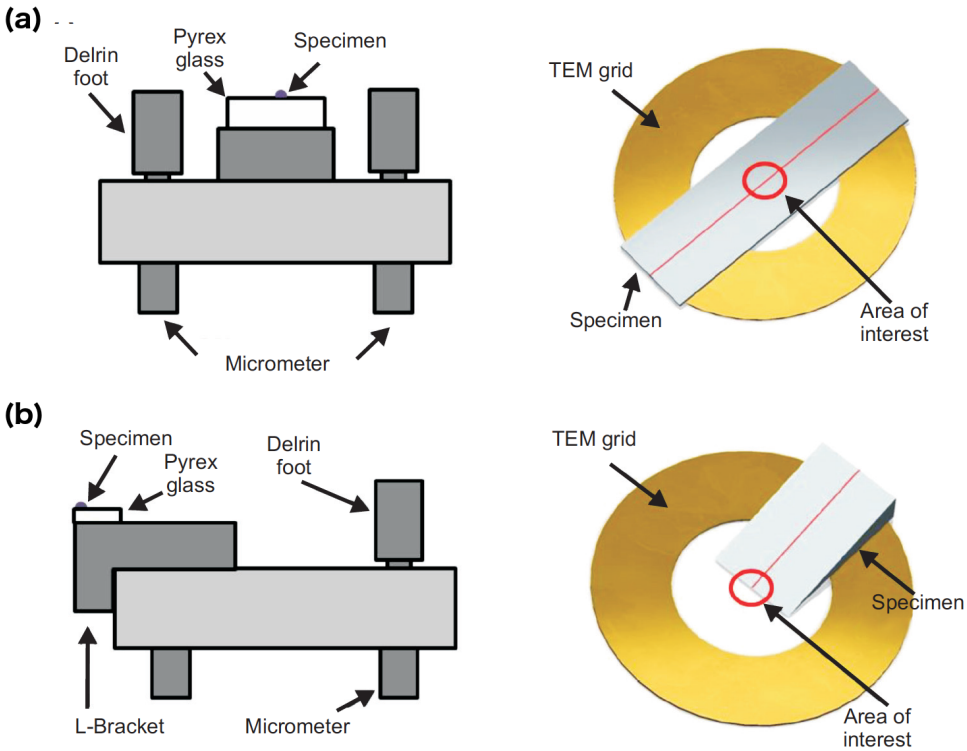

Figure 1-3: Schematics of tripod position and slice/grid geometry, respectively, for (a) flat-type polishing and (b) wedge-type polishing from Cha et al.[29]

For cross-sectional specimens the area of interest is typically a thin film/substrate interface. The specimen is cut and glued to another piece of the specimen to produce several layers using epoxy. This is mounted on a Perspex stub. A mixture of diamond lapping films and colloidal silica are used to polish the sample.[26], [29]

Flat-type polishing using a tripod will create a larger area for analysis than dimple grinding, as well as being easier to prepare, see Figure 1-3 (a). Flat-type polishing is also less time consuming than both dimple grinding and wedge-type polishing. Flat-type polishing thins the entire area, whereas wedge-type polishing can be more localized, meaning it may be more beneficial to samples which have layers of different milling rates or high hardness and mechanical instability, see Figure 1-3 (b).[29]

1.5.3 Ion Milling/Polishing

If the flat polishing tripod technique is used, a final step of broad ion beam milling is performed, which can also be performed after dimpling. The sample is bombarded by high-energy ions or neutral atoms. This is typically Ar ions, which are generated by passing Ar gas through a high voltage between 4 – 6 kV.[26]

The sample is held in vacuum and is typically cooled by liquid nitrogen. The Ar ions are incident on the sample at a low angle of ~20° and gently sputter away material, see diagram in Figure 1-4. The smaller angle means a lower sputter rate. Ion beam thinning is a localised process but the sputter rate is approximately 2 - 3 Å per second, meaning it could take hours to create an electron transparent region, depending on the initial thickness of the sample.[30], [31]

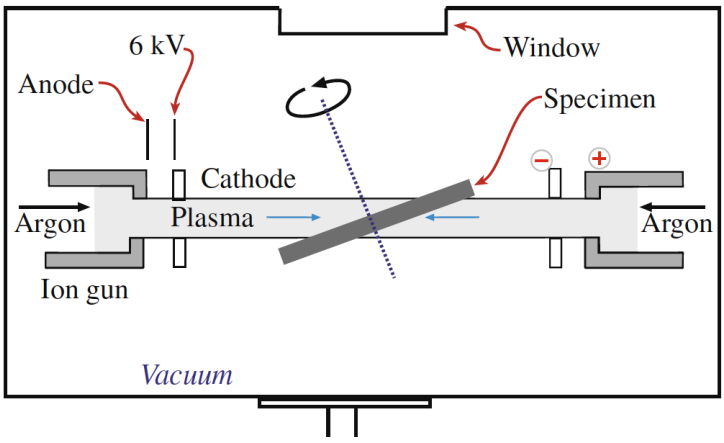

Figure 1-4: Diagram of Ar ion polishing set-up for final thinning of mechanical procedure.[26]

1.5.4 Electrolytic Polishing

Electrolytic polishing is used for conducting samples such as metals/alloys. It is generally easier to polish pure elements such as metals, single crystals or alloys <5% alloying element. It is a relatively fast and inexpensive technique.[32] An electrolytic cell is formed with the sample as the anode. An electric potential is then applied, causing the sample to dissolve. This is stopped once a hole begins to form.

1.5.4.1 Window Technique

The sample is cut into a square sheet of ~10 mm^2. The sheet edges are covered by a lacquer to expose a window. The window of the exposed metal is immersed in an electrolyte, which is usually cooled by water or liquid nitrogen, to slow the rate of dissolution, seen in Figure 1-5 (a). Perchloric acid is usually the electrolyte used. This is surrounded by a cathode.[26]

When a current is applied the material dissolves from the anode (the sample) and deposits on the cathode.[33] Once a hole forms within the window, the sample is removed. The difficulty is controlling the location of the hole within the window.

A commonly used variation of this technique is the jet-polishing technique. This entails using pointed electrodes to spray the electrolyte locally, see schematic in Figure 1-5 (b). The jet helps thinning from both sides and enables a faster polishing process. This method reduces electrolyte use and can create larger electron transparent regions for TEM analysis.[33]

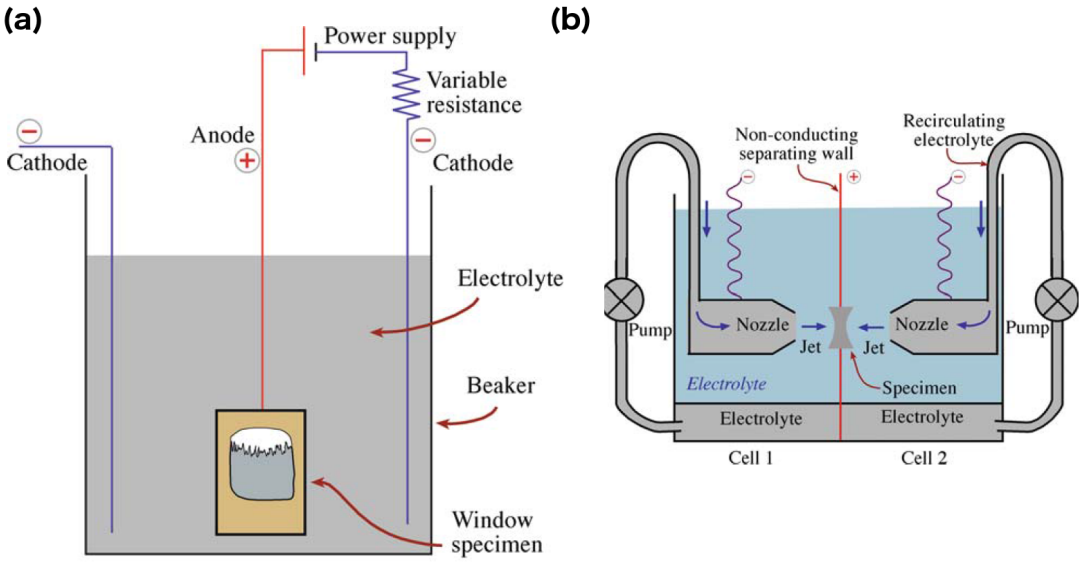

Figure 1-5: (a) Diagram of window technique electrolytic polishing where sheet is lacquered around the edges and is the anode of the electrolytic cell and (b) diagram of twin-jet polishing apparatus.[26]

1.5.5 Placing on TEM Grids

1.5.5.1 Grinding and Crushing

If materials are particularly brittle, such as ceramics and minerals, it can be easier to prepare by grinding or crushing. The sample can be crushed using a pestle and mortar with an inert liquid. Some areas will be sufficiently small and thin to be electron transparent.[32] The liquid can be ultrasonically stirred and the crushed pieces allowed to settle. The supernatant liquid can be dropped using a pipette onto a holey carbon TEM grid, which will evaporate, leaving the particles on the grid for TEM analysis.[26] This method is simple and easy to perform. It is beneficial as the specimen has not been modified by ion milling etc. However, due to the random nature of the crushing, obtaining the correct orientation and area of interest is very difficult and the microstructure characteristics can be significantly altered from the mechanical scraping or crushing.[32]

1.5.5.2 Ultramicrotomy

Ultramicrotomy is a sample preparation method, which involves the sectioning of a specimen using a diamond knife. This method is most suited to cross-sectional sections as opposed to plan-view.[32] This particular method is routinely used for biological specimens or polymers, as these samples tend to be soft.

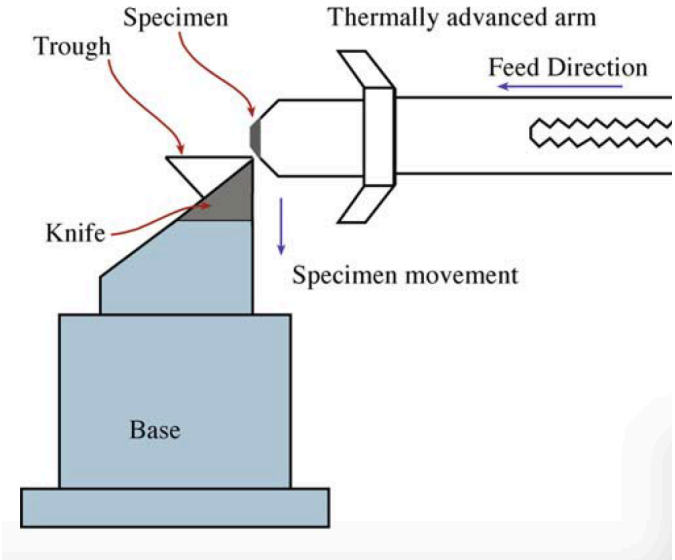

Figure 1-6: Diagram of ultramicrotome set-up where sample is embedded and moved slowly towards knife blade.[26]

The microtome works by moving a specimen past a knife blade. Samples can be embedded in epoxy prior to slicing, shown in Figure 1-6. This method can be beneficial as it leaves the chemistry of the sample unchanged as it is unaffected by ion beam milling etc. But it can lead to unwanted fractures in the sample.[26]

1.5.6 Focused Ion Beam – TEM Sample Preparation

The most commonly used method for TEM sample preparation and what is discussed extensively throughout this thesis is ion milling and more specifically Ga+ Focused Ion Beam milling. Ion beam preparation has become standard TEM specimen preparation for the last few decades for non-biological samples and in particular for cross-sectional samples.[30] The advantages of FIB cross-sectional preparation for TEM include site-specificity at the sub-micrometre scale and uniformity in thinning of the specimen.[34] There are a number of traditional FIB lamella preparation techniques both *ex-situ* and *in-situ*. The following gives a brief description of a variety of traditional techniques for TEM preparation.

1.5.6.1 Conventional Cross-section

Initially, FIB lamella preparation had two main types of techniques used, which both had their advantages and disadvantages. Firstly the H-bar, sometimes referred to as the trench, technique [35] or often times referred to as the conventional cross-section technique.[36]

This technique involves sample preparation before processing the sample in the FIB chamber. Here the specimen is cut and ground into 1 – 2 mm^2 and ~50 μm in thickness. This can be done using a dicing saw.[37], [38] These sections are typically adhered to Cu TEM slot grids, see schematic in Figure 1-7 (a) from Langford *et al*. The sections are named H-bar due to their shape when milling.[39] This cut profile ensures the thinned region of interest has structural support.

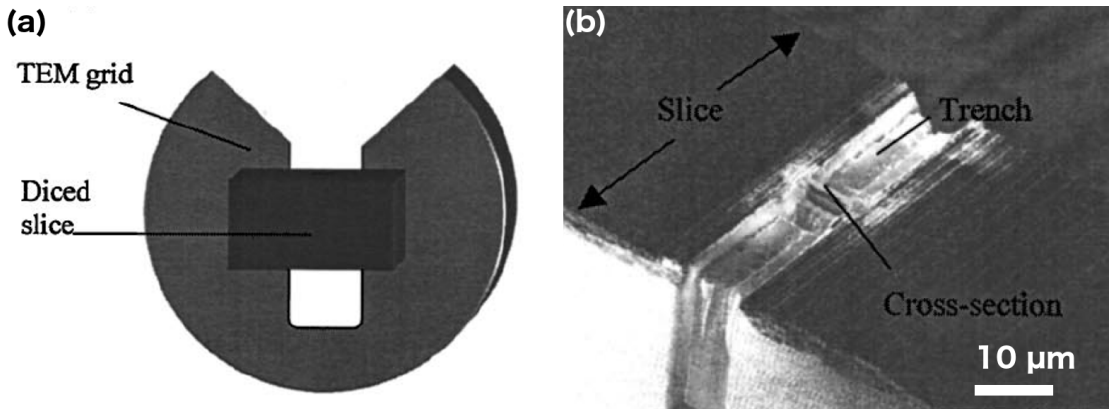

Figure 1-7: (a) Schematic of slice mounted onto a U-shaped TEM grid and (b) the finished trench cross-section, showing the H-bar profile from Langford et al.[35]

Once secured it is placed in a FIB system for thinning. A metal line is deposited onto the sample to provide a protective layer, typically platinum (Pt), to the sample surface to prevent damage and unnecessary sputtering of the surface. It is also beneficial to use this protective strip as an indicator of the location of the area of interest.[36]

This type of procedure involves significant sample preparation prior to FIB milling, which is also quite destructive.[36] This technique means reduced TEM tilt in the holder due to the bulk specimen walls contained on the Cu slot grid, see Figure 1-7 (b). An advantage of this technique is the robust nature of the H-bar profile, as it is adhered securely to a grid it can be removed and re-thinned at any point.

1.5.6.2 Lift-out Technique

Another technique that became a popular alternative to the H-bar was the lift-out technique. The lift-out of a FIB prepared electron transparent lamella from a larger bulk material was first developed for applications in the microelectronics industry.[40] This technique involves no preparation to the sample prior to placing in the FIB system. It is prepared directly from the bulk specimen. Similar to the conventional cross-section method just described, this involves the milling of trenches using the FIB with a protective W/Pt layer deposited prior to ion beam milling. The left side, bottom and part of the right ridge of the cross-section (lamella) are milled, leaving only a small tag of the specimen attached to the bulk, see Figure 1-8 (a) and (b). The sample is then thinned until it is electron transparent for TEM imaging and analysis.

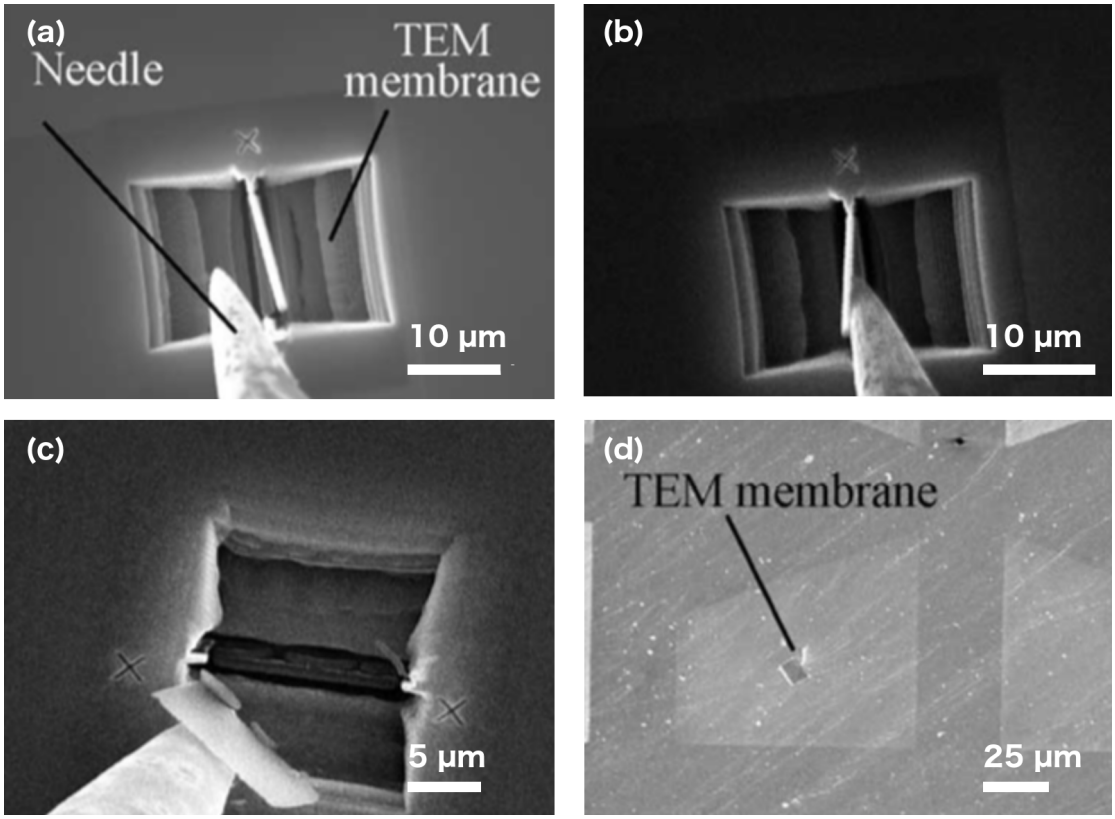

Figure 1-8: Secondary Electron Microscopy images by Langford et al. depicting the ex-situ lift-out procedure, which is typically performed under an optical microscope; (a) milled trenches using Focused Ion Beam with needle approaching lamella, (b) lamella breaking from bulk specimen, (c) lamella lifted out of trench using needle and (d) specimen placed on carbon coated Transmission Electron Microscopy grid.[41]

The specimen is removed from the FIB chamber and the lamella is removed using a glass rod under an optical microscope. Once removed, it is placed onto a carbon coated copper mesh TEM grid, see Figure 1-8 (c) and (d).[42]

The two techniques both have advantages and disadvantages. When it comes to preparation needed prior to FIB milling, the lift-out method is the obvious favourable technique. This is due to the cross-section method being time consuming in terms of the grinding/polishing, to produce the small cross-section to be mounted on the TEM grid. A further limitation of the cross-section technique is the lack of angle rotation in terms of tilting in the TEM, as previously mentioned. The specimen is limited by the bulk sidewalls and bottom of the trench, whereas the specimen prepared using the lift-out technique is only limited by the tilting limits of the TEM itself.

A disadvantage to the lift-out technique is the success rate of placing the cross-section onto the TEM grid without losing it or misplacing it on the glass rod. This can also be material dependent.[35] It also cannot be thinned further if needed unlike the trench method.[36]

An advantage to the lift-out technique is that the surrounding substrate is still intact and unaffected by the preparation of the specimen. Conversely, the trench technique leads to a lot of destructive preparation with the grinding and polishing leading to less if not any of the substrate remaining.[35]

1.5.6.3 In-situ Lift-out

The FIB preparation method progressed to an *in-situ* lift-out (INLO) technique, which combines the best parts of the lift-out method, which from now on will be referred to as the *ex-situ* lift-out method (EXLO), and the conventional/trench method.

Here the specimen is prepared in the same fashion as the EXLO method but a probe/manipulator is brought in contact with the specimen and welded using FIB-assisted metal deposition of Pt/W.[40] The specimen is then attached using the same FIB-assisted metal deposition to a TEM grid with pillars for lamella mounting. The specimen is thinned accordingly using the FIB. The benefit of this technique is the lack of re-sputtering during the final thinning process as the lamella is mounted on a TEM grid as opposed to within the bulk of the material.

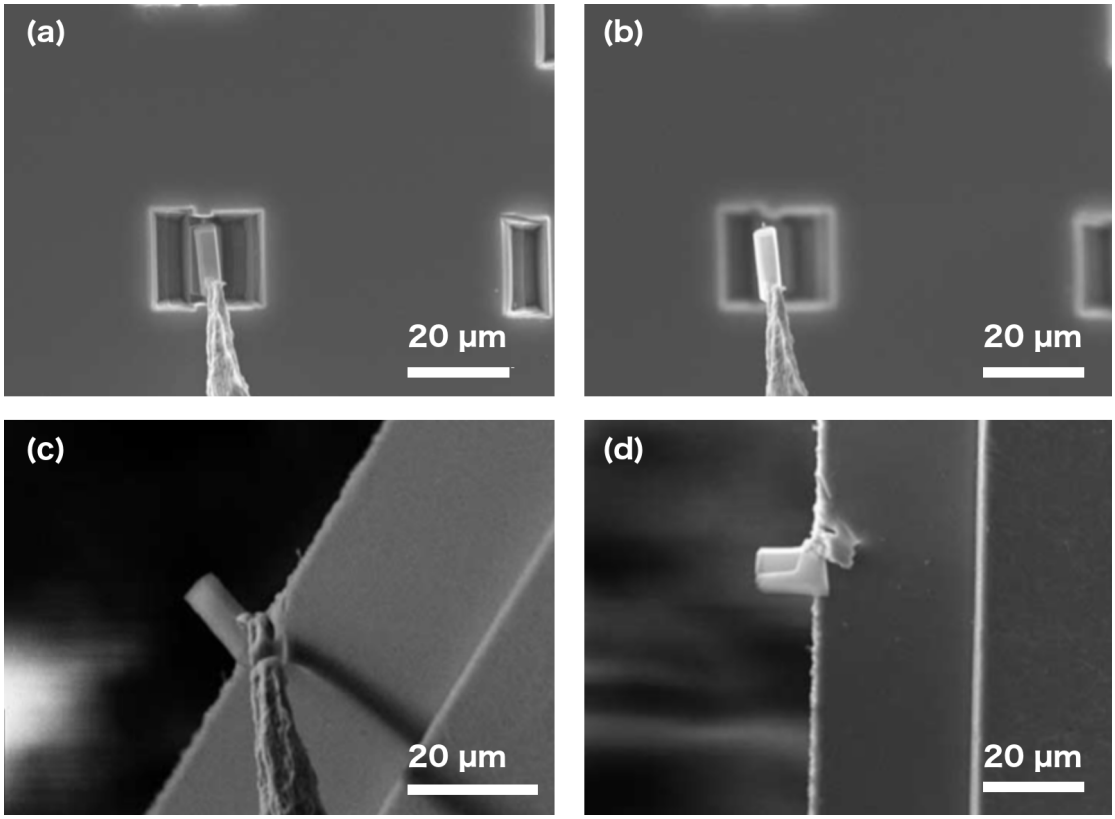

Figure 1-9: Secondary Electron Microscopy images from Langford et al. displaying the in-situ lift-out technique; (a) the welding of the needle to the lamella, (b) lamella removed from the bulk sample trenches with the needle, (c) welding of lamella to Transmission Electron Microscopy (TEM) grid with needle as support and (d) lamella successfully welded and thinned to electron transparency on TEM grid.[41]

A slight upgrade to this technique outlined by Langford *et al.*, is using the INLO method in a dual beam FIB-SEM system, displayed in Figure 1-9.[41] Imaging live in SEM mode while milling and welding enables much higher magnifications than optical microscopy. It also provides more control to the technique. The benefit of live milling ensures the area of interest can be drift corrected if needed, preventing any unwanted milling.

These three main lift-out techniques have been compared and the advantages and disadvantages discussed.[43] The *in-situ* lift-out method has a 90-100% success yield, as opposed to the 50 – 90% success yield of the *ex-situ* method. The trench method has a 100% success yield once the slice has been prepared mechanically. However, there are a lot of drawbacks with this method including destruction to the surrounding sample and limited tilt in the TEM. The advantages of the *in-situ* method include; the possibility of plan-view sections as well as further low-energy milling if necessary.[43]

Among these lift-out techniques, the most used and beneficial technique, which is employed throughout this thesis, is the latter technique of *in-situ* lift-out with micromanipulator bonding. The outline of this technique is explained further in the experimental methods, chapter 3.

1.5.6.4 Reducing FIB Damage

Due to the increasing demand for extremely high-quality lamellae for high-resolution S/TEM imaging and analysis, sample preparation needs to be continually improving. FIB lamella preparation is a popular and commonly used technique but its high beam energies during milling cause damage to the sample creating disruptions to the lattice of the material and complete amorphous regions due to ion implantation.[44], [45] Typically amorphous regions can range between 20 – 40 nm depending on the sample, tilt and energy of the beam.[46] For electron transparent lamellae used within TEM this is not of a high enough standard to obtain high-resolution micrographs.

For this reason the *in-situ* lift-out technique previously described can have many different iterations, which help reduce the damage caused by FIB milling. This damage was seen to significantly reduce by using reduced ion beam energies as an alternative to 30 keV.[47] By slowly reducing the beam energy to as low as 5 keV, the layer of amorphisation can reduce significantly.[48]

In combination with a reduction in FIB beam energies, altering the angle of incidence of the FIB probe can also significantly reduce the damage experienced by the lamella. Schaffer *et al.* details an inverted triangle technique, which incorporates the use of varying exaggerated angles of incidence to the FIB, ±7°. This creates a wedge, which protects the area of interest being polished while also preserving more of the protective Pt layer for the lower beam energies of 2/5 keV, which have broader beams.[49]

An alternative to lowering FIB beam energies is using an Ar^+ ion milling beam to reduce FIB induced damage/amorphisation in the sample. It has been proven to reduce damaged layers by FIB milling for TEM imaging [50] and EELS analysis.[34] This method is analogous to the mechanical preparation method, where a final Ar^+ polish is performed prior to TEM analysis.

Current Ar^+ ion milling technology has greatly improved and now it is possible to image the lamella prior to ion beam polishing and pin point more accurately the area in which milling should occur, with consistently lower beam energies (100 – 500 eV) and greater glancing angles (-15° – 20°).[51]-[53]

1.5.6.5 New/Alternative Preparation Methods

There are a number of alternative preparation techniques to the typical FIB *in-situ* lift-out technique documented in this chapter and described at length throughout this thesis. For example using neon (Ne) ion milling and polishing for TEM preparation doesn't reduce the damage caused by FIB milling significantly, but provides more precise milling and may be useful in cases where any Ga contamination would be detrimental to the specimen.[54]

Another alternative to traditional Ga^+ or Ar^+ ion milling is xenon (Xe) Plasma FIB. The use of Xe^+ by a plasma ion source (i-FIB) enables much faster milling times and also the preparation of lamellae with much larger dimensions, 100 µm x 50 µm as opposed to 20 µm x 10 µm on a Ga^+ FIB. The Xe^+ is more beneficial in terms of large milling areas and rough milling settings, but does not have the same polishing method as Ga^+ FIB due to its increased spot size. However, it has been noted that after using a 30 keV Xe^+ beam, atomic resolution TEM at 300 kV has been obtained. This proves very exciting for the potential pristine samples that could be prepared using lower beam energies.[55]

There are not just different ion species that can be used to prepare *in-situ* cross-sectional TEM lamellae. There are also continually new and exciting cutting edge ideas and geometries being created and developed to prepare lamellae in faster, less damaging and more efficient ways. For example, using a frame lamella structure to support the preparation of both plan- and side- view sections of core shell NWs for TEM analysis.[56]

Another unique method of avoiding FIB damage is a novel masking technique called the umbrella method. This consists of protecting a sensitive area from re-deposition and ion implantation by temporarily placing an optimised block of PDMS on the surface during the milling step.[57] Different milling geometries can also be effectively used to avoid FIB damage and create site-specific plan-view specimens as well as cross-sectional.[58], [59]

1.6 Thesis Outline

This thesis work was industry-led with Intel determining the set goals and outputs of the project on a monthly basis. With this in mind, it is important to note that the overall objectives and outcomes of this PhD work were mainly focused on the production and optimization of as many lamellae of the Cu film and NWs as possible in order to obtain the best possible sample for high-resolution TEM analysis and by extension understand the film microstructure. As opposed to pursuing an in-depth study into the intricate details of the grain boundary structure and potential dopants and how these correlate with the STM data and simulations created, the primary focus of this PhD work became centralized around lamella preparation; both optimization of current adopted methods and also creating and developing novel techniques for various *in-situ* TEM techniques.

The main characterisation technique used throughout was S/TEM. Both Energy-dispersed X-ray (EDX) and Electron Energy-loss Spectroscopies (EELS) were used as complementary techniques to both these imaging modes. These techniques and imaging modes are discussed in more detail in chapter 2. Both Electron Backscattered Diffraction (EBSD) and Transmission Kikuchi Diffraction (TKD) were used to help identify and verify grain boundary misorientation angles and grain orientation of both Cu films and NWs, which is discussed further in chapter 4 and 5.

The main experimental methods used throughout the PhD work are outlined in Chapter 3. This predominantly centres around a detailed and comprehensive description of the traditional and most commonly used lamella preparation techniques throughout this thesis and describes the exact angles, time frames, beam voltages etc. that were used for the preparation of almost all lamellae within this project work.

Chapter 4 discusses the optimization of cross-sectional lamella preparation using Focused Ion Beam (FIB) milling of Cu films. These were 40 nm Cu films on 7 nm SiO_2 on a Si substrate. The purpose of evaporating Cu on a dielectric layer such as SiO_2 was to analyse the Cu films in isolation with no potential interference from barrier layers. Once the lamella preparation had been optimized, characterisation was performed using both TEM and STEM imaging and analysis techniques. The benefits and drawbacks of this particular sample are discussed in detail. Cu films were initially analysed as a testing ground for analysing the Cu microstructure

on the nanoscale and examining whether it was possible to correlate the surface grain information with the cross-sectional, i.e. correlating both C-AFM and STM surface information with the cross-sectional TEM data.

A 50 nm Cu film was prepared at the Intel fabrication facility using Physical Vapour Deposition (PVD) sputtered Cu on a 7 nm Ta barrier layer on a Si substrate. Chapter 5 discusses in detail the difference in sample quality and overall sample characterisation with this alternatively prepared sample with the inclusion of a barrier layer. The optimization of the cross-sectional lamella preparation and also the various methods and initial experimentation employed to prepare high-quality plan-lamella for S/TEM imaging and analysis are outlined and discussed. Due to the successful preparation of plan-view lamellae of the Cu film using FIB milling, through various different methods, a direct correlation of the surface grains and grain boundary information obtained through STM and C-AFM could be achieved. This chapter also outlines the site-specific lamella preparation of Cu NWs on a proprietary liner along with the characterisation of the microstructure of these 100 nm wide Cu NWs throughout the depth of the wire.

After annealing the Cu film for STM analysis, it was observed that the Cu film de-wetted from the substrate. This was investigated through *in-situ* TEM annealing of a lamella cross-sectional of the Cu film prior to annealing. However, the primary focus of this work was in fact the lamella preparation for this *in-situ* TEM analysis. Chapter 6 focuses primarily on the novel *in-situ* lamella fabrication technique, which was created and developed to cater for lamella mounting on MEMS devices for *in-situ* TEM analysis. It describes in detail the attempted trial of the current conventions for lamella mounting and the issues and concerns with this current technique and outlines the method and steps of the novel fabrication technique created over the course of this PhD work. It also details the *in-situ* TEM annealing analysis of these successfully mounted lamellae through imaging and EDX spectroscopy.

The final chapter contains conclusions from all of the chapters detailed above and also contains some suggestions and preliminary data for future work. This is also followed by an appendix and attached memory stick with videos detailing FIB cross-sections and lamella lift-outs.

1.7 Bibliography

[1] G. E. Moore, “Cramming more components onto integrated circuits,” *IEEE SSCS Newsletter*, pp. 1–3, 2008.

[2] “https://en.wikipedia.org/wiki/Transistor_count,” *online*.

[3] A. A. Vyas, C. Zhou, and C. Y. Yang, “On-Chip Interconnect Conductor Materials for End-of-Roadmap Technology Nodes,” *IEEE Trans. Nanotechnology*, vol. 17, no. 1, pp. 4–10, 2018.

[4] “‘The Manufacturing Process’ - Berkeley Notes On IC Design,” pp. 1–30, 2000.

[5] J. P. Gambino, “Copper Interconnect Technology for the 22 nm Node,” *Proc. IEEE*, pp. 1–2, 2011.

[6] H. Havemann, R. H. Havemann, J. A. Hutchby, and J. A. Hutchby, “High-performance interconnects: an integration overview,” *Proc. IEEE*, vol. 89, no. 5, pp. 586–601, 2001.

[7] K. Khoo, J. Onuki, T. Nagano, Y. Chonan, H. Akahoshi, T. Tobita, M. Chiba, T. Saito, and K. Ishikawa, “Influence of Grain Size Distributions on the Resistivity of 80 nm Wide Cu Interconnects,” *MATERIALS TRANSACTIONS*, vol. 48, no. 3, pp. 622–624, 2007.

[8] W. Zhang, O. Richard, B. Brijs, R. Palmans, L. Froyen, K. Maex, and S. H. Brongersma, “Influence of the electron mean free path on the resistivity of thin metal films,” *Microelectronic Engineering*, vol. 76, no. 1, pp. 146–152, 2004.

[9] W. Wu, S. H. Brongersma, M. Van Hove, and K. Maex, “Influence of surface and grain-boundary scattering on the resistivity of copper in reduced dimensions,” *Appl. Phys. Lett.*, vol. 84, no. 15, pp. 2838–2840, 2004.

[10] Z. W. Yang, D. H. Zhang, C. Y. Li, C. M. Tan, and K. Prasad, “Barrier layer effects on reliabilities of copper metallization,” *Thin Solid Films*, vol. 462, pp. 288–291, 2004.

[11] H. Veendrick, *Deep Submicron CMOS ICs: From Basics to ASICs*. pp. 121–122, 1998.

[12] K. C. Saraswat, “Scaling of Minimum Feature size and Chip Area Lecture Notes,” pp. 2–3, 1990.

[13] P. K. Saraswat, “Interconnect Scaling Course Notes,” pp. 1–32, 2005.

[14] B. Li, T. D. Sullivan, T. C. Lee, and D. Badami, “Reliability challenges for copper interconnects,” *Microelectronics Reliability*, vol. 44, no. 3, pp. 365–380, 2004.

[15] C. K. Hu, L. Gignac, E. Liniger, B. Herbst, D. L. Rath, S. T. Chen, S. Kaldor, A. Simon, and W. T. Tseng, “Comparison of Cu electromigration lifetime in Cu interconnects coated with various caps,” *Appl. Phys. Lett.*, vol. 83, no. 5, pp. 869–871, 2003.

[16] M. A. Nicolet, “Diffusion Barriers in Thin Films,” *Thin Solid Films*, vol. 52, pp. 415–443, 1978.

[17] Z. H. Cao, K. Hu, and X. K. Meng, “Diffusion barrier properties of amorphous and nanocrystalline Ta films for Cu interconnects,” *J. Appl. Phys.*, vol. 106, no. 11, pp. 113513–6, 2009.

[18] C. S. Hau-Riege, “An introduction to Cu electromigration,” *Microelectronics Reliability*, vol. 44, no. 2, pp. 195–205, 2004.

[19] J. R. Black, “Mass Transport of Aluminium by momentum exchange with conducting electrons,” presented at the Proceedings of the Annual Reliability Physics Symposium, pp. 1–6, 1967.

[20] D. Burgess and A. Analysis, “ Electromigration History and Failure Analysis,” *Proc. IEEE*, pp. 1–6, 2014.

[21] J. M. E. Harper, E. G. Colgan, C. K. Hu, P. Hummel, L. P. Buchwalter, and C. E. Uzoh, “Materials Issues in Copper Interconnections,” *MRS Bull.*, vol. 19, no. 8, pp. 23–29, 1994.

[22] J. W. Lim, K. Mimura, and M. Isshiki, “Thickness dependence of resistivity for Cu films deposited by ion beam deposition,” *Applied Surface Science*, vol. 217, no. 1, pp. 95–99, 2003.

[23] A. E. Yarimbiyik, A. Emre Yarimbiyik, H. A. Schafft, H. A. Schafft, R. A. Allen, M. D. Vaudin, and M. E. Zaghloul, “Experimental and simulation studies of resistivity in nanoscale copper films,” *Microelectronics Reliability*, vol. 49, no. 2, pp. 127–134, 2009.

[24] J. S. Chawla, F. Gstrein, K. P. O'Brien, J. S. Clarke, and D. Gall, “Electron scattering at surfaces and grain boundaries in Cu thin films and wires,” *Phys. Rev. B*, vol. 84, no. 23, pp. 235423–10, 2011.

[25] W. Steinhögl, G. Schindler, G. Steinlesberger, and M. Engelhardt, “Size-dependent resistivity of metallic wires in the mesoscopic range,” *Phys. Rev. B*, vol. 66, no. 7, pp. 075414–4, 2002.

[26] D. B. Williams and B. Carter, *Transmission electron microscopy*, vol. 13., pp. 173–191, 1973.

[27] “https://en.wikipedia.org/wiki/Electrical_discharge_machining,” *online*.

[28] E. Muller and D. Abou-Ras, "Preparation of cross-section samples for transmission electron microscopy (TEM)," *Elektronenmikroskopie-Zentrum der ETH Zurich (EMEZ),* pp. 1–20, 2004

[29] H.W. Cha, M.C. Kang, K. Shin, and C.W. Yang, "Transmission Electron Microscopy Specimen Preparation of Delicate Materials Using Tripod Polisher," *AM*, vol. 46, no. 2, pp. 110–115, 2016.

[30] J. P. McCaffrey and Á. Barna, "Preparation of Cross-Sectional TEM Samples for Low-Angle Ion Milling," *Microsc. Res. Tech.*, vol. 36, pp. 362–367, 1997.

[31] A. Barna, B. Pécz, and M. Menyhard, "Amorphisation and surface morphology development at low-energy ion milling," *Ultramicroscopy*, vol. 70, no. 3, pp. 161–171, 1998.

[32] L. D. Madsen, L. Weaver, and S. N. Jacobsen, "Influence of Material Properties on TEM Specimen Preparation of Thin Films," *Microsc. Res. Tech.*, vol. 36, pp. 354–361, 1997.

[33] S. Bhattacharyya, "TEM Sample Preparation Course Notes", pp 12, 2017.

[34] N. Miyajima, C. Holzapfel, Y. Asahara, L. Dubrovinsky, D. J. Frost, D. C. Rubie, M. Drechsler, K. Niwa, M. Ichihara, and T. Yagi, "Combining FIB milling and conventional Argon ion milling techniques to prepare high-quality site-specific TEM samples for quantitative EELS analysis of oxygen in molten iron," *J Microsc*, vol. 238, no. 3, pp. 200–209, 2009.

[35] R. M. Langford and A. K. Petford-Long, "Preparation of transmission electron microscopy cross-section specimens using focused ion beam milling," *J. Vac. Sci. Technol. A*, vol. 19, no. 5, pp. 2186-2193, 2001.

[36] L. A. Giannuzzi and F. A. Stevie, "A review of focused ion beam milling techniques for TEM specimen preparation," *Micron*, vol. 30, no. 3, pp. 197–204, 1999.

[37] T. Yaguchi, T. Kamino, T. Ishitani, and R. Urao, "Method for Cross-sectional Transmission Electron Microscopy Specimen Preparation of Composite Materials Using a Dedicated Focused Ion Beam System," *Microsc Microanal*, vol. 5, pp. 365–370, 1999.

[38] T. Yaguchi, T. Kamino, M. Sasaki, G. Barbezat, and R. Urao, "Cross-sectional Specimen Preparation and Observation of a Plasma Sprayed Coating Using a Focused Ion Beam/Transmission Electron Microscopy System," *Microsc Microanal*, vol. 6, pp. 218–223, 2000.

[39] P. R. Munroe, "The application of focused ion beam microscopy in the material

sciences," *Materials Characterization*, vol. 60, no. 1, pp. 2–13, 2009.

[40] L. A. Giannuzzi and F. A. Stevie, "Introduction to Focused Ion Beams: Instrumentation, Theory, Techniques and Practice," pp. 201–245, 2005.

[41] R. M. Langford and C. Clinton, "In situ lift-out using a FIB-SEM system," *Micron*, vol. 35, no. 7, pp. 607–611, 2004.

[42] L. A. Giannuzzi, J. L. Drown, S. R. Brown, R. B. Irwin, and F. A. Stevie, "Focused Ion Beam Milling and Micromanipulation Lift-Out for Site Specific Cross-Section Tem Specimen Preparation," *MRS Proc.*, vol. 480, pp. 19–27, 1997.

[43] R. M. Langford and M. Rogers, "In situ lift-out: Steps to improve yield and a comparison with other FIB TEM sample preparation techniques," *Micron*, vol. 39, no. 8, pp. 1325–1330, 2008.

[44] C. A. Volkert and A. M. Minor, "Focused Ion Beam Microscopy and Micromachining," *MRS Bull.*, vol. 32, no. 5, pp. 389–399, 2007.

[45] J. Mayer, L. A. Giannuzzi, T. Kamino, and J. Michael, "TEM Sample Preparation and Damage," *MRS Bulletin*, vol. 32, no. May, pp. 400–407, 2007.

[46] N. I. Kato, "Reducing focused ion beam damage to transmission electron microscopy samples," *Journal of Electron Microscopy*, vol. 53, no. 5, pp. 451–458, 2004.

[47] L. A. Giannuzzi, R. Geurts, and J. Ringnalda, "2 keV Ga+ FIB Milling for Reducing Amorphous Damage in Silicon," *Microsc Microanal*, vol. 11, no. 2, pp. 1–2, 2005.

[48] M. Baram and W. D. Kaplan, "Quantitative HRTEM analysis of FIB prepared specimens," *J Microsc*, vol. 232, pp. 395–405, 2008.

[49] M. Schaffer, B. Schaffer, and Q. Ramasse, "Sample preparation for atomic-resolution STEM at low voltages by FIB," *Ultramicroscopy*, vol. 114, pp. 62–71, 2012.

[50] Z. Huang, "Combining Ar ion milling with FIB lift-out techniques to prepare high quality site-specific TEM samples," *J Microsc*, vol. 215, no. 3, pp. 219–223, 2004.

[51] M. Mitome, "Ultrathin specimen preparation by a low-energy Ar-ion milling method," *Microscopy (Tokyo)*, vol. 62, no. 2, pp. 321–326, 2013.

[52] J. Scott, F. T. Docherty, M. MacKenzie, W. Smith, B. Miller, C. L. Collins, and A. J. Craven, "Sample preparation for nanoanalytical electron microscopy using the FIB lift-out method and low energy ion milling," *J. Phys.: Conf. Ser.*, vol. 26, no. 1, pp. 223–226, 2006.

[53] A. Lotnyk, D. Poppitz, U. Ross, J. W. Gerlach, F. Frost, S. Bernütz, E. Thelander,

and B. Rauschenbach, “Focused high- and low-energy ion milling for TEM specimen preparation,” *Microelectronics Reliability*, vol. 55, no. 9, pp. 2119–2125, 2015.

[54] T. C. Pekin, F. I. Allen, and A. M. Minor, “Evaluation of neon focused ion beam milling for TEM sample preparation,” *J Microsc*, vol. 264, no. 1, pp. 59–63, 2016.

[55] A. Delobbe, O. Salord, T. Hrncir, A. David, P. Sudraud, and F. Lopour, “High Speed TEM Sample Preparation by Xe FIB,” *Microsc Microanal*, vol. 20, no. 3, pp. 298–299, 2014.

[56] F. Lenrick, M. Ek, D. Jacobsson, M. T. Borgstrom, and L. R. Wallenberg, “FIB Plan and Side View Cross-Sectional TEM Sample Preparation of Nanostructures,” *Microsc Microanal*, vol. 20, pp. 133–140, 2014.

[57] T. Vermeij, E. Plancher, and C. C. Tasan, “Preventing damage and redeposition during focused ion beam milling: The umbrella method,” *Ultramicroscopy*, vol. 186, pp. 35–41, 2018.

[58] H. C. Floresca, J. Jeon, J. G. Wang, and M. J. Kim, “The Focused Ion Beam Fold-Out: Sample Preparation Method for Transmission Electron Microscopy,” *Microsc Microanal*, vol. 15, pp. 558–563, 2009.

[59] C. Li, G. Habler, L. C. Baldwin, and R. Abart, “An improved FIB sample preparation technique for site-specific plan-view specimens: A new cutting geometry,” *Ultramicroscopy*, vol. 184, no. Part A, pp. 310–317, 2018.

2. Instrumentation and Theory

2.1 Ion Microscopy - Focused Ion Beam

Lamella preparation was performed on a Zeiss Auriga dual beam instrument. Dual beam indicates it contains both a Focused Ion Beam (FIB) and Scanning Electron Microscope (SEM) column. This is to ensure live milling during sample preparation. The SEM column is mounted vertically while the FIB column is mounted at an angle with respect to the vertical SEM column, 54° for the Zeiss Auriga, schematic shown in Figure 2-1. It uses a gallium (Ga) Liquid Metal Ion Source (LMIS) and Gas Injection System (GIS).

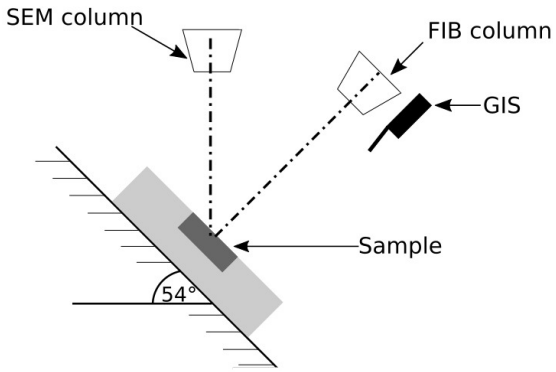

Figure 2-1: Schematic of dual-beam Focused Ion Beam/Scanning Electron Microscope.

2.1.1 Liquid Metal Ion Source

2.1.1.1 Why use Gallium?

There are many reasons for using a Ga^+ LMIS source:

- Ga has a low melting temperature (29.8°), which helps simplify the system as it reduces the chemical and physical interactions between the liquid metal and the field emitter.
- Gallium has an atomic mass of (69.72). This is an intermediate mass, which makes Gallium ions suitable for efficient sputtering with a wide range of substrates.
- Low volatility at the melting point conserves the supply of metal and yields a long source life.

- Low surface free energy promotes viscous behavior on the tungsten (W) substrate.
- Its low vapor pressure allows Ga to be used in its pure form instead of an alloy source.
- Excellent mechanical, electrical and vacuum properties.
- Emission characteristics enable high angular intensity with a small energy spread.
- Ga has a very fine probe size.[1] [2]

The LMIS has the ability to provide a source ions of ~5 nm in diameter. The LMIS contains a W needle attached to a reservoir, which stores the metal source material, here Gallium. The emission of the Ga+ ions occurs as follows: Ga is heated, flows and wets a W needle. The needle typically has a radius between 2 – 5 μm. Once the Ga is heated, an electric field is applied to the end of the wetted tip causing the Ga to form a Taylor-Gilbert cone of a radius of approximately 2 – 5 nm.[1] This creates a very high spatial coherence, i.e. a very focusable beam.[3]

The conical shape results from the balancing of the electrostatic and surface tension force due to the applied electric field. The current density of ions that may be extracted is of the order of ~ 1 x 10^8 A/cm^2.[1]

2.1.2 Ion Column

To reach a probe size of 10 nm the source needs to be de-magnified. This is done through the column. As the Ga^+ ions are extracted from the LMIS, they are accelerated through a potential down the ion column. Typical accelerating voltages can range between 5 – 50 kV. These will vary throughout the experimental process. This will be explained in more detail in chapter 3 discussing sample preparation.[1], [2]

The simplest most widely used ion beam columns consist of two electrostatic lenses (a condenser and an objective lens).[4] Electrostatic lenses are used as opposed to electromagnetic for electron beam due to the heavy nature of the ions in comparison to electrons.[2] Condenser lenses define the beam (probe forming lens) and objective lenses focus on the sample. There are a range of apertures of varying diameters to also help in defining the beam size and current.[4] The beam aperture is the most important part of the

column. It controls the beam current incident on the sample, see Figure 2-2. This means it controls the milling rate and image quality. At low beam current apertures the beam diameter is reduced which produces higher resolution images.[5] The larger beam diameter allows beam currents of several nanoamps (nA) to interact with the sample causing sputtering of material. A range of beam currents can be utilized in the FIB, from a few pA to as high as 20 – 30 nA. It contains cylindrical octopole lenses, which have multiple functions including stigmation correction, beam deflection and alignment. Beam blankers deflect the beam quickly off the sample onto a beam stop such as a Faraday cup.[2], [4], [5]

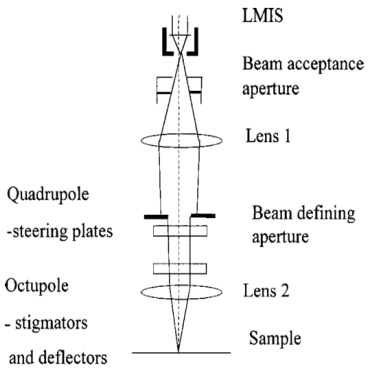

Figure 2-2: Schematic of Focused Ion Beam column.[6]

2.1.3 Detectors

Two detectors are usually used to image in the FIB. A multi-channel plate (in-lens) mounted directly above the sample and an electron multiplier (secondary electrons/ions) mounted at a 45° angle to the incident beam. The secondary electron (SE) detector can be biased to detect either secondary electrons or secondary positive ions emitted from the sample. The SE detector in the Auriga operates at a potential of 300 V. Secondary ion imaging provides channeling contrast for different grain orientations for polycrystalline material. The Auriga does not have the capability of secondary ion imaging.[1], [5]

2.1.4 Charging

Sample charging can be caused by the bombardment of positive Ga ions to the sample. If the sample is insulating, it will accumulate excessive positive charge. This means any emitted secondary electrons will be attracted back to the now positive surface and not to the detector.

The regions which are charging will appear darker in the FIB SE image, as the SEs from this region aren't reaching the detector.[1]

2.1.5 Gas Injection System

The GIS can be used in conjunction with the ion beam to provide site-specific deposition of metals or insulators or to provide enhanced etching capabilities. Metals are deposited using ion beam-induced deposition (IBID). IBID is a process where gas molecules are adsorbed onto the surface of a sample and are dissociated in the presence of an ion beam to form films of material that will deposit and adhere to the sample, see Figure 2-3.[5] Repeated adsorption and decomposition result in the buildup of material in the ion scanned region. A similar process is used for electron beam-induced deposition (EBID), which is essential for initial deposition on sample surface, due to ion damage caused by beam directly interacting with the surface. As detailed in the section 3.1.2, chapter 3, EBID is performed prior to IBID.[1], [5]

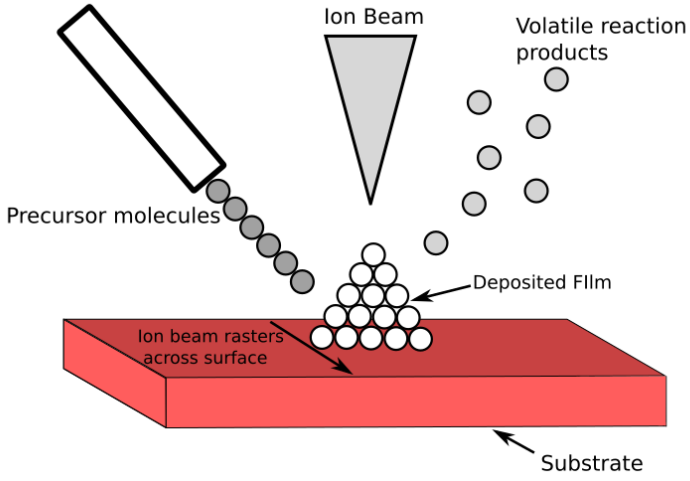

Figure 2-3: Schematic of Ion Beam Induced Deposition adapted from Avishai et al.[7]

2.1.6 Ion-Solid Interactions

Ion-solid interactions are the core of using a FIB. The ability to mill, image and deposit material using a FIB is due to the very nature of ion-solid interactions. When an ion collides with the solid, it loses kinetic energy through interactions with the sample atoms. This can result in many different processes occurring: atomic sputtering and ion emission, ion reflection and

back scattering, electron emission, electromagnetic radiation, sample damage and sample heating.[1]

When a solid material is bombarded with an ion beam, two categories of mechanisms slow down the ion and dissipate the energy: elastic (nuclear energy loss) and inelastic (electron energy loss) collisions.[1] With inelastic interactions, the energy lost from the incoming ion can generate secondary electrons, x-rays, cathodoluminescence and phonons (heat), see Figure 2-4 (a). In elastic interactions, this energy can be transferred as translational energy to screened target atoms resulting in displacement of lattice atoms, defects generation (amorphisation) and sputtering.[2] Sputtering in FIB processes typically occurs in energy ranges dominated by nuclear energy losses. Therefore, we focus mainly on the elastic collision processes here.[2], [4]

2.1.6.1 Collision Cascade

If the translational energy transferred to a target atom during a collision exceeds a critical value called the displacement energy, the atom will be knocked out of its original site.[4] The initial recoil atom may have sufficient energy to displace further sample atoms. These are called secondary recoils (collision cascade). This generates a volume containing a large number of atoms with excess kinetic energy, see Figure 2-4 (b).[4] If a displacement collision occurs near the surface, the recoil atom may be emitted from the solid and result in sputtering. The displacement energy is typically of the order of 20 eV, which is much larger than the binding energy for the atoms (approximately 1 eV).[1], [4], [8], [9], [10]

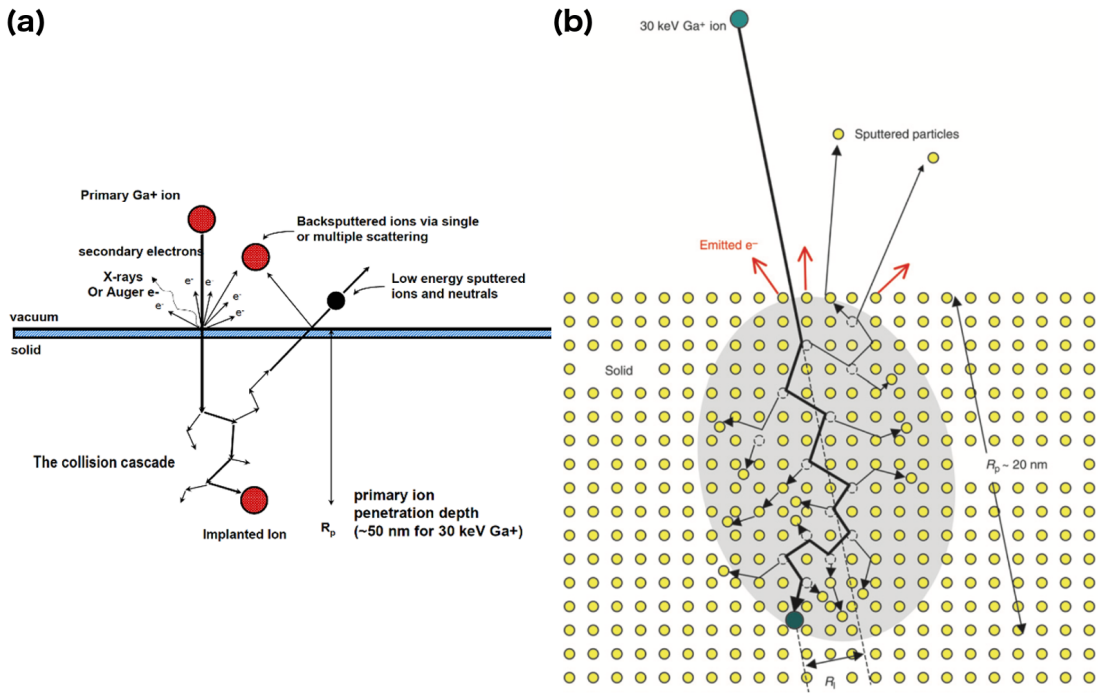

Figure 2-4: (a) Diagram of ion-solid interactions [11] and (b) schematic illustration of a collision cascade generated by a 30 keV Ga^+ ion incident on a crystal lattice, showing the damage created in the collision cascade volume, and the projected range R_p and lateral range R_l of the implanted ion.[4]

The stopping and range of matter is an integral part of understanding the ion-solid interactions. Ion interactions can be modeled using Monte Carlo simulations. This is done using Transport of Ions in Matter (TRIM) software. Figure 2-5 (c) – (f) displays the Ga ion penetration depth in copper (Cu) for an angle of incidence of 88° and beam energy while Figure 2-5 (b) displays the sputter yield of the various beam energies at incidence angles: 89°, 88°, 83° and 0°. Figure 2-5 (a) displays a schematic of the geometry of the incident angle.[12]

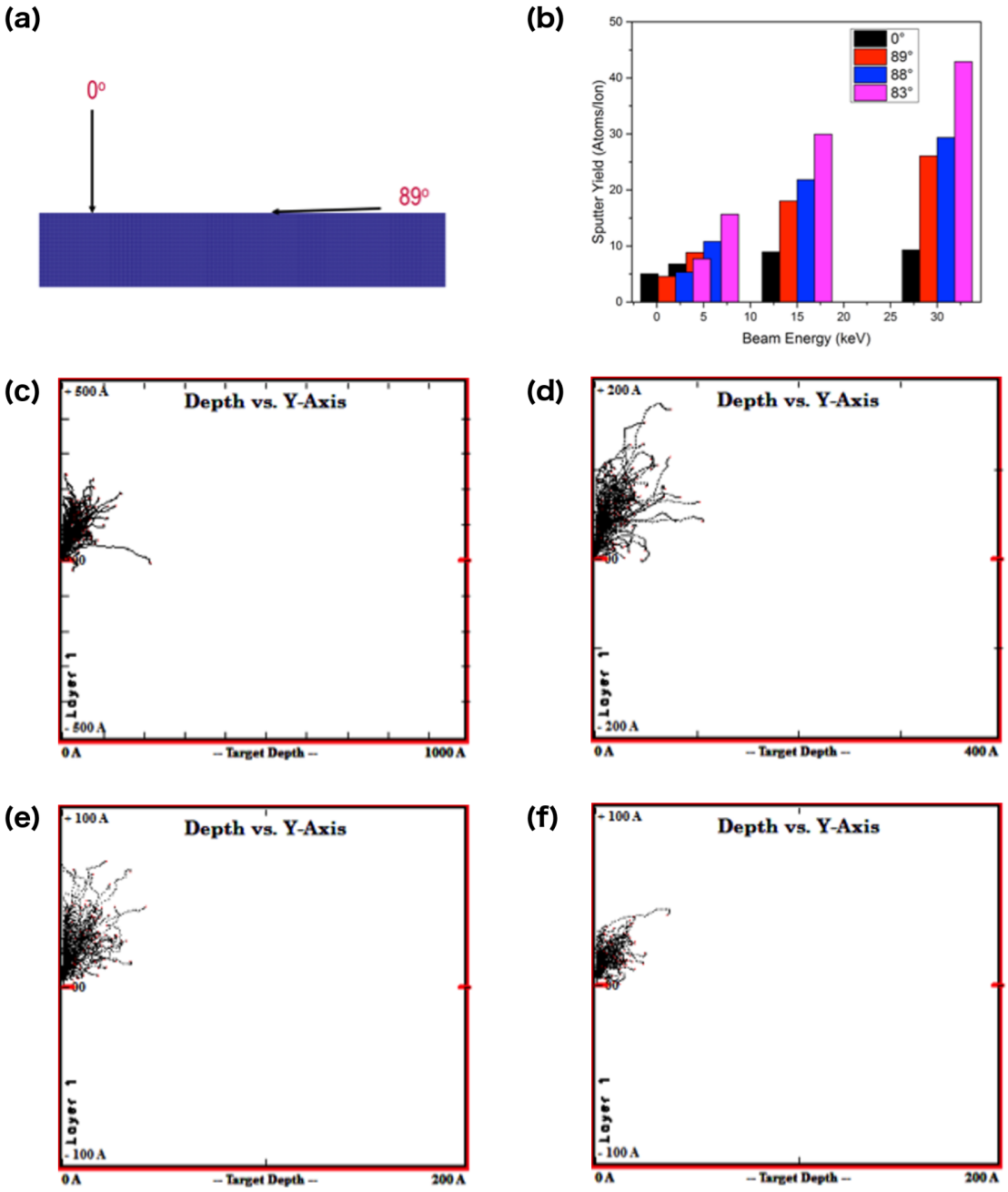

Figure 2-5: (a) Ion-Solid Incidence Angle Convention [11], (b) Graph of Sputter Yield against Beam Energy generated using data from TRIM software. TRIM calculations of penetration depth at differing beam energies (500 ions) at an angle of incidence of 88° (c) Ga 30 keV (d) Ga 15 keV (e) Ga 5 keV (f) Ga 2 keV.

2.2 Electron Microscopy

Electron microscopy was developed by Ruska and Knoll in 1920's due to the resolution limit of optical microscopy being ~ 200 nm. Although electron microscopy provides much higher resolution than that of the visible light microscope (VLM), it also provides a range of other structural and chemical information about materials, which can be discovered through the numerous interactions, which occur by the electron interaction with the sample. It generates a wide range of interactions such as elastically and inelastically scattered secondary, backscattered, and Auger electrons as well as characteristic X-rays, as can be seen in Figure 2-6. The early stages of research in electron microscopy in the 30's and 40's led to the development of two distinct groups of electron microscopy: transmission electron microscopy (TEM), which also includes scanning transmission electron microscopy (STEM) and SEM. The former deals with the forward scattered electrons while the latter deals with the more surface-sensitive interactions such as the secondary and backscattered electrons. [13], [14]

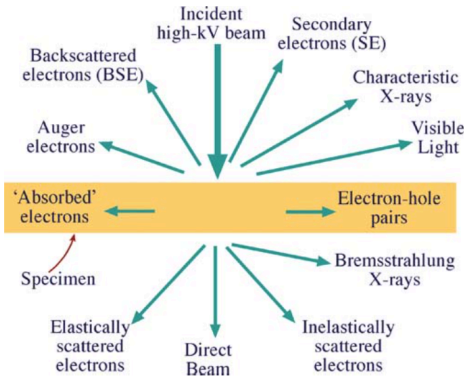

Figure 2-6: Schematic of the different signals generated when a high intensity electron beam interacts with a sample.[15]

The diffraction limit of electron microscopy is given by the Rayleigh criterion, relating the minimum resolving distance, δ and the wavelength of the imaging wave, λ:

$$\delta = \frac{0.61\lambda}{\mu Sin\beta} \qquad (2.1)$$

where μSinβ is the numerical aperture, for a transmission electron microscope $\frac{0.61\lambda}{\mu Sin\beta} \approx \frac{0.61}{\beta}$ since μ ≈ 1 in a vacuum and Sinβ ≈ β when β is small (approximately 10^{-2} radians). The De Broglie wavelength is related to the accelerating voltage by the following:

$$\lambda = \frac{h}{\left[2m_0 eV\left(1 + \frac{eV}{2m_0 c^2}\right)\right]^{\frac{1}{2}}} \qquad (2.2)$$

Inputting values into this equation, would suggest a wavelength of close to 2 pm for an accelerating voltage of 300 kV, which will be the typical operating voltage for the TEM imaging and analysis performed throughout this thesis. Unfortunately, this type of value is not consistent with experimentally observed imaging. This is due to aberrations caused by the lenses within the microscope.[13]

2.2.1 Transmission Electron Microscopy

2.2.1.1 Imaging

The TEM instrument contains 3 main sections: the illumination system, the objective lens/stage and the imaging system.

The illumination system consists of the gun and the condenser lenses. This system can be operated in two different modes: parallel beam or convergent beam. Parallel beam refers to traditional TEM mode and convergent refers to STEM.

In parallel mode, the traditional most commonly used mode of TEM, uses its array of electromagnetic lenses to create a parallel beam of electrons, which pass through the sample (transmit). This electron beam collides with the electron transparent sample (<100 nm) and numerous interactions occur, similar to the FIB. There are both elastic and inelastic collisions and of those there are both coherent and incoherent, elastic and inelastic scattering. The different types of scattering can help produce images and data containing different but often complementary information. We can distinguish between imaging mode or diffraction mode as shown in the schematic Figure 2-7.[15], [16]

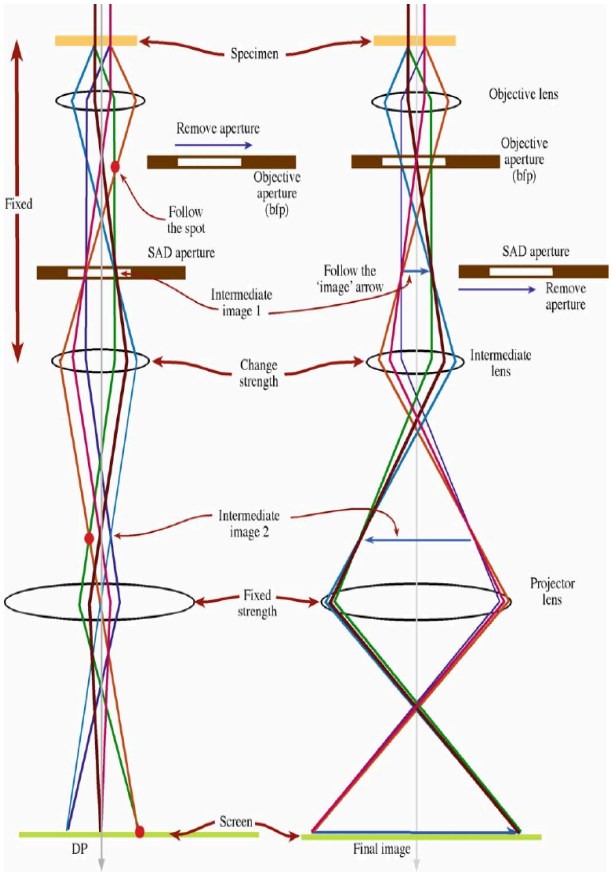

Figure 2-7: Schematic showing diffraction and imaging mode of Transmission Electron Microscope.[15]

2.2.1.2 Amplitude Contrast

As the electron wave passes through the sample its amplitude changes, this gives rise to image contrast, which is the difference in intensity between two adjacent areas. There are two types of amplitude contrast: mass-thickness contrast and diffraction contrast. The apertures in the TEM can be used to select certain transmitted beams and omit others in order to form different types of contrast. After the incident beam interacts with the sample it is transformed into a non-uniform intensity beam. This change in intensity translates into contrast in the image. The diffraction pattern shows this variation in intensity as it separates the direct beam from the diffracted beams, which have been scattered throughout the sample. The diffraction pattern is only showing the electrons, which have undergone Bragg diffraction. By using the objective aperture different beams (direct or diffracted) can be selected to create contrast within the image and highlight certain regions of the sample. This is what leads to bright and dark field imaging. In bright field (BF) imaging the high order diffracted beams are removed, meaning the more diffracted thicker material or defects appear darker. Conversely, in dark field (DF) imaging the beam is tilted so that the diffracted images are allowed to pass through

the aperture. This makes the image predominantly dark with regions of diffraction appearing bright, see Figure 2-8.[15]

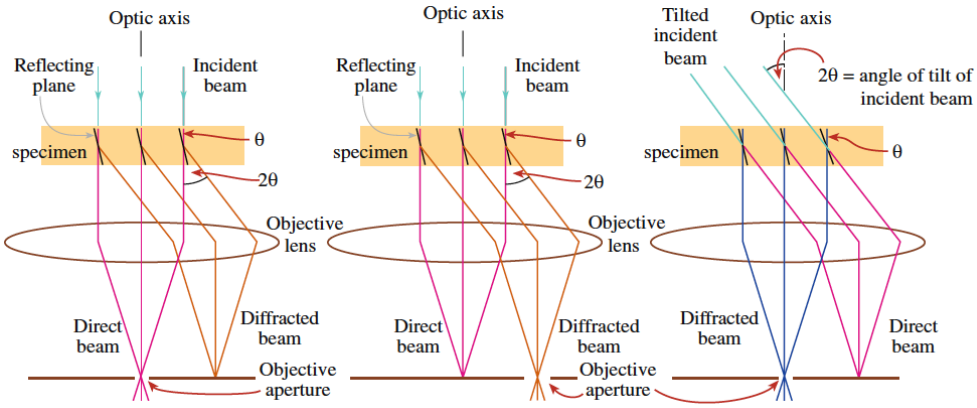

Figure 2-8: Set-up of bright and dark field imaging.[15]

2.2.1.3 Diffraction Patterns

Periodicity in a crystal enables the formation of diffraction patterns. When electrons elastically scatter at the same angle they reach the same position in the back-focal plane (BFP) of the objective lens. This is due to the fact that these scattered electrons are satisfying Bragg's law which states that the electrons will constructively interfere when the following occurs:

$$n\lambda = 2d_{hkl}sin\Theta_B \qquad (2.3)$$

Where n is the integer denoting the diffraction order of the fringe, λ is the wavelength of the incident electrons, d_{hkl} is the lattice spacing of a set of crystal planes in real space and Θ_B is the Bragg angle. The objective lens takes the electrons emerging from the exit surface of the sample and disperses them to create a diffraction pattern in the BFP. This recombines to form an image in the image plane. In order to view the diffraction plane, the imaging system is adjusted so that the BFP is now the object plane of the intermediate lens and the diffraction pattern is then viewed on the image plane. This is extremely useful for determining crystallographic orientation and phase information about the material.[16]

Mass-thickness contrast is due to a difference in the thickness in regions of the sample. It arises from the incoherent elastic scattering (Rutherford scattering) of electrons. As Rutherford scattering is a strong function of the atomic number Z, it is strongly dependent on the mass of the sample and also the thickness of the specimen. In a BF image, thicker regions will appear darker and thinner brighter and vice versa for DF images.[16]

2.2.1.4 Phase Contrast

After passing through the sample, waves of the diffracted beam interfere with each other, creating constructive and destructive interference patterns. This leads to fringes being created, most commonly Moiré patterns. These are formed by two sets of interfering lattice fringes with nearly common periodicities. Lattice fringes are especially important to high-resolution TEM (HRTEM) analysis as the lattice periodicity correlates to the periodicity of the crystal structure. Inserting apertures creates image contrast, but at high magnification it limits the resolution significantly. Therefore to get HRTEM images, phase contrast must be used while imaging. This consists of not using an aperture or using a very large aperture and interpreting the phase of the electron waves after they have been transmitted through the sample. The sensitivity of this contrast is the reason why atomic structure can be imaged in this setting.[16]

2.2.1.5 Aberration Correction

As mentioned earlier in section 2.2, aberrations are present in an electron microscope. There are 3 main types of aberrations which occur in the electron microscope; astigmatism, chromatic aberration and spherical aberration. Astigmatism occurs when the electron spiraling around the optic axis senses a non-uniform magnetic field. Astigmatism can be reduced by using stigmators, small octopoles that introduce a compensating field to counteract the non-uniform field causing the astigmatism.[15]

Chromatic aberration is related to the energy of an electron. It occurs due to the energy spread of the electron beam. This results in electrons of different energies being focused in different planes. Electrons that have experienced a large amount of energy loss are more strongly deflected than those that have lost no energy or considerably less when passing through the sample. This variation causes a disc of least confusion, which has a range of focus points and appears as a smear in the image. [15], [17]

The radius of the disc of least confusion, see Figure 2-9 is calculated as follows:

$$r_{chr} = C_c \frac{\Delta E}{E_0} \beta \qquad (2.4)$$

where C_C is the chromatic aberration coefficient of the lens, ΔE is the energy loss of the electrons, E_0 is the initial beam energy and β is the collection angle. Chromatic aberration is reduced by using a monochromator and a fixed aperture to narrow the energy spread.[15]

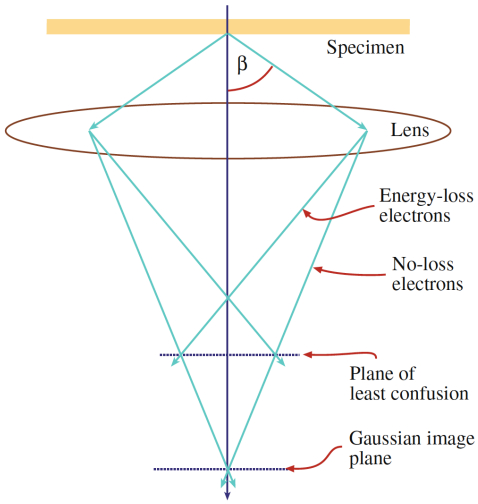

Figure 2-9: The disc of least confusion.[15]

Spherical aberration arises when electrons in trajectories further away from the optic axis are bent more strongly by the lens magnetic field than those rays near the axis. As a result, the point object is imaged as a disk rather than a point. The smallest disk occurs just in front of the Gaussian image plane and is called the spherical aberration disk of least confusion.[18] The diameter of this is given by:

$$d_s = 0.5 C_s \beta^3 \qquad (2.5)$$

where C_s is the spherical aberration coefficient and β is the collection angle. A corrector compensates for spherical aberration by creating a diverging lens, which spreads out the off-axis beams so that they re-converge to a point instead of a disk in the Gaussian-image plane.[15]

2.2.2 Scanning Transmission Electron Microscopy

By combining the TEM and the SEM technology, a STEM is created. STEM mode uses a convergent probe to scan across the sample point by point. The main advantage of using STEM is the Z-contrast mechanism. STEM uses annular detectors beneath the sample, which can detect electrons scattered at high angles. There are 3 different types of detectors used in STEM: bright field (BF), annular dark field (ADF) and high angle annular dark field (HAADF), see Figure 2-10. Z-contrast is obtained by detecting the electrons scattered at high angles, therefore the HAADF detector is used to collect these electrons and create a DF Z-contrast image. The ADF collects electrons that are both Bragg and Rutherford scattered creating a mixture of diffraction and Z-contrast. The BF detector detects the directly transmitted beam and the very low-angle (inelastic incoherently) scattered electrons. These inelastic incoherently scattered electrons are what is used in Electron Energy Loss Spectroscopy (EELS) analysis.[15], [16]

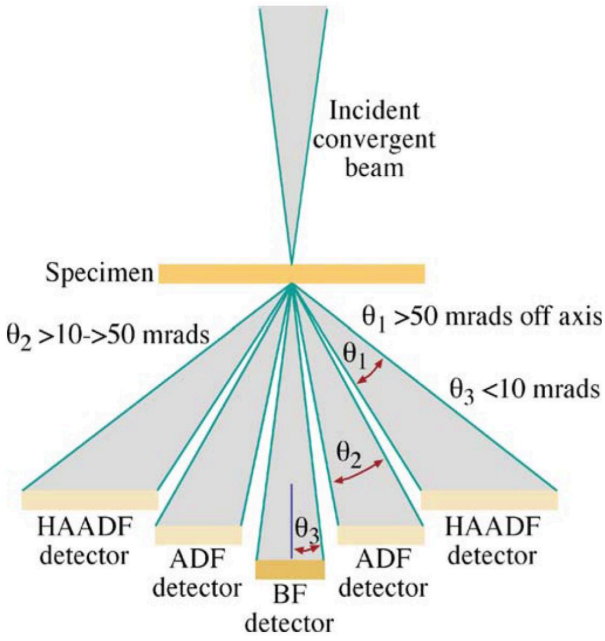

Figure 2-10: Diagram of imaging system and detectors in Scanning Transmission Electron Microscope.[15]

2.2.3 Scanning Electron Microscopy

SEMs operate a lot like a FIB, instead of an ion beam being scanned it is an electron beam. Electrons are emitted from a thermionic, Schottky or field-emission cathode which are

accelerated through a voltage difference between a cathode and an anode. Unlike TEM, SEM can image and analyse bulk specimens.[19]

2.2.3.1 Electron-Specimen Interactions

Similar to TEM and FIB when the electron beam strikes the sample it interacts with the target atoms creating a range of different interactions and collisions. Figure 2-11 (a) shows the most important interaction processes and their interaction volume. The energy spectrum of the electrons emitted consists of contributions from secondary electrons (SEs), backscattered electrons (BSEs) and Auger electrons (AEs). SEs and AEs are highly susceptible to elastic and inelastic scattering and can leave the sample only from a very thin surface layer, usually of the order of a few nanometers. The broad spectrum of BSE between 50 eV and the primary electron energy is caused by the deceleration of electrons that have suffered multiple energy losses and undergone multiple scattering through large angles. Some BSE energies show a pronounced peak followed by plasmon losses, see Figure 2-11 (b). This depends on primary energy, the take-off angle and the tilt of the sample.[19]

2.2.3.2 Detectors

SE and In-lens detectors used have already been mentioned previously. Another detector, which is highly valuable, is the BSE detector. BSE travel in straight trajectories unlike SEs, which means the detectors are mounted with a large collection angle. The most important contrast mechanism of BSE is its dependence on the atomic number, Z. With a detector below the pole piece and with high take-off angles, material contrast is mainly observed, suppressing the topographic contrast. SE detector images also contain material contrast due to the SEs generated by BSE.[19]

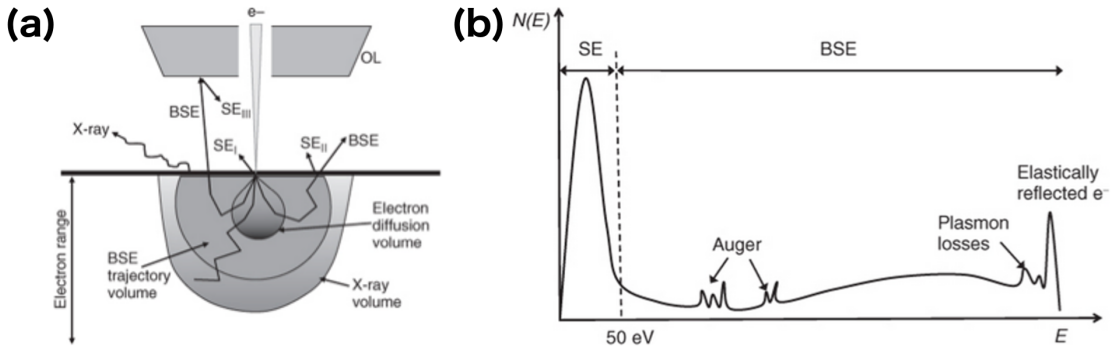

Figure 2-11: (a) Beam/specimen interaction in Scanning Electron Microscope showing the resulting electron trajectories, generated signals and respective interaction volumes [14] and (b) schematic energy spectrum of electrons emitted consisting of secondary electrons with E_{SE} ≤ 50eV, low-loss electrons (LLE) with energy losses of a few hundreds of eV, backscattered electrons with E_{BSE} > 50eV and peaks of Auger electrons (AE).[19]

2.2.4 Electron Backscatter Diffraction/Transmission Kikuchi Diffraction

Electron backscatter diffraction (EBSD) is a SEM technique, in which a stationary electron beam is diffracted by the crystal lattice of the sample and the spherical diffracted beams (Kikuchi cones) are detected by the phosphor screen of the EBSD detector. The formation of Kikuchi cones observed in the EBSD pattern is determined by Bragg's law of diffraction, as seen in Figure 2-12. The ESBD pattern is characteristic of the lattice parameters of the particular crystal and its orientation in space.[20], [21], [22]

EBSD operates by placing a flat highly polished sample at an incident beam angle of 20°, meaning a stage tilt of 70°. It is performed at moderately high beam voltages (between 20 – 30 kV) with typical working distances of between 8 – 10 mm.[20]

EBSD gives a lot of information about grain size, shape, texture, orientation; grain boundary type and misorientation as well as phase information. It can obtain resolution of approximate grain sizes of 100 nm with an increase in resolution available after the use of an added technique called Transmission Kikuchi Diffraction (TKD) or Transmission Electron Backscattered Diffraction (t-EBSD). TKD uses transmission diffraction by using electron-transparent samples in the same geometry as EBSD but with slightly higher accelerating voltages. The advantages of TKD are; a considerably improved lateral spatial resolution of ~10 nm in comparison with ~100 nm for traditional EBSD and also a small energy distribution, which can potentially enable analysis of finer structure than current EBSD methods. The TKD method is high favourable for analysing focused ion beam milled samples, in particular for this particular thesis work, plan-view lamellae.[23]

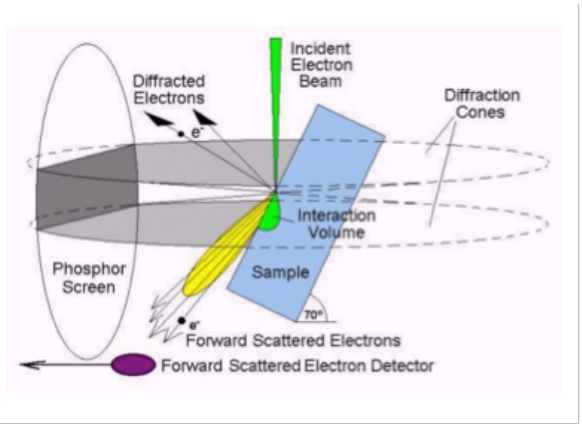

Figure 2-12: Schematic of the electron diffraction and the corresponding Kikuchi diffraction cones.[21]

2.2.5 Energy-dispersive X-Ray Spectroscopy

As mentioned previously, the interaction of electrons with the specimen causes a series of both elastic and inelastic collisions. One of the interactions, which is beneficial for elemental analysis is the emission of X-rays from inelastic scattering.

As an incoming electron in the microscope causes the removal of a core-shell electron, a hole is created, which is then filled by the decaying of another electron to this shell. This decaying of an electron leads to the emission of an X-ray. This emitted X-ray has an equivalent energy to the difference in energy between the two shells and hence can be used to identify specific elements.

The characteristic X-rays of the various electron shells (K, L, M) of specific elements can then be identified through EDX spectroscopy. The EDX spectrometer measures the energy of these characteristic X-rays. This is done through the X-ray being absorbed into an Si/Li semiconductor detector. The energy of these X-rays is converted into electron-hole pairs within the semi-conductor. The quantities of these pairs corresponds to a certain characteristic X-ray energy and hence certain elements are identified through this.

This technique is useful for obtaining compositional information and can be used to analyse individual atoms or averaged over a pixel (STEM) or over an illuminated region (TEM). Information such as bonding etc. cannot be determined. EDX spectra are easier to interpret for qualitative analysis than EELS spectra and have much higher signal-to-noise ratio.[13]

2.2.6 Electron Energy-loss Spectroscopy

EELS is an analytical technique which measures the energy lost by electrons that have been inelastically scattered after interaction with a specimen. The beam of transmitted electrons is directed to a high-resolution electron spectrometer, which separates the electrons according to their kinetic energy and hence produces an electron energy-loss (EEL) spectrum.[24]

An EEL spectrum is comprised of 3 main sections; the zero-loss peak, the low-loss region and the core-loss region, see Figure 2-13. The zero-loss peak comprises of the electrons which have been experienced no loss in energy, elastically forward scattered electrons and excited phonon modes which have experienced energy loss but are below the experimental energy resolution. The zero loss peak is an important feature in calculating the absolute thickness of samples, which will be discussed later in this section.[24], [25]

The low-loss region which typically ranges from 0 to 50 eV, corresponds to the excitation of the electrons in the outermost atomic orbitals. The low-loss region is dominated by plasmon scattering. The core loss region, typically beyond the 100 eV region, corresponds to the excitation of the inner-shell electrons and as inner-shell binding energies are dependent on atomic number, the ionization edges indicate the elements occurring in the spectrum. Core-loss edges also contain chemical information about the elements including valence, oxidation state, bonding information and atomic spacing.[24], [26]

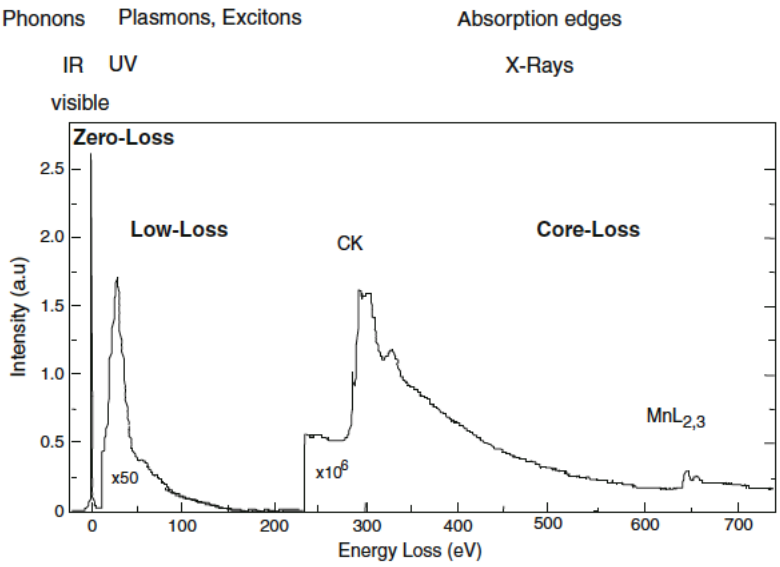

Figure 2-13: A typical Electron Energy-loss spectrum indicating the zero, low and core-loss regions of the spectrum as well as the different interactions and phenomena, which occur at certain characteristic energies.[25]

The EELS log-ratio technique for determining sample thickness was established by Malis *et al.* This ratio technique can give an accuracy of +-20% for inorganic specimens.[27] Sample thickness can be calculated using the following equation:

$$\frac{t}{\lambda} = \ln\left(\frac{I_t}{I_0}\right) \qquad (2.6)$$

Where t is the local thickness, λ is the inelastic mean free path of the primary electron, I_t and I_0 are the integrated intensities of the total and zero loss peaks in the EELS spectrum, respectively. t/ λ provides a measure of the relative thickness across regions of the sample but if absolute thickness is required the inelastic mean free path must be determined.[28]

The inelastic mean free path, λ is dependent on the atomic number Z of the material in question, the incident electron beam energy E_0 in keV and β the collection semiangle in mrad.[27]

The formula to determine λ is as follows:

$$\lambda \approx \frac{106\,F\left(\frac{E_0}{E_m}\right)}{\ln\left(2\beta\,\frac{E_0}{E_m}\right)} \qquad (2.7)$$

Where F is a relativistic factor given by:

$$F = \frac{1 + (\frac{E_0}{1022})}{(1 + \frac{E_0}{511})^2} \qquad (2.8)$$

and E_m is an average energy-loss term and is dependent on the atomic number Z:

$$E_m = 7.6Z^{0.36} \qquad (2.9)$$

2.2.7 Energy-Filtered Transmission Electron Microscopy

In TEM spectrum imaging can be achieved by using energy-filtered TEM (EFTEM). This means, rather than recording a spectrum at each pixel, the beam is dispersed and only electrons of a certain energy window are allowed through a slit to then form an image. EFTEM couples the parallel beam imaging of TEM with the principles of EELS to get a filtered image or an elemental map. Essentially an EFTEM map is an energy slice through a complete STEM-EELS dataset.[13] EFTEM is a great method for quickly mapping the distribution of a single element, or a more complete compositional dataset an be built up by changing the filtered energy across some desired range.[29] EFTEM is useful to acquire relative thickness measurements of a sample. This is done by acquiring an unfiltered and elastic or zero-loss image from the same region under identical conditions. By using the t/ λ equation mentioned in section 2.2.6, a relative thickness can be acquired once the unfiltered and elastic image have been captured.[30]

2.2.8 *In-situ* Transmission Electron Microscopy

In-situ TEM has become an essential technique within the field of material science as real-time observations of dynamic changes within materials becomes increasingly more important. Understanding how materials react upon the application of external stimuli is increasingly recognised as vital to understanding the fundamental processes taking place during materials synthesis, processing and functioning.[31]

Thermal experimentation within the TEM has provided a new and interesting perspective on many material sets.[32]-[35] *In-situ* annealing has progressed from heating entire sample grids to using Micro-Electro-Mechanical Systems (MEMS) devices to enable localised heating. This technology provides greater temperature control due to the small volume and reduced thermal mass of the heater. Moreover, it considerably reduces specimen drift and settling time.[36] The use of this technology for *in-situ* annealing experiments has enabled the process to become fast and reliable, offering new insights into material morphology.[37], [38]

Within this PhD work *in-situ* TEM annealing is performed using a DENSsolutions Wildfire S3 and double-tilt Lightning heating holder. Electron transparent samples are secured over a through-hole window contained within the MEMS device and securing this device within a specialized single-tilt TEM holder, shown in Figure 2-14 (a) and (b). The MEMS device acts like a TEM grid. The *in-situ* annealing apparatus consists of a low-drift TEM holder with electrical connections (schematic of holder shown in Figure 2-14 (c)), MEMS based heating device, a computer to control the heating system and a control box.[39]

The MEMS device consists of a molybdenum (Mo) spiral encapsulated between two SiN_x membranes. The Mo spiral heats the localised area via joule heating controlled by a 4-point probe feedback loop. As well as the Mo heating spiral, there are a series of through-hole windows (5–20 µm).[40] The electron transparent sample is positioned over a window close to the centre of the heating spiral as shown in Figure 2-14 (a). The MEMS device can reach a maximum temperature of 1300°C, with temperature stability of < 1°C at 1300°C. It has a heat rate of 200°C per millisecond and a settling time of < 2 seconds.

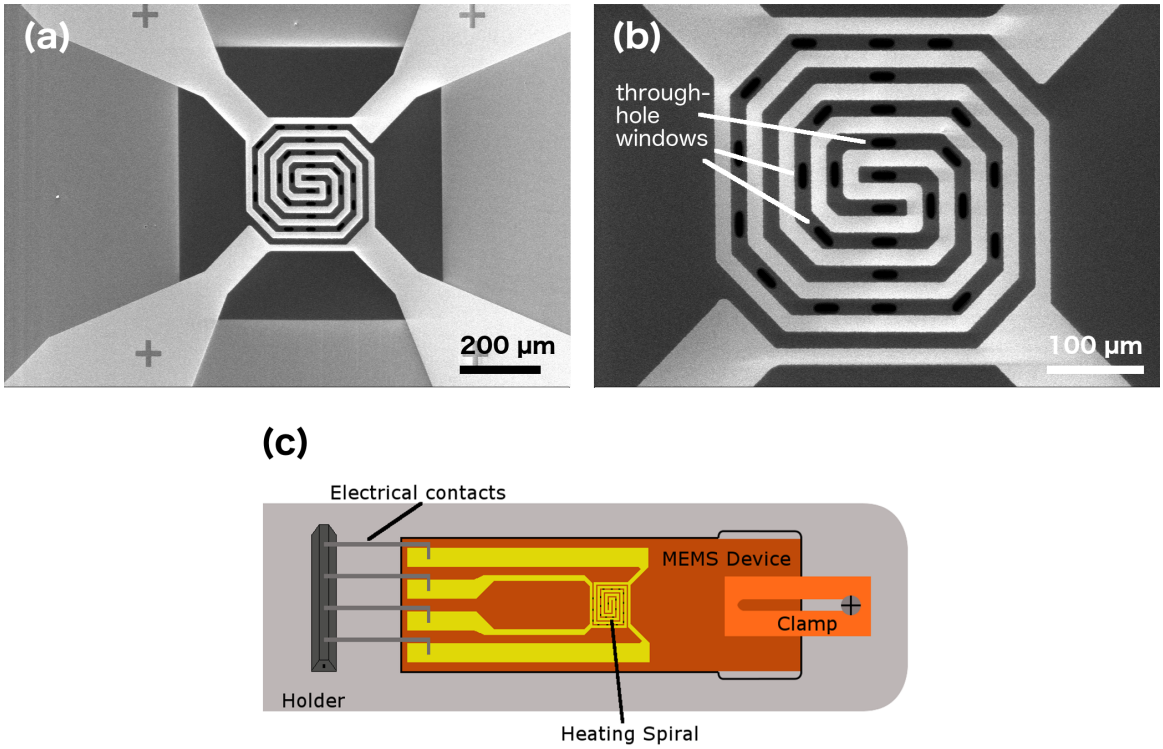

Figure 2-14: (a) Scanning Electron Microscopy (SEM) image of Micro-Electro-Mechanical Systems *(MEMS) device displaying the 4-point geometry, (b) SEM image of MEMS device showing the heating spiral and through-hole windows and (c) schematic of heating holder and MEMS device.*

2.3 Scanning Tunneling Microscopy

This technique was not used by myself, however it was undertaken by our collaborator Dr. Xiaopu Zhang and for completeness I have outlined the basic principles.

Scanning Tunneling Microscopy (STM) is a non-optical microscopy, which involves measuring the tunneling current between a conductive tip and the sample surface when a potential is applied between them, see Figure 2-15.This allows a 3D image of the surface to be created. It was developed by Gerd Binning and Heinrich Rohrer at IBM.[41] As the tunneling probability is exponentially dependent on the distance, the topography can be mapped out by keeping the current constant and measuring the height of the tip. If the distance d between specimen and tip is small enough, electrons “tunnel” across the vacuum barrier. When a voltage V is applied between the specimen and the tip, the tunneling effect results in a net electron current. This is the tunneling current.[42]

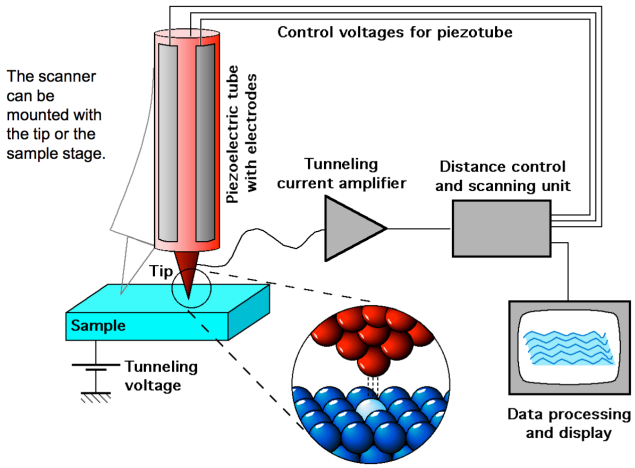

Figure 2-15: Schematic of the operation of a Scanning Tunneling Microscope.[42]

2.4 Conductive-Atomic Force Microscopy

Similar to the previous description in section 2.3, this technique was undertaken by Intel researcher-in-residence Mr. Peter Gleeson and the basic principles are detailed below for completeness.

Atomic Force Microscopy (AFM) stems from STM but is not limited to conducting surfaces as STM is. This technique can be used to test mechanical and electrical properties of surfaces. The AFM can be operated in 3 different modes: tapping, contact and non-contact. In contact mode the tip is scanned across the surface and any deflection in the cantilever is recorded, as can be seen from the schematic in Figure 2-16. The cantilever deflection represents the force and can be described by Hooke's Law, F = -kz where k is the spring constant of the cantilever and x is the distance of the deflection. According to Hook's Law F = -kz, the force interaction between the tip and the sample is proportional to the tip bending and the cantilever stiffness. Stiffness for contact mode cantilever can vary from 0.01 to several N/m.

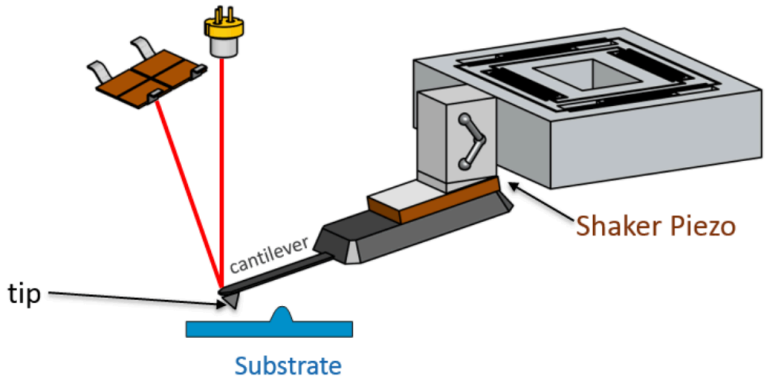

Figure 2-16: A laser beam is transmitted to the Atomic Force Microscope probe cantilever which then reflects the beam onto the four quadrant photo detector, the vertical and horizontal displacement of the cantilever deflections are then identified through the photo detector.[43]

Conductive Atomic Force Microscopy (C-AFM) is a branch of AFM, which involves scanning a conductive tip, which is in contact with the sample surface while a voltage is applied between the tip and the sample, generating a current image. Concurrently, a topographic image is also generated.[44] After acquiring a topographic image the tip can be moved to a region of interest and the voltage can be ramped while the current is measured, generating local current versus voltage curves (I-V). The main advantage of C-AFM over all electrical measurement techniques is its high spatial resolution. It has capabilities of being able to identify differences in conductivity across grain boundaries and within grains. This type of feature is critical for the particular work, which has been outlined in this thesis.

2.5 Bibliography

[1] L. A. Giannuzzi and F. A. Stevie, “Introduction to Focused Ion Beams: Instrumentation, Theory, Techniques and Practice,” pp. 1-11, 2005.

[2] L. Repetto, G. Firpo, and U. Valbusa, “Applications of Focused Ion Beam in Material Science,” *Materials and Technology*, vol. 42, no. 4, pp. 143–149, 2008.

[3] J. Reuteler, “Introduction to FIB - SEM: Basic Physics and Applications. Notes Swiss Federal Institute of Technology,” pp. 1–31, 2008.

[4] C. A. Volkert and A. M. Minor, “Focused Ion Beam Microscopy and Micromachining,” *MRS Bull.*, vol. 32, no. 5, pp. 389–399, 2007.

[5] P. R. Munroe, “The application of focused ion beam microscopy in the material sciences,” *Materials Characterization*, vol. 60, no. 1, pp. 2–13, 2009.

[6] R. M. Langford and A. K. Petford-Long, “Preparation of transmission electron microscopy cross-section specimens using focused ion beam milling,” *J. Vac. Sci. Technol. A*, vol. 19, no. 5, p. 2186-2193, 2001.

[7] A. Avishai, “Introduction to Dual Beam Focused Ion Beam SCSAM Short Course Notes.”

[8] C. A. Volkert, A. M. Minor, G. Editors, and B. May, “Focused Ion Beam Micromachining,” vol. 32, pp. 389–399, 2007.

[9] B. I. Prenitzer, F. A. Stevie, L. A. Giannuzzi, C. A. Urbanik-Shannon, S. R. Brown, R. B. Irwin, and T. L. Shofner, “The Correlation between Ion Beam/Material Interactions and Practical FIB Specimen Preparation,” *Microsc Microanal*, vol. 9, no. 3, pp. 216–236, 2003.

[10] P. Sigmund, “Theory of Sputtering. I. Sputtering Yield of Amorphous and Polycrystalline Targets,” *Physical Review*, vol. 184, no. 2, 1969.

[11] L. A. Giannuzzi, “Imaging and Patterning with a Focused Ion Beam,” pp. 1–57.

[12] J. F. Ziegler, J. P. Biersack, and M. D. Ziegler, “SRIM The Stopping and Range of Ions in Matter,” pp. 11–2–11–27, 2008.

[13] E. Long, "Two-dimensional Nanomaterials: characterising properties and structures in real environments," pp. 17–26.

[14] D. C. Bell and N. Erdman, *Low Voltage Electron Microscopy: Principles and Applications*. 2012.

[15] D. B. Williams and B. Carter, *Transmission electron microscopy*, vol. 13., pp. 1-171, 1973.

[16] V. Nicolosi, “Introduction to Transmission Electron Microscopy Course Notes,” 2013.

[17] H. C. Boswell, “Towards Fully Quantative Electron Energy-loss Spectroscopy with High Spatial Resolution.”

[18] J. Goldstein, D. Newbury, D. Joy, C. Lyman, P. Echlin, E. Lifshin, and L. Sawyer, “Scanning Electron Microscopy and X-Ray Microanalysis,” pp. 48–50, 2007.

[19] L. Reimer, “Scanning Electron Microscopy: Physics of Image Formation and Microanalysis,” pp. 3–9, 1998.

[20] T. Maitland, “Electron Backscattered Diffraction,” *Advanced Materials and Processes*, pp. 34–36, 2004.

[21] K. Dicks, “Introduction to EBSD - Oxford Instruments Analytical,” pp. 1–68, 2018.

[22] D. Mainprice, "A personal and practical guide to the history, installation and future of the Electron Back-Scattered Diffraction (EBSD) system," European Microbeam Analysis Society Regional Meeting, pp. 1–43, 2012.

[23] R. R. KELLER and R. H. GEISS, “Transmission EBSD from 10 nm domains in a scanning electron microscope,” *J Microsc*, vol. 245, no. 3, pp. 245–251, 2011.

[24] R. Egerton *Electron Energy-Loss Spectroscopy in the Electron Microscope*. Boston, MA: Springer US, 2011.

[25] S. J. Pennycook and P. D. Nellist, *Scanning Tranmisson Electron Microscopy: imaging and Analysis*, pp. 164–170, 2011.

[26] R. Brydson, *Electron Energy-Loss Spectroscopy*, pp. 29–32, 2001.

[27] T. Malis, S. C. Cheng, and R. F. Egerton, “EELS Log-Ratio Technique for Specimen-Thickness Measurement in the TEM,” *Journal of Electron Microscopy Technique*, vol. 8, pp. 193–200, 1988.

[28] R. F. Egerton, “Electron energy-loss spectroscopy in the TEM,” *Rep. Prog. Phys.*, vol. 72, no. 1, pp. 016502–26, 2008.

[29] S. Subramanian, G. Clark, K. Ly, and T. Chrastecky, “Energy-Filtered Transmission Electron Microscopy (EFTEM) of Semiconductor Devices,” *Electronic Device Failure Analysis*, vol. 13, pp. 20–28, 2011.

[30] “http://www.eels.info/how/eftem/workflow/thickness-map,” *online*.

[31] P. J. Ferreira, K. Mitsuishi, and E. A. Stach, “*In Situ* Transmission Electron Microscopy,” *MRS Bull.*, vol. 33, no. 2, pp. 1–8, 2008.

[32] H. Saka, T. Kamino, S. Arai, and K. Sasaki, “In Situ Heating Transmission Electron Microscopy,” *MRS Bull.*, vol. 33, no. 2, pp. 1–8, 2008.

[33] M. Miyasaka, K. Makihira, T. Asano, E. Polychroniadis, and J. Stoemenos, “In situ

observation of nickel metal-induced lateral crystallization of amorphous silicon thin films," *Appl. Phys. Lett.*, vol. 80, no. 6, pp. 944–4, 2002.

[34] A. Rath, R. R. Juluri, and P. V. Satyam, "Real time nanoscale structural evaluation of gold structures on Si (100) surface using in-situ transmission electron microscopy," *J. Appl. Phys.*, vol. 115, no. 18, pp. 184303–7, 2014.

[35] R. Dannenberg, E. A. Stach, J. R. Groza, and B. J. Dresser, "In-situ TEM observations of abnormal grain growth, coarsening, and substrate de-wetting in nanocrystalline Ag thin films," *Thin Solid Films*, vol. 370, no. 1, pp. 54–62, 2000.

[36] L. F. Allard, W. C. Bigelow, M. Jose-Yacaman, D. P. Nackashi, J. Damiano, and S. E. Mick, "A new MEMS-based system for ultra-high-resolution imaging at elevated temperatures," *Microsc. Res. Tech.*, vol. 72, no. 3, pp. 208–215, 2009.

[37] N. P. Young, M. A. van Huis, H. W. Zandbergen, H. Xu, and A. I. Kirkland, "Transformations of gold nanoparticles investigated using variable temperature high-resolution transmission electron microscopy," *Ultramicroscopy*, vol. 110, no. 5, pp. 506–516, 2010.

[38] M. A. van Huis, N. P. Young, G. Pandraud, J. F. Creemer, D. Vanmaekelbergh, A. I. Kirkland, and H. W. Zandbergen, "Atomic Imaging of Phase Transitions and Morphology Transformations in Nanocrystals," *Adv. Mater.*, vol. 21, no. 48, pp. 4992–4995, 2009.

[39] M. Duchamp, Q. Xu, and R. E. Dunin-Borkowski, "Convenient Preparation of High-Quality Specimens for Annealing Experiments in the Transmission Electron Microscope," *Microsc Microanal*, vol. 20, no. 6, pp. 1638–1645, 2014.

[40] L. Mele, F. Santagata, E. Iervolino, M. Mihailovic, T. Rossi, A. T. Tran, H. Schellevis, J. F. Creemer, and P. M. Sarro, "A molybdenum MEMS microhotplate for high-temperature operation," *Sensors & Actuators: A. Physical*, vol. 188, pp. 173–180, 2012.

[41] G. Binning, H. Rohrer, C. Gerber, and E. Weibel, "Surface Studies by Scanning Tunneling Microscopy," *Phys. Rev. Lett.*, vol. 49, no. 1, pp. 57–61, 1982.

[42] L. Zhang, "Lecture 6 Scanning Tunneling Microscopy (STM) Notes," pp. 1–23, 2013.

[43] "https://www.nanosurf.com/en/how-afm-works/afm-operating-principle," *online*.

[44] "https://www.nrel.gov/materials-science/conductive-atomic.html," *online*.

3. Experimental Methods

3.1 TEM Sample Preparation

3.1.1 Film Deposition

Initial samples analysed consisted of a 40 nm copper (Cu) layer, 7 nm silicon dioxide (SiO_2) on a silicon (Si) substrate. This was prepared using evaporation and was undertaken by Mr. Peter Gleeson in CRANN, Trinity College Dublin. This was later replaced by samples from the Intel fabrication facility, which consisted of a 50 nm Cu layer, 7 nm tantalum (Ta) layer on a Si substrate. These samples were prepared by sputter Physical Vapour Deposition (PVD).

3.1.2 Initial Preparation Process

There are many different methods to use the Focused Ion Beam (FIB) for Transmission Electron Microscopy (TEM) sample preparation. I chose the most commonly used, *in-situ* lift out technique (INLO), which has been proven to be quite effective. As described in chapter 1, this technique is a combination of the H-bar technique and the lift-out technique. The initial preparation for INLO is very similar to the *ex-situ* lift-out technique (EXLO) except the region of interest is milled to a larger thickness of ~1 – 2 µm. The success rate of the INLO method is 90 – 100%.[1]

As mentioned in chapter 1, the main advantage of INLO compared to EXLO is that the secondary electron (SE) imaging achieves higher magnification than optical microscope imaging. This makes the lift out process more controllable and therefore increases the overall success rate. It also allows for re-thinning of the lamella, which is not possible with EXLO technique. The EXLO technique consists of milling a freestanding region to electron transparency in the FIB. It is then removed from the FIB chamber and removed using a glass needle attached to a micromanipulator, viewed under an optical microscope. The glass needle is pushed at the specimen until it attaches electrostatically to the needle and is removed from the bulk sample. It is then placed on a carbon (C) coated TEM support grid. Due to the low optical magnification it can be difficult to remove the lamella with ease, hence performing the lift-out within the FIB system would be a preferred technique.[2]-[4]

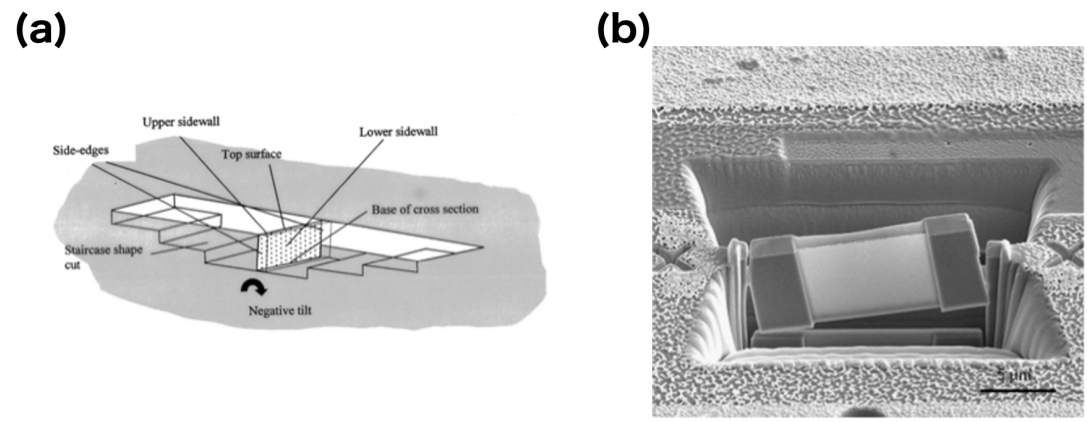

Figure 3-1: (a) Schematic of a cross-section specimen prepared using the in-situ lift out technique [5], (b) Secondary Electron Microscopy image of a Transmission Electron Microscopy cross-section. The lamella has received final thinning and has been freed ready for ex-situ 'lift-out'.[6]

The primary advantage of using the lift-out technique over other sample preparation methods is that the starting bulk material needs little to no initial preparation. It just needs to be small enough to fit within the chamber of the FIB.

The sample is cut to dimensions of about 1 cm x 1 cm. It is secured to an aluminium stub using a carbon tab and the edges are coated with silver paint to further prevent charging of the sample. The bulk sample is first coated with carbon in a Cressington 108HR. This is done by thermal evaporation of the carbon. A carbon source in the form of a rod is sharpened to approximately 16 mm and mounted in the Cressington vacuum system between two high-current terminals. When the carbon source is heated to its evaporation temperature, a fine stream of carbon is deposited onto the film.[7] This has multiple purposes; to ensure further protection of the area of interest in the sample and also to provide an amorphous area, which can be used to focus in the ronchigram for high-resolution Scanning Transmission Electron Microscopy (HRSTEM) analysis and to reduce sample charging. It was initially coated with gold/palladium (Au/Pd), but that created an ion channeling effect, which caused further damage to the sample. This is described further in chapter 4.

Once coated the sample is then mounted in the FIB/SEM chamber. An omniprobe TEM grid with 3 pillars is also mounted in the centre of the Zeiss TEM sample holder. Using SEM imaging (120 µm aperture, high current mode) the sample is brought to a working distance of about 10 – 12 mm. At this point the eucentric point is determined by finding an edge and adjusting the M-axis (the z-axis for the FIB) to bring it back to centre at various angles; 0°, 5°, 0°, 11°, 0°, 54°,

0°, 54°. Once the eucentric point has been determined, the sample is kept tilted at 54°. It is re-focused to make sure it is at the correct working distance. It is brought to 6 mm, refocused and finally brought to the point of coincidence between the SEM and FIB, 5 mm. The FIB gun is turned on, once a vacuum below 5 X 10^{-5} mbar is reached. Toggling between SEM and FIB the height is slightly adjusted until the centred image is the same in both SEM and FIB while the magnification is locked in both systems.

The stage is lowered back to a working distance of 6 mm, at which point the Gas Injection System (GIS) needle is brought in, selecting the platinum (Pt) channel, which has been heated to ~ 73°C. The stage is then slowly brought back to a working distance of 5 mm and eucentric is determined. In typical SEM operating mode, at 5 keV beam energy, a reduced raster box of ~14 x 2 µm is set and the GIS valve is opened. The optimum value is ~3 keV. An extra long Pt strip of 14 µm is used as the beam's scan rate home position causes a scalloping effect at the end of the strip which causes a problem when thinning by producing a curtaining effect.[5]

All deposition is performed at 54° tilt, ideally electron beam-induced deposition (EBID) should be done at 0° for best results. A small spot of Pt is laid down in the centre of the box to avoid drift. The beam shift is then used to monitor and correct drift in real time. EBID is deposited for ~ 15 – 20 minutes. This usually lays down ~ 500 nm of Pt. This is the ideal height, as the ions will not penetrate this depth to the sample surface. After this, using the 30 kV 20 pA beam, occasionally a 30 kV 50 pA beam the ion beam-induced deposition (IBID) is performed for between 15 – 30 minutes depending on the beam current used, see Figure 3-2 (a). The overall height of the Pt was found to be between 1.5 – 2 µm.[6]

Once the deposition is completed, the GIS valve is closed and the needle is removed. The beam current is now changed to 30 kV 2 nA. This is the most common current used for coarse milling for this technique. Sometimes stronger beam currents such as 4 nA and occasionally 10 nA can be used depending on the stability of the beam. To ensure minimal spread of the beam and clean lines, for most lamella preparation the 2 nA beam is used. Using the trapezoid shape, a trench of depth of 10 µm is milled either side of the protective Pt strip, see Figure 3-2 (b). A lot of re-deposition can occur during this part of the process. To help reduce the amount of re-deposition, the trench is milled over the same area 3 times (layers option on Zeiss system), to help mill through the re-deposited material and to observe the undercut. Another advantage of using the INLO technique is that there is minimal re-deposition of the material

once it is removed from the trench, as it is not in a confined space. In the other techniques, it is confined to the trench, whereas when the lamella is welded to the TEM grid, the sputtered material is simply removed by the vacuum.

Once the two trapezoid trenches have been milled, a rectangular trench of 12 µm in depth is milled on the third side of the lamella. Either side of the lamella is milled for approximately a minute with a 2 nA beam to reduce the wedge shape at the bottom of the lamella, see Figure 3-2 (c). The stage is then tilted to 7° to perform the undercut, which allows for the removal of the lamella from the bulk. Before tilting the GIS must be removed as they will come in contact with the stage, see GIS geometry in Figure 3-2 (d). The undercut is usually milled at a depth of 5 – 7 µm along the lamella, Figure 3-2 (e). After this the stage is tilted to 20° to ensure the undercut is visible right through the lamella as shown in Figure 3-2 (f).

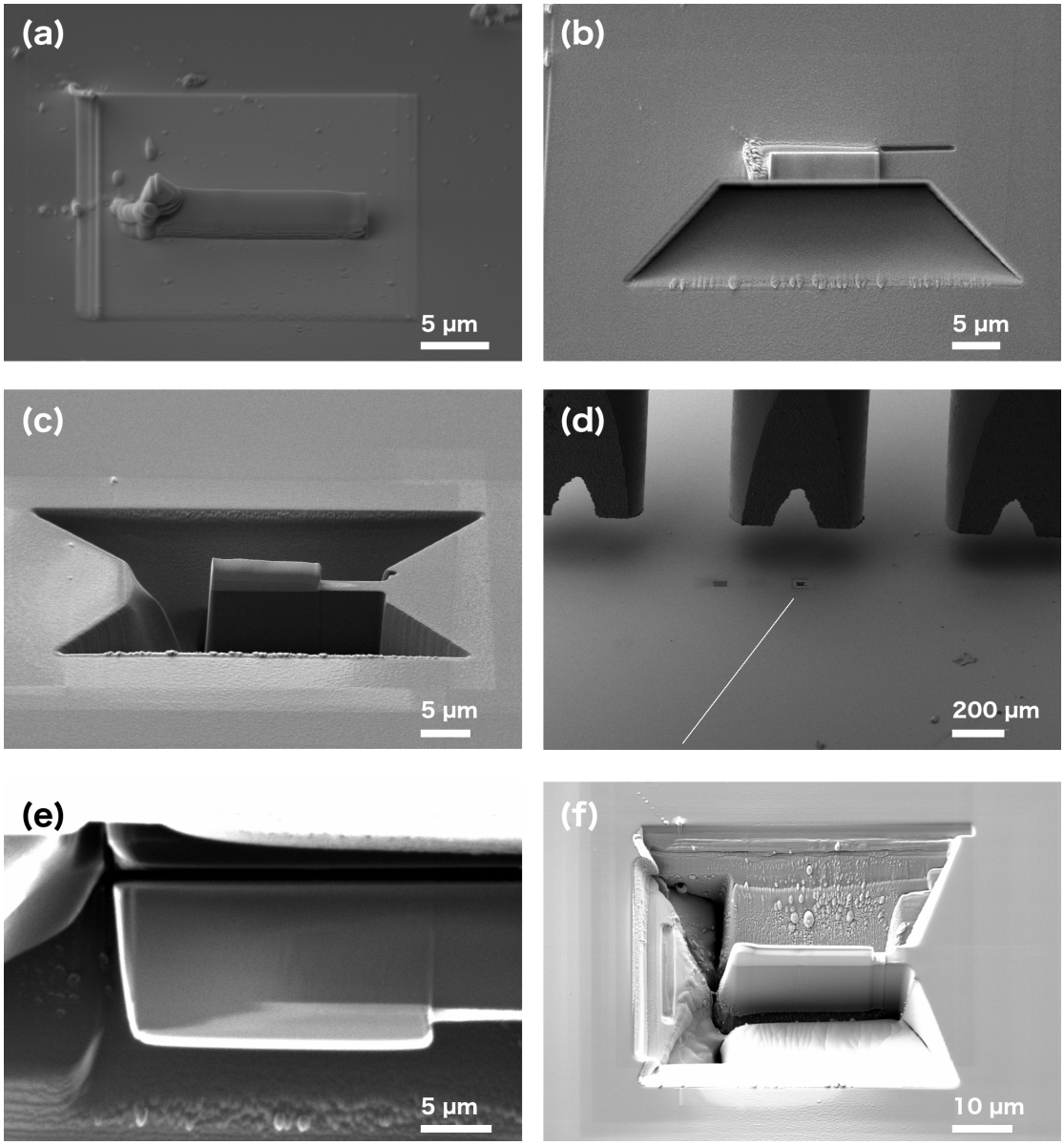

Figure 3-2: Scanning Electron Microscopy images of the coarse milling process of lamella preparation; (a) both e and i beam platinum deposition, on the left of strip notice scalloping due to beam raster, (b) top view of trapezoid trench with gradual slope, re-deposition visible, (c) two trenches and side trench, (d) Gas Injection System needle geometry above lamella, (e) undercut view from Focused Ion Beam perspective at 7° stage tilt and (f) undercut visible at 20° stage tilt.

Once the trenches and undercut have been milled, the stage is tilted back to 54° and the Kleindiek micromanipulator needle is brought to the coincidence working point. This has been checked prior to the preparation to make sure it is inserted at ~ 4.8 mm so as to not crash into the stage at 5 mm.

The needle is then slowly inserted next to the free lamella sidewall. The GIS valve is opened once again, before contact of the needle. The needle is welded to the side of the lamella. Again, like previously the Pt is deposited using either a 30 kV 20pA or a 30 kV 50pA. After welding, the fourth wall of the lamella is milled away with a 30 kV 2 nA beam current, see Figure 3-3 (a) and (b).

The lamella is then removed from the bulk very slowly and with extreme care using the Kleindiek needle micromanipulator. The stage is then lowered to a safe working distance (anything from 12 – 18 mm) and is rotated to the centre of the TEM grid. The GIS needle is reinserted. The stage is slowly raised back to the working distance of 5 mm ensuring that the lamella welded to the needle is in the centre between 2 pillars of the grid. The lamella is moved towards the middle pillar. The lamella is welded high enough up the pillar to prevent sputtering of the Cu grid below and not too close to the rounded edges at the top of the pillar, to ensure a flat contact point for the best weld possible. The GIS valve is opened once again and the lamella is welded to the grid pillar using only EBID-Pt. The needle is removed by milling with a 30 kV 2 nA ion beam. The lamella is welded on the other side to ensure a secure hold to the grid pillar, see Figure 3-3 (c) – (f).

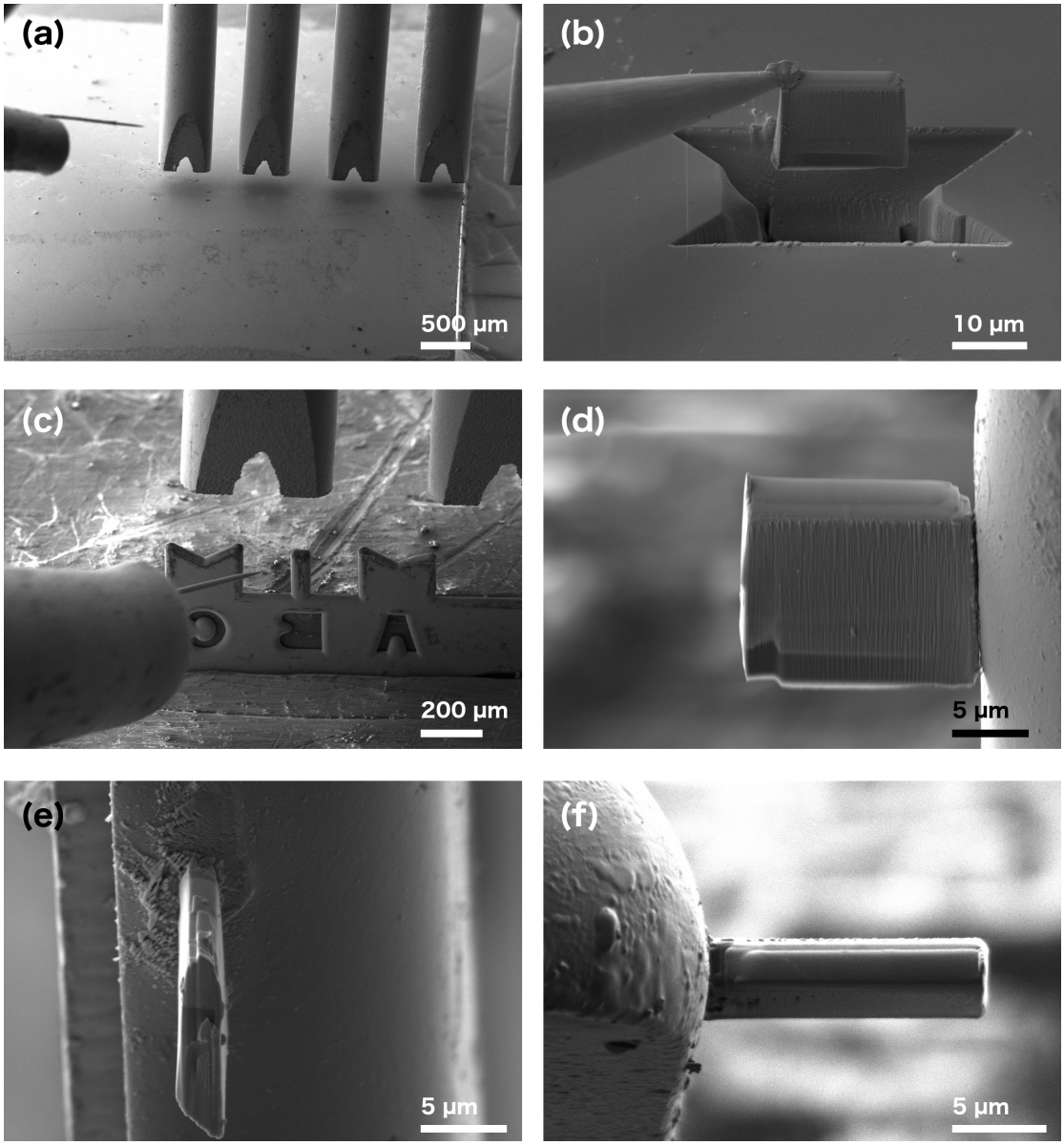

Figure 3-3: Scanning Electron Microscopy images of (a) low magnification image of Kleindiek needle (left), sample and Gas Injection System needles, (b) platinum weld of needle to lamella, removal of fourth wall detaching lamella from bulk sample and careful lift-out of lamella from trench, (c) lamella slowly brought to middle pillar of Transmission Electron Microscope grid (d) lamella welded to pillar, (e) side on view of welded lamella and (f) top-down Focused Ion Beam view of welded lamella.

3.1.3 Thinning & Polishing Process

During the initial stages of this PhD work, the lamellae were prepared using the *in-situ* lift-out method of 1 – 3° tilt (with respect to the FIB) and imaged with a 5 kV SEM. The lamella was initially thinned with 30 kV 240 pA both sides, until it reached a thickness of about 800 nm – 1 µm in width. 15 kV 200 pA thinning until thickness of ~ 250 – 300 nm is reached. It is good to perform the lower energy thinning and polishing at a slightly thicker lamella width to remove

the damage layers. As, if the lamella becomes too thin, there will be no crystalline material, only amorphous material, see Figure 3-4.[6], [8]

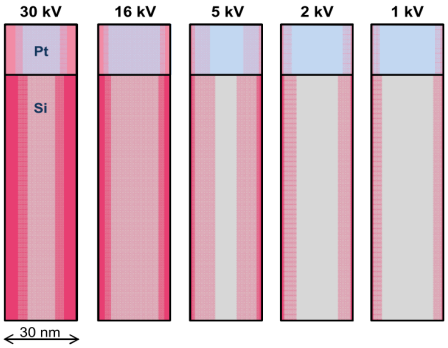

Figure 3-4: Schematic of knock-on damage and atomic displacement caused by various beam energies.[9]

Using 5 kV 20 pA either sides are thinned until they become transparent with 5 kV 3 nA beam in SEM mode. Due to the high beam current in SEM, exposure time should be limited. This indicates a thickness of about 100 nm. Using 3 kV SEM, a 5 kV FIB polish is performed until the image becomes transparent. This indicates a thickness of approximately 50 – 70 nm, suitable for TEM analysis. Also, when preparing the lamella, with each change of beam energy the lamella shape is slowly tapered in so that eventually only the last 2 – 3 µm are electron transparent and the remaining 8 µm provide stability and also can be used to prepare future lamellae for that sample. See sequential steps in Figure 3-5 (a) – (f). It also provides structural integrity and reduces warping. Most of the lamellae prepared are approximately 12 – 14 µm in length, 6 – 8 µm in depth and ~50 – 80 nm in thickness.

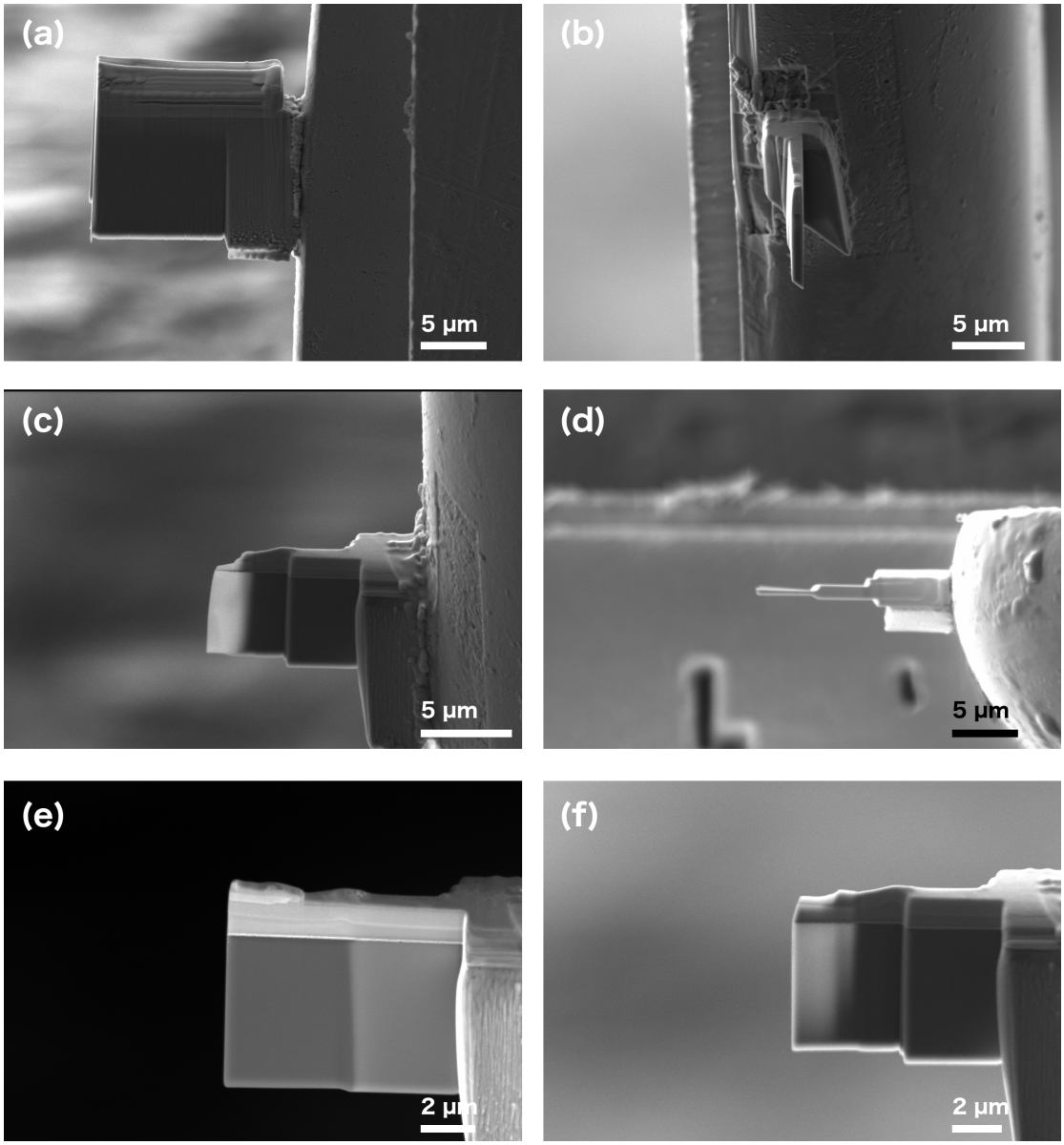

Figure 3-5: (a) Scanning Electron Microscope (SEM) image of 30 kV mill of lamella, (b) side view of lamella after 30 kV mill, (c) side view of lamella preparation, (d) Focused Ion Beam image, top-down of tapered profile for lamella preparation, (e) SEM in-lens image of gradual 15 kV polish and (f) SEM image of 5 kV polish.

3.1.4 Inverted Triangle "wedge" Technique and 2 kV Polish

Milling rates differ from the top to bottom of the lamella due to the tails of the ion beam profile. This can lead to a preferential thinning of the top layer and hence the protective Pt layer, hence why in this project the new "wedge pre milling" technique from M. Schaffer *et al.* (2012) has been employed. This involves a gradual reduction in the ion beam energy during the thinning and polishing process. To further protect the sample surface, an incident beam angle of approximately 6° – 7° is used along with an extra thick protection layer (2 µm), see

Figure 3-6. Due to this new technique it was now possible to use a lower energy, 2 kV 20 pA.[8]

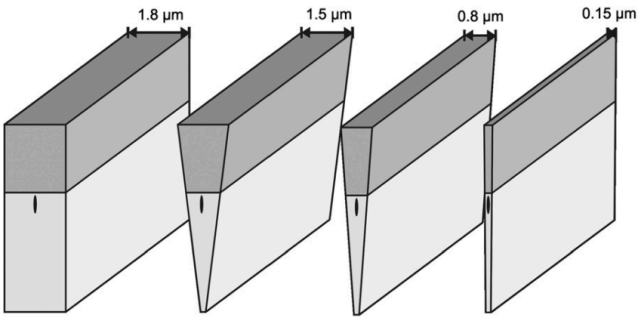

Figure 3-6: *Schematics of "wedge pre-milling". Features of interest close or at the top surface (black ellipse) stay fully protected and protection layers are kept intact and parallel for final thinning steps.[8]*

The lamella is tilted to 7° with respect to the FIB. The same beam currents and dimensions were used to determine when to lower the beam currents but it was kept at this tilt. The tilt varied for each lamella as each individual lamella preparation is different. If more Si from the bottom of the lamella is being milled away too quickly, then the tilt is decreased by 1 – 2° to alleviate the aggressive milling accordingly and vice versa with the Pt layer. Examples of wedge profile at reduced beam energies shown in Figure 3-7 (a) – (f).

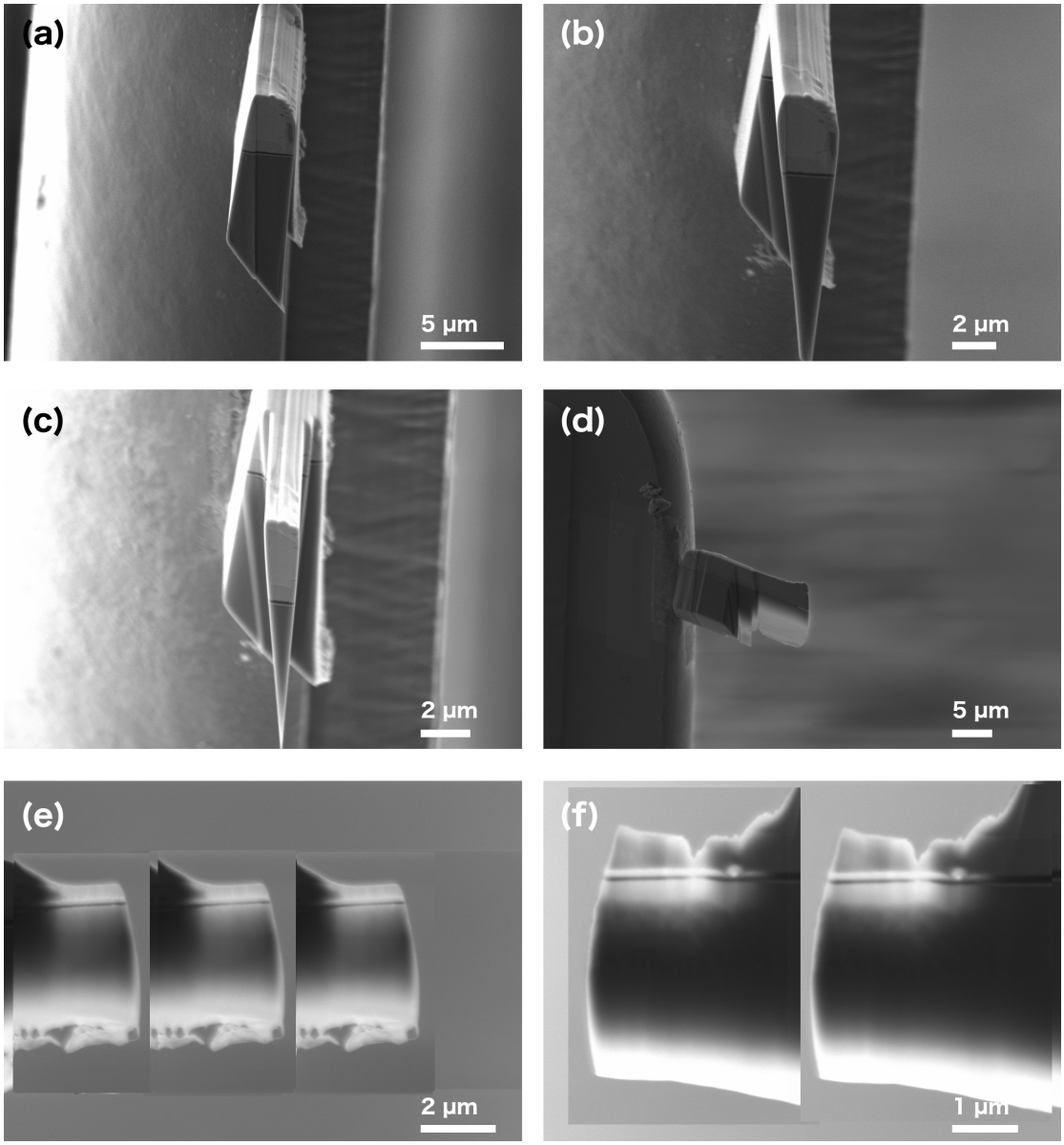

Figure 3-7: (a) – (d) Scanning Electron Microscopy (SEM) images of side profile wedge shape at reducing beam energies, (e) and (f) SEM images of low 2 kV polishing of lamella, now possible with new wedge technique.

3.1.5 Issues & Artefacts generated from the FIB

There are also drawbacks to using a Ga^+ FIB for sample preparation. The sputtering process can implant Ga and create vacancies and interstitials, which depending on the material can coalesce to form dislocations or if there is sufficient density, an amorphous layer. This is not ideal for doing HRTEM imaging and analysis. In addition, local composition and phase changes can also occur.[10]

Damage at the sidewalls of the lamella has also been reported. Two techniques are used to reduce this sidewall damage in this study. The sample is tilted at 7° with respect to the FIB beam axis. This glancing angle has been proven to reduce damage and protect the Pt layer. Secondly, the beam energy was reduced to 15 kV, to 5 kV and then finally to 2 kV.[10]

Usually for a 30 kV beam the amorphous layer and damaged produced by Ga in Si is between 20 – 35 nm thick. By employing the methods of reducing the ion beam energy and reducing the incident angle, it can be significantly reduced, see schematic in Figure 3-8. Thompson *et al.* showed after a 5 kV clean-up that the Si amorphous layer was reduced from 40 nm to 5 nm and to ~ 1 nm for a 2 kV beam.[11], [12]

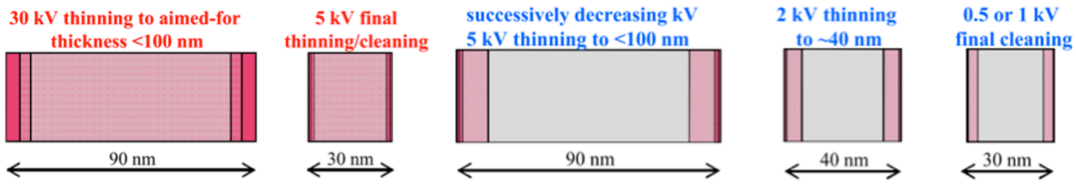

Figure 3-8: Comparison of different amorphous regions generated by reducing beam energies at different thicknesses.[9]

3.2 The relationship between Cu and FIB milling – How does it react?

For Si, the amorphous layer and damage produced by Ga is documented to be ~ 20 – 30 nm amorphous for 30 kV and 13 nm for 10 kV.[13]-[15] There is a need to address how the Cu layer evolves as well. Kiener *et al.* performed a number of thinning experiments ranging from 30 kV to 5 kV. The TEM results show a ~10 nm amorphous layer for 30 kV and less than ~3 nm for 5 kV. However at all energies, including low energies, dislocation-like damage is still observed at 5 kV.[16] Kiener *et al.* state an amorphous region of up to ~50 nm for a 30 kV 2 nA beam. The penetration depth of the ions can also be reduced by reducing ion energy and impact angle, 15 nm to 5 nm from 30 kV to 5 kV.[16]

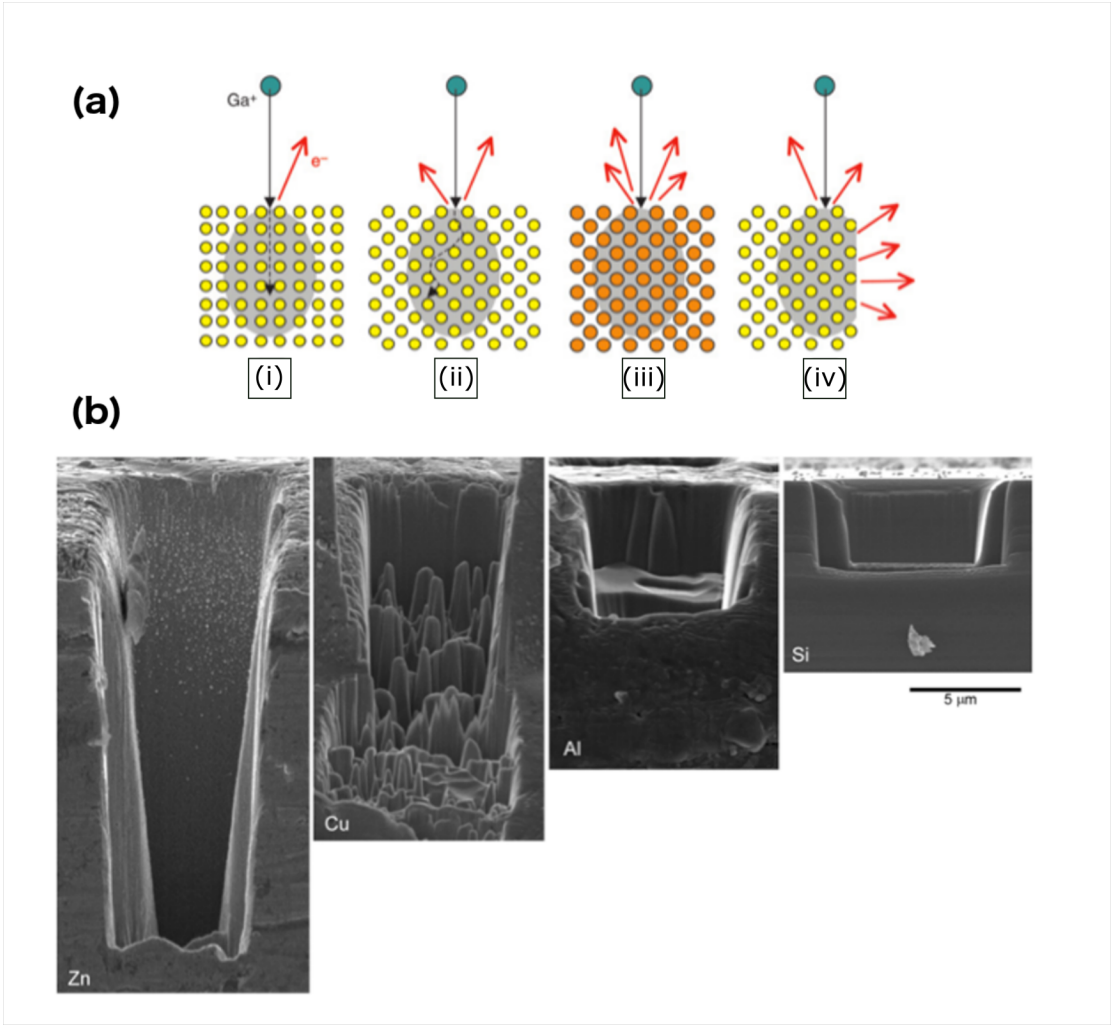

Figure 3-9: (a) *Schematics showing the influence of (i), (ii) crystal orientation, (iii) atomic mass, and (iv) surface geometry on 30 keV Ga^+ collision cascades and ion-induced secondary electron image contrast formation. The orange atoms in (iii) are more massive than the yellow atoms in (i), (ii), and (iv) [17] and (b) Different sputtering rates of different materials.[18]*

The beam can cause other types of damage to the Cu. For example, due to the different grain orientations of Cu, channeling of the ions can make it difficult to mill the Cu or it can help reduce the sputtering yield and therefore increase the penetration depth, see Figure 3-9 (a) and (b).[19], [20] It has also been noted that high intensity ion beam milling can induce oriented grain growth or Ga-intermetallic growth.[21]-[23]

3.3 Bibliography

[1] R. M. Langford and M. Rogers, “In situ lift-out: Steps to improve yield and a comparison with other FIB TEM sample preparation techniques,” *Micron*, vol. 39, no. 8, pp. 1325–1330, 2008.

[2] L. A. Giannuzzi and F. A. Stevie, “Introduction to Focused Ion Beams: Instrumentation, Theory, Techniques and Practice,” pp. 201–245, 2005.

[3] R. M. Langford and C. Clinton, “In situ lift-out using a FIB-SEM system,” *Micron*, vol. 35, no. 7, pp. 607–611, 2004.

[4] J. Mayer, L. A. Giannuzzi, T. Kamino, and J. Michael, “TEM Sample Preparation and Damage,” *MRS Bulletin*, vol. 32, no. May, pp. 400–407, 2007.

[5] R. M. Langford and A. K. Petford-Long, “Preparation of transmission electron microscopy cross-section specimens using focused ion beam milling,” *J. Vac. Sci. Technol. A*, vol. 19, no. 5, p. 2186-2193, 2001.

[6] P. R. Munroe, “The application of focused ion beam microscopy in the material sciences,” *Materials Characterization*, vol. 60, no. 1, pp. 2–13, 2009.

[7] “https://www.leica-microsystems.com/science-lab/brief-introduction-to-coating-technology-for-electron-microscopy/,” *online*.

[8] M. Schaffer, B. Schaffer, and Q. Ramasse, “Sample preparation for atomic-resolution STEM at low voltages by FIB,” *Ultramicroscopy*, vol. 114, pp. 62–71, 2012.

[9] M. Schaffer, “FIB sample preparation for aberration corrected TEM / STEM at low kV,” 2012.

[10] R. M. Langford, “Focused Ion Beams Techniques for Nanomaterials Characterization,” vol. 549, no. May, pp. 538–549, 2006.

[11] J. P. McCaffrey, M. W. Phaneuf, and L. D. Madsen, “Surface damage formation during ion-beam thinning of samples for transmission electron microscopy,” *Ultramicroscopy*, vol. 87, no. 3, pp. 97–104, 2001.

[12] K. Thompson, D. Lawrence, D. J. Larson, J. D. Olson, T. F. Kelly, and B. Gorman, “In situ site-specific specimen preparation for atom probe tomography,” *Ultramicroscopy*, vol. 107, no. 2, pp. 131–139, 2007.

[13] S. Rubanov and P. R. Munroe, “FIB-induced damage in silicon,” *J Microsc*, vol. 214, no. 3, pp. 213–221, 2004.

[14] N. I. Kato, “Reducing focused ion beam damage to transmission electron microscopy samples,” *Journal of Electron Microscopy*, vol. 53, no. 5, pp. 451–458, 2004.

[15] T. Ishitani, T. Ishitani, T. Yaguchi, and T. Yaguchi, “Cross-sectional sample preparation by focused ion beam: A review of ion-sample interaction,” *Microsc. Res. Tech.*, vol. 35, no. 4, pp. 320–333, 1996.

[16] D. Kiener, C. Motz, M. Rester, M. Jenko, and G. Dehm, “FIB damage of Cu and possible consequences for miniaturized mechanical tests,” *Materials Science and Engineering: A*, vol. 459, no. 1, pp. 262–272, 2007.

[17] C. A. Volkert and A. M. Minor, “Focused Ion Beam Microscopy and Micromachining,” *MRS Bull.*, vol. 32, no. 5, pp. 389–399, 2007.

[18] B. I. Prenitzer, F. A. Stevie, L. A. Giannuzzi, C. A. Urbanik-Shannon, S. R. Brown, R. B. Irwin, and T. L. Shofner, “The Correlation between Ion Beam/Material Interactions and Practical FIB Specimen Preparation,” *Microsc Microanal*, vol. 9, no. 3, pp. 216–236, 2003.

[19] T. L. Matteson, L. A. Giannuzzi, S. W. Schwarz, E. C. Houge, and B. W. Kempshall, “Electron backscattering diffraction investigation of focused ion beam surfaces,” *Journal of Elec Materi*, vol. 31, no. 1, pp. 33–39, 2002.

[20] B. W. Kempshall, R. B. Irwin, B. W. Kempshall, F. A. Stevie, L. A. Giannuzzi, S. M. Schwarz, B. I. Prenitzer, and B. I. Prenitzer, “Ion channeling effects on the focused ion beam milling of Cu,” *J. Vac. Sci. Technol. B*, vol. 19, no. 3, p. 749, 2001.

[21] J. Michael and J. R. Michael, “Gallium Phase Formation in Cu During 30kV Ga+ FIB Milling,” *Microsc Microanal*, vol. 12, no. 2, pp. 1248–1249, 2006.

[22] R. Spolenak, L. Sauter, and C. Eberl, “Reversible orientation-biased grain growth in thin metal films induced by a focused ion beam,” *Scripta Materialia*, vol. 53, no. 11, pp. 1291–1296, 2005.

[23] J. D. Casey, M. Phaneuf, C. Chandler, M. Megorden, K. E. Noll, R. Schuman, T. J. Gannon, A. Krechmer, D. Monforte, N. Antoniou, N. Bassom, J. Li, P. Carleson, and C. Huynh, “Copper device editing: Strategy for focused ion beam milling of copper,” *J. Vac. Sci. Technol. B*, vol. 20, no. 6, p. 2682, 2002.

4. Optimisation of the TEM Cross-sectional Lamella Preparation Technique for 40 nm Cu Films on SiO_2

4.1 Introduction

The ultimate goal of this work was to investigate the microstructure of copper (Cu) interconnects i.e. nanowires (NWs), however initial investigations were carried out on Cu films as these are readily synthesized and analysed. Therefore, in this chapter the following investigations are described: a) the optimisation of the cross-sectional lamella preparation process of these Cu films and b) the Scanning/Transmission Electron Microscopy (S/TEM) imaging and analysis of the Cu microstructure. All the Cu films were prepared by Intel Ireland.

Nanocrystalline thin films have been widely used for decades, in particular nanocrystalline metals, as they are widely used as electrical contacts and interconnects in ultra large-scale integrated circuits.[1] Many aspects of nanocrystalline thin films have been investigated, including grain growth and strain release.[2], [3] The main attraction of nanocrystalline films is their increased strength and hardness due to their reduced grain size and film thickness. Nanocrystalline materials are single or multi-phase crystal materials with sub-micron grain sizes, usually in the range of 1 – 100 nm. Due to the small dimensions of nanocrystalline materials, they have varying properties to that of their micron-sized counterpart. This reduction in dimensions can lead to changes in the physical, mechanical and chemical properties of the material in comparison to its bulk state.
This is mainly due to the fact that, at reduced dimensions, grain boundaries and interface boundaries occupy a considerably larger fraction of the film and hence alter the properties of the material.[4], [5]

In this chapter, the progressive and iterative improvement of the lamella preparation through high-resolution S/TEM (HRS/TEM) imaging as well as supporting thickness measurements through Energy-Filtered TEM (EFTEM) mapping is described. The overall grain sizes, grain boundaries and crystallinity of the Cu film will be analysed as well as the damage induced to the sample by the electron beam. This chapter will briefly outline the initial process of the lamella preparation optimization by Focused Ion Beam (FIB) milling, pertaining to a 40 nm Cu

film deposited on 7 nm silicon dioxide (SiO_2) on silicon (Si) substrate. This is one of two different Cu films and liners used throughout this project. The second being a 50 nm Cu film on 7 nm tantalum (Ta) liner on Si substrate. The preparation method varies slightly to the preparation of the SiO_2 liner. The SiO_2 liner is prepared through Plasma Enhanced Chemical Vapour Deposition (PECVD) as opposed to sputter Physical Vapour Deposition (PVD) for the Ta liner. As noted previously, both variants were investigated, however eventually the 50 nm Cu films on 7 nm Ta liner became the primary sample of interest and remained the focus throughout the majority of this PhD work.

The decision for using SiO_2 for a liner was determined by Intel. The reasoning behind this was to investigate the properties of the evaporated Cu film without the interaction of a typical liner material but an insulating material with little interaction with the Cu at low temperatures and with no electrical bias applied. Using SiO_2 was ideal to investigate the Cu without the contribution of other materials/external factors. SiO_2 has been used as a dielectric material and a barrier in the semiconductor industry for decades. Hence why the diffusivity of other metals into this material has been investigated thoroughly.[6] At elevated temperatures it has been noted that Cu diffusion occurs into SiO_2 dielectric layers due to the low-temperature electric field applied and this diffusivity is significantly accelerated at increasing high temperatures.[6], [7]

4.2 Experimental Methods

The Cu was PVD in a Temescal e-beam evaporator, and the SiO_2 was deposited by PECVD. They were 40 nm and 7 nm in thickness respectively. The Cu NWs used for the Conductive-Atomic Force Microscopy (C-AFM) data acquisition were 100 nm wide wires with a depth of approximately 150 – 160 nm, with a proprietary protective barrier layer on a Si substrate.

All TEM and STEM images were acquired on an FEI Titan at either 80 kV or 300 kV. Energy-dispersive X-ray (EDX) spectra were acquired using an EDAX EDX detector with spatial resolution ~0.5 nm. All Scanning Electron Microscopy (SEM) and FIB imaging acquired for lamella preparation and optimisation procedures were performed on a dual beam Zeiss Auriga.

All samples used for Scanning Tunnelling Microscopy (STM) analysis were etched with a glacial acetic acid and loaded into an ultra-high vacuum (UHV) system equipped with a low-temperature scanning tunneling microscope. It was also gently sputtered and annealed at ~300°C prior to imaging. C-AFM data was collected on a Bruker Multimode AFM.

4.3 Optimisation of Lamella Preparation

The first criterion, which needed to be met for this project was to produce lamellae at an approximate thickness of < 50 nm. There were many attempts at adjusting the thinning and polishing protocol in order to produce the desired lamellae. The aim was to produce lamellae of ideally < 50 nm thickness, a condition necessary to observe crystalline Cu films and to achieve atomic resolution S/TEM imaging and analysis along the Cu grain boundaries. Many lamellae were prepared of this particular sample to achieve the desired thickness. Approximately 10 cross-sectional and 2 plan-view lamellae were prepared to this effect. Furthermore, there were approximately 10 further re-thins of these lamellae. Re-thinning simply describes using a lamella, which has already been welded to a TEM Omniprobe grid pillar but with an unsuccessful initial polish. It may have been too thick for TEM imaging and characterisation. The lamella can be cut to remove the "unusable" area and it can be re-polished without having to start the preparation from the bulk sample again. This was to try and obtain the best and most pristine crystalline sample to produce the highest quality images. The main parameters optimized were milling angle, platinum (Pt) deposition height and lamella size. A lot of this lamellae preparation was a slow and iterative process, which took approximately a year and a half to master. Due to the large volume of lamellae prepared and the subsequent data analysis generated, I will only highlight the significant adaptations to the sample preparation, including unsuccessful attempts, which I feel are significant to the overall result achieved without going into detail about each lamella prepared in the process.

4.3.1 Gold/Palladium Coating

Initially lamellae were prepared using the *in-situ* lift-out procedure as described in the previous experimental methods chapter, section 3.1.2. Samples of 40 nm Cu/ 7nm SiO_2/Si substrate were coated in ~ 30 nm layer of gold/palladium (Au/Pd) to protect the sample from any damage due to the FIB beam. This additional layer protects the Cu film for longer while it is being thinned under the FIB beam, especially at lower beam energies. The sample was coated with a further protective ~1 - 2 μm layer of Pt.

Most lamellae were prepared using a reduced beam energy technique. Going from 30 kV 240 pA to 15 kV 200 pA and finally to 5 kV 20 pA. Reducing the beam energies is of great importance, as it helps reduce the amorphisation of the material. Figure 4-1 (a) and (b) shows the initial samples prepared with the Au/Pd coating and with a final beam polish of 5 kV 20pA at a tilt of approximately ±3° with respect to the FIB. This beam voltage and current were used at ~300 nm thickness and the polishing would continue on either side of the lamella until it became bright in contrast to the other parts of the lamella at 3 kV in the SEM image.

As can be seen from the image in Figure 4-1 (d) it is difficult to obtain any significant grain information about the Cu film. The greatest technical challenge with this particular preparation method is the coating step, which can be seen in the TEM images in Figure 4-1 (c) and (d). The deposited Au/Pd coating creates columnar structures and gaps within the film leading to failure to act as a protective layer, which leaves the Cu film exposed in terms of ion irradiation and damage.[8] It was also noted that there was insufficient lattice information from the grains and grain boundary in the sample. Therefore, it was determined the preparation method needed to be adapted and improved, especially the varied milling rate of Cu needed addressing. The dimensions of the Cu film also made it extremely difficult to thin uniformly and without significant damage to the sample.

Thickness maps were obtained of the thin region of interest using EFTEM mapping. These depicted a log ratio, described in section 2.2.6 (t/λ) of 0.21 – 0.29 at the Cu/SiO_2 interface with lower values closer to the film surface, near the Au/Pd coating, where they were typically found to be 0.1. Even though the intensity ratios obtained are quite low, the compromise was visible with regards the crystallinity of the film. Some regions were found that had the desired thinness and desired electron transparency (<50 nm) but no atomic resolution imaging and analysis could be achieved due to the amorphisation of the material leading to a lack of crystallinity in the film.

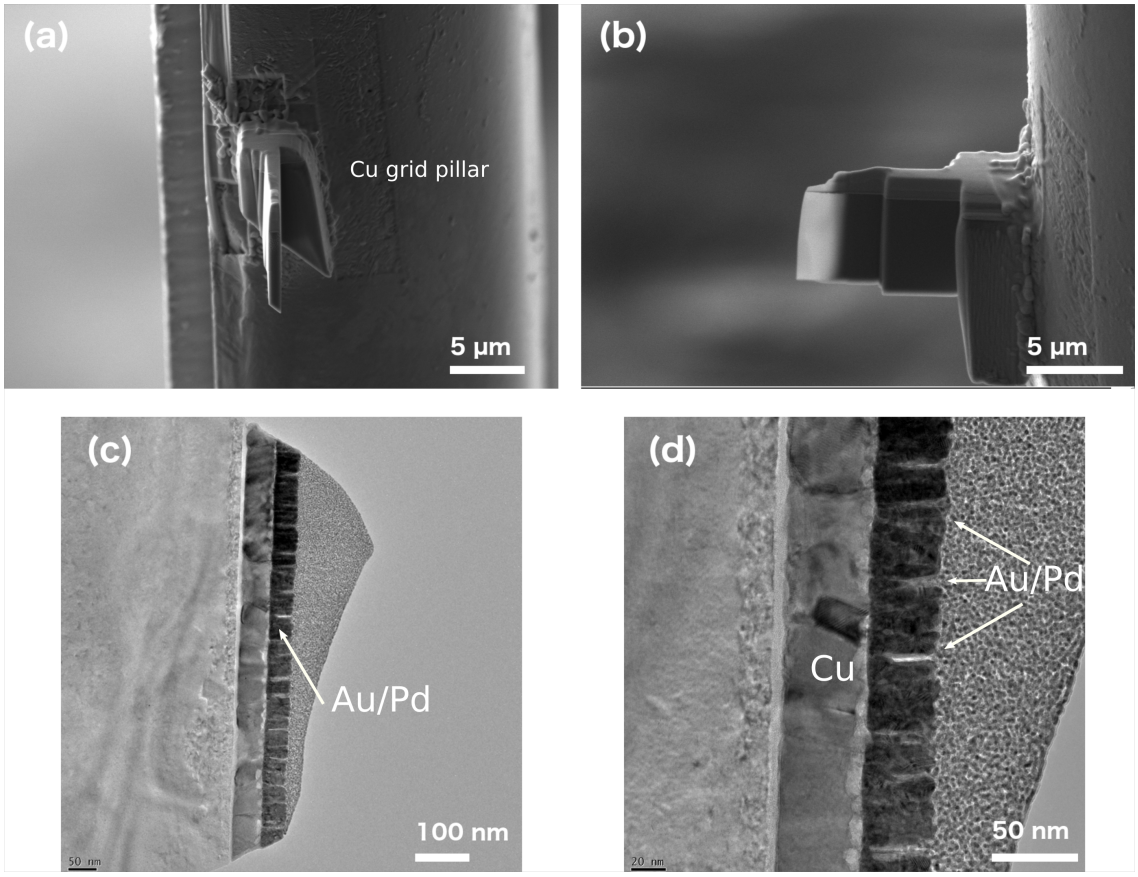

Figure 4-1: (a) Scanning Electron Microscopy (SEM) image of side-on profile of the lamella, (b) SEM image of the lamella after its final 5 kV 20 pA polish, (c) 300 kV Transmission Electron Microscope (TEM) image of gold/palladium (Au/Pd) and platinum (Pt) coated lamella and (d) TEM image with arrows marking large columns/gaps in the Au/Pd coating. (Notation in images: Cu=copper, Au/Pd=gold/palladium, Pt=platinum)

4.3.2 Adopted Weld Technique

Another technique adopted during lamella preparation was the weld of the lamella to the pillar of the TEM Omniprobe grid. Due to the geometry of the Gas Injection System (GIS), FIB and SEM columns in the Zeiss dual-beam systems, it was very challenging to weld the lamella to the grid with ion beam-induced deposition (IBID)-Pt. This type of weld would be preferable to the electron beam induced deposition (EBID)-Pt, as it is much stronger weld and strength is of vital importance if the lamella is to be analysed on multiple occasions in different microscopes. However, the lamella was nevertheless welded securely using an EBID-Pt weld and the micromanipulator was removed. The GIS was securely parked before continuing on with this method, as there would be a stage touch. Once this was checked, the stage was tilted to 7°. Once tilted, the lamella was then viewed in the FIB and with some minor stage movements the lamella appeared upside down on the pillar in the centre of the image. This is depicted in Figure 4-2 (a) and (b) which display the SEM and FIB view at the 7° stage tilt,

respectively. A reduced raster box is carefully placed at an ion beam voltage and current of 30 kV 2 nA respectively, on the area of the pillar directly adjacent to the lamella. A slight overlap was milled between the area of the pillar beside the lamella and the edge of the lamella itself. This ion bombardment milled into both the EBID-Pt weld and the Cu pillar, fusing the two into a stronger weld. This was then repeated, carefully, at the top of the lamella and the opposite side to ensure a secure weld. It must be stressed to be as careful as possible when moving the reduced raster box to a different area of the lamella, as sometimes the reduced function can focus on the middle of the lamella, which can lead to unwanted milling/damage of the lamella.

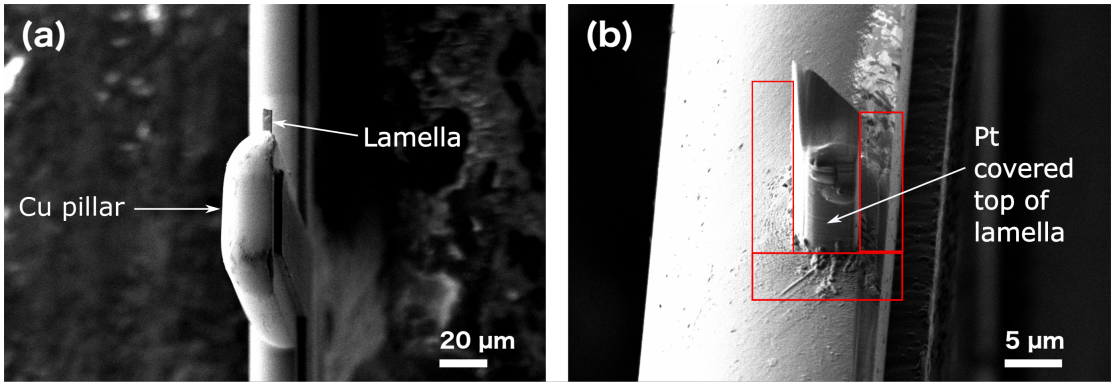

Figure 4-2: (a) Scanning Electron Microscopy view of pillar and lamella at 7° and (b) Focused Ion Beam view of lamella on pillar at 7° with the boxes indicating the regions in which the beam is placed to create a stronger weld.

4.3.3 No Additional Coating

Due to the essentially destructive nature of Au/Pd protective coating, the following lamellae were prepared with no coating prior to the Pt protective layer deposited using both EBID-Pt and IBID-Pt *in-situ* within the SEM/FIB system. Again, this lamella was prepared in the bulk of the sample using the *in-situ* lift-out method as described in section 3.1.2 of chapter 3.

The bulk thinning at 30 kV 240 pA was done at an angle of 0° with respect to the FIB. At the lower polishing energies, more specifically the final low 5 keV beam energy, the lamella was tilted to an angle of 1 – 2° with milling times of ~5 minutes either side of the lamella.

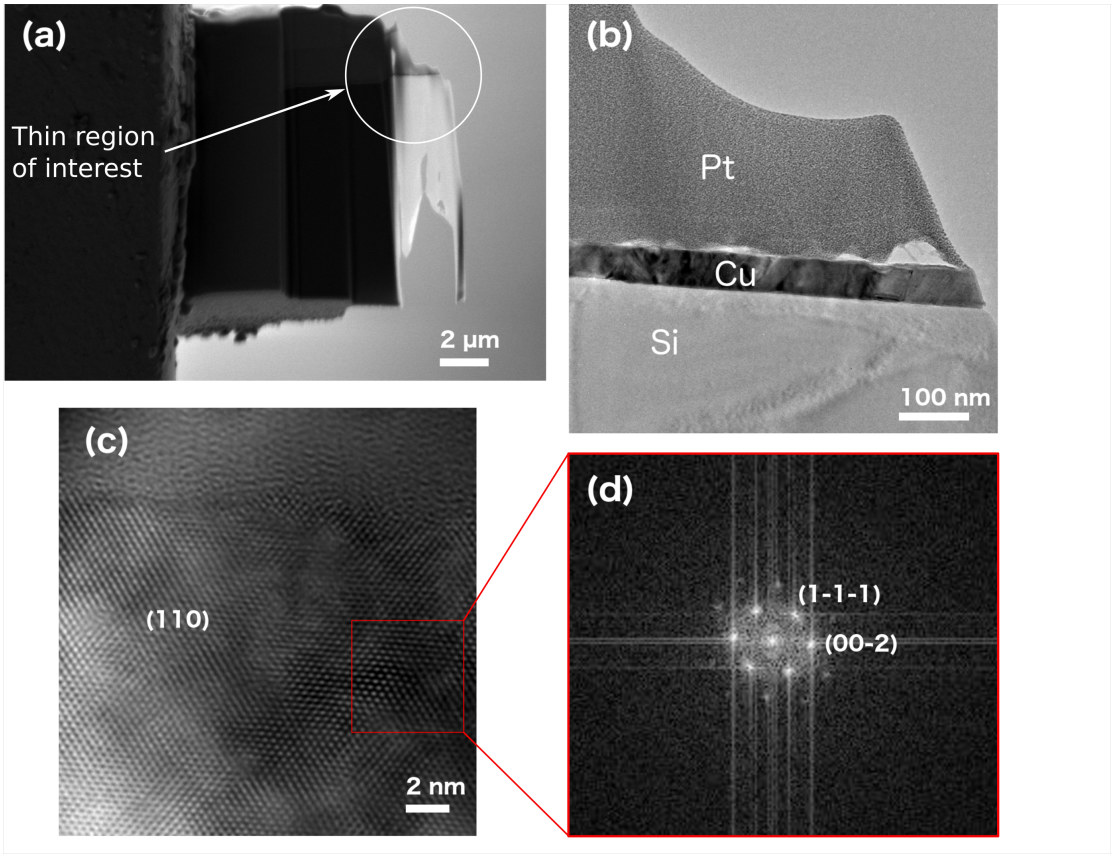

Figure 4-3: (a) Scanning Electron Microscopy image at 3 kV of final lamella prepared with 5 kV polish, (b) 300 kV Transmission Electron Microscopy (TEM) image of lamella, (c) High-resolution 300 kV TEM image of silicon (Si) substrate with (d) the indexed fast Fourier Transform (FFT) of the area highlighted in red. (Notation in images: Cu=copper, Pt = platinum, Si=silicon)

Figure 4-3 (a) shows a SEM image of the final 5 kV thinning of the lamella, with the thinnest region and hence the region of interest for TEM analysis highlighted. The TEM image of this highlighted region is displayed in Figure 4-3 (b). The Pt layer provides a significant layer of protection, which compensates for the lack of an extra protective layer such as Au/Pd. The changes in preparation technique lead to distinct improvements as shown in the high-resolution TEM image of the Si substrate interface with the SiO_2 layer shown in Figure 4-3 (c). Producing this kind of high-resolution imaging proves extremely promising in terms of optimising lamella preparation and ultimately gaining insights into the microstructural properties of the Cu film. The Fast Fourier Transform (FFT) shown in Figure 4-3 (d) highlighted again that at this early stage of optimizing the sample preparation that atomic resolution information of the Si substrate can be consistently obtained. An Energy-Filtered TEM (EFTEM) thickness map of the thinned region of interest was acquired and the t/λ value was found to still be relatively low at the Cu/SiO_2 interface with values between 0.28 – 0.35 and even lower still at ~0.22 at the top of the Cu film, closer to the Pt protective layer. Using the formula

outlined in chapter 2, equation 2.7, a rough estimation for λ for Cu is ~78 nm, giving a thickness of ~17 nm. This is quite a low value and is of the thinnest region visible in the thickness map. It may not have the most crystalline region. These variations in thickness were as expected, although the average thickness was still thicker than the thicknesses achieved using the method previously described using the Au/Pd coating. Nevertheless, the quality and crystallinity of the lamella produced via the adapted method was clearly evident while still maintaining the electron transparency and sufficient thinness of the lamella.

4.3.4 Carbon Coating, Wedge Technique and 2 kV Polish

Multiple lamellae were prepared following this adapted method, without any significant improvement occurring in terms of reducing the thickness of the Cu film. As mentioned in the previous experimental methods chapter, Schaffer *et al.* have developed an inverted triangle "wedge" technique to maximize the protection and reduce damage of the layer of interest within the lamella. They predominantly do this through creating a technique which creates an "ice cream cone" type shape, as can be seen in the side-on SEM image of the lamella mounted on the TEM grid pillar shown in Figure 4-4 (a). By employing this new wedge technique, the area of interest was further protected from the gallium (Ga) beam. Furthermore, there was less aggressive milling of the Pt, which meant that 2 kV 20 pA could be used to further polish the lamella. There were other helpful precautionary measures to further reduce the chances of damaging the lamella used by Schaffer *et al*. These included coating the bulk sample with a layer of carbon (C) and depositing a further 500 nm extra Pt compared to traditional lamella preparation techniques. Schaffer *et al*. stress that these procedures are of particular importance when the area of interest is near the sample surface, which is the case for all the samples used over the course of this PhD work. Hence adopting the approach developed by Schaffer *et al.* allowed for a 2 kV polish to be used without causing damage to the lamella as previously shown.[9] This "ice cream cone" approach resulted in a thinner lamella with less apparent damage compared with the previous lamellae produced using just a 5 kV polish. Prior to this technique, it was very difficult to use the 2 kV 20 pA beam as it is very broad and would damage and mill away most of the very fine Pt layer that was left after a 5 kV final polish.

An EFTEM thickness map of the thinned region highlighted in Figure 4-4 (b) and (c) was acquired and the t/λ intensity ratio of this region was found to be slightly lower than the

previous Pt protected lamellae with values of 0.24 – 0.26 at the Cu/SiO_2 interface and similar values of 0.22 at the top of the Cu film near the C layer.

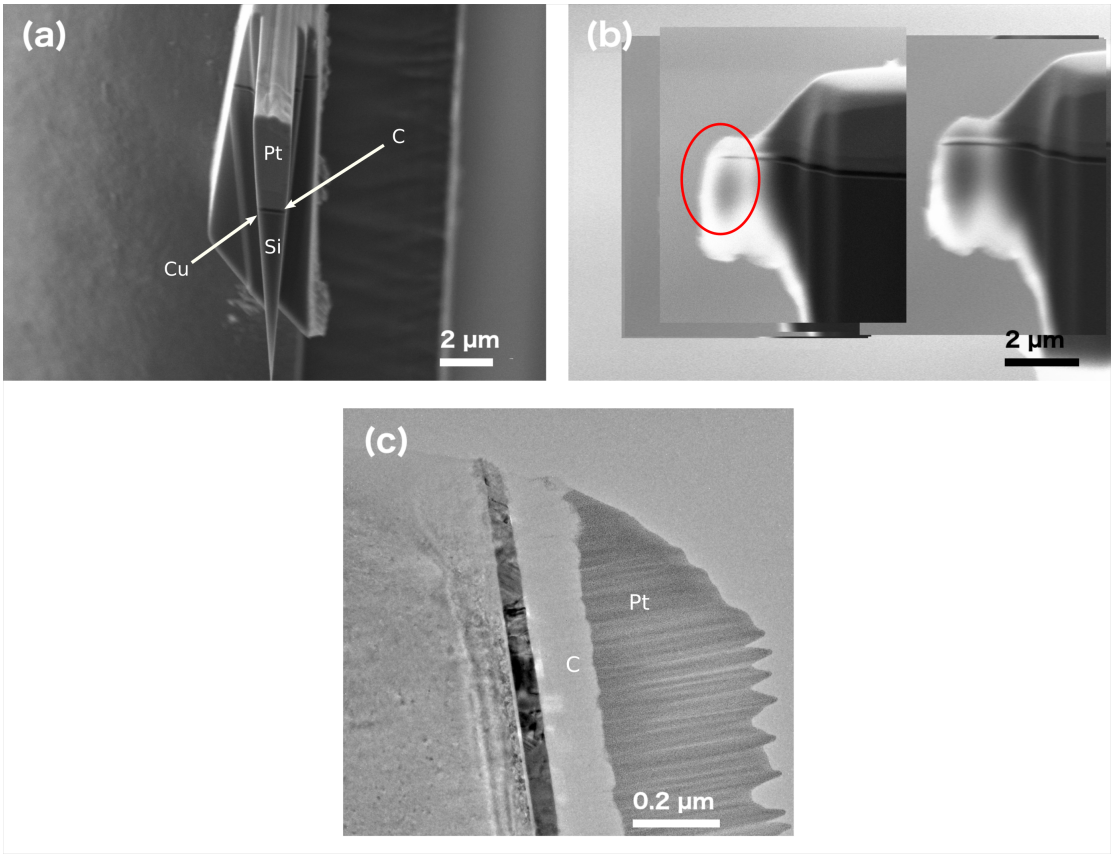

Figure 4-4: (a) Scanning Electron Microscopy (SEM) image of side-on view of an inverted triangle "wedge" shaped lamella, (b) 3 kV SEM image of final 2 kV 20 pA polish of cross-sectional lamella (circle marking area of interest for Transmission Electron Microscope (TEM)) and (c) TEM image showing the low kV polished lamella. (Notation in images: Cu=copper, C=carbon, Si=silicon, Pt=platinum)

4.4 Cu Film Microstructure Characterisation

4.4.1 Grain & Grain Boundary Size and Structure

As can be seen throughout the lamella preparation optimization process detailed in chapter 3, determining the grain size distribution throughout the cross-sectional lamella was quite challenging. The main challenge was to reduce the thickness of the lamellae sufficiently, particularly in the early stages. Another challenge was to preserve crystallinity as a lot of the over-thinned regions were damaged by the FIB beam due to milling and as a consequence had lost most of their structure.

It is worth nothing at this point that it is evident from the high-resolution images shown in the figures thus far that there is a range of different and complex grain shapes and grain boundaries present within this particular Cu film.

In Figure 4-5 (a) and (b) we can see the mixture of columnar grains with grain boundaries almost perpendicular to the Cu film and others with a distinct angle. The visible grains were found to be comprised mainly of columnar grains which ran the depth of the Cu film i.e. had a depth of ~40 nm. The width of these columnar grains ranged from 25-100 nm. There were also some more irregular shaped grains, which were less rectangular in their two-dimensional (2D) structure. They were found to have a height of 40 nm with curved grain boundaries.

It is difficult to determine from a cross-sectional perspective the statistical distribution of both low-angle grain boundaries (LAGB) and high-angle grain boundaries (HAGB) within the film. Grains can be defined by the misorientation angle between them. A LAGB is a misorientation between two grains, which is less than 10-15°, this is material dependent**.** They are generally comprised of an array of dislocations and their structure and properties are correlated with the misorientation. HAGBs have a misorientation greater than 10 – 15°. Unlike LAGB, HAGB properties are generally found to be independent of misorientation.[10] As shown in Figure 4-5 (c) and (d) there is a complex mixture of grain sizes and grain boundaries with many being extremely complicated boundaries incorporating a mixture of misorientations from both the tilt and twist direction. It has been reported that there is poor Cu grain texture on SiO_2 barrier layers, particularly a weak (111) surface texture, which could be contributing to the varied mixture of grain and grain boundaries observed.[11]

Another grain feature observed in Figure 4-5 (b) and (d) is grain boundary grooving. Grain boundary grooving is a process when surface diffusion redistributes the diffused atoms at the grain boundary triple junction, which creates equilibrium of the surface tensions of all the contributing interfaces.[12] Grain boundary grooving is closely linked to film de-wetting, which will be discussed further in chapter 6, when discussing *in-situ* techniques.[13] It has been observed that normal grain growth stagnates when the average diameter of the columnar grains is 2 – 3 times the size of the film thickness. This is known as the specimen thickness effect. Mullins *et al.* stated that this stagnation is linked with grain boundary grooving occurring when the grain boundary meets the free surface of the film.[14]

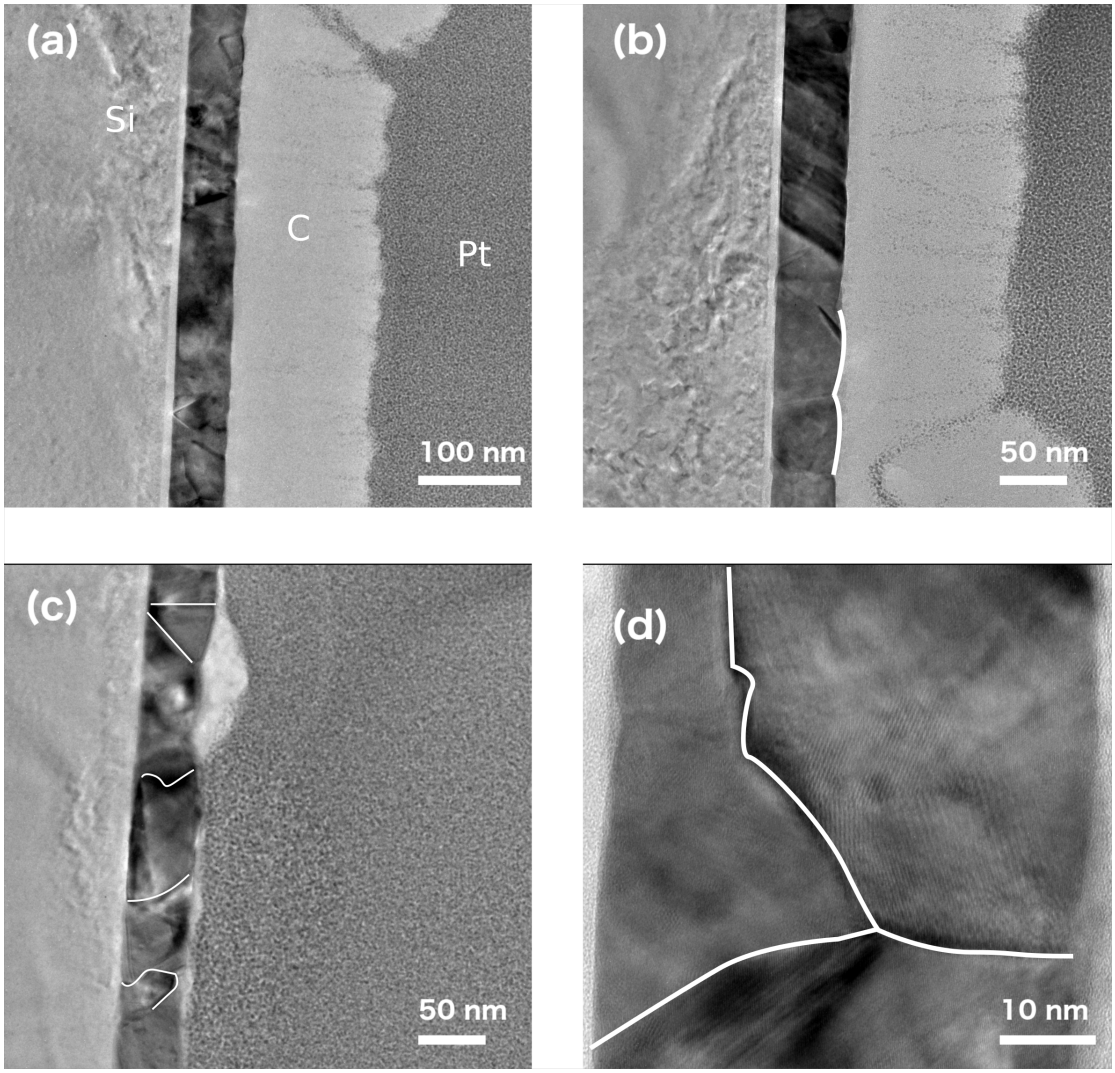

Figure 4-5: Transmission Electron Microscopy images at 300 kV of (a) visible grains and grain boundaries within the 40 nm copper (Cu) layer of lamella (b) grain boundary grooving within the film, c) and d) high-resolution imaging revealing the angles between different grains. (Notation in images: Si= silicon, Pt=platinum, Cu=copper and C=carbon)

4.4.2 Intra-grain Features

4.4.2.1 Twinning

Deformation twinning occurs in a crystal when part of the crystal lattice undergoes a homogenous shear, which changes the original orientation of the crystal lattice. Another way of describing this is to say that a twin boundary is a mirror image of a crystal's lattice structure, see Figure 4-6 (a). They can form through the mechanism of partial slip through close packed layers {111} for this particular face centred cubic (fcc) crystal.[15], [16]

It is noted from the literature that deformation twinning greatly increases in metals when they are reduced from coarse grained (micron size) to below 100 nm grain diameter. Both grain size and stacking fault energy affect the formation of twins in nanocrystalline fcc metals.[17], [18]

High mechanical strength and low electrical resistivity are very important and are ideal properties for Cu interconnects within integrated circuits.[19] In this instance, twinning could potentially enhance the mechanical strength of nanocrystalline Cu interconnects. However, even though introducing defects can strengthen a nanomaterial, sometimes it can have adverse effects on electrical conductivity due to defects/dislocations potentially affecting the transmission/reflection probability of electron transport.[18] Cu interconnects with high density of {111} coherent twin boundaries reduce electromigration as the twin boundaries slow down the diffusion of vacancies/Cu atoms.[20] The triple point where a grain boundary meets a twin boundary reduces surface and grain boundary electromigration by an order of magnitude.[19]

However, twin boundaries are preferable to HAGBs as their electron scattering coefficient is an order of magnitude lower.[21] From a thermodynamic point of view, the formation of twin boundaries reduces the overall interfacial energy as the excess energy for coherent twin boundaries is much smaller than that for conventional HAGBs.[22]

Cu synthesized with a high density of nanoscale growth twins has been found to exhibit considerably higher tensile strength than coarse-grained Cu, but the former retains the electrical conductivity comparable with that of pure Cu.[22] The electrical conductivity of nanocrystalline Cu without twins was at least one order of magnitude lower. Resistivity of grain boundaries in Cu at 295 K is known to be 3.6×10^{-16} Ωm^2 and twin boundaries is 1.7×10^{-17} Ωm^2.[18], [23] The presence of twin boundaries within the Cu film may not have such an adverse effect on the electrical conductivity as opposed to HAGBs.

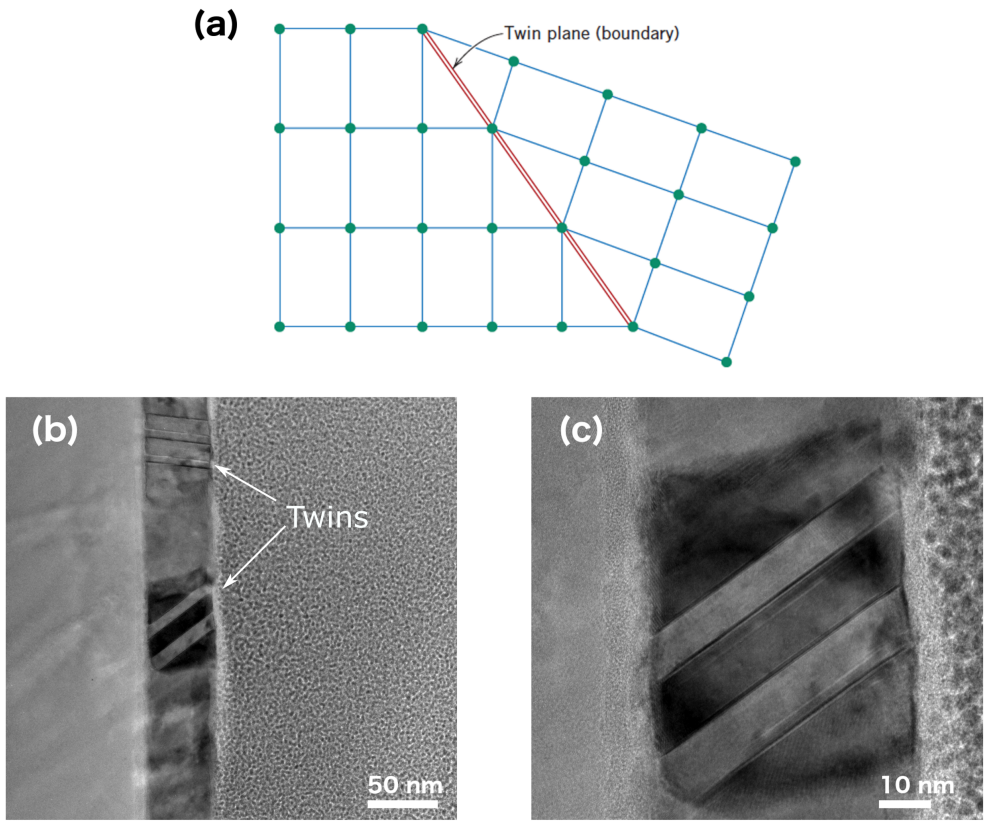

Figure 4-6: (a) Schematic of twin plane/boundary, mirror image of crystal lattice is shown here [24]*, (b) Transmission Electron Microscopy image of the copper (Cu) film containing multiple twins and (c) grains taken from central region shown in (b) with twins at angles to film surface.*

As can be seen from the images in Figure 4-6 twinning is present in the Cu film. Figure 4-6 (b) and (c) display twin boundaries typically running the depth of the Cu film primarily at angle of ~54.6°, with some running at angles of ~81.7° to the Cu film surface. The size of these twins range from 10-30 nm in width. There is a correlation between the thickness of the twins and resulted increase in strength of nano-twinned Cu.[25]

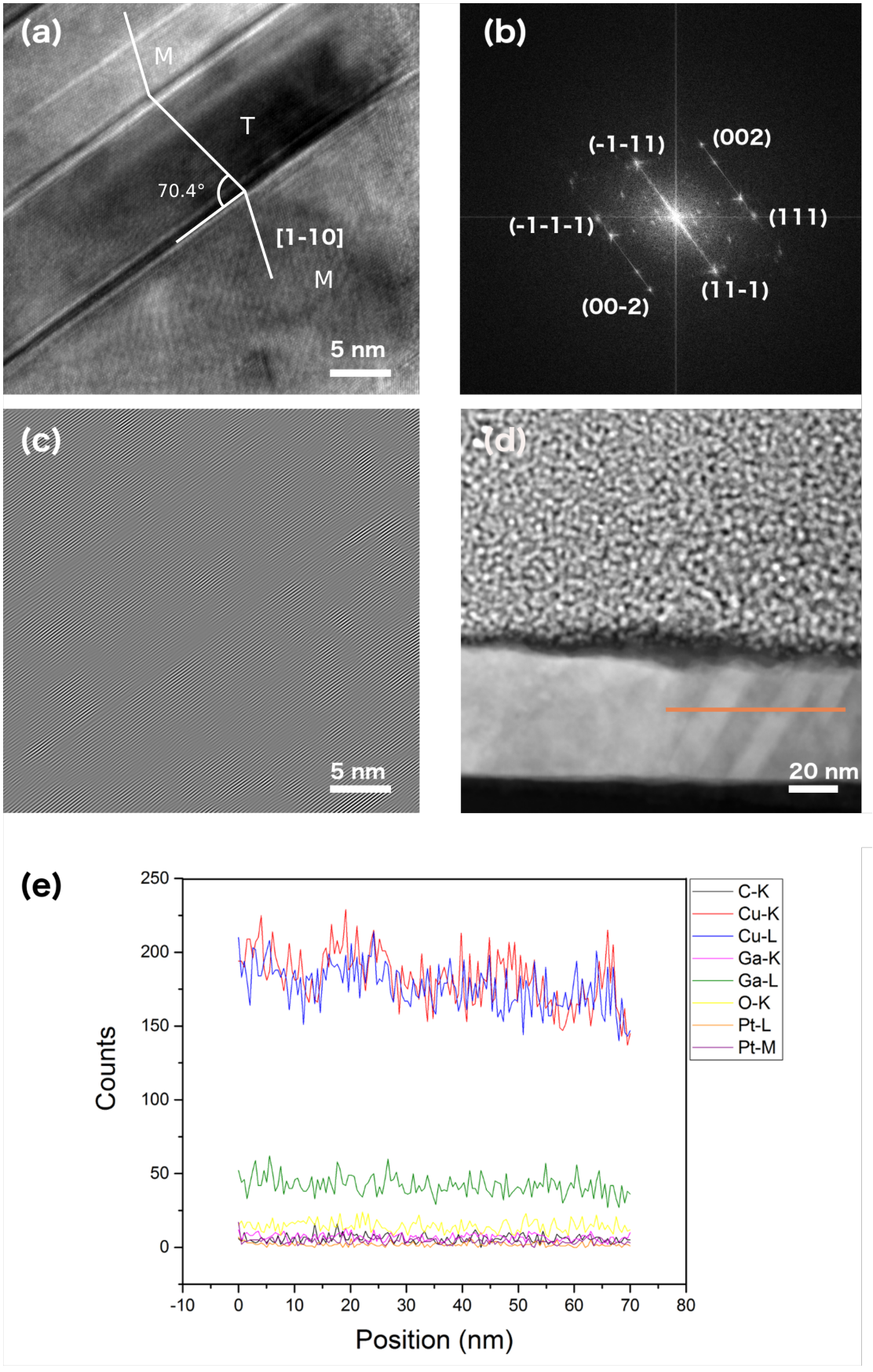

Figure 4-7: (a) High magnification Transmission Electron Microscopy (TEM) image of twins highlighted in Figure 4-6 (b) with a 70.4° tilt with respect to the matrix lattice (b) indexed fast

Fourier Transform (FFT) of twin in (a), looking at the [1-10] beam direction, (c) inverse FFT of the (11-1) and (-1-11) diffraction spots from part (b) confirming the twin boundary plane, (d) Area in which Energy-dispersive X-ray line scan was obtained across the twin boundary and (e) graph displaying the elemental spectra obtained from (d). (Notation in images: M=matrix lattice, T=twin)

Using HRTEM imaging, mainly coherent twin boundaries were observed. An example can be seen in Figure 4-7 (a). The indexed FFT in Figure 4-7 (b) displays two spots in close proximity to each other. These spots represent the twin boundary lying in the (11-1) plane. The beam direction is the [1-10] direction.

The FFT of this particular twin also displays the mirror symmetry with an angle of ~70.4° with the boundary lying in the (11-1) plane, which is in agreement with the expected value for twin boundaries in Cu, see also inverse FFT of the twin boundary plane in Figure 4-7 (c).[16] This could potentially be of interest as it has been investigated that Cu interconnects with a significant number of {111} coherent twin boundaries can potentially lead to increased resistance in electromigration of the Cu. Therefore these particular twin boundaries could potentially slow down the diffusion of vacancies or Cu atoms.[20]

An EDX line scan was acquired across the double twin boundary with the element spectra plotted across the line scan distance, as shown in Figure 4-7 (d) and (e). There was no change in the chemical composition of the Cu but there is a noticeable change in the Cu counts across the twin boundary with the peak rising again once within the grain. Concurrently, the counts are consistently reducing across the entire boundaries due to the reduced thickness of the region itself.

As can be seen from Figure 4-8 (a), twins could potentially be propagating from the dislocations at the SiO_2/Cu interface. There are also twins running parallel with the Cu film surface which terminate at the grain boundary interface, as is marked in Figure 4-8 (b). This could be interesting in terms of twins being more energetically favourable than other grain boundary types. There were also incidents of 5-fold twins within the Cu film, see Figure 4-8 (c).

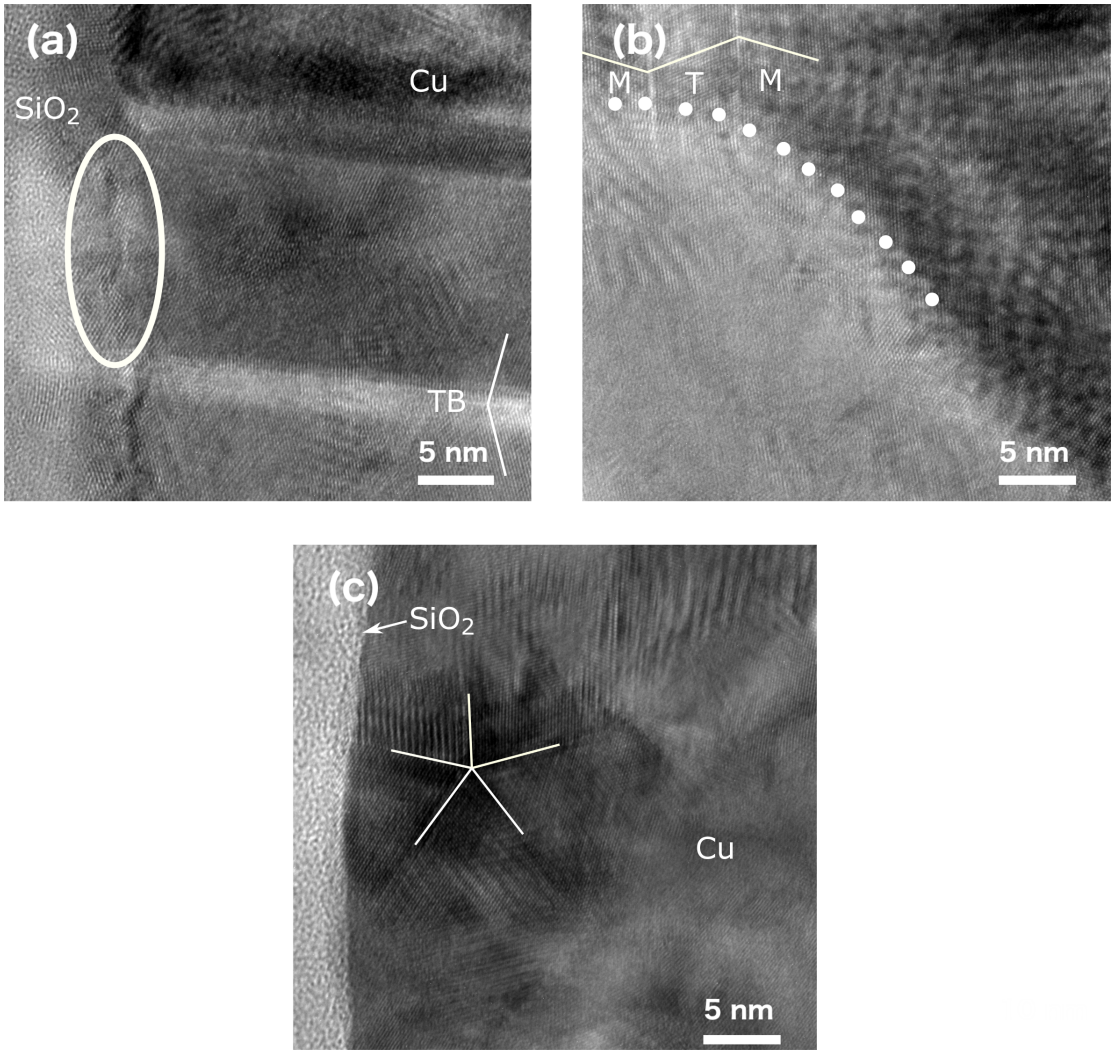

Figure 4-8: Transmission Electron Microscopy (TEM) image at 300 kV of (a) twin boundary (TB) in copper (Cu) film with dislocations highlighted at interface, (b) TB within Cu grain parallel to the Cu film with boundary terminated by asterisks and (c) 5-fold twin within grain in Cu film. (Notation in images: SiO_2=silicon dioxide, Cu=copper, M=matrix lattice, T=twin, TB=twin boundary)

4.5 Damage of Cu Film

Damage under the electron beam was observed in the thin lamellae. The Cu layer was showing significant structural damage as well as movement of the Cu material, particularly in thinner areas of the lamellae. This is most likely due to the quality of the Cu film, which led to some structural deformation under the electron beam. There was a considerable amount of crystallites within the grains themselves, as shown in the TEM image in Figure 4-9. It is clear from the image that there is a lot of damage to the lattice within the grains themselves. These

small areas of crystallinity proved extremely difficult to index as well as to interpret the grain structure.

The small nano-crystallites showed the quality of this particular evaporated Cu film on the SiO_2 liner. The grains were not uniform in crystallinity and this affected the structural integrity/stability of the film.

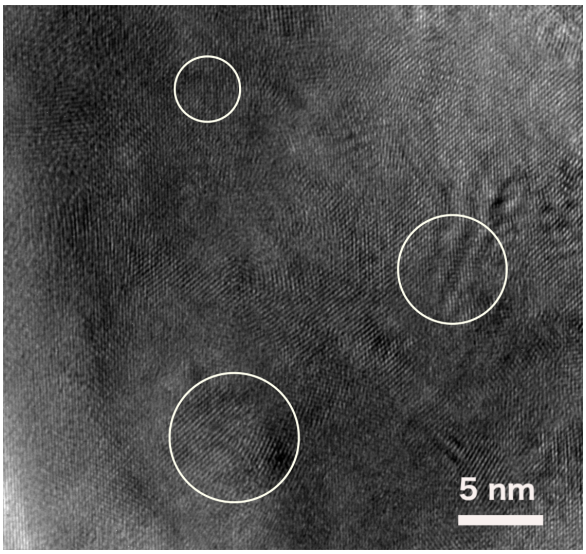

Figure 4-9: Transmission Electron Microscopy image showing the crystallites within copper grains in 40 nm film.

The effects of FIB milling on and the potential damage to the Cu are discussed in the section 3.2. In order to confirm whether the damage was related to the electron beam, a series of images were obtained over an 8 min time period, as shown in Figure 4-10 (a) and (b). An EDX line scan was also acquired across the Cu/SiO_2 interface, confirming the presence of Cu across the SiO_2 and into the Si substrate, see Figure 4-10 (c). The Cu spectra does reduce across the interface, but still has a significant presence in Si, shown in Figure 4-10 (d). The corresponding video of the damage induced over time can be found in the Appendix A1. There are two main mechanisms of sample damage in the TEM: knock-on damage and ionization damage (radiolysis). Knock-on damage, also called displacement damage, describes the event when fast electrons from the beam transfer sufficient energy to atoms in the sample to knock them out of their sites. This mechanism is caused by elastic scattering of the beam. Conversely, radiolysis is due to inelastic scattering of beam electrons breaking chemical bonds in the sample. The minimum amount of energy needed to cause atomic displacement or sputtering in a specific sample can be calculated if the displacement energy threshold of the material and

the incident energy of the electrons are known.[26], [27] It is noted that most metals experience knock-on damage. Although the thickness of the sample also has a role in the damage occurring as thicker sample experience increase radiolysis compared to thinner samples of the same composition.

According to Egerton *et al.* the displacement energy, E_d for Cu is 20 eV and the threshold energy for displacement of Cu is found to be 93 keV and 147 keV for surface and bulk sputtering thresholds, respectively.[28] Hence, damage is most likely caused by the sputtering of the Cu by the electron beam. However, it is likely that both damage mechanisms play some role in the damage observed.

All imaging in the TEM thus far had been done at an accelerating voltage of 300 kV, which was above the threshold for both damage mechanism. The beam voltage was reduced to 80 kV to reduce the damage occurring as this was thought to slow the damage process according to the energy thresholds stated in the literature and mentioned above.[28]

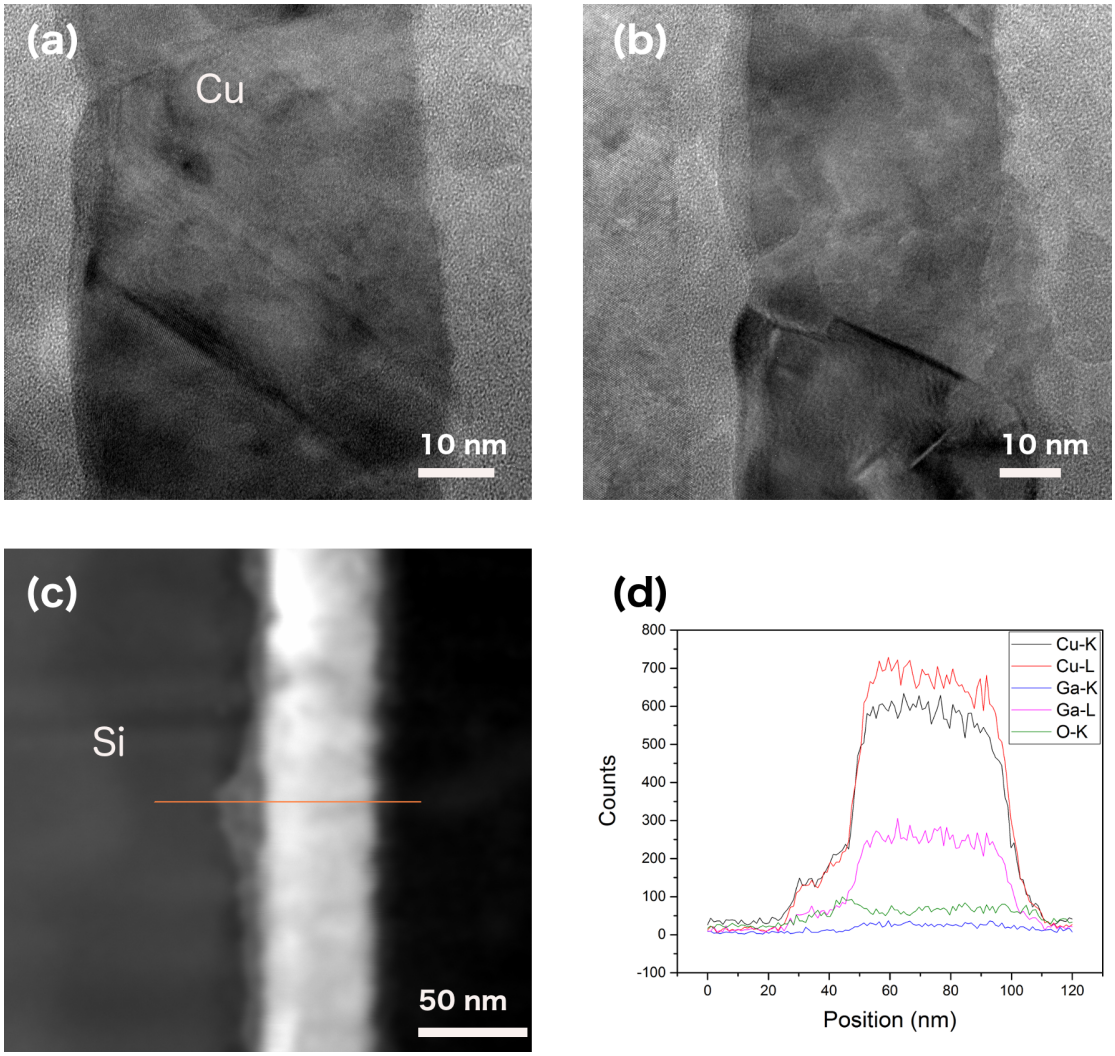

Figure 4-10: Transmission Electron Microscopy image showing the structural damage to the copper (Cu) film (a) before and (b) after 8 minutes of beam exposure at 300 kV, (c) The area in which an Energy-dispersive X-ray Spectroscopy line scan was acquired over the damaged area, (d) graph displaying the elemental spectra obtained from (c) showing a significant presence of Cu in the silicon (Si) substrate.(Notation in images: Cu=copper, Si=silicon)

Figure 4-11 displays images taken of the Cu film at 80 kV within the TEM. Unfortunately, there is still a significant amount of damage occurring, making it extremely difficult to image and analyse the grain structure of the Cu film. There was a slight increase in the time window available to image without significant visible damage to the material.

The small time window available to image and analyse the sample was challenging as in order to obtain high-resolution data more time tuning the instrument and higher doses of electron irradiation are needed to image and analyse the lamellae. The damage of the Cu film persisting at 80 kV was unexpected which could suggest that the Cu material itself is making the sample more susceptible to damage. As mentioned earlier in this chapter, this particular

Cu film does not have long-range order and there are many smaller crystallites contained within its grains. This structural instability could be increasing the probability of sputtering and it also could be hindering the film from dissipating heat more efficiently. Therefore resulting in an increased susceptibility to damage under the electron beam.

A significant portion of the damage in the 80 kV shown in the images in Figure 4-11 is visible in the SiO_2 layer. Due to its insulating properties, this layer experiences a significant amount of radiolysis, resulting in what appears to be mass-loss as can be seen in Figure 4-11 (a) and (b) (change in layer thickness marked in red). The heating of the insulating SiO_2 layer, could subsequently be annealing the Cu film and damaging its structure.[28]

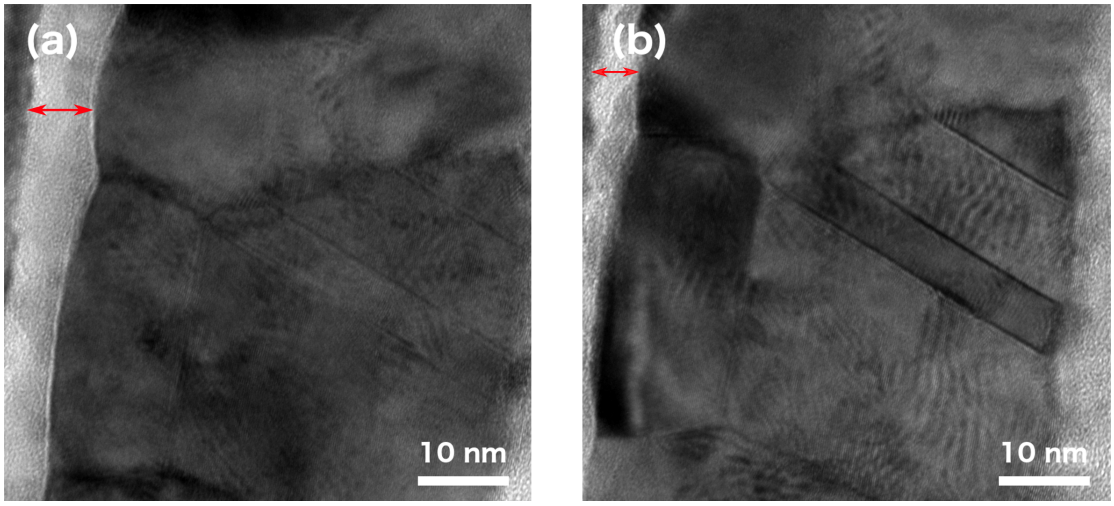

F*igure 4-11: Transmission Electron Microscopy image showing the reduction in thickness of the silicon dioxide layer (a) before and (b) after 8 min of electron beam exposure at 80 kV.*

4.6 Comparative Scanning Tunneling Microscopy and Conductive-Atomic Force Microscopy

Concurrently, both the STM and C-AFM spokes of this project were also experiencing challenges albeit different to what was experienced using TEM when attempting to obtain high-resolution data from this particular sample. Both of these techniques were studying the sample surface and experienced challenges in terms of oxidation of the sample. In addition, the films surface was simply too rough to obtain any atomic resolution data, particularly in terms of the STM. The STM data suggested that the bulk of the Cu film could be crystalline but the surface of the material was not. As has been shown in this chapter, there were also some

crystallinity issues within the bulk of the Cu film also. Figure 4-12 (a) and (b) show the STM images of the Cu film surface. It was very challenging to obtain any atomic information especially with regards grain boundary identification and characteristics.

In terms of C-AFM, it was again extremely challenging to obtain any useful surface information from the Cu film as surface roughness, oxide formation and degradation hampered the capabilities of the AFM. As can be seen in Figure 4-12 (c) and (d), both the topography and conductivity show very little in terms of grain size or boundary frequency along the wire, with no data obtained in relation to grain size, distribution and grain boundary structure.

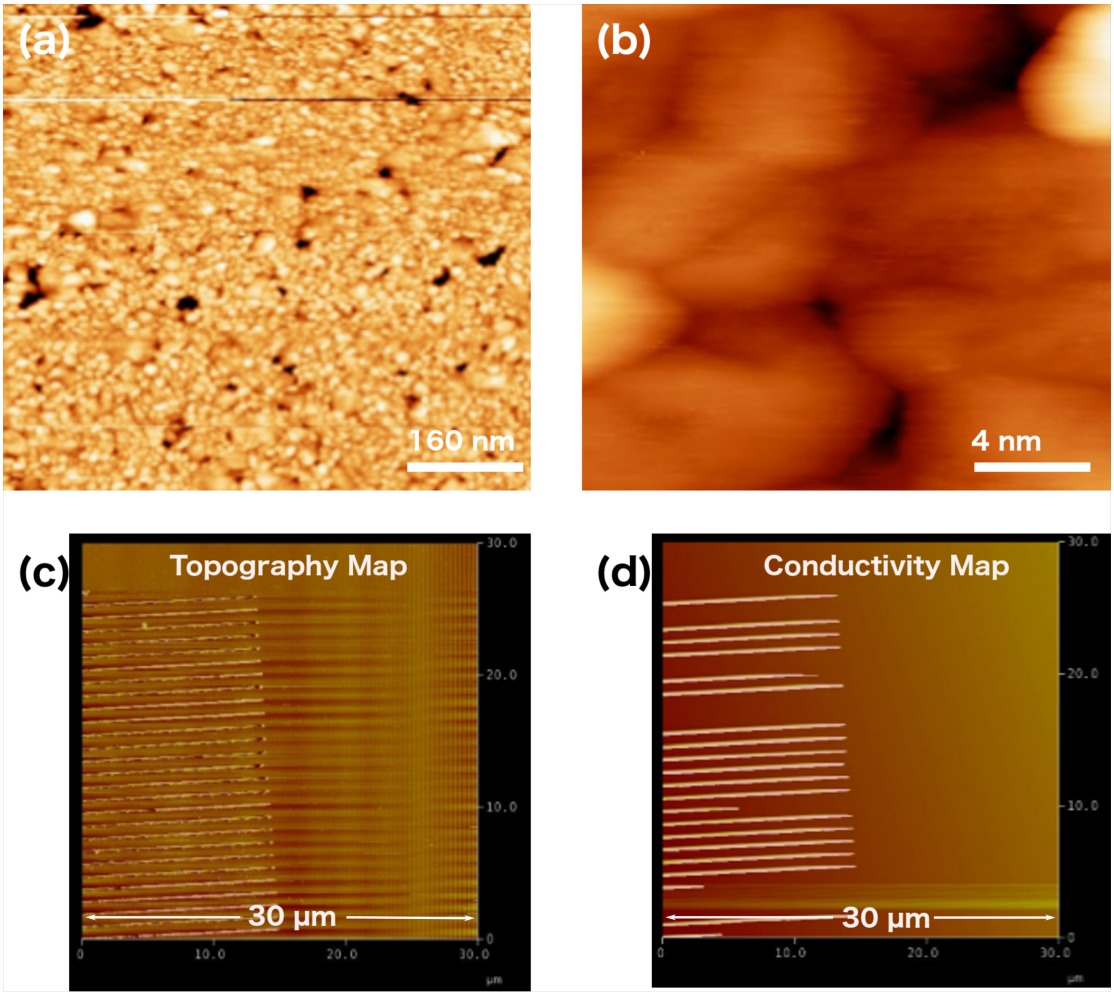

Figure 4-12: (a) & (b) Scanning Tunneling Microscopy images of copper (Cu) film surface with the silicon dioxide (SiO_2) liner, (c) and (d) displaying Conductive-Atomic Force Microscopy topography and conductivity maps respectively of the Cu nanowires on SiO_2.

The combined challenges faced using the different characterisation methods suggested that the Cu films were overall of too poor quality and susceptible to intra-grain disorder and amorphisation to successfully and reliably image and analyse at high resolution. It was

therefore decided to explore a different Cu film thickness on a different liner and Ta was thought to be a good alternative candidate and the results of this investigation are described in the next section. The sample consisted of 50 nm Cu film with a 7 nm Ta liner, on a Si substrate. This sample was prepared by sputtered PVD as opposed to the evaporated Cu on SiO_2. This sample instantly produced better results but this new liner came with its own set of drawbacks in terms of the sample preparation for TEM analysis. This will be discussed in chapter 5.

Although the SiO_2 sample produced less than optimal results, the time analysing it was not wasted. The lamellae preparation technique was steadily improved and optimised in the process to provide the highest quality lamellae necessary to observe the microstructure of the Cu film.

4.7 Tantalum Liner

The Ta liner lamellae were prepared in an identical fashion to the optimised technique used for the SiO_2 liner. The wedge technique was adopted with a final polish of 2 kV 20 pA and an extra protective layer of C as well as Pt were deposited.

The Cu film deposited onto the Ta liner is of significantly better quality, as can be seen from the images in Figure 4-13 (a) and (b). Little to no damage was visible when imaging at 80 kV and 300 kV, suggesting that the damage experienced with the previous sample was most likely due to knock-on damage/sputtering resulting from the disordered nature of the grains within the sample. In absence of noticeable knock-on damage, using 300 kV is preferential as imaging at 80 kV a) requires thinner samples – a difficult task for low kV prepared lamellae – and b) also results in lower image resolution. The HRTEM images in Figure 4-13 (c) and (d) show that the lamella preparation had finally been successfully optimized as the crystallographic and atomic structure information are now observable in the images of the lamellae.

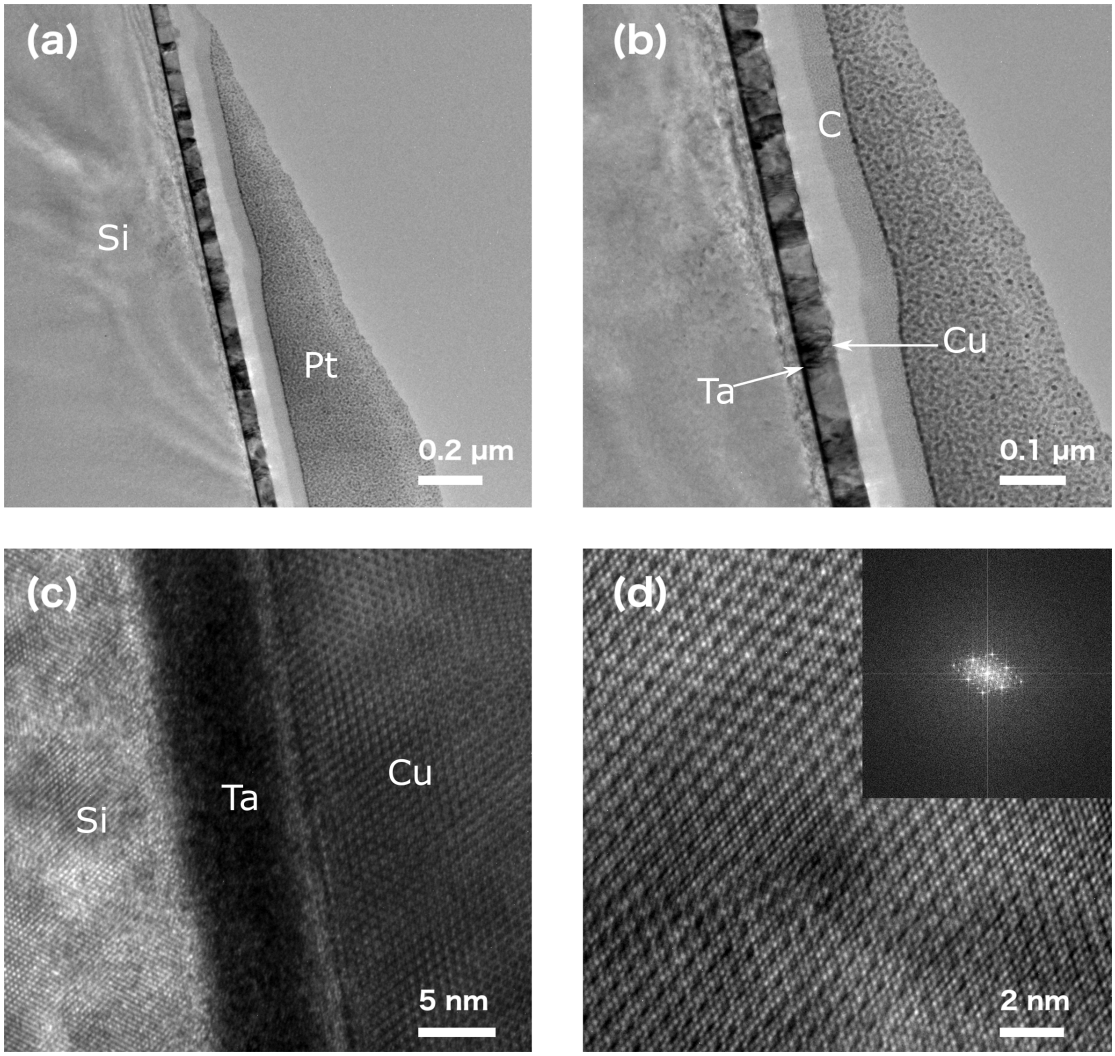

Figure 4-13: Transmission Electron Microscopy (TEM) images acquired at 300 kV of (a) lamella overview, (b) copper (Cu) layer, (c) silicon, tantalum and Cu interfaces and (d) atomic structure of Cu layer with fast Fourier Transform (inset). (Notation in images: Cu=copper, Si=silicon, Ta=tantalum, Pt=platinum, C=carbon)

The images suggest that the grains are relatively columnar in nature, running the whole depth of the film, as shown in Figure 4-13 (a) and (b). This has some similarities to that of the SiO_2 sample as it also had regions of columnar grains. However, there were a significantly larger number of irregular grains present in the SiO_2 than the Ta sample. The grain sizes running from ~30-100 nm were found to be similar in both sample types. HRTEM images in Figure 4-13 (d) show the intragranular nature of the Cu film on the Ta liner which were found to be significantly different from the ones in the Cu film on SiO_2. Crystallinity within the grains was clearly visible in the Ta sample, making it easier to obtain atomic resolution images of the film. This was achieved after preparing only three lamellae. This was in stark contrast to the SiO_2 sample, which contained a large number of dislocations and crystallites. EFTEM thickness maps were acquired and the intensity ratio t/λ at the Cu/Ta interface was found to be

considerably higher than that of the Cu/SiO_2, at ~0.35, with a lower value at the Cu/C interface of ~0.19-0.22. This was not unexpected as Ta is a much heavier material than Cu and consequently has different sputter rates. It is very challenging to mill materials of varying sputter rates within the same film, especially when they are only nanometres apart. Consequently, a variation in thickness has to be expected in these samples, thus explaining the thicker region of Cu than what has previously been recorded up until this point. But the quality of the Cu film is of a higher standard meaning there appears to be a trade-off between sample thickness and sample crystallinity. This data supported the decision to pursue all further experiments, preparation and characterisation using the Cu film on Ta liner.

4.8 Conclusions

This chapter has shown the successful optimisation of the lamellae preparation technique for both the 40 nm Cu film on SiO_2 and 50 nm Cu film on Ta. In order to achieve this optimisation, the Schaffer *et al.* wedge technique along with low kV milling and additional Pt protection layer deposition were employed.[9] The overall grain sizes, grain boundaries and crystallinity of the Cu film on SiO_2 were imaged and characterised using HRTEM imaging. The damage induced to the film by the electron beam irradiation was investigated. The characterisation and imaging at both 80 kV as well as 300 kV suggested that the SiO_2 samples were not suitable for atomic resolution analysis of the Cu grains, their boundaries or the interface of the film and liner.

A new sample type was investigated next: 7 nm Ta liner with 50 nm Cu films deposited by PVD. The lamella preparation technique optimised from the previous sample type was successfully adopted and high quality lamellae were effectively prepared. It became evident through HRTEM imaging of these lamellae and by comparing the data of the previous sample type to the new sample type using the Ta liner that lamellae produced from the latter sample type contained more uniform, crystalline Cu films of which atomic resolution imaging could be achieved.

From this analysis, an extensive amount of lamellae preparation was executed with respect to both the SiO_2 and the Ta liner samples. This led to a comprehensive comparison of both types of Cu film and ultimately led to the decision of using the Ta sample for the remainder of the

PhD work. The next chapters will be focusing on various lamella preparation techniques developed and optimised for the analysis of Cu on Ta in various different forms.

4.9 Bibliography

[1] "International Technology Roadmap for Semiconductors: Interconnect Chapter," pp. 1–106, 2014.

[2] S. Simões, R. Calinas, M. T. Vieira, M. F. Vieira, P. J. Ferreira, and P. J. Ferreira, "In situ TEM study of grain growth in nanocrystalline copper thin films," *Nanotechnology*, vol. 21, no. 14, p. 145701 (1-12), 2010.

[3] L. Lu, N. R. Tao, L. B. Wang, B. Z. Ding, and K. Lu, "Grain growth and strain release in nanocrystalline copper," *J. Appl. Phys.*, vol. 89, no. 11, pp. 6408–6414, 2001.

[4] K. Lu, "Nanocrystalline metals crystallized from amorphous solids: nanocrystallization, structure, and properties," *Materials Science & Engineering R*, vol. 16, pp. 161–221, 1996.

[5] C. Suryanarayana and C. C. Koch, "Nanocrystalline materials – Current research and future directions," *Hyperfine Interactions*, vol. 130, pp. 5–44, 2000.

[6] J. D. McBrayer, R. M. Swanson, and T. W. Sigmon, "Diffusion of Metals in Silicon Dioxide," *Journal of Electrochem. Soc. Solid State Science and Technology*, pp. 1242–1246, 1986.

[7] Y. Shacham-Diamond, A. Dedhia, D. Hoffstetter, and W. G. Oldham, "Copper Transport in Thermal SiO_2," *J. Electrochem. Soc.*, pp. 1–6, 2005.

[8] E. Montoya, S. Bals, M. D. Rossell, D. Schryvers, and G. Van Tendeloo, "Evaluation of top, angle, and side cleaned FIB samples for TEM analysis," *Microsc. Res. Tech.*, vol. 70, no. 12, pp. 1060–1071, 2007.

[9] M. Schaffer, B. Schaffer, and Q. Ramasse, "Sample preparation for atomic-resolution STEM at low voltages by FIB," *Ultramicroscopy*, vol. 114, pp. 62–71, 2012.

[10] "https://en.wikipedia.org/wiki/Grain_boundary," *online*.

[11] H. Lee and S. D. Lopatin, "The influence of barrier types on the microstructure and electromigration characteristics of electroplated copper," *Thin Solid Films*, vol. 492, no. 1, pp. 279–284, 2005.

[12] H. J. Frost, "Microstructural evolution in thin films," *Materials Characterization*, vol. 32, no. 4, pp. 257–273, 1994.

[13] R. Saxena, M. J. Frederick, G. Ramanath, W. N. Gill, and J. L. Plawsky, "Kinetics of voiding and agglomeration of copper nanolayers on silica," *Phys. Rev. B*, vol. 72, no. 11, pp. 31–7, 2005.

[14] W. W. Mullins, "The Effect of Thermal Grooving on Grain Boundary Motion," *Acta*

Metallurgica, vol. 6, pp. 414–427, 1958.

[15] D. Hull and D. J. Bacon, *Introduction to Dislocations*. Butterworth Heinemann, pp. 12–13, 2011

[16] C. Hammond, *The Basics of Crystallography and Diffraction*. Oxford University Press, pp. 21–27, 2009.

[17] X. L. Wu and Y. T. Zhu, "Inverse Grain-Size Effect on Twinning in Nanocrystalline Ni," *Phys. Rev. Lett.*, vol. 101, no. 2, pp. 025503–4, 2008.

[18] Y. T. Zhu, X. Z. Liao, X. Z. Liao, and X. L. Wu, "Deformation twinning in nanocrystalline materials," *Progress in Materials Science*, vol. 57, no. 1, pp. 1–62, 2012.

[19] K. C. Chen, W. W. Wu, C. N. Liao, L. J. Chen, and K. N. Tu, "Observation of Atomic Diffusion at Twin-Modified Grain Boundaries in Copper," *Science*, vol. 321, no. 5892, pp. 1066–1069, 2008.

[20] D. Xu, V. Sriram, V. Ozoliņš, J.-M. Yang, K. N. Tu, G. R. Stafford, C. Beauchamp, I. Zienert, H. Geisler, P. Hofmann, and E. Zschech, "Nanotwin formation and its physical properties and effect on reliability of copper interconnects," *Microelectronic Engineering*, vol. 85, no. 10, pp. 2155–2158, 2008.

[21] O. Anderoglu, A. Misra, H. Wang, F. Ronning, M. F. Hundley, and X. Zhang, "Epitaxial nanotwinned Cu films with high strength and high conductivity," *Appl. Phys. Lett.*, vol. 93, no. 8, pp. 083108–4, 2008.

[22] L. Lu, Y. Shen, X. Chen, L. Qian, and K. Lu, "Ultrahigh Strength and High Electrical Conductivity in Copper," *Science*, vol. 304, pp. 422–426, 2004.

[23] K. M. Mannan and K. R. Karim, "Grain boundary contribution to the electrical conductivity of polycrystalline Cu films," *J. Phys. F: Met. Phys.*, vol. 5, no. 9, pp. 1687–1693, 1975.

[24] W. D. Callister Jr and D. G. Rethwisch, *Materials Science and Engineering: An Introduction*, vol. 7. John Wiley & Sons, Inc., pp. 94, 2007.

[25] K. Lu, L. Lu, and S. Suresh, "Strengthening Materials by Engineering Coherent Internal Boundaries at the Nanoscale," *Science*, vol. 324, pp. 349–352, 2009.

[26] P. Li, R. F. Egerton, and M. Malac, "Radiation damage in the TEM and SEM," *Micron*, vol. 35, no. 6, pp. 399–409, 2004.

[27] R. F. Egerton, "Control of radiation damage in the TEM," *Ultramicroscopy*, vol. 127, pp. 100–108, 2013.

[28] R. F. Egerton, R. McLeod, F. Wang, and M. Malac, "Basic questions related to electron-induced sputtering in the TEM," *Ultramicroscopy*, vol. 110, no. 8, pp. 991–

997, 2010.

5. Development and Optimisation of Various Cross-sectional, Plan-view and Site-specific Lamella Preparation Techniques for 50 nm Cu Film on Ta

5.1 Introduction

As discussed in the introduction chapter of this thesis, due to the multiple issues encountered when copper (Cu) reacts with the silicon (Si) substrate, the interlayer dielectric material and several other parts of the transistor, it is necessary for a barrier layer to be used. This barrier encapsulates the entire copper interconnect from all sides. It is different from aluminium (Al) interconnections, which only need a diffusion barrier for one interface.[1]

However, the total encapsulation of the Cu interconnect leads to an increased resistivity due to the thickness of the diffusion barrier beginning to dominate the space filled by the Cu interconnect. Aside from preventing the Cu diffusing and poisoning other layers, a diffusion barrier needs to fulfil several other requirements: a) it must be thermodynamically stable between the two materials it is separating; b) it must provide strong adhesion with both materials; c) it should also be resistant to mechanical and thermal stress as well as d) being both highly thermally and electrically conducting.[2]

Tantalum (Ta) is a commonly chosen liner for interconnects due to the fact that it is a heavy refractory metal, which is a good barrier layer, preventing Cu poisoning of the Si substrate. Ta has been shown to be an excellent diffusion barrier, particularly its β – phase. Although the Ta lacks adequate adhesion to SiO_2, its adhesion to Cu is excellent.[3]

In addition to the properties described above, another major factor to consider is the electromigration performance of the barrier. Therefore, Ta is the barrier of choice for what is described here as it shows the best electromigration lifetime and the lowest electrical resistance in comparison to tantalum nitride (TaN) and Ta/TaN. Ta is generally in the form of amorphous, tetragonal (β-phase) or bcc (α-phase). The orientation and phase of the Ta liner discussed within this chapter cannot be disclosed due to it being of a proprietary nature.[4], [5]

Generally, the microstructure and electromigration properties of electro-plated Cu are highly dependent on the type of barrier layer used. Ta is a popular choice for barrier liner. This is due

to its higher ratio of (111) Cu to (200) in both the seed layer and electro-plated Cu. This ratio is higher than for various other barrier layer choices. It also exhibits good adhesion with Cu, reducing the interface diffusion between the two.[6]

As shown in section 4.7 of chapter 4, the lamellae prepared using the 50 nm Cu film on 7 nm Ta samples were found to be of a much higher quality in comparison with the 40 nm Cu film on 7 nm silicon dioxide (SiO_2) samples, which were also prepared differently. Therefore, for the work described in this chapter we chose to investigate the Ta samples further. The cross-sectional information of the film is examined further while also describing other types of lamella preparation techniques in a variety of forms such as; plan-view lamellae and site-specific lamella preparation.

This chapter will discuss in detail the development and methodologies behind these sample preparation techniques. It will also provide experimental data to show that these techniques can be successfully applied to reveal microstructural information about the film under investigation.

The current most used technique for preparing plan-view lamella will be investigated and why this technique was not well suited to this particular type of sample preparation will be discussed. The technique that was developed for this sample preparation and its benefits for this particular sample type will then be described.

Two other different techniques for plan-view lamellae preparation will also be outlined and the merits of both will be discussed. All the plan-view methods outlined will be accompanied by supporting Transmission Electron Microscopy (TEM), Scanning TEM (STEM) and Energy-dispersive X-ray spectroscopy (EDX) analysis.

Next, results from cross-sectional site-specific lamella of Cu nanowires (NWs) as prepared by Focused Ion Beam (FIB) milling and analysed through high-resolution S/TEM (HRS/TEM) and aberration-corrected STEM will be described.

5.2 Experimental Methods

The Cu films were deposited using sputtered Physical Vapour Deposition (PVD) at the Intel wafer fabrication plant. The Cu films discussed in this chapter were 50 nm in thickness and deposited on a 7 nm Ta barrier layer on a Si substrate. The Cu NWs were ~100 nm wide with a

depth of approximately 150 - 160 nm. These were provided by Intel's researcher-in-residence in CRANN, Mr. Peter Gleeson.

All S/TEM images were acquired on an FEI Titan at 300 kV. EDX spectra were acquired using an EDAX EDX detector at a stage tilt of ~15° with a spatial resolution of ~0.5 nm. High-angle annular dark field (HAADF) imaging was performed at a convergence semiangle of 10 mrad with a collection semiangle of 39 mrad. Aberration-corrected high-resolution STEM images and EELS spectra were acquired at 100 kV on a NION UltraSTEM at SuperSTEM, Daresbury, courtesy of Prof. Quentin Ramasse and Dr. Patricia Abellan. The convergence semiangle was 37 mrad with a 39 mrad collection semiangle for HAADF imaging.

All Scanning Electron Microscopy (SEM) and FIB imaging performed during lamella preparation and optimisation procedures was performed on a dual beam Zeiss Auriga with the exception of the xenon difluoride (XeF_2) etched lamella, which was performed on an FEI Strata FIB. All hydrofluoric (HF) acid etched experiments were performed in a class 100 cleanroom, where strict lab safety rules were followed and a buddy system was employed. All Electron Backscatter Diffraction (EBSD) and Transmission Kikuchi Diffraction (TKD) data was acquired on a Zeiss Supra SEM using a Bruker EBSD Detector and bespoke TKD holder.

All samples used for Scanning Tunneling Microscopy (STM) analysis were etched with a glacial acetic acid and loaded into an ultra-high vacuum system equipped with a low-temperature scanning tunneling microscope. It was also gently sputtered and annealed at ~300°C prior to imaging. Conductive-Atomic Force microscopy (C-AFM) data was collected on a Bruker Multimode AFM.

5.3 Cross-sectional Lamella Preparation and Aberration-corrected Imaging

As mentioned at the end of the results chapter 4, after the refinement of the sample preparation with the SiO_2 sample it was realised that the sample itself was not of the best quality for high resolution imaging and characterisation with S/TEM. The project then progressed onto using a different liner, Ta. In this PhD work we were only interested in the Cu film and its interaction with the Ta, so for the purposes of our experimentation, a Ta layer directly on a Si substrate without an additional TaN layer, for example, was suitable for current

analysis. There was also a slight increase in the Cu film depth, 50 nm as opposed to the 40 nm in the previous samples.

Once the optimised lamella preparation technique was used with the Ta liner sample, the results were significantly improved, although using the Ta liner also came with its own setbacks. The main disadvantage of using Ta as a liner is that it is a heavy metal, which is extremely challenging to mill next to the Cu film and the Si substrate as they have very different mill rates. This makes it challenging to create lamellae of relatively uniform thickness and to maintain the structural integrity of the lamella while also having a sufficiently thin region of Cu film to image and analyse at high resolution within the S/TEM. Due to these challenges, it took 3 – 4 more iterative processes to create cross-sectional lamellae of suitable quality.

Again, the process was similar to the results chapter 4 and also the methods detailed in section 3.1.2 of chapter 3. A cross-sectional lamella was polished to a thickness of between 50 – 70 nm with final low kV polishing of 2 kV 20 pA, see Figure 5-1 (a). The thinnest region of this lamella was then imaged using high resolution TEM. The overview of this region is shown in Figure 5-1 (a) and also in Figure 5-1 (b) at a higher magnification. Prior to the deposition of the platinum (Pt) protective layer described in chapter 3 an additional step of sputtering of a 50 nm protective layer of carbon (C) was introduced in the preparation of these particular lamellae to further protect the sample from damage.

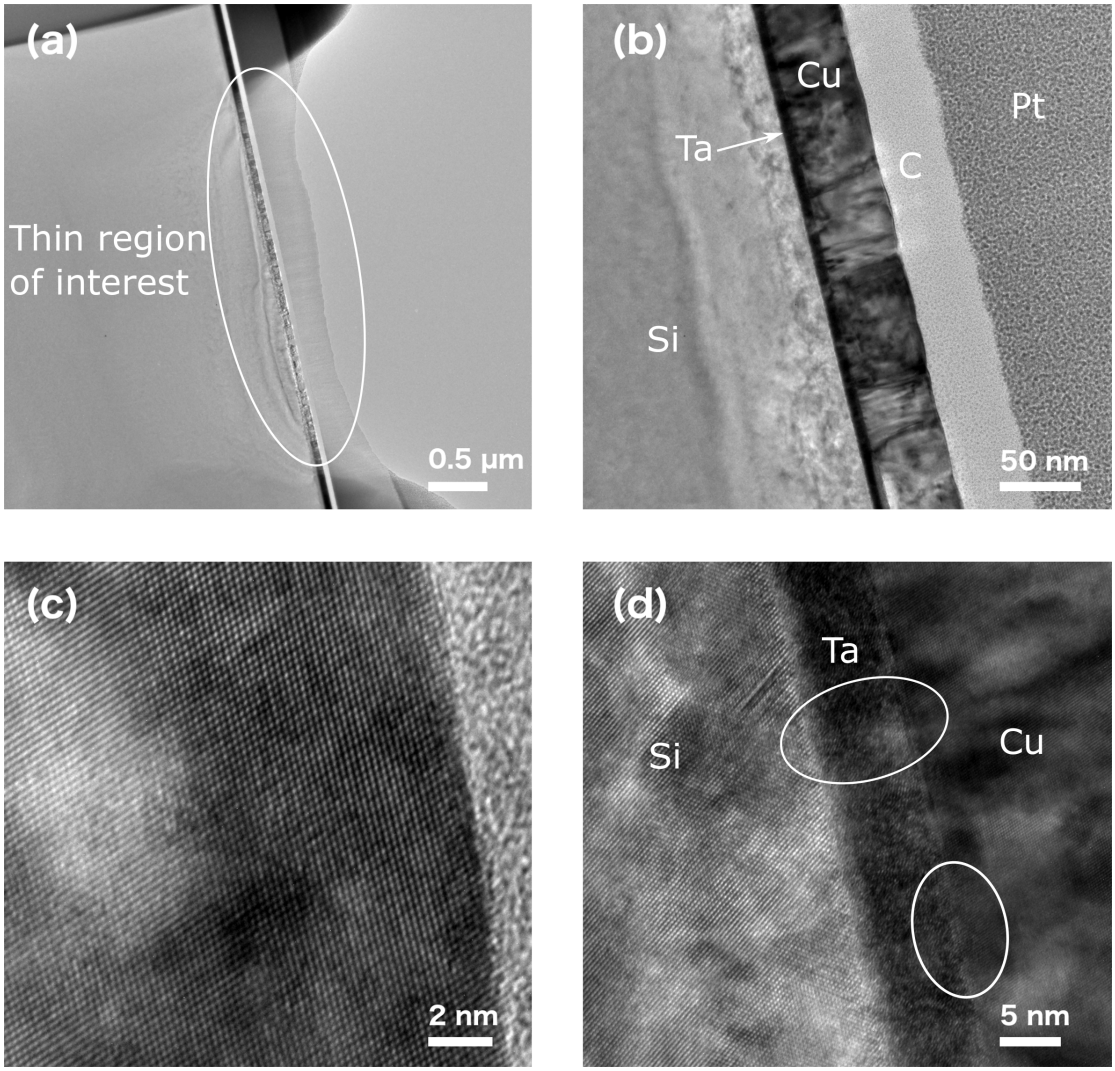

Figure 5-1: Transmission Electron Microscopy (TEM) images acquired at 300 kV of (a) the overview of lamella, showing the protective carbon (C) and platinum (Pt) coating and the thin region of interest highlighted, (b) columnar "bamboo" like grain structure apparent in copper (Cu) film, (c) High-resolution TEM image of uniform crystalline Cu grain with C protective layer and (d) thin regions of tantalum (Ta) highlighted at Cu/Ta interface. (Notation in images: Cu=copper, Ta=tantalum, C=carbon, Pt=platinum, Si=silicon)

On initial TEM imaging, it was noticeable that this Ta liner lamella showed some significant difference to that of the 40 nm Cu on SiO_2 sample from the results chapter 4. It was evident that the grain boundary structure is more uniform with considerably less visible damage to the film as shown in Figure 5-1 (b). The Ta liner, also appears to be significantly thicker than the SiO_2 liner, most likely due to the Ta atoms being heavier and more difficult to mill. However, the single most significant difference between the two different samples is the large reduction in amorphous and disordered regions of Cu, especially within the grains. There was consistently more uniform crystallinity within the Cu grains in the Ta liner samples, which was not present in previous samples (shown in Figure 5-1 (c)). The Ta liner appeared to be thinner

in some regions, as shown in the regions highlighted in Figure 5-1 (d). This is an indication of how the preparation has been optimised and the quality of the lamellae that were being produced with the FIB milling.

The interaction of the Cu with the Ta layer can be seen clearly in Figure 5-1(d). There is a clear, abrupt line where the Cu meets the Ta. This relationship between Ta and Cu will be investigated further in the following chapter 6 on *in-situ* annealing in the TEM. In order to understand and examine the relationship between the barrier layer and the Cu interconnect, annealing experiments are performed as a way to test barrier compatibility and reliability.

Since the lamella was prepared to an extremely high quality with relatively low amorphisation and disordered regions and reduced thickness, it was found suitable to be analysed using aberration-corrected STEM. From initial overview images shown in Figure 5-2 (a) and (b), we can see that the grains run the entire length of the film, with some slight variations in the grain boundary shape in different regions, that could be due to a slight thickness variation throughout the lamella. As noted in the previous results chapter 4 with the 40 nm Cu film on SiO_2 the grain boundaries are experiencing some grooving at the top of the Cu film and also minor grooving and voids at the Cu/Ta interface.

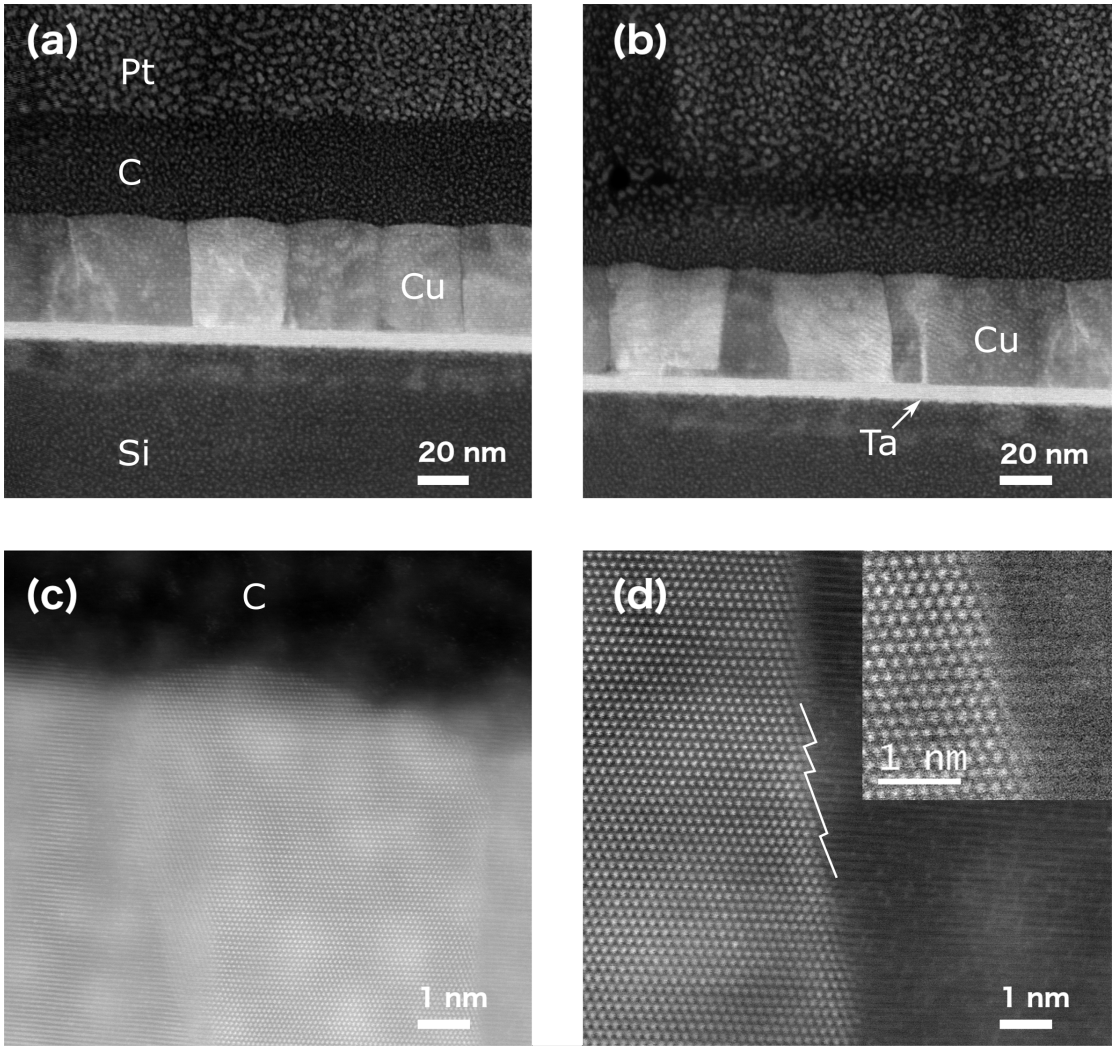

Figure 5-2: Aberration-corrected Scanning Transmission Electron Microscopy (STEM) High-angle annular dark field (HAADF) imaging acquired on a NION UltraSTEM at 100 kV showing (a) uniform bamboo like copper (Cu) grains running the depth of the film, with widths matching that of the film thickness, (b) more complex grain boundary orientations in slightly thicker areas of the lamella, (c) top of Cu grain with protective carbon (C) layer showing that atomic resolution imaging has become achievable and (d) step/faceted grain boundary and inset atomic resolution grain boundary on zone axis with neighbouring grain tilted out of plane. (Notation in images: Cu=copper, Ta=tantalum, C=carbon, Pt=platinum, Si=silicon)

The aberration-corrected images shown in Figure 5-2 highlight the high-quality sample preparation can be achieved using FIB low kV milling. The primary focus of this PhD work was to produce lamellae that were of a quality to produce high-resolution imaging, more specifically atomic resolution imagery. This is finally being achieved in these aberration-corrected STEM images. Using this type of high-resolution analysis can give us unprecedented insight into the grain boundary structures within the sample. Figure 5-2 (c) depicts a high-resolution image of the top of one grain within the Cu film, bordering with the C protective layer. Taking a closer look at the grain boundary in Figure 5-2 (d) with inset, we can see that

the boundary has a step or faceted feature. Faceting occurs thermodynamically to reduce the grain boundary free energy. It typically occurs parallel to the most densely packed plane of coincidence sites lattice and can disappear with increasing temperature.[7], [8] It is challenging to assess the relationship between neighbouring grains here as one grain is out of focus, indicating that it is potentially tilted away from the boundary. This gives us a better indication of the types of grain boundaries that are present within the Cu grains. These boundaries are a mix of both tilt and twist, a complicated boundary, see Figure 5-3 (c). This can be observed clearly in the aberration-corrected STEM and high-resolution TEM images in Figure 5-3 (a) and (b) respectively. It appears that the boundaries are primarily tilt with an additional twist component. The grain orientation is slightly off the zone axis indicating the tilt and twist nature of the boundary. Tilting this individual grain onto its zone axis is extremely challenging and the tilt is so minor in comparison to the increments of the stage tilt, it would be extremely challenging to measure accurately.

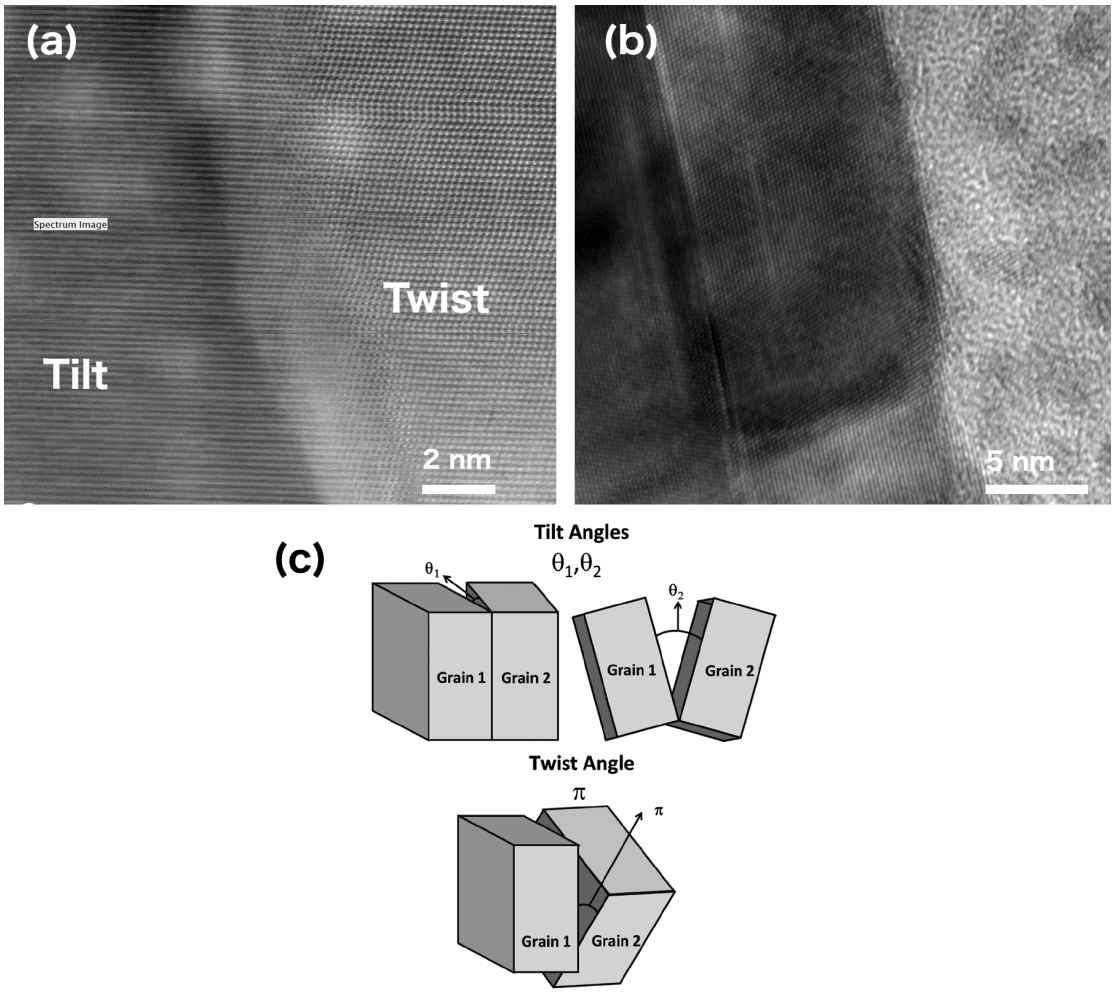

Figure 5-3: (a) Aberration-corrected Scanning Transmission Electron Microscopy (STEM) High-angle annular dark field (HAADF) image taken at 100 kV, (b) Transmission Electron Microscope

(TEM) image at 300 kV marked with arrows showing the tilt and twist nature of the grain boundaries present in the 50 nm copper (Cu) film on 7 nm tantalum (Ta) liner and (c) schematic of tilt and twist grain boundary geometry.[9]

In order to achieve the resolution shown in images in Figure 5-1 and 5-2, the lamella thickness of the sample had to be less than ~50 nm. However, in order to more accurately measure the absolute thickness of the region of interest on the lamella, Electron energy-loss spectroscopy (EELS) was used. EELS spectra of the zero-loss peak (ZLP) region along with EELS spectra of the core-loss (CL) region of the area of interest were obtained. The fundamental theory behind this type of thickness measurement is described in detail in section 2.2.6 in chapter 2. In short, the ratio of the intensities of the zero-loss (ZL) spectra and the rest of the energy-loss spectra is used along with the inelastic mean free path, which is specific to the sample analysed, to obtain the absolute thickness information of this Cu film. Prior to this, the ZLP spectra were used to align both the ZL spectra and CL spectra by energy. Once the ZLP was aligned, the absolute thickness was calculated using an effective atomic number of 29. The resulting absolute thickness map is shown in Figure 5-4 (c), displaying a thickness gradient (in the map, white regions denote the thickest regions of the film and the black the thinnest). Using this method, the average thickness was found to be ~30 nm.

EELS maps were also acquired across grain boundaries. The EELS spectra were processed in the following manner: First the background to the peak of interest was subtracted for each spectra in the map, then the EELS maps were integrated for specific energy loss windows to show the intensity distribution for specific peaks of interest. The Cu $L_{2,3}$ edge can be spatially mapped in this manner by integrating over the intensity of the 958 – 959 eV energy loss. An example of this is shown in Figure 5-4 (e) and the corresponding STEM image in Fig 5-4 (d). This range was selected as it is a strong EELS edge for Cu and also there is no overlap with other EELS features of the materials present in the sample. The individual spectra shown in Figure 5-4 (f) of the Cu $L_{2,3}$ edge demonstrate that there was no energy shifts in the spectra within the grains or across the grain boundary. This shows that chemical compositional change in the Cu across the grain boundaries is unlikely.

Figure 5-4 (h) shows the integrated EELS map of the area shown in Figure 5-4 (g) after background subtraction and intensity integration for energy-losses between 937.5 – 959 eV. In Figure 5-4 (i) the spectrum displays a slight increase in intensity in the left grain, possibly indicating a mass-thickness contrast between the grains.

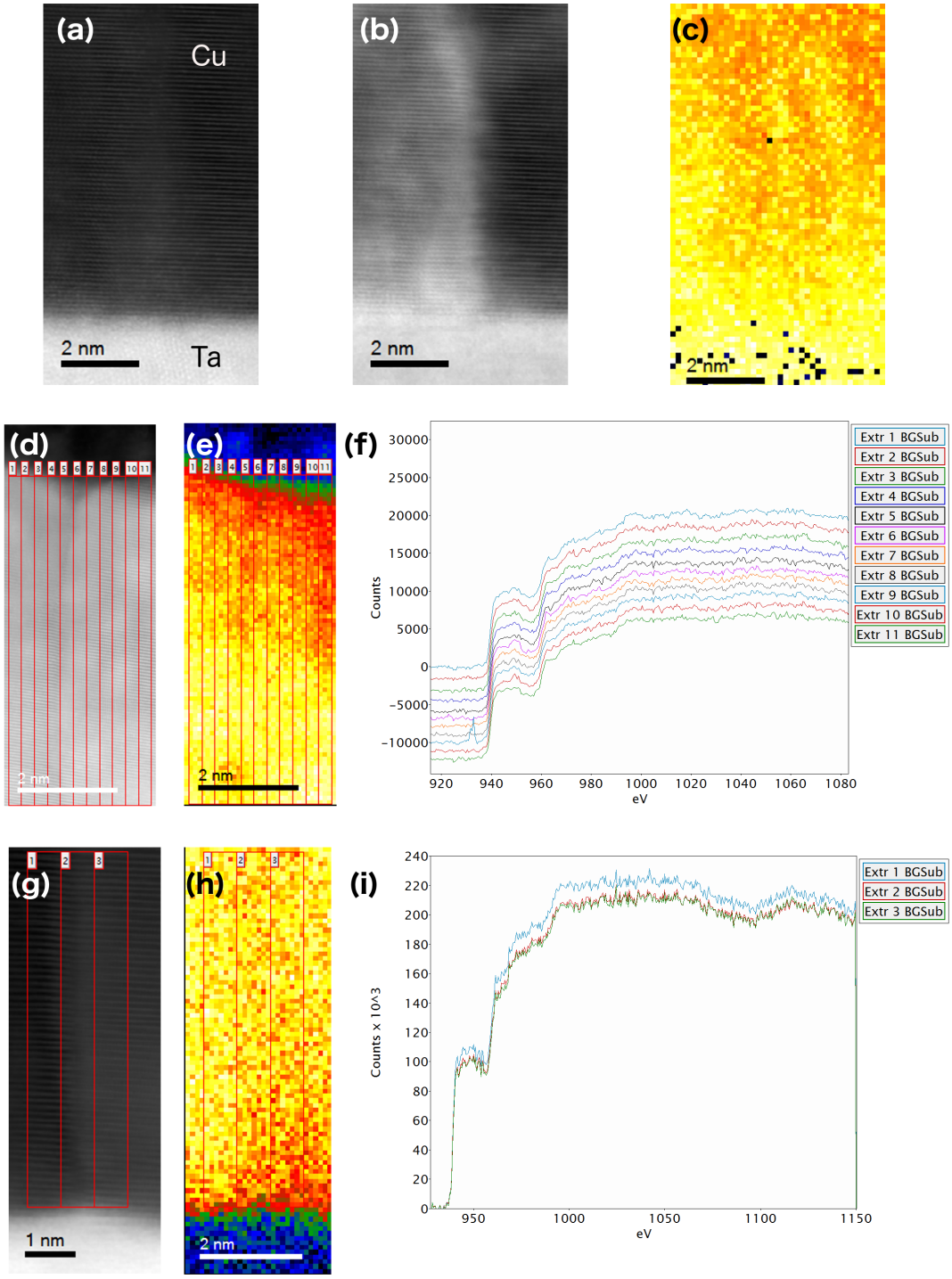

Figure 5-4: (a) Aberration-corrected High-angle annular dark field (HAADF) Scanning Transmission Electron Microscopy (STEM) image of copper (Cu) grain boundary and Cu/tantalum (Ta) interface, (b) aberration-corrected Medium-angle annular dark field (MAADF) STEM image of the same boundary featured in (a), (c) absolute thickness map of area in which the zero-loss peak (ZLP) has been aligned to reduce any shifts, (d) HAADF STEM image of Cu grain boundary at top of Cu film with carbon (C) protective layer annotated with the areas in which spectra were collected, (e) integrated Electron Energy-loss Spectroscopy (EELS) map of image (d) with background subtraction and intensity integration for energy losses between 958 – 959 eV, (f) displays each spectra taken across the image (d) showing the Cu $L_{2,3}$

edge across the boundary, (g) HAADF STEM image of Cu boundary and Cu/Ta interface with corresponding integrated EELS map displayed in, (h) with background subtraction and intensity integration for energy losses between 937.5 – 959eV and (i) displays the spectra acquired across image in (g), comparing the Cu $L_{2,3}$ edge signal intensity across the boundary. (Notations in image: Cu=copper, Ta=tantalum)

A further investigation into the grains and grain boundaries observed on the 7 nm Ta liner was performed. Twin boundaries were also noted within the Cu film. Figure 5-5 (a) displays a twin boundary, which is running parallel to the Cu film as opposed to perpendicular, which has been the most common grain boundary observed thus far. However, Figure 4-8 (b) in chapter 4 did display a twin, which terminated at the grain boundary. As mentioned in previous chapters, twin orientation in fcc metals corresponds to a misorientation of 70.5° about a <110> axis and 60° about a <111> axis. As can be seen from Figure 5-5 (b), there is a ~70.5° difference between crystal orientation of the two grains, with the grain boundary defined as 70.5° [1-10](111). The twin boundary is also incoherent, with the atoms of each grain not perfectly aligned. This has an approximate misalignment of 70.5° ± 1-2°.

A key component to this project was the collaboration between Prof. Boland's group performing STM analysis and Mr. Peter Gleeson, Intel researcher-in-residence, undergoing C-AFM experiments. The ultimate goal was to achieve clear corroboration of data from each element of the project. A paper published on this work in particular from Dr. Xiaopu Zhang, who ran all STM experiments and analysed the data collected, describes in detail the effect of the grain boundaries on the surface have on nanocrystalline films. Figure 5-5 (c) displays an atomic resolution STM image of a low-angle grain boundary (LAGB), which has a pure tilt component, in the <111> direction. The viewing direction of the TEM is <1-10>. It is a valley grain boundary with a 3° out-of-plane angle and a periodic sequence of edge dislocations with an approximate width of 3 nm.[10]

The slight misalignment of the twin boundary inclination observed in the TEM, see Figure 5-5 (a) and (b) could potentially be contributing/causing the out-of-plane rotation of the grains on the surface of the film, which have been investigated through STM imaging and simulations by Zhang *et al*. According to Zhang *et al.* the slight inclination caused by the misalignment here at the twin boundary could confirm the out-of-plane rotation of grains at the film surface. This slight misorientation observed in TEM could possibly be the contributing angle of $\varphi/2$ as seen in Figure 5-5 (d). Zhang *et al.* discovered that nanocrystalline films are never flat, with this out-of-plane rotation causing grain boundaries to form ridges and valleys to lower the energy of the grain boundary itself. A valley grain boundary imaged in STM is shown in Figure 5-5 (c).

This misalignment observed in TEM, could help confirm what the simulations and STM data have been suggesting about these grain boundaries.[10] This will need to be investigated further in the future through high-resolution aberration-corrected STEM.

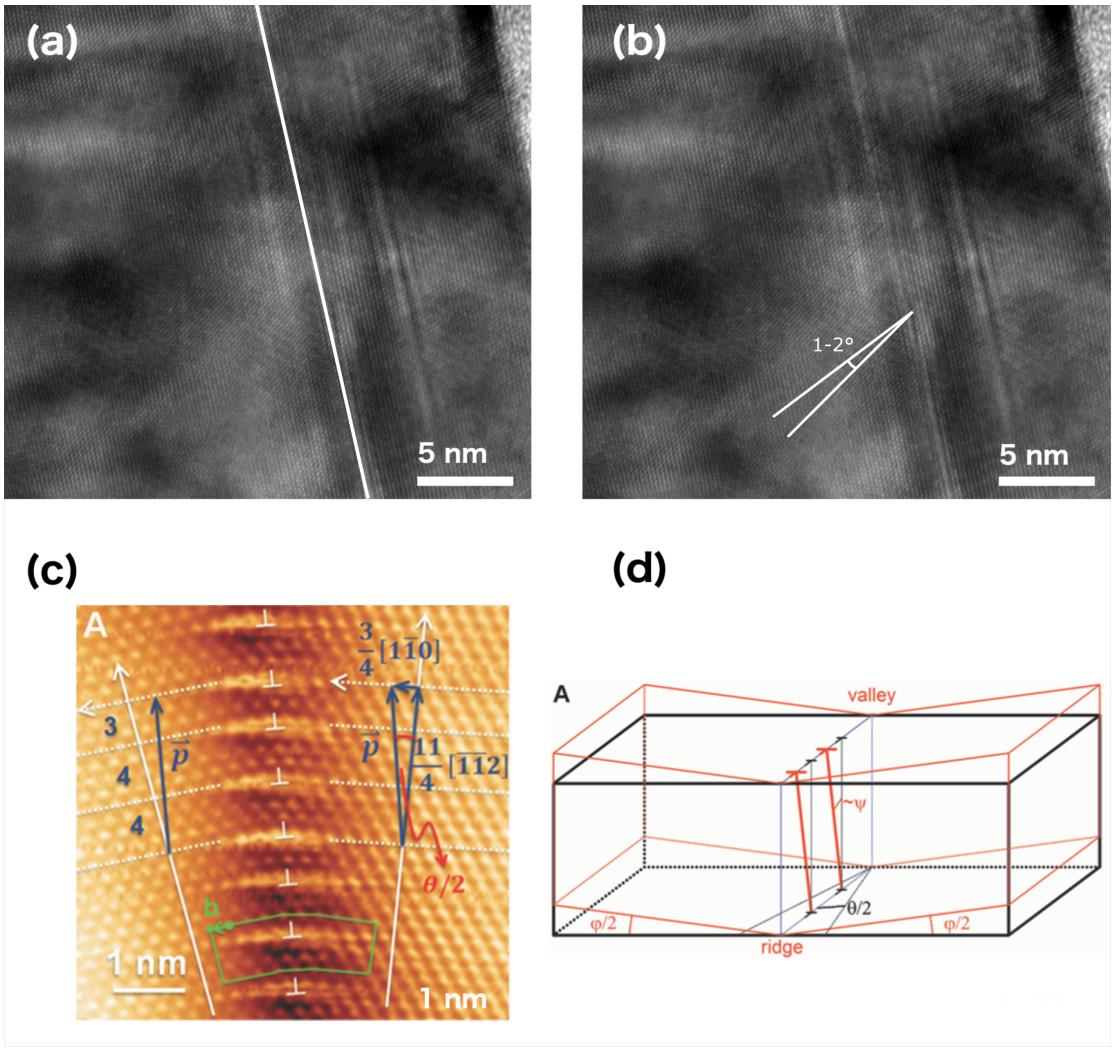

Figure 5-5: (a) High-resolution Transmission Electron Microscopy (HRTEM) image of copper (Cu) grain with twin boundary running parallel to the Cu film; (b) indication of the small ~1-2° misalignment of the twin boundary featured in (a), (c) atomic resolution Scanning Tunneling Microscopy (STM) image of a valley grain boundary with periodic edge dislocations and an out-of-plane angle of ~3°, the green arrows indicate the path of the burger's vector circuit solid and dotted lines indicating the <-1-12> and <1-10> planes respectively [10] and (d) schematic of the low-angle grain boundary (LAGB) induced film tilting with in-plane angle ϑ and out-of-plane angle φ with Ψ representing the angular difference between the dislocation line and the surface normal.[10]

5.4 Plan-view Lamella Preparation

5.4.1 Motivation and Testing Developed Methods

As the cross-sectional lamellae were prepared successfully and the microstructure of the Cu film was successfully imaged and analysed, the next step in the process was to focus on plan-view lamella preparation and to investigate and optimise the various preparation techniques involved. In order to have a more complete, direct and cohesive comparison of data between STM, C-AFM and S/TEM within the project, it was necessary to investigate plan-view lamella preparation.

There have been many different techniques developed for plan-view lamellae preparation.[11]-[14] Plan-view lamellae preparation can be a challenging process and its success can be highly material dependent and even location dependent as different regions of interest within the sample can vary.

Within this project work, a well established technique as developed by Mayer *et al.* was attempted.[15] This technique involved first covering the area of interest in a protective Pt layer, deposited by a Gas Injection System (GIS), in a manner similar to that of cross-sectional lamella preparation.

The main difference being that prior to the lift-out, the TEM omniprobe Cu grid was placed in the horizontal position on a carbon adhesive tab. This ensured that the 3 pillars were left protruding over the tab/SEM stub, as opposed to being clamped in the upright position as done during traditional preparation. Any contact between the carbon tab and the area of interest would make it extremely challenging to remove the grid at a later stage and not cause damage to the lamella.

The critical difference between this plan-view lift-out and traditional cross-sectional preparation technique is the angle at which the milling is performed. A protective Pt layer of 4 x 8 µm using both EBID-Pt and IBID-Pt was deposited to a height of ~2 µm. This was performed at the commonly used angle of 54° i.e. a 0° incident FIB beam.

The trenches either side of the lamella were then milled at a stage angle tilt of 0°, so the FIB incident beam was at an angle of 54° and then at a stage tilt of -10°, so the FIB was at an angle of 64°. Figure 5-6 (a) shows the trenches after successful milling. The remainder of the bulk

preparation was performed in a similar manner to the cross-sectional preparation (for more details see the preparation described in section 3.1.2 in chapter 3). Once the side trench was milled, the micromanipulator needle was carefully inserted and welded to the side of the lamella. The final sidewall connecting the lamella to the bulk material was then removed using a 30 kV 2nA ion beam, see Figure 5-6 (b). The lamella was welded to the horizontally positioned TEM grid and once secured, the micromanipulator was removed. The system was vented, the grid gripped in the clamp in the typical upright position and placed back into the microscope chamber. Figure 5-6 (c) shows a SEM image of the plan-view lamella welded to the TEM grid after flipping the orientation of the lamella. The peaked region in the image shows the Si substrate and the mounded region shows the Pt protective layer.

By flipping the orientation of the lamella, the entire Cu film now covers the depth of the lamella, which is extremely beneficial for the thinning process. This means regardless of which region of the lamella was thinned to the desired thickness, it contained the entire Cu film. Initially, the Cu side was milled minimally. The majority of the Pt protective layer was milled until both sides of the lamella started to even out. As shown in Figure 5-6 (c) (annotated), there was a large amount of Pt to mill in contrast to the Cu and Si substrate.

Once a thickness of 300-400 nm was reached, with this type of lamella preparation a new challenge of knowing when the Cu layer had been reached became apparent. With the material in question in Fox *et al.*, the end point detection for thinning was when the nanoparticles were visible.[16] Unfortunately, the Cu film contained no such defining features, making it challenging to differentiate between the Cu and Pt layer. It is not possible using this technique to have no Pt layer as the ion beam would cause too much damage to the surface, making this technique ineffective for our purposes. Therefore, an additional step had to be introduced into the protocol to observe the 50 nm Cu film in plan-view.

The lamella was polished with a final ion beam voltage and current of 15 kV 200 pA , see Figure 5-6 (d). As can be seen from the TEM image in Figure 5-6 (e) the plan-view lamella contained regions of significant damage with almost no grain information observable. EDX spectra of the region (as shown in Figure 5-6 (f)) were acquired to determine whether; a) the thinned area was in fact the Cu film, b) it still contained some Ta liner or c) the Cu film had been completely milled through and only contained the remaining Si substrate. The EDX confirmed that the Pt side of the lamella had been milled too aggressively and the milling had continued into the Cu film and the lamella in question now contained mainly Si and by

extension Ta as well as potentially some Cu film. This low presence of Cu would make it extremely challenging to detect any Cu crystallinity within the lamella in the TEM.

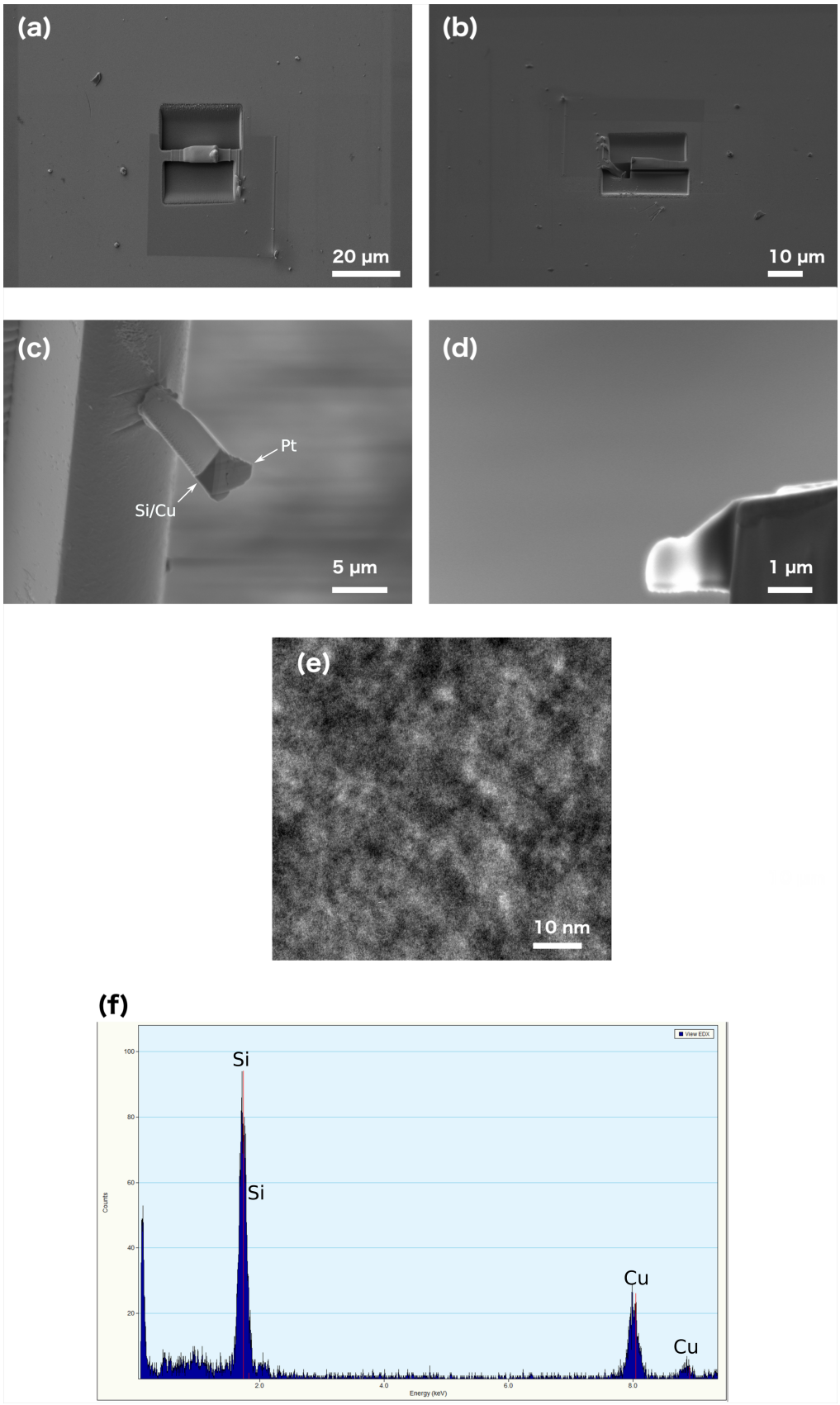

Figure 5-6: (a) Scanning Electron Microscopy (SEM) image acquired at 0° stage tilt with Focused Ion Beam (FIB) cuts milled at high angles to create plan-view lamella, (b) SEM image at 54° stage tilt with side trench and undercut milled at 30 kV 2 nA, (c) the plan-view lamella welded with perpendicular geometry to traditional Transmission Electron Microscopy (TEM) grid pillar weld with copper (Cu) and platinum (Pt) sides of the lamella marked, (d) SEM image showing final 15 kV 200 pA ion beam polish, (e) TEM image of thin region of lamella showing a lack of visible crystallinity in the region and (f) Energy-dispersive X-ray (EDX) spectroscopy of area of interest within the lamella displayed strong silicon (Si) peak, confirming presence of the Si substrate, suggesting that milling has gone too far into the sample. (Notation in images: Si=silicon, Cu=copper, Pt=platinum)

5.4.2 HF Etch: An Alternative Lamella Preparation Procedure

This section details an alternative and unique approach to obtaining a plan-view Cu film lamella. This method was used as a trial for a potentially new plan-view preparation technique. To develop the technique, many samples were needed and therefore, non-annealed samples were used as they were readily available and provide a comparable representation of the Cu film that we typically observe with the annealed films.

Etching the Cu films with HF is a technique used for fast analysis to strip back Cu metallizations stacks within the semiconductor industry to inspect the bare Si for anomalies or damage. It is not traditionally used for the preparation of lamellae for TEM analysis. This is a novel approach.

The HF etches the underlying oxide layers of the sample (normally SiO_2) and this gently lifts off the Cu thin film. Deionised (DI) water is placed in a 2nd beaker to rinse off any excess acid drips from the plastic tweezers and thin film, see steps 1 -3 in Figure 5-7.

HF is widely used as an oxide etchant in industry. However, as this approach, to effect lift off, is not standard, it was deemed necessary to fully risk assess the procedure. With appropriate risk mitigation (for example, trained buddy system, Personal Protective Equipment (PPE), dedicated sign off sheets and so on), it was deemed safe to proceed.

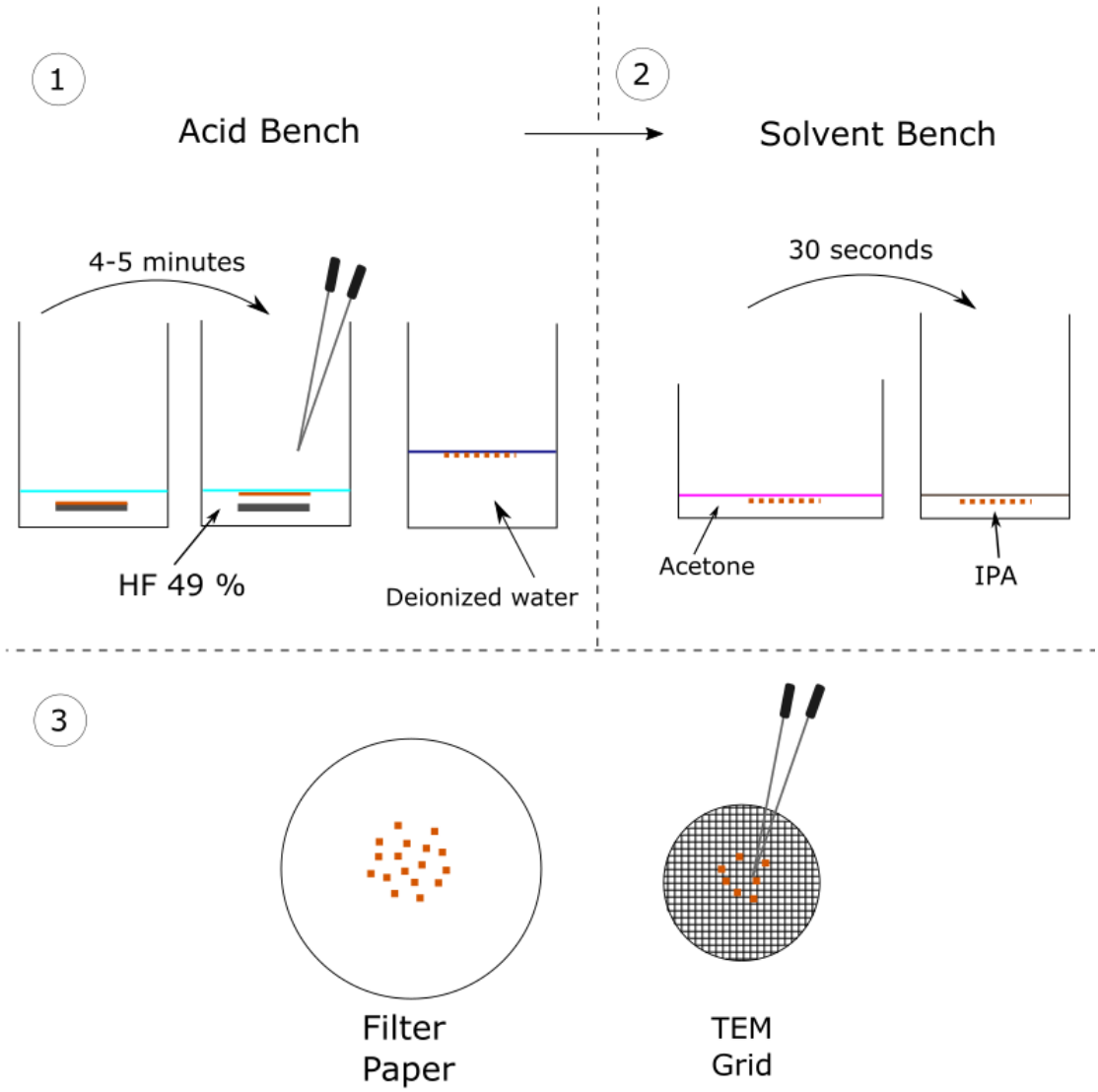

Figure 5-7: Schematic of the Hydrofluoric (HF) acid etch process in three steps: 1) the copper (Cu) film on tantalum (Ta)/silicon (Si) substrate is placed in a beaker of 49% HF for 4-5 minutes, once the Cu film has lifted from the substrate it is placed in deionised water for ~1 minute, 2) The Cu film is then placed in acetone and isopropanol for 30 seconds respectively, 3) The Cu film is left to dry on filter paper prior to being dropped onto a lacey carbon Transmission Electron Micoscope (TEM) grid.(Notation in schematic: HF=hydrofluoric acid, IPA=isopropanol)

The technique used a small amount (20 ml) of 49% HF in a small Teflon beaker. The sample was placed into this beaker and after 2-3 minutes the Cu film lifted off from the underlying Si substrate. The thin film was then gently lifted out of the HF and placed into the DI water to rinse. It was then gently lifted out of the DI water and placed into beakers for a final rinsing with acetone and isopropanol (IPA) solutions on the solvent bench. The thin films were left to dry after this final rinse and were then placed onto a standard TEM grid for analysis.

A TEM image of the HF etched plan-view film placed on a lacey carbon TEM grid is shown in Figure 5-8 (a). A STEM image of the grain overview within the Cu film in the lamella is shown in Figure 5-8 (b). The grain sizes range from 20-70 nm. This result correlates well with the general grain sizes noted for the cross-sectional lamellae. This technique successfully allowed the acquiring of general grain information about the Cu film from a top-down perspective. As a significant amount of grain and lattice information was obtained from this particular technique, see Figure 5-8 (c), it confirmed the successful removal of the majority of the Si substrate. However, there was a small amount of Ta detected shown by the EDX spectra in Figure 5-8 (e) and (f) (the location where the spectra were collected is shown in Figure 5-8 (d)). This highlights how challenging it is to remove the Ta layer. The disadvantage to this preparation technique is the instability of the "lifted" film. The films' large lateral size (several mm in width with a thickness of 50 nm) makes the film extremely fragile, which can compromise the integrity of the film and in the worst case lead to film breakage. In addition, as mentioned previously, there was still the partial presence of the Ta layer. This type of preparation was a once-off technique, meaning no re-polishing/milling can be done to the sample. It is similar to *ex-situ* lift-out (EXLO) lamella preparation in this way.

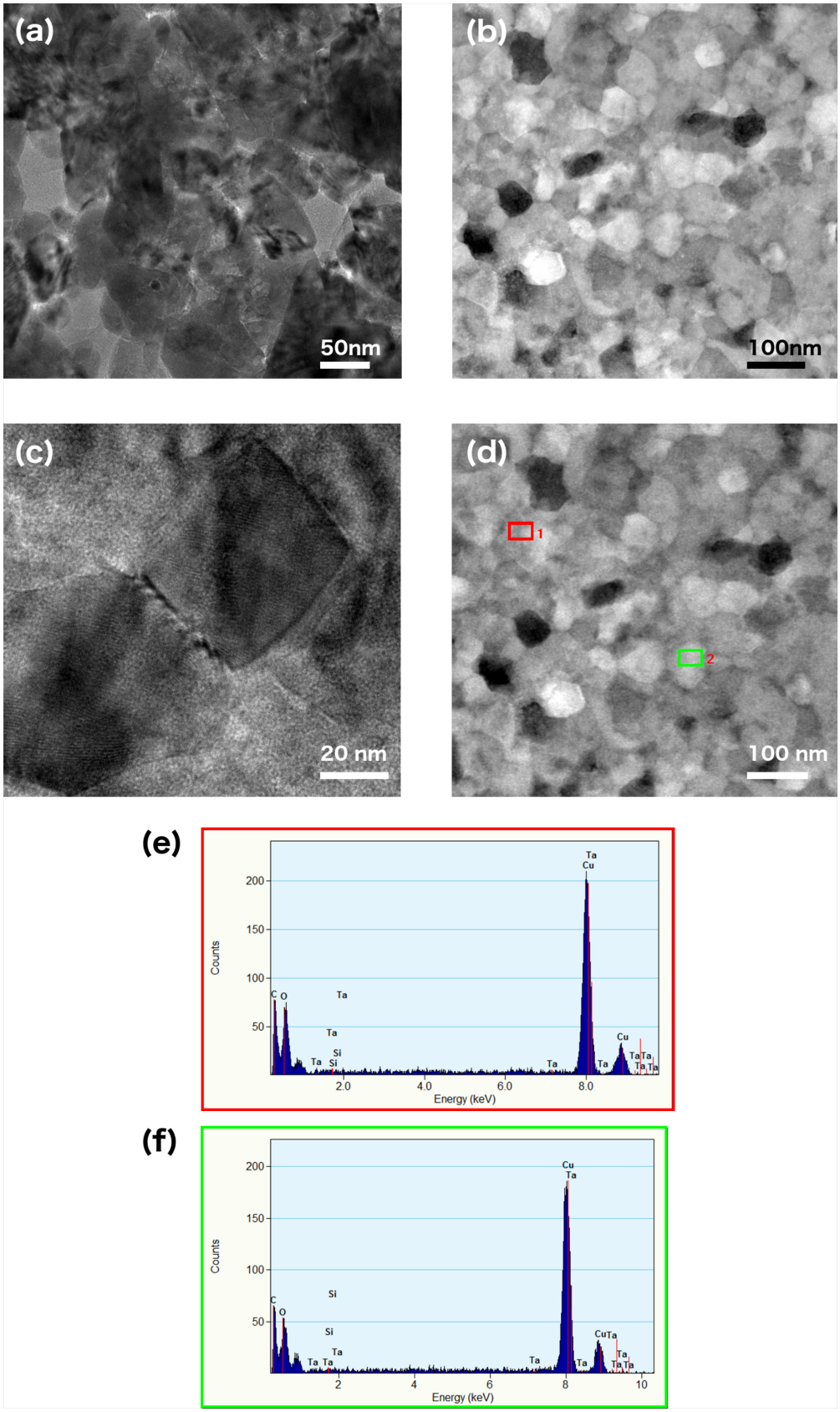

Figure 5-8: (a) Transmission Electron Microscopy (TEM) image of Hydrofluoric (HF) acid etch prepared lamella placed on lacey carbon (C) TEM grid, (b) Scanning TEM (STEM) image of HF etched plan-view lamella showing grain size distribution overview, (c) TEM image of two neighbouring grains within the plan-view lamella, (d) locations of Energy-dispersive X-ray (EDX)

spectra collection annotated in the image from (b), (e) and (f) EDX spectra collected from area 1 and 2, respectively, with Cu and Ta presence detected.

5.4.3 Side-profile Mounting Plan-view Lamella Preparation

As the previously described FIB-based technique proved challenging to execute and failed to achieve high-resolution images of the Cu film, an alternative procedure was established. Firstly prior to the bulk sample preparation, the sample itself was mounted on its side ensuring that the height did not obstruct the geometry within the microscope chamber and would still allow a working distance of 5 mm, shown Figure 5-9 (a). It was also ensured that the new sample geometry did not interfere with the GIS system. The initial bulk preparation stages were identical to those described in section 3.1.2, chapter 3. There was a slight variation to the preparation technique employed here; there was no need for a second trapezoidal trench, as the area of interest was the surface of the material. Hence, there was only a need to mill behind the surface, as shown in Figure 5-9 (b). The dimensions of this lamella are also slightly altered in comparison with the cross-sectional lamella preparation observed thus far.

The top width of the lamella was quite short compared to previously prepared cross-sectional lamellae, with a length of 2 - 3 µm. The depth of the lamellae was considerably longer, between 15 - 20 µm. The altered dimensions are favourable in the context of this work, as when the thinning is successful, the entire 3 x 15 µm surface will consist of the Cu layer. The benefit of the entire lamella containing the Cu film is that there is less of a need for such a large protective Pt layer due to the depth of the lamella. In this case, it does not matter which part of the lamella thins first.

The lamella was then lifted out and welded to the TEM grid in the traditional format, as can be seen in Figure 5-9 (c) and (d). The big benefit of changing the position of the sample compared to the method previously described, is that the TEM grid can be mounted in the upright position, without the need for placing it horizontally on a carbon adhesive tab. This reduces the amount of times the microscope chamber is vented in between the lift-out and thinning steps while also reducing the risk of damaging the TEM grid and potentially losing the lamella by removal from the adhesive. After welding to the TEM grid pillar, the lamella was only thinned and polished from the bulk Si side as the Cu should remain untouched for as long as possible, see Figure 5-9 (e). The thinning and polishing procedure was identical to that descibed in section 3.1.3, chapter 3. The sample was tilted and milled with 30 kV 240 pA, 15 kV 200 pA and a final 5 kV 20 pA polish, see Figure 5-9 (f).

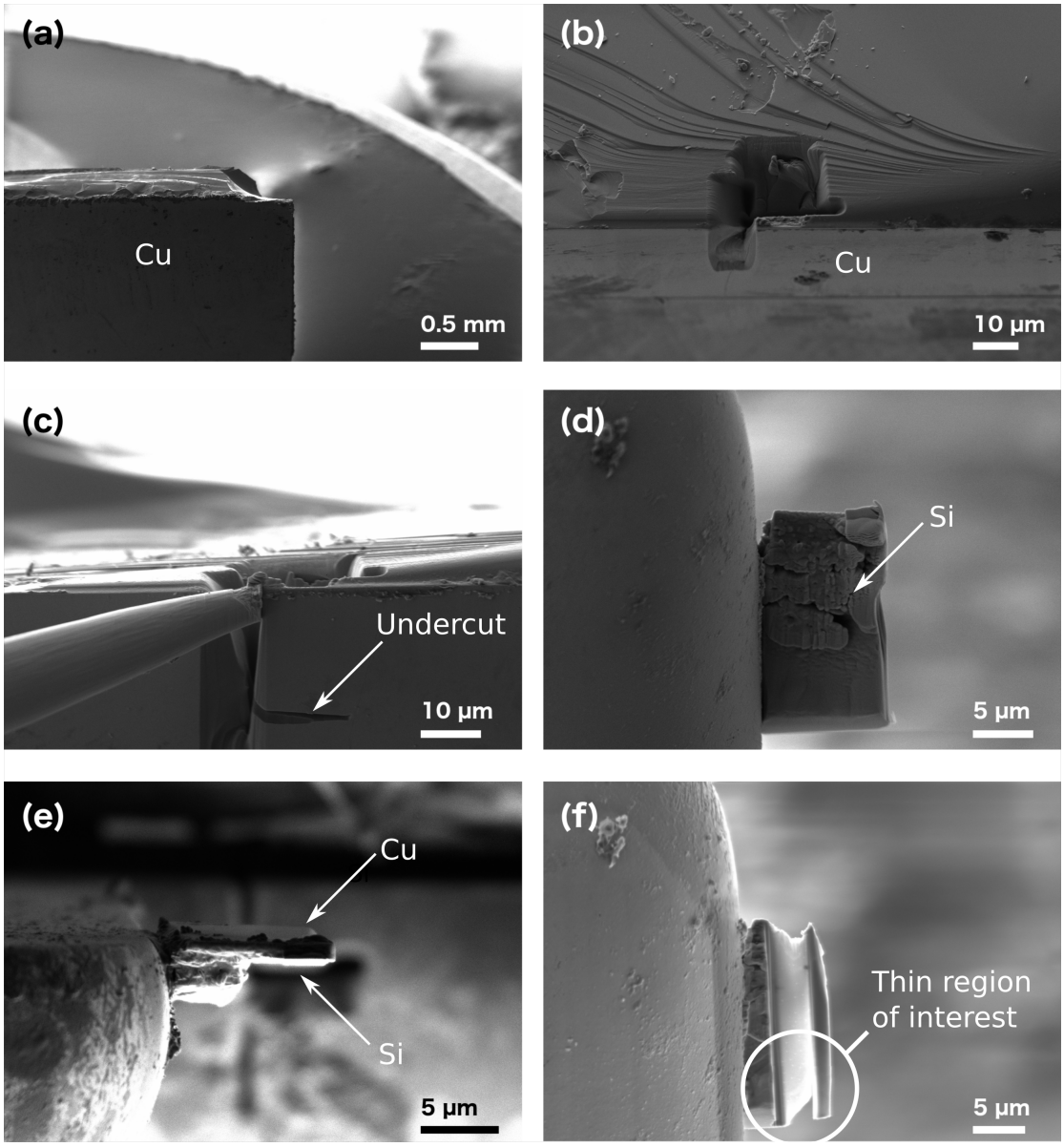

Figure 5-9: Side-profile mounted lamella preparation in steps: (a) Scanning Electron Microscopy (SEM) image of side-mount sample on SEM stub in microscope chamber, (b) SEM image of top-down view of sample surface with the trapezoidal and side trench milled, (c) micromanipulator welded to side of lamella after undercut has been milled at 7° stage tilt, (d) Plan-view lamella successfully welded to Transmission Electron Microscope (TEM) grid pillar, viewing the silicon (Si) substrate side, (e) Focused Ion Beam (FIB) image of top-down view of 30 kV 240 pA milled plan-view lamella welded to TEM grid pillar, milling is only performed from the Si substrate side of the lamella, while the copper (Cu) side remains untouched and (f) SEM image of final 5 kV 20 pA polish of plan-view with thin region of interest highlighted. (Notation in images: Cu=copper, Si=silicon)

5.4.4 New Step: Removal of the Si Substrate using XeF_2 Etch

An additional/alternative step was then incorporated into the plan-view lamellae preparation technique. It was discovered that a XeF_2 etch could successfully remove the Si substrate

without as much time and beam precision as needed with the reduced beam milling technique. Once the Si was removed, a final low 5 kV 20 pA polish was performed to remove any excess Ta. By using this technique a significantly larger area of lamella was thinned and available for high-resolution S/TEM imaging, in comparison to the previous techniques. Later, we found that this technique had already been described in Kim *et al.* and Liebig *et al*. The main advantage using this etching technique is that it can provide a large area with uniform thickness at a better sputter rate than FIB milling.[17], [18]

The plan-view lamella lift-out was prepared using the side-profile method, just described in a Zeiss Auriga dual beam FIB/SEM. Once the lamella was welded onto the grid it was then milled and etched using an FEI Strata as this instrument has XeF_2 etch capabilities. Initial thinning of the bulk of the lamella was performed at an ion beam voltage and current of 30 kV 1300 pA and was gradually lowered to 30 kV 300 pA. The region was approximately 2 x 5 µm in area. The lamella was thinned to approximately 500 nm in thickness. Using a 5 kV e-beam, the Si was slowly and consistently etched for approximately 1 – 2 hours. As previously mentioned, once the image contrast depicted a significant reduction in thickness and the lamella was approximately 60 – 80 nm in thickness the etching was stopped and the lamella was returned to the Zeiss Auriga FIB for the final low 5 kV 20 pA polish, see Figure 5-10 (a). Figure 5-10 (b) displays a SEM image of another successful XeF_2 etch in which a larger area was polished. As small grain structure of Cu was visible, it was an indication to complete the final polish, as the desired thickness had been reached. This final polish was to remove any excess Si, which still remained and more importantly it was to remove any of the remaining 7 nm Ta barrier layer.

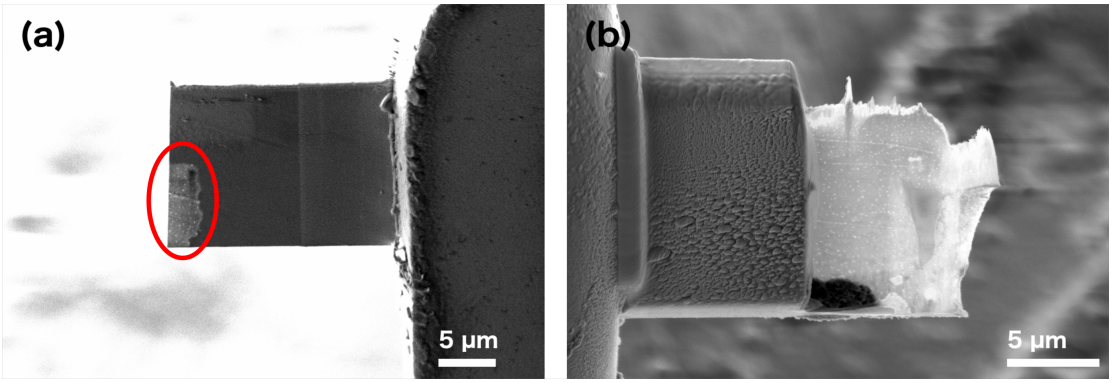

Figure 5-10: (a) Scanning Electron Microscopy (SEM) image of xenon difluoride (XeF_2) etched silicon substrate with copper (Cu) and tantalum layer exposed (b) SEM image of another XeF_2 lamella where grain structure of Cu layer exposed after 5 kV 20 pA polish of area of interest.

Once the lamella was polished to the required thickness, Transmission Kikuchi Diffraction (TKD) was then performed. This technique is described in detail within section 2.2.4, chapter 2. It essentially uses the same principles as EBSD but instead of bulk samples it uses lamellae or thin films usually prepared for TEM analysis.

The TEM grid containing the lamella was secured on a customised holder which allows for a high angle tilt of 70° to be used. Ultimately this customized holder, enabled the acquisition of high-resolution maps and ultimately enabled the resolving of grains as small as 20 nm as opposed to 100 nm achieved in traditional EBSD. From the (Inverse Pole Figure) z-direction map displayed within Figure 5-11 (b) we see from the legend (inset) that the dominant grain orientation on the surface is (111), confirming the observations from STM as seen in Figure 5-5 (c). Figure 5-11 (a) shows that the grain sizes range from 10 – 40 nm. This was further confirmed by C - AFM obtained from the surface of similar Cu film as shown in Figure 5-11 (e) and (f) which displays the topography and conductivity respectively. The freshly removed oxidation layer as well as the just visible grains from beneath are shown in the conductivity map. This was a huge step forward for C-AFM analysis, as the corrosion often leads to loss of information obtainable from the surface of these films. It was also a very challenging technique requiring a highly skilled operator as the correct amount of driving force was needed to mechanically scrape away the oxide layer without damaging or destroying the grains and grain boundaries under investigation.

Through the TKD analysis, statistics were collated of the average grain size, which was found to be ~13 nm and the frequency of certain misorientation angles was also studied. In Figure 5-11 (d) the misorientation of some specific grains were measured with typical values ranging between 20°-30°. It was challenging to confirm whether these grain angle measurements were a true indication of the actual misorientation as the grain size was quite small and pushing the resolution limit of the instrument.[19] Also, ideally TKD performs better with slightly thicker samples than would be ideal for TEM and with a plan-view lamella the Cu layer is only 50 nm thick, which is not ideal for TKD. Another issue could have been that there was still some Si or Ta remaining in the sample that could have caused the wrong indexing to occur when trying to interpret the patterns in the map.

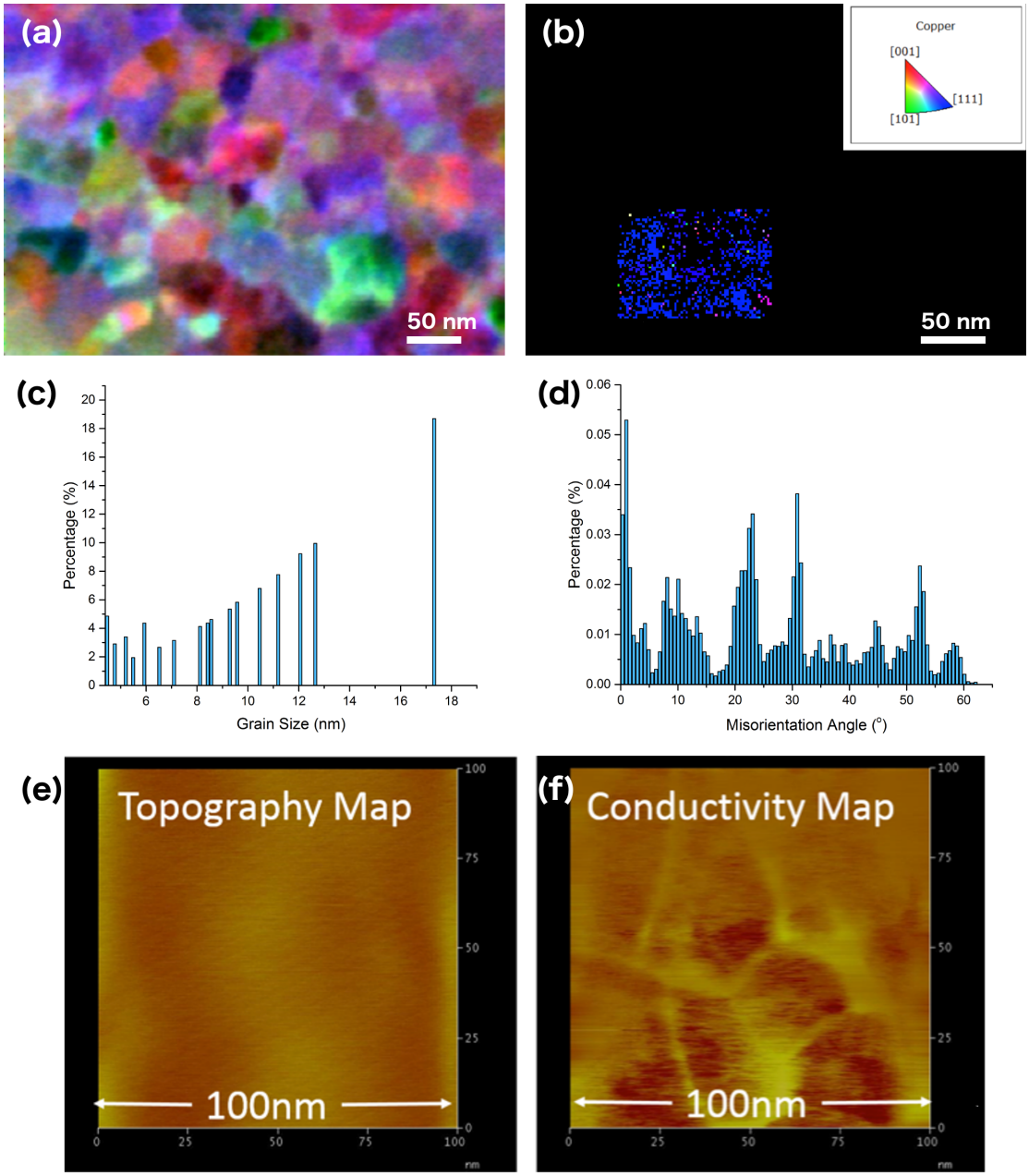

Figure 5-11: (a) Forward-scattered ARGUS image obtained from detector displaying the grain distribution of the copper (Cu) plan-view lamella, (b) grain orientation Inverse Pole Figure (IPF) map in the z-direction (surface) displaying a uniform (111) Cu orientation with the grain orientation legend inset, (c) graph displaying grain size distribution of mapped area in (b), (d) graph of misorientation angles between the grains mapped in part (b), (e) and (f) topography and conductivity obtained by Conductive-Atomic Force Microscopy of Cu surface displaying the grain information available which is comparable to the surface information obtained from the Transmission Kikuchi Diffraction (TKD) data.

Figure 5-12 displays the STEM and TEM images of the plan-view lamella obtained through FIB milling and XeF_2 etching. The images give an overview of grain shape and size and also shows high-resolution STEM images of specific grain boundaries within the film. As previously

discussed in this chapter, Zhang *et al.* have discovered that nanocrystalline films are never flat and experience out-of-plane rotation, which results in the formation of ridges and valleys within the film to reduce the grain boundary energy. As can be seen from the TEM image in Figure 5-12 (b) and the STEM images in Figure 5-12 (c) and (d) there are "zipper" like structures appearing along the grain boundary. In both TEM and STEM mode, it was impossible to confirm that this was the exact structure seen with STM. However, the dimensions were found to be similar: between the zipper it was found to be 1 – 2 nm and the zipper widths 3 nm. This complements the STM data, as shown in Figure 5-12 (e) part (i) and (ii) with the depth and height profile of both valleys and ridges noted in Figure 5-12 (e) part (iv). The next step would be to achieve atomic resolution at the grain boundary interface in both TEM and aberration-corrected STEM, where the potential structures could be potentially confirmed as the ridges and valleys. The possibility that these structures could be an effect of imaging interference needs to be excluded as well.

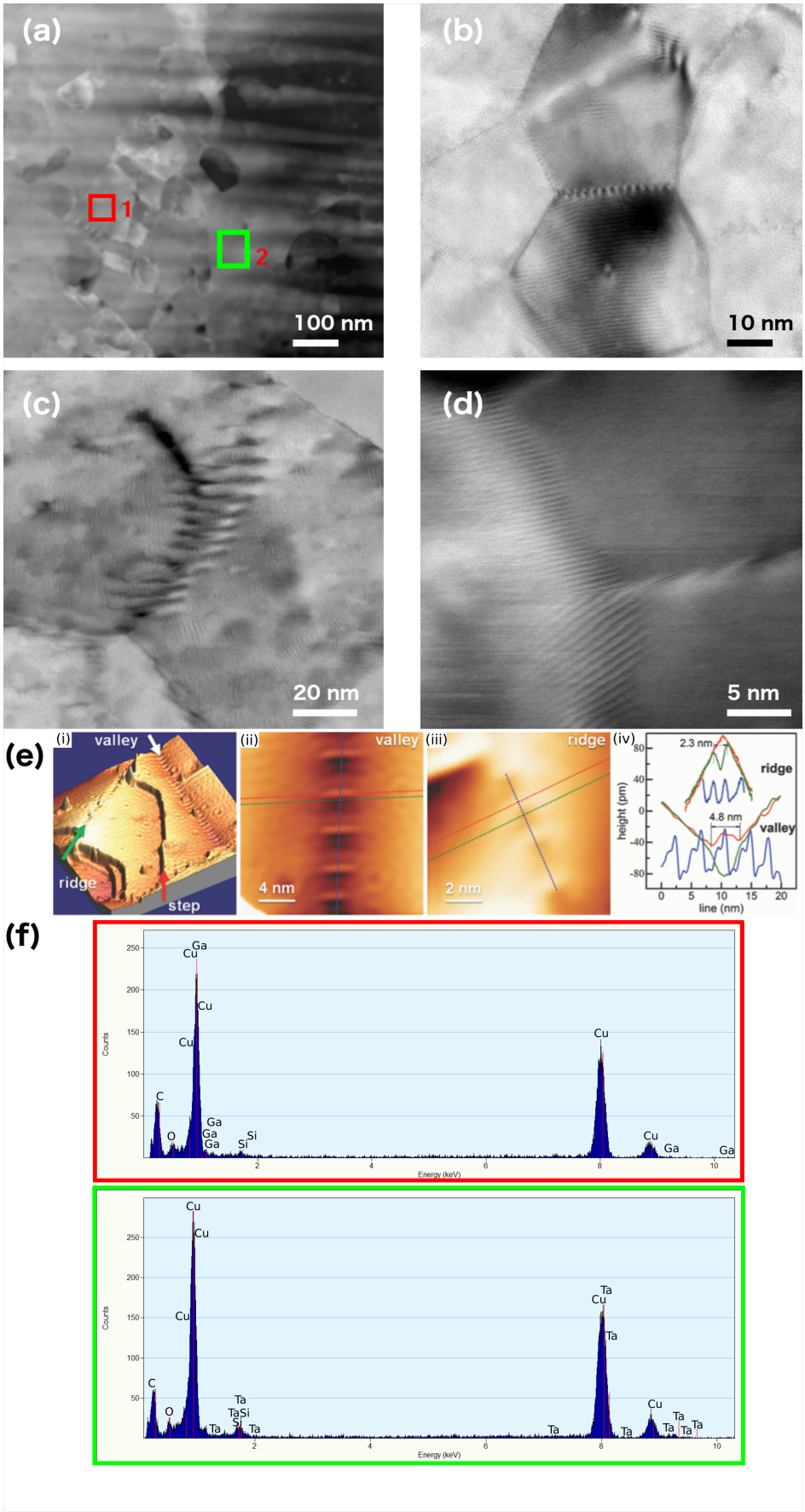

Figure 5-12: (a) Scanning Transmission Electron Microscopy (STEM) images of the 50 nm plan-view copper (Cu) film over a large area displaying the grain size overview with Energy-

dispersive X-ray (EDX) spectra locations marked, (b) TEM image of particular grain boundary with small "zipper"-like defects, which can be repeatedly seen across many grain boundaries, such as (c) and (d) and (e)(i) is a perspective view of the Scanning Tunneling Microscopy (STM) topography of the nanocrystalline Cu film with tunneling parameters I = 20 pA and U = 0.2 V; (ii) high magnification STM image of a grain boundary valley location; (iii) high magnification STM image of a grain boundary ridge location; (iv) Profile of ridge and valley line cross-sections marked by the dashed lines in the previous images.[10]

5.5 Site-specific Cross-sectional Lamella of Cu Nanowires

There was a huge amount of investigation into the 50 nm Cu film and how it relates to the 7 nm Ta liner. A vast amount of knowledge and data was acquired in terms of Cu microstructure and more specifically lamella preparation through FIB milling. However, as mentioned in the introductory chapters of this thesis the ultimate goal of this project was to investigate the resistivity issue within Cu interconnects. This means, analysing actual Cu NWs to try and replicate the kinds of dimensions typically dealt within a transistor. After all the lamella preparation and optimisation part was completed, this part of the project could commence.

The aim was to develop a correlative approach to the experimentation and analysis on this particular sample. More specifically, the aim was to make it possible to pinpoint a specific wire and perform various analytical techniques on this particular wire to make the data as exact and comparable as possible. We were interested to observe how the Cu behaved within a Cu NW in terms of its grain size and distribution as well as the grain boundary structure.

Cu NWs were fabricated at the Intel fabrication facility with NW dimensions of 100 nm wide with ~160 nm depth and with a proprietary barrier of 10-12 nm thickness. These NWs were prepared using the dual-damascene process. A Cu seed layer of a few nm in thickness was deposited using PVD, with the remaining Cu deposited using electroplating creating an overburden of ~200 nm in height, where the excess is then removed using CMP (Chemical Mechanical Planarisation). As this sample was prepared within the Intel fabrication, certain information such as the barrier element and the thickness of the seed is proprietary information, which was not disclosed during the course of the PhD.

5.5.1 Electron Backscattered Diffraction (EBSD)

Firstly, a general overview of the grains on the surface of the bulk sample of Cu NWs was observed using the EBSD technique. The sample was placed at a WD of 9.8mm with a stage tilt of 70° with the EBSD detector at a working distance (WD) of 17 mm. The maps were acquired for 2.5 hrs. An EBSD map of the specific NW and the surrounding NWs was acquired.

Figure 5-13 (a) shows the EBSD map acquired from the area highlighted in Figure 5-13 (c) with grain orientation legend in Figure 5-13 (b). The general grain orientation was again found to be (111), similar to the films surface. Although there is a slightly larger variation in the other grains. This could be potentially due to the restriction of the NWs, causing smaller grains of various orientations to form. It is evident from the EBSD map in Figure 5-13 (a) that the pattern of grains which run across several wires are the "daughter grains" left from the overburden as opposed to smaller grains forming due to the Cu seed layer. It has been hypothesised that there are two competing grain growths influenced either between the overburden or the seed layer. Recrystallisation seems to favour the seed layer, when the overburden is particularly thin, and the "mother grains" of the overburden overpower the seed layer, when the overburden is significantly thicker. If the overburden is the cause of this, it would explain the lack of consistency for a more uniform (111) orientation on the surface, as we have consistently observed in previous samples.[20]

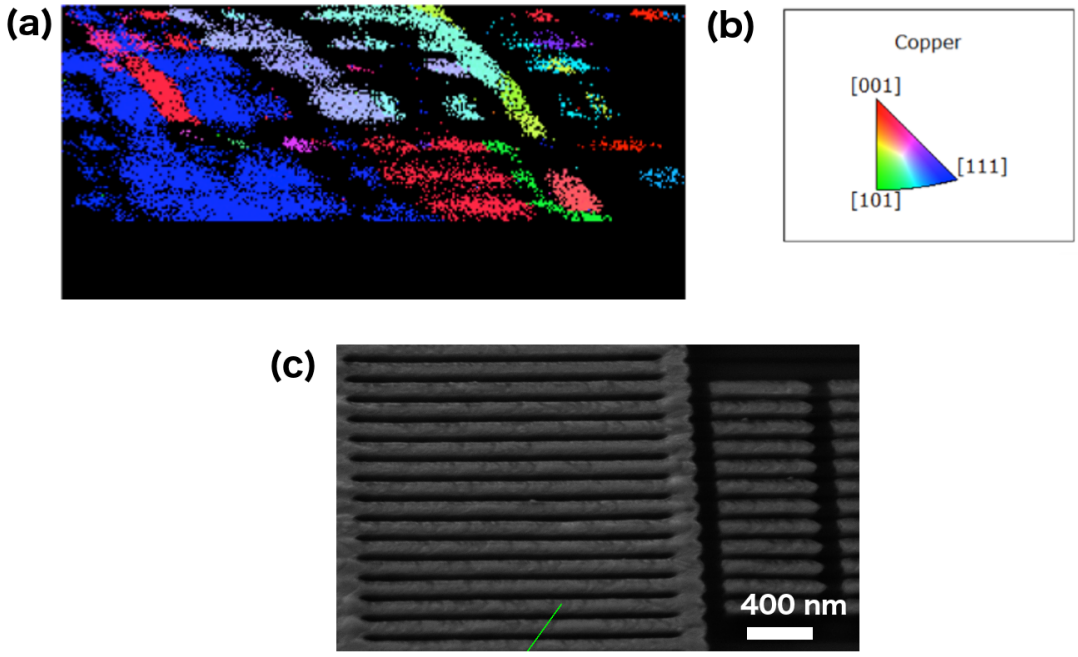

Figure 5-13: (a) Electron Backscatter Diffraction (Inverse Pole Figure) z-direction map of 100 nm copper (Cu) nanowire (NW) array surface, (b) grain orientation legend for Cu and (c) Scanning Electron Microscopy image of Cu NWs highlighted in (a).

5.5.2 Conductive-Atomic Force Microscopy

Next, C-AFM was performed on the sample. Unfortunately it was extremely challenging in both these techniques to pinpoint the exact location of a particular Cu NW. The sample was analysed close to the site-specific Cu NW.

As can be seen from Figure 5-14 (a) there was clear topographical information obtained from the C-AFM, which was extremely challenging to obtain with the previously prepared samples. The wires were clearly visible and some grain information evident from Figure 5-14 (a), displaying the difference in resolution between the differing samples. The most exciting and interesting map is the conductivity map in Figure 5-14 (b). This map shows the successful passing of current through these wires, clearly visible. This information was virtually impossible to obtain from previous samples due to the oxidation and corrosive layers formed on these NWs and films due to the better sample preparation and different barrier layer. This was a clear step in the right direction. Combining this data with the cross-sectional information will form a more coherent investigation of the microstructure of the Cu NWs. Unfortunately, to-date we were unable to obtain any STM data from these NWs. This work in progress is discussed further in the future work section of this thesis.

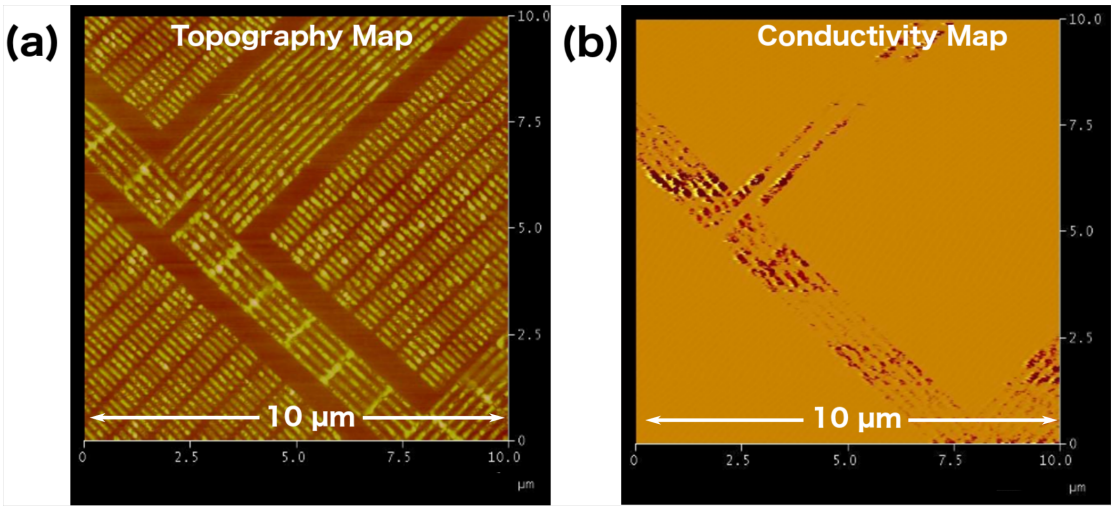

Figure 5-14: (a) Conductive-Atomic Force Microscopy (C-AFM) topography map of copper (Cu) nanowires (NWs) with grain structure becoming visible and (b) C-AFM conductivity map of Cu NWs.

5.5.3 Site-Specific Lamella Preparation of Cu Nanowires Cross-sections for Transmission Electron Microscopy

Once the Cu NW had been analysed by all other techniques, the lamella preparation process began, as it was the most invasive and destructive of all the processes. It was an extremely challenging task to prepare a site-specific lamella of a 100 nm Cu NW for TEM analysis.
Before any initial preparation began, several SEM and FIB images of the entire sample were obtained. It was extremely important to mark exact the distance of the particular Cu NW from the sample edge.

A specific Cu NW was selected using SEM imaging, shown in Figure 5-15 (a) and (b), where the selected NW position was marked using both 0° and 54° stage tilt. Marker pinholes were milled 1- 2µm either side of the wire of interest, as a simple indicator of where the position of the NW was, see Figure 5-15 (c). It was later discovered that this method was previously used for site-specific lamellae preparation by Pettersson *et al.* [21] Using beam parameters of 30 kV 50 pA in spot mode for 60-120 seconds, the markers were milled to a depth of ~5 µm. It was crucial to have the trench/spot with a significant depth of at least 2-3 µm and a width of ~500 nm to ensure it was clearly visible during the milling/thinning process, as shown in Figure 5-15 (d) and (g).

The bulk lamella preparation was prepared in the previously described method used from cross-sectional preparation, with a slightly extended section including some extra wires, which also served as markers for the navigation of the NW of interest. The lamella was mounted onto a TEM grid and the NWs that were not coated in a protective Pt layer gave an indication of the approximate location of the wire of interest, see Figure 5-15 (e). The lamella was thinned using the method as described in section 3.1.3, chapter 3. There was a slight alteration to this preparation, as the angle of milling was reduced to 1-2° with respect to the FIB beam. As this was a more targeted lamella, it was important to not create an over exaggerated angle, see Figure 5-15 (f), showing a very straight side-profile as opposed to the wedge shape previously shown. This needs to be implemented as an exaggerated angle could lead to milling too far into the wire of interest and thinning the incorrect wire. The lamella was polished with gradual reducing beam energies with a final polish performed at 2 kV 20 pA, see Figure 5-15 (h). The lamella was then imaged in both, TEM and STEM mode.

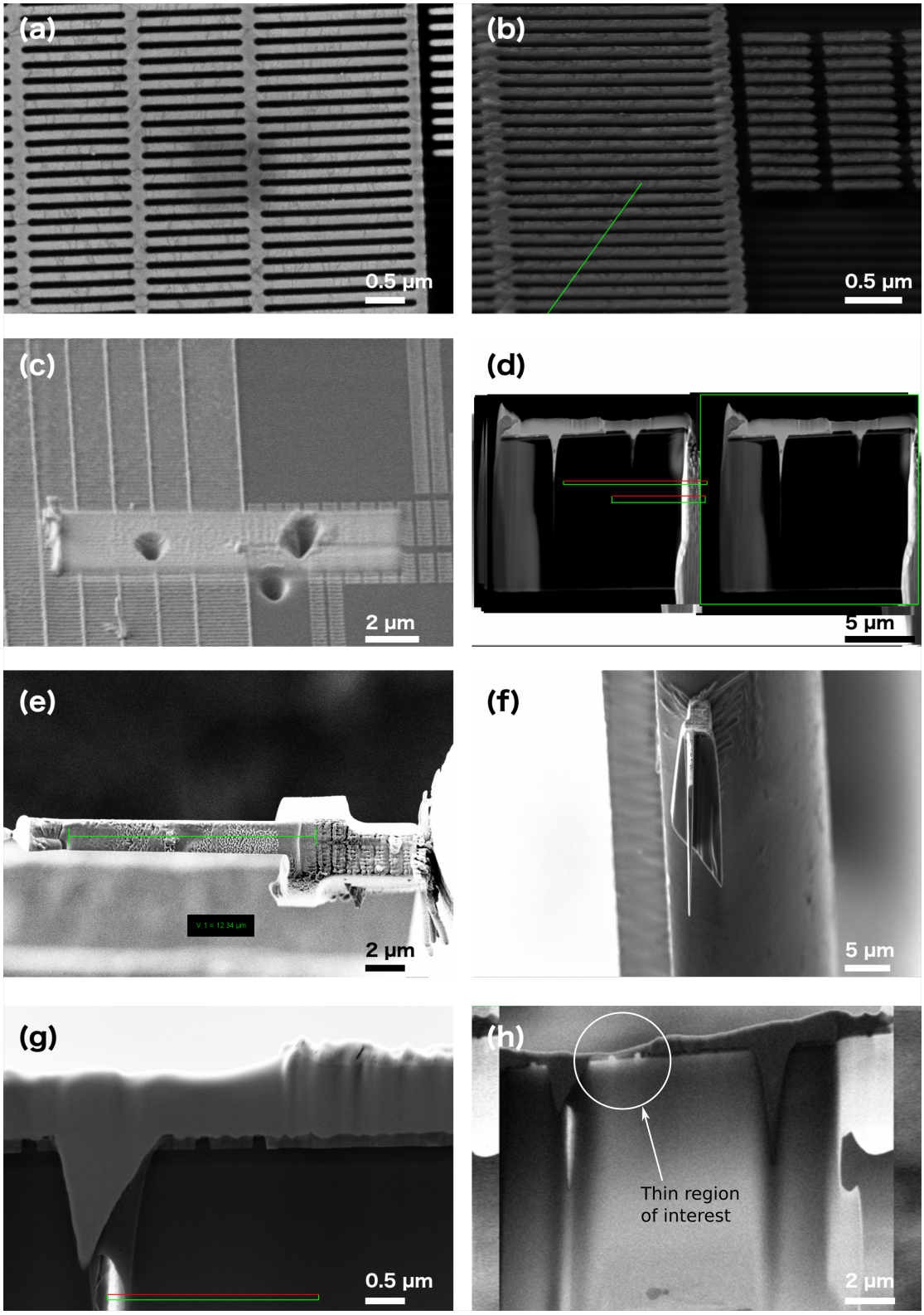

Figure 5-15: Scanning Electron Microscopy (SEM) images of (a) and (b) with markers of position of copper (Cu) nanowire (NW) at 0° and 54° stage tilt respectively, (c) and (d) pinholes markers milled into substrate to use when milling, (e) Focused Ion Beam (FIB) image of wires kept untouched from platinum (Pt) to use as navigation markers for milling and polishing, (f) SEM image of straight side-on profile of lamella during thinning procedure, (g) some "wave" like feature appearing along top of wires and (h) SEM image of final 2 kV 20 pA polish.

5.5.4 Scanning/Transmission Electron Microscopy Imaging

The area of interest highlighted in Figure 5-15 (h) was imaged in TEM. The lamella preparation technique was successful as high-resolution TEM images containing lattice information was achievable, as shown in Figure 5-16 (a). Also in Figure 15-6 (b) is a high-resolution aberration-corrected image of the Si substrate with FFT inset taken at 200 kV using the NION Ultra STEM microscope at the Advanced Microscopy Lab, Trinity College Dublin. Achieving atomic resolution with this sample shows the precision and expert skills employed in the preparation of these site-specific lamellae.

In contrast to the Cu films, the Cu NWs had a consistent mix of grain sizes and grain boundaries. In both, the SEM and EBSD analysis, bamboo-type grain structure is prevalent on the surface of the Cu NWs. It was unclear whether these structures ran throughout the depth of the wire. It can be seen in Figure 5-16 (c) and (d) that there were areas of dips of 30-40 nm in depth, which occur frequently across the cross-section of the wire. This could correlate with the bamboo structure on top, suggesting that it does not run through the entire depth of the wire.

Using STEM imaging, the variety of grain structure and size became apparent. Almost no grains run the depth of 150 nm Cu NW, with a mixture of grains running in parallel and perpendicular to the NW, shown in Figure 5-16 (e) and (f). There is a definite mix of both high-angle and low-angle grain boundaries with grain sizes ranging from 20-200 nm.

Taking a closer look at the grains and grain boundary interaction, it can be observed, as shown in Figure 5-16 (a), that these have similar grain orientation to previously observed. It can also be seen at this grain boundary junction that twin boundaries are also present within the NWs.

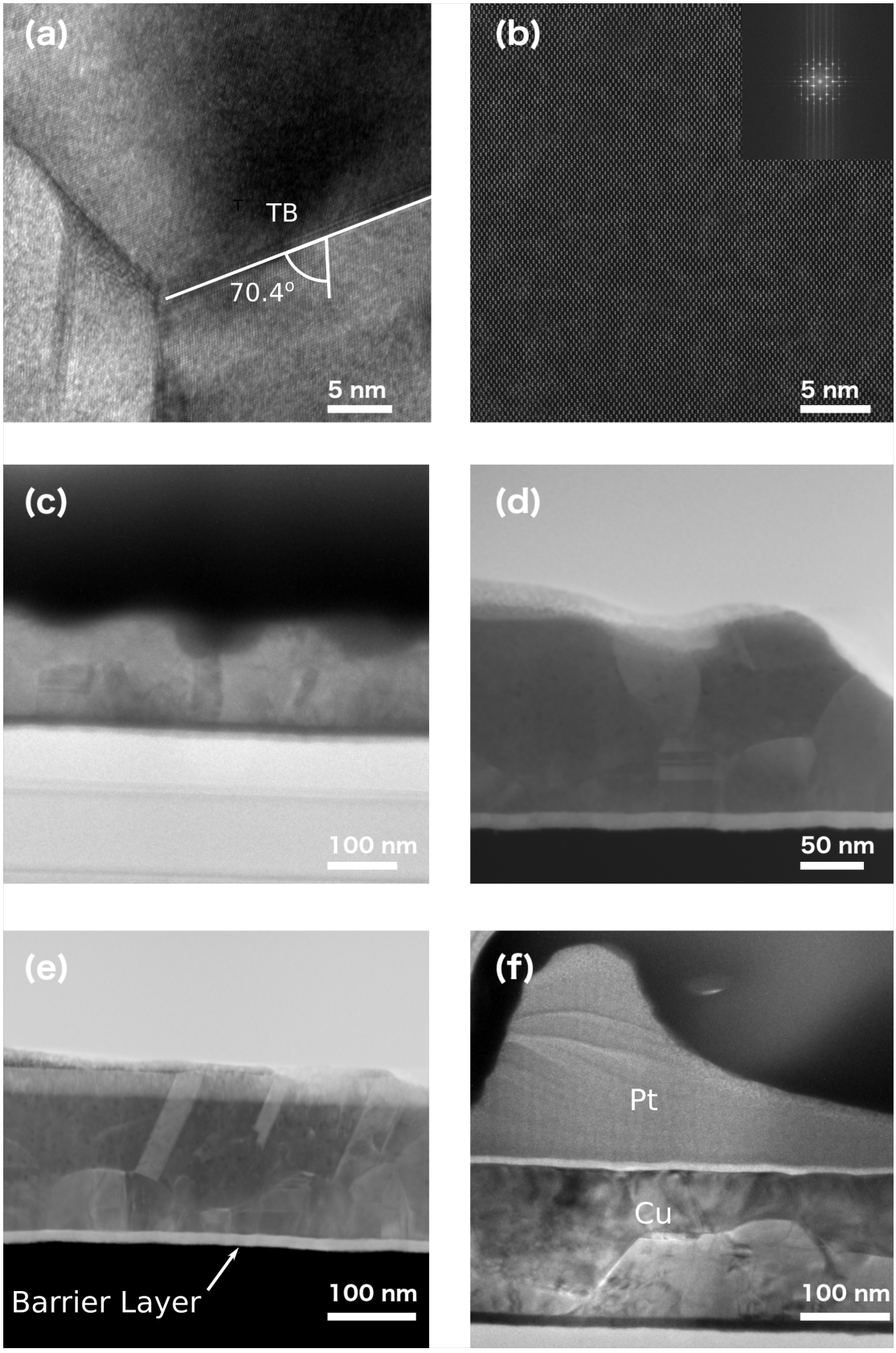

Figure 5-16: (a) High-resolution Transmission Electron Microscopy (TEM) image of twin boundary within copper (Cu) nanowire (NW) cross-section, (b) aberration-corrected High-angle annular dark field (HAADF) Scanning TEM (STEM) image of the silicon (Si) substrate after 2kV 20pA milling, with fast Fourier Transform (FFT) inset, (c) and (d) and TEM and HAADF STEM

images displaying the "dents" and "bumps" of approximately 40 nm in depth, (e) HAADF STEM image of Cu NW grain overview, due to thickness difference, much less grains running through the depth of the film and (f) TEM image of Cu NW cross-section with protective mound of platinum (Pt). (Notations in image: TB = Twin boundary, Cu=copper, Pt=platinum)

5.6 Conclusions

The microstructure of Cu films deposited on Ta liners was investigated through a variety of different preparation and characterisation techniques.

Numerous lamella preparation techniques were employed and optimised specifically for this particular sample. Taken into consideration the challenges encountered due to the preferential milling of Cu and the hardness of Ta and its reluctance to mill at the same rate as Cu, cross-sectional lamellae of Ta liner Cu films were prepped to an extremely high quality using low kV FIB milling. This allowed the microstructure to be analysed using aberration-corrected STEM with a reported thickness of ~30 nm. Similar to the SiO_2, twin boundaries were also present in this Cu film, but the amorphisation and smaller crystallites present within the previous samples were significantly reduced and sometimes absent within this film. Incoherent twin boundaries with slight misalignment of 1-2° running parallel with the Cu film could potentially confirm the out-of-plane rotation of grains visible using STM. Providing high-resolution imaging and analysis of the grains and microstructure from the cross-sectional perspective is extremely important and was very beneficial to this project as it illuminated an aspect of the film/material that was needed to further the project in terms of both STM and C-AFM. Without this initial cross-sectional information, it would be very challenging to interpret the films as a whole.

Plan-view lamella preparation proved extremely successful across a number of different techniques, in particular, the use of the side on lamella preparation and the XeF_2 etch with a final low kV FIB polish. Again, this data was analysed using TKD, TEM, STEM and EDX confirming the type of grain structure observed by the other surface techniques, C-AFM and STM. This helped in supporting the findings.

Finally, site-specific lamellae were a natural progression as Cu interconnects investigation was the ultimate goal of this project in terms of linking the grain structure with point-specific resistivity and conductivity measurements. Cu NWs prepared using the dual damascene process were analysed. Using EBSD, the overall grain structure and orientation of the NW

surface was analysed. The cross-sectional lamella of the NW was also analysed through STEM and TEM, through the highly skilled task of selecting a specific NW of just 100nm in thickness in SEM and proceeding to mill this NW, using conventional ion beam milling procedure. This led to significant findings in the grain shape, size and orientation and distribution throughout the NW, which were previously undetectable in both STM and C-AFM.

Through a variety of lamella preparation and many other complementary characterisation techniques, the microstructure of Cu and its relationship with Ta had been investigated. Extremely high-quality data and analysis had also been produced through the consistent optimisation of the highly skilled technique of lamella preparation.

5.7 Bibliography

[1] T. Laurila, “Tantalum-Based Diffusion Barriers for Copper Metallization,”, pp. 1-59, 2001.

[2] M. A. Nicolet, “Diffusion Barriers in Thin Films,” *Thin Solid Films*, vol. 52, pp. 415–443, 1978.

[3] D. Edelstein, C. Uzoh, C. Cabral Jr., P. DeHaven, P. Buchwalter, A. Simon, E. Cooney, S. Malhotra, D. Klaus, H. Rathore, B. Agarwala, and D. Nguyen, “A High Performance Liner for Copper Damascene Interconnects ,” *Proc. IEEE*, pp. 9–11, 2001.

[4] Z. H. Cao, K. Hu, and X. K. Meng, “Diffusion barrier properties of amorphous and nanocrystalline Ta films for Cu interconnects,” *J. Appl. Phys.*, vol. 106, no. 11, pp. 113513–6, 2009.

[5] Z. W. Yang, D. H. Zhang, C. Y. Li, C. M. Tan, and K. Prasad, “Barrier layer effects on reliabilities of copper metallization,” *Thin Solid Films*, vol. 462, pp. 288–291, 2004.

[6] H. Lee and S. D. Lopatin, “The influence of barrier types on the microstructure and electromigration characteristics of electroplated copper,” *Thin Solid Films*, vol. 492, no. 1, pp. 279–284, 2005.

[7] R. Hadian, B. Grabowski, M. W. Finnis, and J. Neugebauer, “Migration mechanisms of a faceted grain boundary,” pp. 1–8, 2018.

[8] B. B. Straumal, O. A. Kogtenkova, A. S. Gornakova, V. G. Sursaeva, and B. Baretzky, “Review: grain boundary faceting–roughening phenomena,” *Journal of Materials Science*, vol. 51, no. 1, pp. 382–404, 2015.

[9] S. Gokhale, K. H. Nagamanasa, R. Ganapathy, and A. K. Sood, “Grain growth and grain boundary dynamics in colloidal polycrystals,” *Soft Matter*, vol. 9, no. 29, pp. 6634–11, 2013.

[10] X. Zhang, J. Han, J. J. Plombon, A. P. Sutton, D. J. Srolovitz, and J. J. Boland, “Nanocrystalline copper films are never flat,” *Science*, vol. 357, pp. 397–400, 2017.

[11] C. Li, G. Habler, L. C. Baldwin, and R. Abart, “An improved FIB sample preparation technique for site-specific plan-view specimens: A new cutting geometry,” *Ultramicroscopy*, vol. 184, no. Part A, pp. 310–317, 2018.

[12] F. Lenrick, M. Ek, D. Jacobsson, M. T. Borgstrom, and L. R. Wallenberg, “FIB Plan

and Side View Cross-Sectional TEM Sample Preparation of Nanostructures ," *Microsc Microanal*, vol. 20, pp. 133–140, 2014.

[13] M. B. Ward, N. A. Porter, P. Sinha, R. Brydson, and C. H. Marrows, "Preparation of plan-view Co-doped FeSi thin film TEM specimens using FIB," *J. Phys.: Conf. Ser.*, vol. 522, pp. 012044–5, 2014.

[14] M. Jublot and M. Texier, "Sample preparation by focused ion beam micromachining for transmission electron microscopy imaging in front-view," *Micron*, vol. 56, pp. 63–67, 2014.

[15] J. Mayer, L. A. Giannuzzi, T. Kamino, and J. Michael, "TEM Sample Preparation and Damage," *MRS Bulletin*, vol. 32, no. May, pp. 400–407, 2007.

[16] D. Fox, R. Verre, B. J. O'Dowd, S. K. Arora, C. C. Faulkner, I. V. Shvets, and H. Zhang, "Investigation of coupled cobalt–silver nanoparticle system by plan view TEM," *Progress in Natural Science: Materials International*, vol. 22, no. 3, pp. 186–192, 2012.

[17] J.-S. Kim, S.-Y. Nam, Y.-H. Choi, and J.-C. Park, "Preparation Method of Plan-View Transmission Electron Microscopy Specimen of the Cu Thin-Film Layer on Silicon Substrate Using the Focused Ion Beam with Gas-Assisted Etch," *AM*, vol. 45, no. 4, pp. 195–198, 2015.

[18] J. P. Liebig, M. Göken, G. Richter, M. Mačković, T. Przybilla, E. Spiecker, O. N. Pierron, and B. Merle, "A flexible method for the preparation of thin film samples for in situ TEM characterization combining shadow-FIB milling and electron-beam-assisted etching," *Ultramicroscopy*, vol. 171, no. c, pp. 82–88, 2016.

[19] P. W. Trimby, "Orientation mapping of nanostructured materials using transmission Kikuchi diffraction in the scanning electron microscope," *Ultramicroscopy*, vol. 120, pp. 16–24, 2012.

[20] R. Galand, K. Haxaire, L. Arnaud, E. Petitprez, L. Clement, P. Waltz, and Y. Wouters, "Microstructure and texture analysis of narrow copper line versus widths and annealing for reliability improvement," *Microelectronic Engineering*, vol. 88, no. 5, pp. 661–665, 2011.

[21] H. Pettersson, S. Nik, J. Weidow, and E. Olsson, "A Method for Producing Site-Specific TEM Specimens from Low Contrast Materials with Nanometer Precision," *Microsc Microanal*, vol. 19, pp. 73–78, 2013.

6. Novel *in-situ* Lamella Fabrication Technique for *in-situ* Transmission Electron Microscopy Annealing Experiments

6.1 Introduction

The methods described in this chapter outline an innovative and reproducible technique for cross-section lamella preparation for *in-situ* Transmission Electron Microscopy (TEM) experimentation using a gallium $(Ga)^+$ Focused Ion Beam (FIB), as well as an improved method for mounting electron-transparent lamellae directly onto a research platform – in this case, the Micro-Electro-Mechanical Systems (MEMS) device.[1] This represents a great improvement compared to preparing larger, bulk-like sample sizes, which generally leads to anisotropic heat distribution throughout the sample.

FIB sample preparation is a well understood and frequently used technique, as it is an efficient and reliable method for preparing high-quality electron-transparent samples with minimal damage.[2]-[7] A method for lamella lift-out for MEMS device mounting has been developed previously by Duchamp *et al.*[8] In the technique presented here lamella transfer is achieved by the chemo-mechanical securing of the lamella to the MEMS device, eliminating the need to use the platinum (Pt) weld technique. Avoiding the use of electron beam-induced deposition (EBID)-Pt comes with two distinct advantages: 1) no re-deposited Pt spray from the deposition process, which would contaminate the lamella; and 2) no risk of damaging the MEMS device during the thinning process.

The technique detailed in this chapter not only provides a new improved lamella preparation method for *in-situ* annealing, but also presents a novel means for preparing cross-sectional lamellae for applications across many different analytical platforms.

Real-time observations of materials undergoing dynamic changes upon the application of external stimuli are increasingly recognised as vital to understanding the fundamental processes taking place during materials synthesis, processing and functioning.[9] In technological applications, a material is exposed to a variety of environmental stress and external stimuli. The response of a material to these stimuli often influences their functionality. Based on this reasoning, *in-situ* TEM has become an essential technique within the field of material science. *In-situ* techniques such as annealing [10], biasing [11], cryogenics

[12], liquid/gas [13]-[15], mechanical interrogation [16], [17] and electrochemical analysis [18], have been developed to track the evolution of materials under such external stimuli.

Thermal experimentation within the TEM has provided a new and interesting perspective on many material sets.[19]-[22] *In-situ* annealing has progressed from heating entire sample grids to using MEMS devices to enable localised heating. This technology provides greater temperature control due to the small volume and reduced thermal mass of the heater. Moreover, it considerably reduces specimen drift and settling time.[23] The use of this technology for *in-situ* annealing experiments has enabled the process to become fast and reliable, offering new insights into material morphology.[24], [25] Despite all the progress that has been made using *in-situ* annealing experiments, studying dynamic processes *in-situ* within the TEM presents several important challenges, including specimen preparation and sample transfer.

6.2 Experimental Methods

The technique developed and described in this chapter utilises a Zeiss Auriga cross-beam FIB-SEM system for complete lamella fabrication as well as lamella transfer to the MEMS device. (MEMS devices were purchased from DENSsolutions). The MEMS device consists of a molybdenum (Mo) spiral encapsulated between two SiN_x membranes. The Mo spiral heats the localised area via joule heating controlled by a 4-point probe feedback loop. As well as the Mo heating spiral, there are a series of through-hole windows (5–20 μm).[26] The lamella is positioned over a window close to the centre of the heating spiral as shown in Figure 6-1. The MEMS device can reach a maximum temperature of 1300°C, with temperature stability of < 1°C at 1300°C. It has a heat rate of 200°C per millisecond and a settling time of < 2 seconds.

The standard proof-of-concept specimen is bulk silicon (Si) for reproducible, reliable fabrication and analysis. SEMGlu (Kleindiek Nanotechnik GmbH, Reutlingen) was used for securing lamellae to the MEMS device. SEMGlu is a vacuum-compatible adhesive that is cured by electron-beam irradiation, providing a mechanically robust and thermally stable bond between the lamella and the MEMS device.[27]

A reduced electron-beam current of ~ 10 pA permits working with the glue under SEM observation. Adhesive curing is achieved by irradiating with the condensed electron probe for

one minute using an electron beam current density of 10 pA/µm^2, on the SEMGlu, causing the adhesive to harden. The incident electrons trigger a polymerisation process and change the physical properties of the glue (elasticity, tensile strength). The electron-beam voltage determines the penetration depth (approximately 100 nm per kV) into the glue and thus the glue's curing volume.

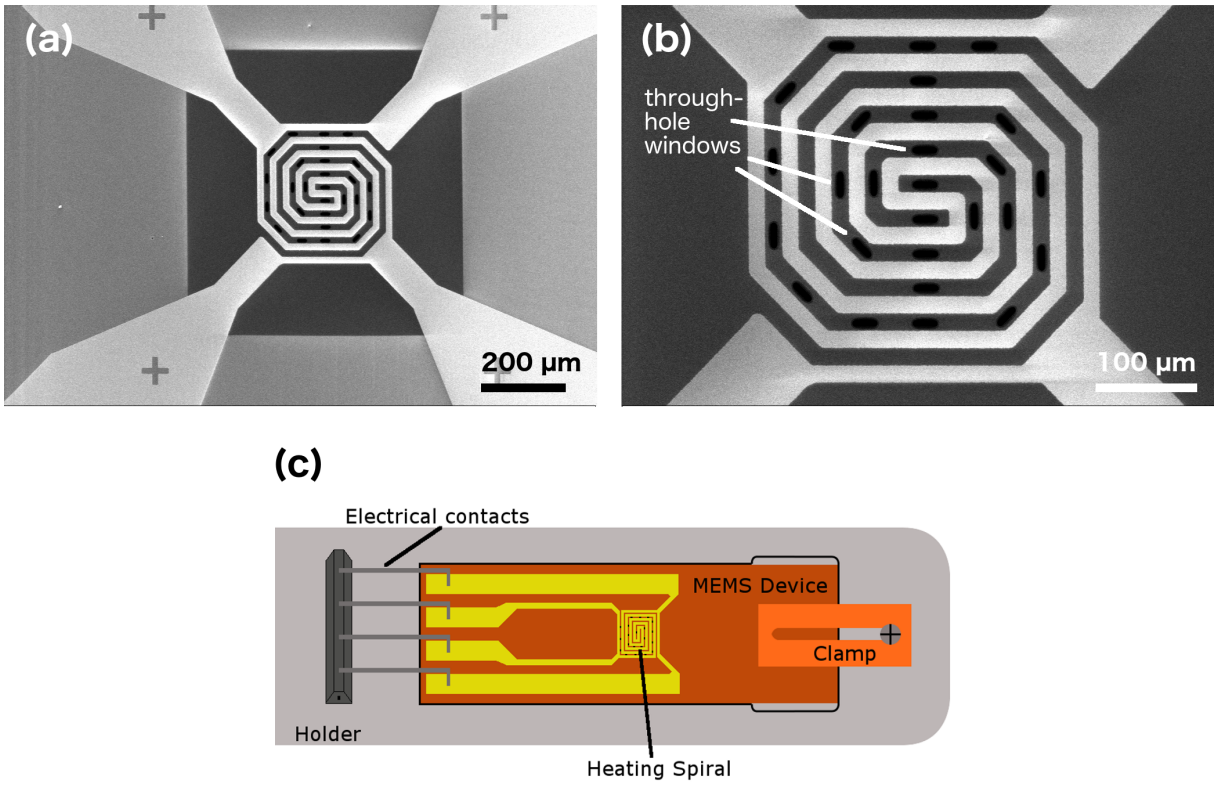

Figure 6-1: (a) Scanning Electron Microscopy (SEM) image of Micro-Electro-Mechanical Systems (MEMS) device displaying the 4-point geometry, (b) SEM image of MEMS device showing the heating spiral and through-hole windows and (c) schematic of heating holder and MEMS device.

The application of the SEMGlu and the removal of the lamella were performed using a roof-mounted Kleindiek micromanipulator fitted with RoTip and microgrippers for lamella lift-out. The ROTIP-EM is a rotational axis plug-in for the MM3A-EM micromanipulator that enhances the system by providing a fourth degree of freedom, which is ideal for this particular technique. All images pertaining to the video created for this work were recorded on an FEI Quanta 200 3D.

In this study we used a DENSsolutions Wildfire S3 and a double-tilt Lightning heating holder, however the technique is compatible with other heating holders. The system comprises of a single tilt holder with the MEMS device replacing the standard TEM grid. The TEM holder has a tilt range of +/- 30° with maximum sample drift of 0.5nm/min at 800°C. S/TEM imaging and analysis is performed on a FEI Titan TEM at 300 kV. Energy-dispersive X-ray (EDX) spectra were collected at an angle of 15° on an EDAX EDX detector using a non-annealed 50 nm Cu film on 7 nm Ta on a Si substrate. All high-angle annular dark field (HAADF) imaging was at a convergence semiangle of 10 mrad and a collection semiangle of 39 mrad.

6.3 Motivation

6.3.1 Mounds – 50 nm Cu Annealed Film

As mentioned in previous chapters, the 50 nm Cu film/7 nm Ta on Si was annealed prior to Scanning Tunneling Microscopy (STM) analysis. It was annealed under ultra-high vacuum (UHV) to approximate temperatures of between 300-400°C for 10 min with a temperature ramp time of 10 min. It underwent an acetic etch to remove the first 1-2 nm of the film surface to remove any oxide and reduce surface roughness. So as to create a cohesive analysis of the Cu film and its microstructure, the subsequent FIB lamella preparation and TEM analysis was performed using the annealed 50 nm Cu film. Areas of the Cu film were noted to have de-wetted. Within these circular areas of de-wetting, small mounds had formed (~1 µm in size). From the literature, the mounds are created from an intermixing of the Cu and Si to form a η'' – Cu_3Si precipitate.[28]-[30]

The formation of these types of mounds has been previously observed in studies of the reaction of Cu/Ta/Si at increasing temperatures. The temperatures noted here were considerably higher, ~600°C.[28], [29] A lot of the previous analysis of this type of material has been done with thicker films using SEM, cross-sectional TEM, resistance measurements and Rutherford backscattering spectroscopy (RBS). It has also been observed with different liners other than Ta. Chen *et al.* investigate the diffusion barrier properties of sputtered TiB_2 and similar mounds form on the surface of the Cu film at ~800°C.[31] It has also been investigated how the deposition of the Ta liner at ultra-high vacuum (UHV) and high vacuum (HV) can effect the temperature at which the Ta barrier fails and again the formation of these mounds occurs.[32] Clevenger *et al.* noted that the variation in failure temperature was significant within these different environments. HV deposited Ta barriers failed from 560 to 630°C and

UHV deposited Ta barriers between 310-630°C. Also studied within this paper was the effect of oxygen dosed and non-dosed samples and the change in failure temperatures.[32]

De-wetting of films (also known as film agglomeration) has a direct link with grain boundary grooving, which has been mentioned in previous results chapters. The surface diffusion of atoms causes grooving, which in turn leads to de-wetting when the temperature is increased as atom mobility increases with increasing temperature. There is typically a characteristic temperature at which de-wetting occurs and this is dependent on film thickness.[33] It has been stated that there is a critical ratio of grain size to film thickness that must be reached before agglomeration can occur.[34] De-wetting typically occurs in films to try and reduce the surface and interfacial energy.[35] There is a direct link between the agglomeration/de-wetting and the barrier layer, as Cu directly deposited onto SiO_2 does not experience any agglomeration.[34] Therefore, adhesive quality of the barrier layer plays a major role in the de-wetting of the film. Ruthenium (Ru), for instance, has good adhesion properties with Cu film and has lower wetting angles with the Cu film than Ta, meaning it is less likely to agglomerate than the Ta. Ru could be used as a glue layer between Cu and Ta to provide better adhesion, while still using Ta's good diffusion barrier properties. It is important to study the de-wetting properties of the Cu films as this has been linked to electromigration resistance. [36]

We were interested in finding out how these mounds formed in real-time and observe the behaviour of the Ta liner under these conditions. Holloway *et al.* had shown that these mounds usually contained a Cu_3Si intermixing along with a $TaSi_2$ forming along the top of the mound. We wanted to observe in real time the formation of these mounds and the critical point at which the Cu diffusion and intermixing began, along with the migration of the Ta to the surface of the mound. We also wanted to confirm if the temperatures of the diffusion varied due to the reduced film thickness. We were using a 7 nm Ta layer as opposed to 50 nm previously used. The reduction in the Cu film thickness from 100 nm as commonly used, including by Holloway *et al*., to 50 nm Cu film used here could lead to variations in the temperature dynamics. [28], [29]

This first process of investigation was done using SEM analysis. Figure 6-2 shows SEM images of the mounds at various angles. To confirm whether Ta or Cu was present at the surface of the mounds, EDX spectroscopy would ideally be performed. Unfortunately, it was challenging to perform EDX analysis on these mounds as they were, at less than 1 µm in diameter, below

the resolution limit as the interaction volume for EDX at a beam voltage of 20 kV is ~2 µm. It also proved challenging to successfully perform EDX of a FIB cross-section due to the obstructing geometry of the set-up at a stage tilt of 54°.

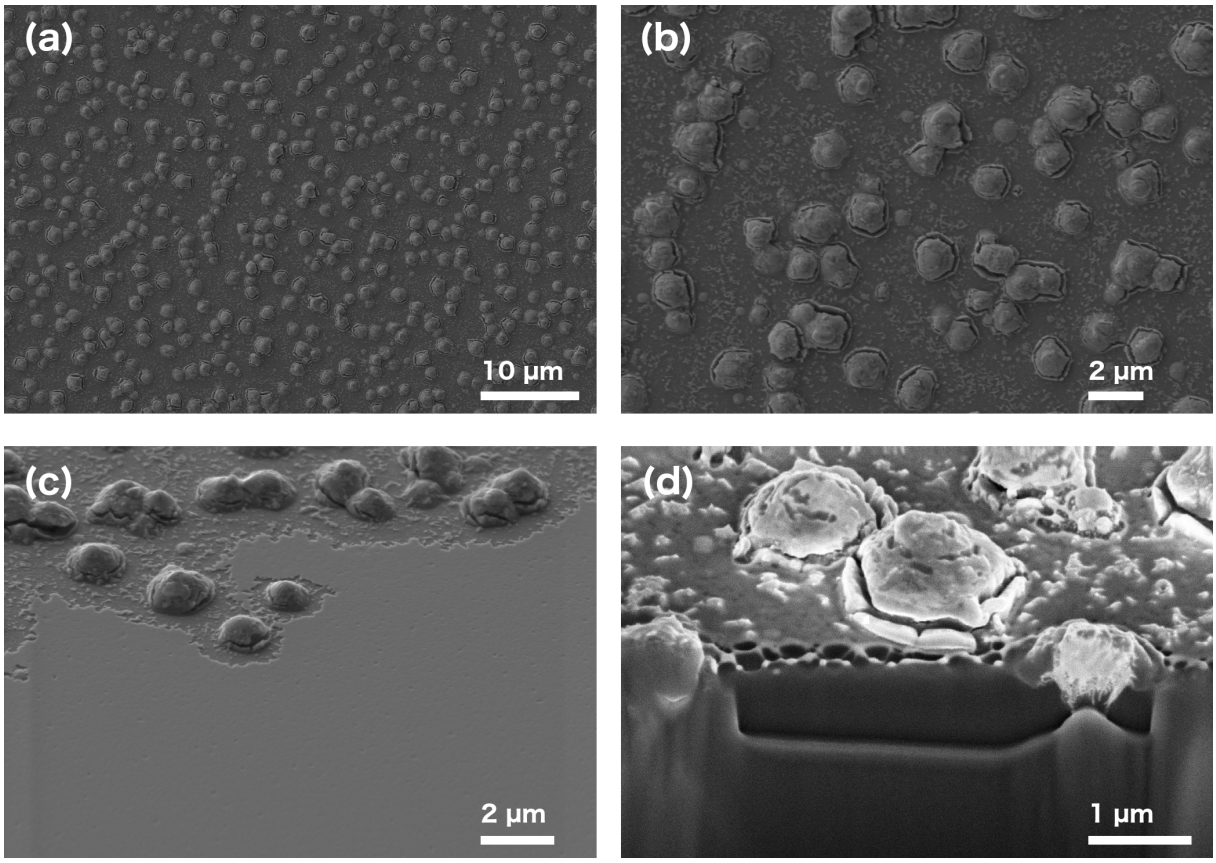

Figure 6-2: Scanning Electron Microscopy (SEM) images of mounds formed on copper (Cu) film surface due to annealing at (a) 0° at low magnification, (b) 0° at high magnification, (c) at 54°at high magnification and high magnification image of mound used for Focused Ion Beam (FIB) cross-sectioning and (d) specific mound in which FIB cross-section was milled.

To get a better understanding of the internal geometry of the mound as well as above the film surface, cross-sectional FIB analysis was performed on the sample. This was done by tilting the sample to 54° so as to be parallel with the FIB. Due to the dual-beam nature of the Zeiss Auriga FIB, it is possible to live image with the SEM while simultaneously mill the sample with the FIB.

Included in Appendix A2 is a slice-and-view cross-sectional video, set up so that an image is taken every 20 seconds. This FIB cross-section along with the slice-and-view video confirmed that the mound that formed ruptured the Ta barrier layer, intermixing the material above and below the surface. It can be seen from the comparison in Figure 6-3 the Cu_3Si precipitate

formed is bound by the Si (111) and the Si (100) planes with an angle of 54.7°. The Cu_3Si formed within the Si substrate is trapezoidal in shape, which is similar to that of Jung *et al*., Holloway *et al*. and Chen *et al.* This is one of the preferred orientations of the Cu_3Si precipitate within the Si (100) substrate.[37]

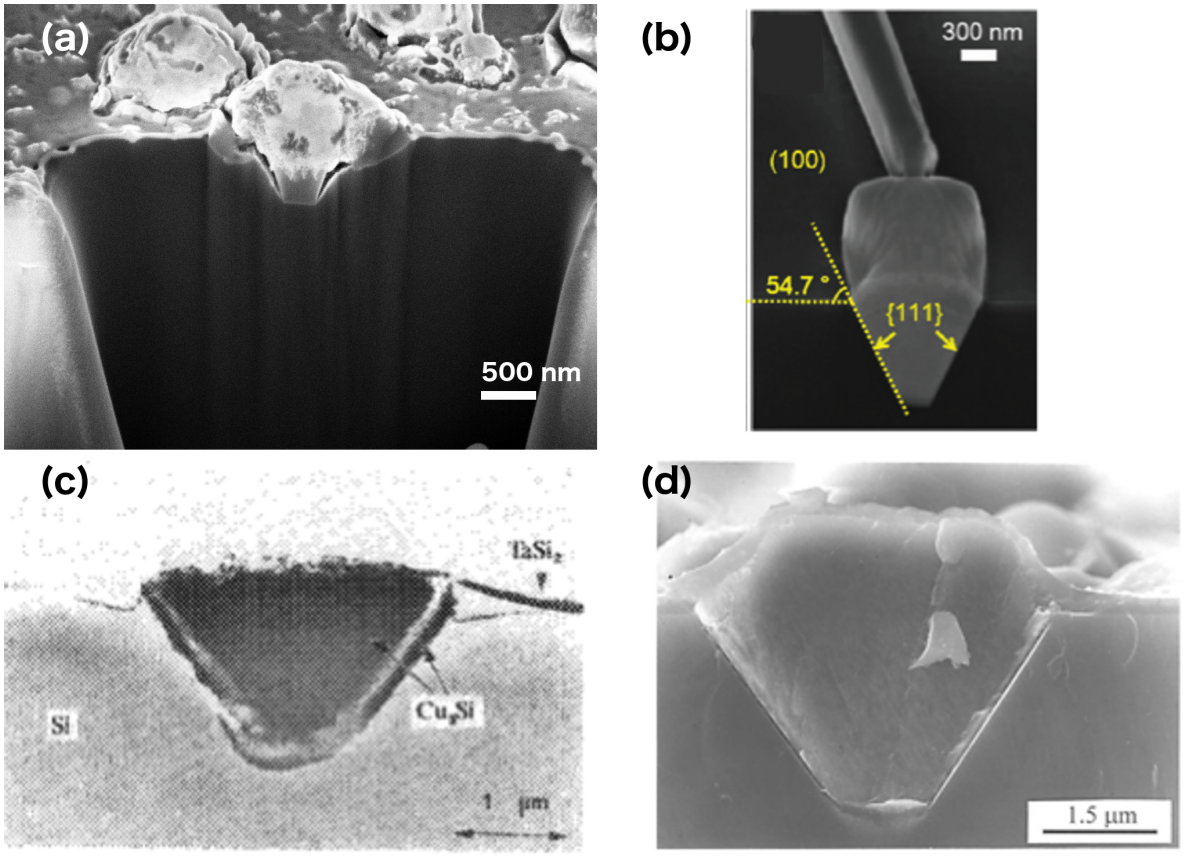

Figure 6-3: (a) Scanning Electron Microscopy (SEM) images of mound cross-section (b), (c) and (d) Jung et al., Holloway et al. and Chen et al. respectively, showing similar mounds forming upon annealing the films.[28], [31], [38]

When noticing the internal structures of the mound from the slice and view data collected from the FIB/SEM analysis, the question was raised as to whether the Si or Cu had migrated across the Ta layer. From what we can see with Holloway *et al*., they determined using Rutherford Backscattered Spectroscopy (RBS) and cross-sectional TEM analysis that the Ta layer had migrated to the top of the mound but had also intermixed with the Si to form $TaSi_2$. [28], [29]

In order to confirm that the Ta had migrated to the top of the mound and that the Cu had intermixed with the Si, a cross-sectional lamella for TEM analysis was prepared using the *in-situ* lift-out FIB technique. This was a tricky process, unlike previously described *in-situ* lift-out

TEM lamella preparation. This was more analogous to a site-specific lamella, as we wanted to examine the middle of the mound, to find the most interesting and useful data. The lamella was milled from the outer edges of a larger circle of mounds, shown in Figure 6-4 (a) and (b). The mound was placed as centred as possible within the bulk lamella in both the x- and y-direction. Its position was marked by depositing a localised spot of Pt. The final polish of lamella was performed at 5 kV 20 pA.

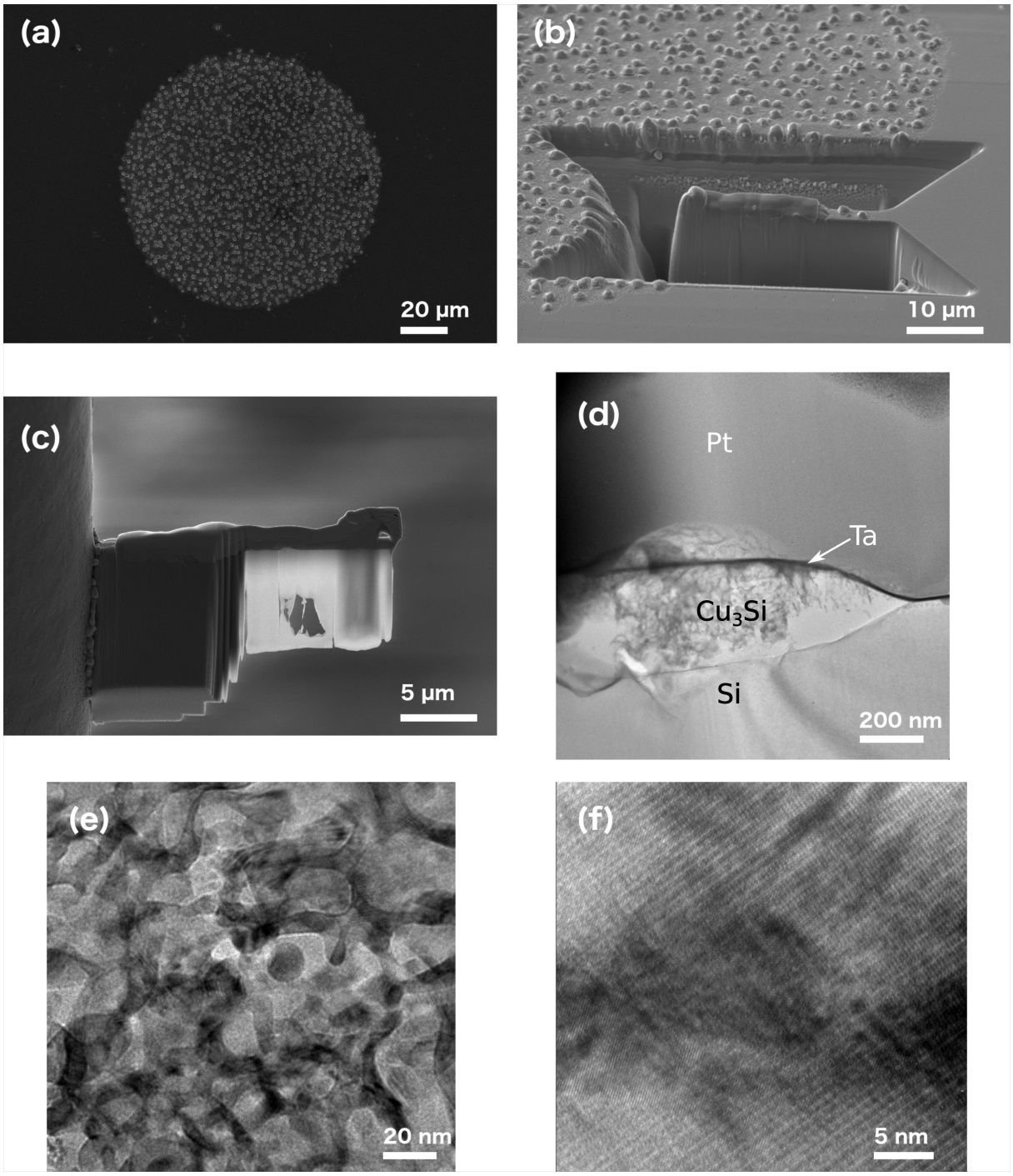

Figure 6-4: (a) Scanning Electron Microscopy (SEM) image of area of annealed film containing mounds, (b) SEM image of lamella cross-section prior to lift-out, (c) SEM image of final thinning

stages of lamella preparation, (d) Transmission Electron Microscopy (TEM) image of lamella containing copper silicide (Cu_3Si) precipitate within silicon (Si) substrate, (e) high magnification TEM image of Cu_3Si, and (f) high-resolution TEM image of Cu_3Si structure. (Notation in the images: Pt=platinum, Ta=tantalum, Si=silicon, Cu_3Si=copper silicide)

As can be seen from Figure 6-4 (c), it was challenging to thin the mounds within the lamella, as parts were porous containing no material, which led to a lot of potential mounds being lost in the thinning process. As can be noted from Figure 6-4 (d) the Ta layer does appear to be pushed from the Si surface upwards toward the top of the mound. It was challenging to capture the very defined trapezoidal shape of the root of the mound, due to the milling. But it can be noted that the mound forms well below the Si surface (~150 nm). It is clearly evident from Figure 6-4 (d) that the Ta layer has migrated from the Si surface to the top of the mound with the Cu diffusing with the Si in the bulk/centre. Figure 6-4 (e) and (f) show high magnification images of the Cu_3Si mound, noting the lattice information available, showing it was not completely damaged by the FIB thinning.

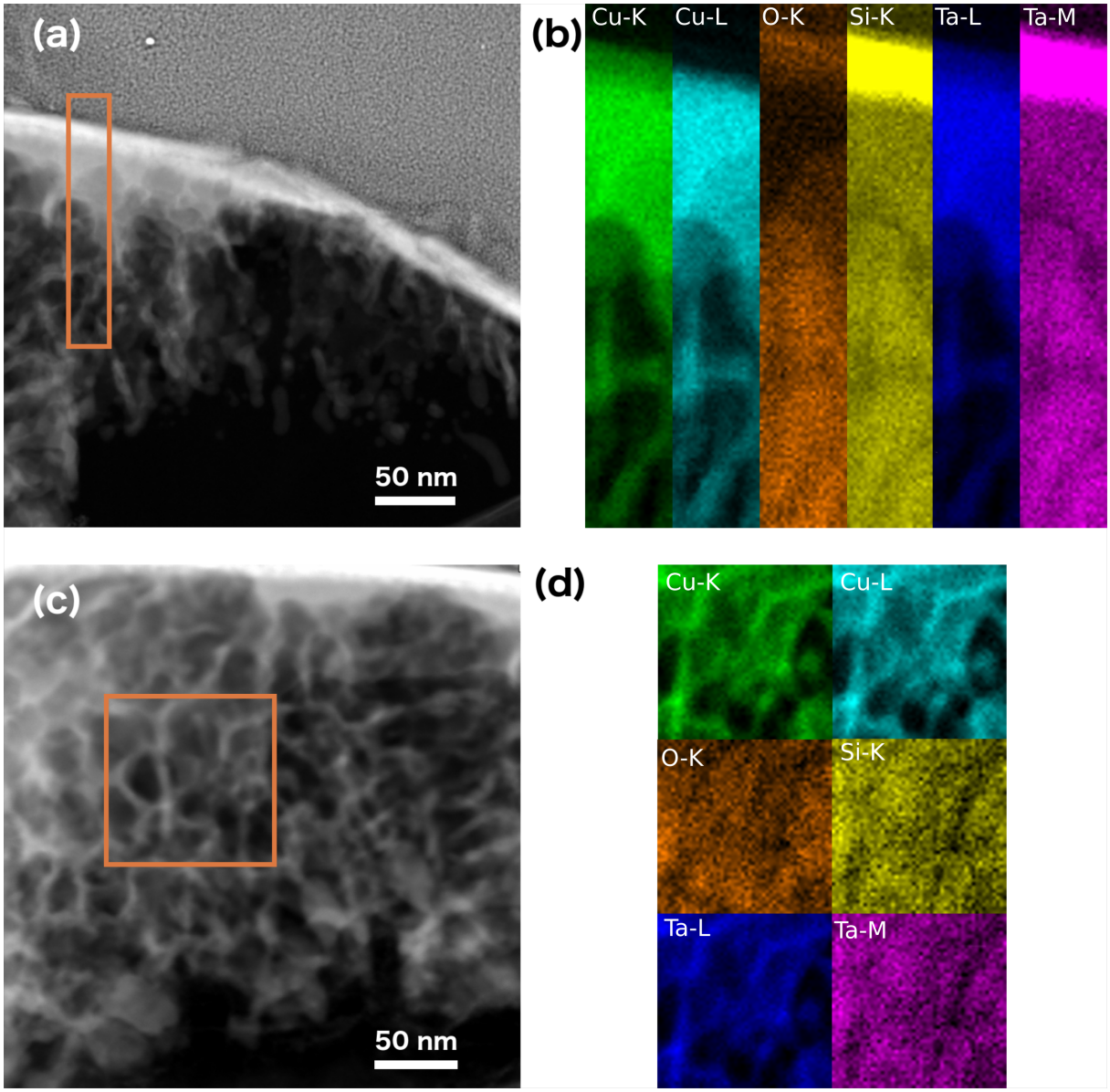

Figure 6-5: *(a) Scanning Transmission Electron Microscopy (STEM) image with highlighted area at the mound surface/platinum interface in which Energy-dispersive X-ray (EDX) map was obtained, (b) Extracted individual elemental maps from area highlighted in (a); (copper (Cu), tantalum (Ta), silicon (Si) and oxygen (O)), (c) STEM image with highlighted area of internal structure of the Cu_3Si precipitate in which EDX map was obtained, (d) Extracted individual elemental maps from area highlighted in (c); (Cu, Ta, Si and O).*

Using EDX mapping it was confirmed that the surface of the mound does contain a mixture of Ta and Si, shown in Figure 6-5 (a) and (b), while also showing the presence of both Cu and Si within the mound itself, shown in Figure 6-5 (c) and (d). It is challenging to determine whether it is singularly Ta or Si at the surface of the mound, as there is overlap of the Si-K and Ta-M lines, with energies 1.74 keV and 1.71 keV respectively. Also the Ta-L overlaps with the Cu-K line. The high contrast in the TEM image itself does suggest the possibility of Ta but the work

by Holloway *et al. and* Laurila *et al.* and many others suggests that it is a mixture of Ta and Si, $TaSi_2$, which tends to form at the surface. [28]-[30] This needs to be investigated further.

We wanted to observe in real time on the microscale what was happening to the Cu/Ta/Si within the mound when the temperature was increasing. This could be done by preparing a cross-sectional TEM lamella of the pristine non-annealed Cu film and placing it within an *in-situ* TEM heating holder and observing what happens to the Cu/Si formation and more importantly, how the Ta reacts under the differing temperature environments.

Although it has been investigated before, it has not been investigated in real-time. Observing what happens to the Ta barrier layer by *in-situ* TEM as the temperature increases could provide exciting new information about how the Cu diffuses through it at higher temperatures and why it is pushed or migrates to the surface forming $TaSi_2$. It is also interesting to observe the exact temperatures at which the Cu begins to diffuse or when the Ta breaks down. The RBS data obtained by Holloway *et al.* is discrete data with only a small number of temperatures observed due to the nature of the experimentation. [28], [29] The *in-situ* microscopy data that will be achieved from this technique will help establish a more continuous timeline of the progression of the Ta migration and Cu diffusion. We can be much more precise in the pinpointing of critical changes in the reaction.

6.3.2 Initial Lift-out Attempts

A method for preparing lamella for MEMS device mounting was established by Duchamp *et al.*[8] This method was attempted without the aid of a flip stage, meaning an alternative approach had to be adopted. This involved placing a 3-pillared Cu TEM Omniprobe grid flat on a carbon tab, with the pillars protruding out over the edge of the tab, so as not to contaminate or damage the pillars with the welded lamella, see Figure 6-6 (a).

A lamella lift-out was performed as previously described with the lamella lifted out and welded to the middle pillar of the TEM grid. Due to the different geometry of the grid, as it was laying flat, the lamella was welded perpendicular to the pillar as opposed to parallel, see Figure 6-6 (c) and (d). The lamella was welded using EBID-Pt and ion beam-induced deposition (IBID)-Pt and once secure, the micromanipulator weld was removed. The system was then vented and the grid rotated 90° by being placed in the traditional upright position. Once returned to the chamber of the SEM/FIB system, the micromanipulator was then welded to

the bottom right corner of the lamella, which was easily accessible due to perpendicular orientation of the lamella.

Prior to this a MEMS device had been placed securely on carbon tabs. The device is then tilted to the recommended tilt of 13°. The lamella is carefully placed over the desired MEMS device window, see Figure 6-6 (e) and (f). Unfortunately it was not possible to successfully place the lamella over the window and perform Pt deposition at 13° as the geometry of the GIS was not compatible. The amount of Pt deposited at this angle was not sufficient to secure the lamella to the device. The method outlined in this paper was attempted numerous times but the geometry of the Zeiss Auriga system did not work with the method outlined due to the lack of a flip stage. Due to this, a new novel method had to be developed and optimised to successfully mount lamella onto MEMS devices for *in-situ* experimentation within the TEM.

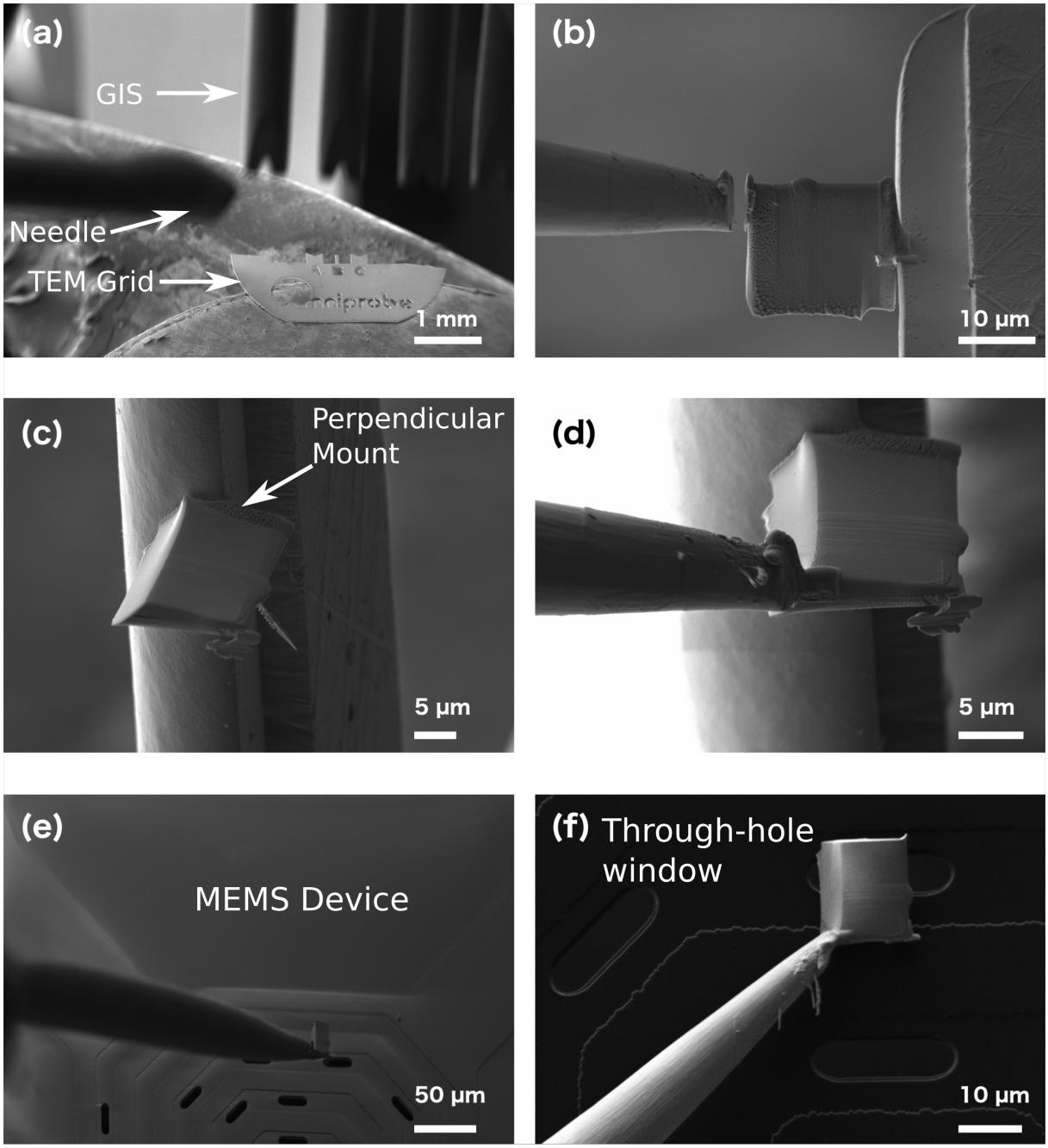

Figure 6-6: Scanning Electron Microscopy (SEM) image of (a) Transmission Electron Microscopy (TEM) grid placed flat on carbon tab, note geometry of the needle and Gas Injection System, (b) lamella placed perpendicular to pillar while flat on carbon tab, (c) lamella after needle has been removed and TEM grid has been placed in the upright position, (d) needle is welded to bottom right corner of lamella, (e) and (f) SEM and Focused Ion Beam (FIB) images respectively, of the attempt to place lamella securely over Micro-Electro-Mechanical Systems (MEMS) device window.

6.4 Protocol for Novel *In-Situ* Lamella Lift-out Technique for MEMS Device Mounting

The fabrication process begins by mounting a through-hole MEMS device on to a standard SEM stub using carbon adhesive. A separate reservoir of SEMGlu is also placed in the chamber away from the MEMS device. Before the lamella is placed on the area of interest, the MEMS device is pre-loaded with SEMGlu. A micromanipulator needle was dipped into the SEMGlu reservoir forming a teardrop-shaped portion at the tip of the needle. The needle is driven to the MEMS device and lowered until the SEMGlu makes contact with the SiN_x surface. The stage is slowly moved in the x- and y- direction to gently disperse the SEMGlu around the desired windows, Figure 6-7 (a). As can be seen from Figure 6-7 (a), dispersing the glue around several windows provides a greater number of locations for mounting the lamella, increasing the success rate of the lift-out.

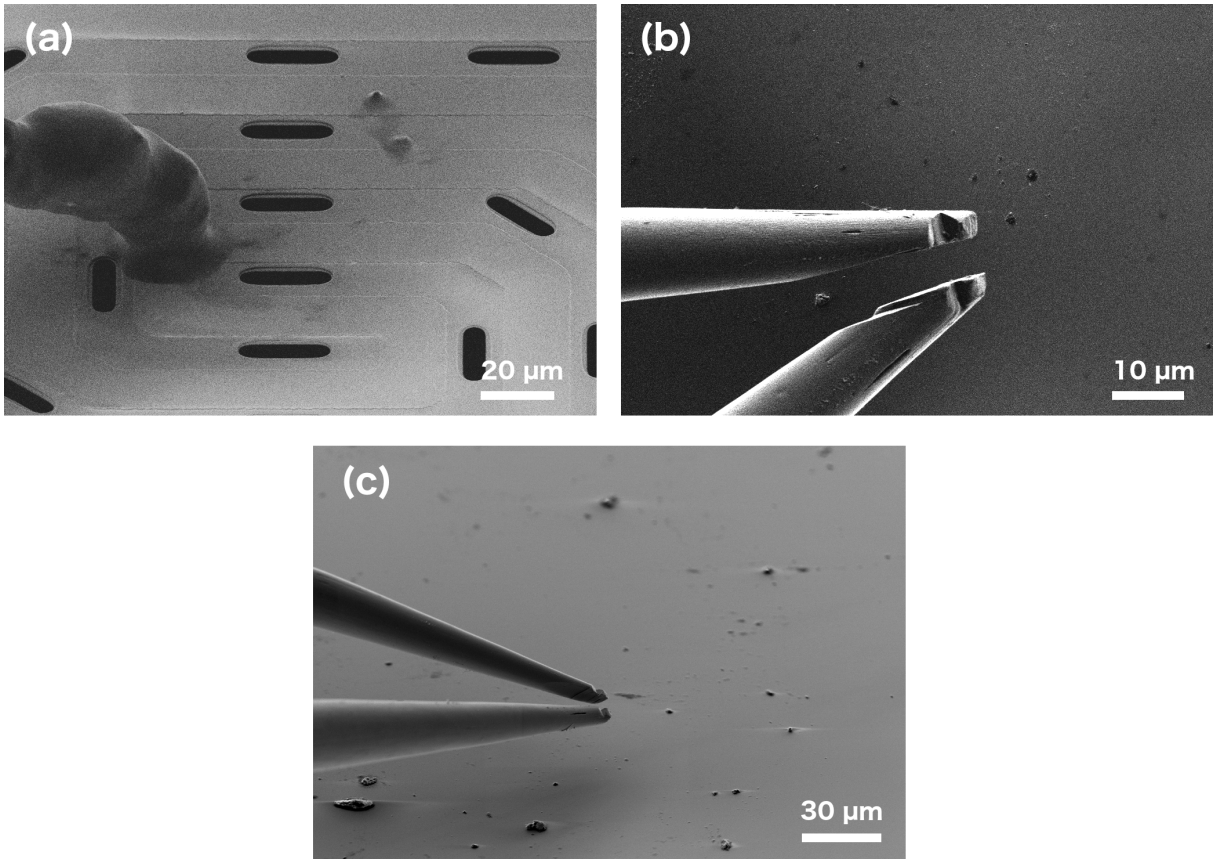

Figure 6-7: (a) Scanning Electron Microscopy (SEM) image showing the application of SEMGlu around the surrounding windows of the Micro-Electro-Mechanical Systems (MEMS) device using a micromanipulator needle, (b) and (c) Focused Ion Beam and SEM images respectively, showing the correct positioning of the microgrippers prior to lift-out.

After SEMGlu application the needle is replaced with the microgrippers and RoTip attachment, providing full 360° rotation. Figure 6-7 (b) and (c) show FIB and SEM images of the correct positioning of the grippers with respect to the lamella. For accurate positioning of the microgrippers during lift-out, they are tilted to 54°, parallel to the FIB, using the RoTip.

The bulk lamella preparation was based on the procedure as developed by Langford *et al.* and Giannuzzi *et al.*[4], [5] Table 1 outlines the parameters for sample preparation. Both EBID-Pt and IBID-Pt are deposited over an area of approximately 2 µm x 22 µm, using the standard Zeiss deposition mode setting, as shown in Figure 6-8 (a) and (b). The electron and ion beam voltages and currents used are 5 kV 3 nA and 30 kV 20 pA, respectively. A large area of deposited Pt is needed to fabricate an extra-long lamella, which provides a large cross section for the microgrippers to handle. Large trapezoid trenches are milled using the mill for depth setting on each side of the lamella. These trenches have approximate dimensions of top length: 40 µm, bottom length: 50 µm, trench width: 15 µm and trench depth: 15 µm, Figure 6-8 (c). The side trench (30 µm x 10 µm) is milled using the mill for depth setting with an approximate depth of 15 µm. All are performed at a tilt of 54°. The undercut (1 µm x 24 µm) is performed at a tilt of 7°. It is milled using the mill for time setting until the undercut is clearly visible, see Figure 6-8 (d). All milling was performed at an ion beam voltage of 30 kV 4 nA with the exception of the undercut, which was performed at 30 kV 2 nA.

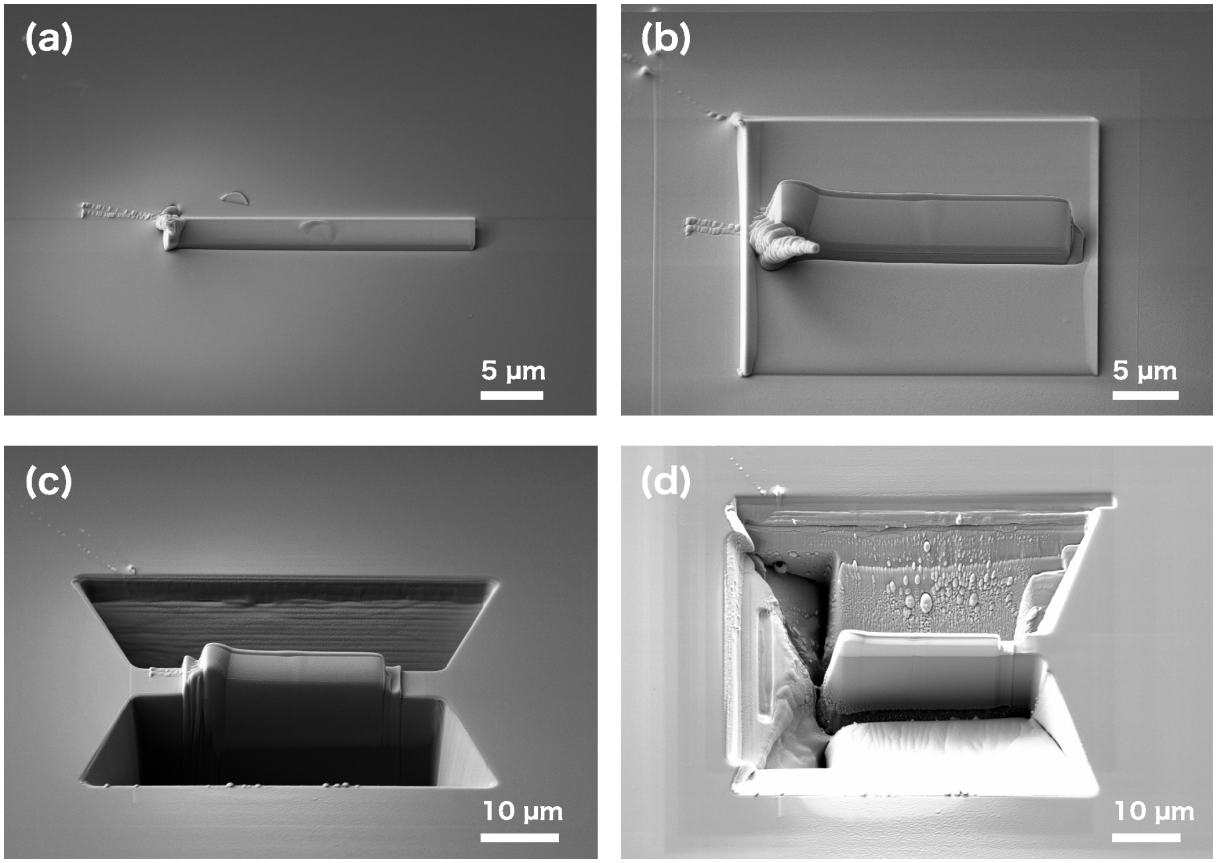

Figure 6-8: Scanning Electron Microscopy images showing overview of bulk preparation for lamella lift-out: Protective platinum (Pt) strip deposited by (a) electron beam-induced deposition and (b) ion beam-induced deposition, (c) two trapezoid trenches milled to a depth of approximately 15 µm, and (d) side trench and undercut viewed at 20° stage tilt.

Preparation Step	Primary Mode	SEM Voltage	E-Beam Current	FIB Voltage	I-Beam Current	Depth	Tilt	Details
MEMS device preparation	Imaging: e-beam	5 kV	3 nA				54°	Using the manipulator needle, SEMGlu is applied carefully around the windows of the MEMS device
EBID-Pt	Deposition: e-beam	5 kV	3 nA			0.5–1 µm	54°	Dimensions of 2 µm x 22 µm
IBID-Pt	Deposition: i-beam	5 kV	3 nA	30 kV	20 pA	1.5–2 µm	54°	Dimensions of 2 µm x 22 µm
Trenches	Milling: i-beam	5 kV	3 nA	30 kV	4 nA	15 µm	54°	Dimensions of 40 µm x 50 µm x 15 µm
Side Trench	Milling: i-beam	5 kV	3 nA	30 kV	4 nA	15 µm	54°	Dimensions of 30 µm x 10 µm
Undercut	Milling: i-beam	5 kV	3 nA	30 kV	2 nA	3–4 µm	7°	Dimensions of 1 µm x 24 µm
Final sidewall removal	Milling: i-beam	5 kV	3 nA	30 kV	2 nA	15 µm	54°	Dimensions of 2 µm x 2 µm
Lamella lift-out	Imaging: e-beam	5 kV	3 nA	30 kV	20 pA		54°	Sample lifted out using microgrippers
Thinning in RoTip microgrippers – Stage 1	Milling: i-beam	5 kV	3 nA	30 kV	240 pA		58 - 59°	Milled to a thickness of approximately 700–800 nm (4 – 5° tilt with respect to FIB)
Thinning in RoTip microgrippers – Stage 2	Milling: i-beam	5 kV	3 nA	15 kV	200 pA		58 - 59°	Milled to a thickness of approximately 200–300 nm (4 – 5° tilt with respect to FIB)
Thinning in RoTip microgrippers – Stage 3	Milling: i-beam	3/5 kV	3 nA	5 kV	20 pA		57 - 58°	Milled to a thickness of approximately 50–70 nm (3 – 4° tilt with respect to FIB)
Transfer of lamella to device	Imaging: e-beam/i-beam	3 kV	10 pA	30 kV	20 pA		0°	Lamella and MEMS device both at coincidence point. SEM voltage and beam current lowered to reduce charging and prevent any unnecessary curing of the SEMGlu prior to the final stages of the transfer.
Securing lamella over MEMS device window	Curing: e-beam	30 kV	6 nA				0°	Lamella successfully placed over the window. Thicker end of lamella over SEMGlu exposed to a high beam voltage for approximately 30 min to ensure a secure placement.

Table 1. Complete set of parameters for in-situ lamella preparation

After the bulk of the lamella is prepared, the microgrippers are inserted to lift the lamella away from the substrate to perform fine polishing. The rotating microgrippers are inserted near the bulk lamella. Before reaching the lamella, the grippers are opened to allow for the lamella to easily fit between them.

By switching between both SEM and FIB imaging, the lamella is placed between the microgrippers. Once in the correct position, the grippers are carefully closed until they begin to slide along the lamella, indicating that the lamella is secure, shown in Figure 6-9 (a). The remaining sidewall connected to the bulk is removed using a 30 kV 2 nA ion beam, Figure 6-9 (b).

Release of the lamella from the substrate is realised by a slight shift in the lamella position with respect to the bulk. The microgrippers are tightened to ensure the lamella is securely gripped and slowly lifted out of the trench. When the lamella is lifted clear of the bulk, the substrate is moved away from the lamella/gripper by lowering the stage, Figure 6-9 (c) and (d).

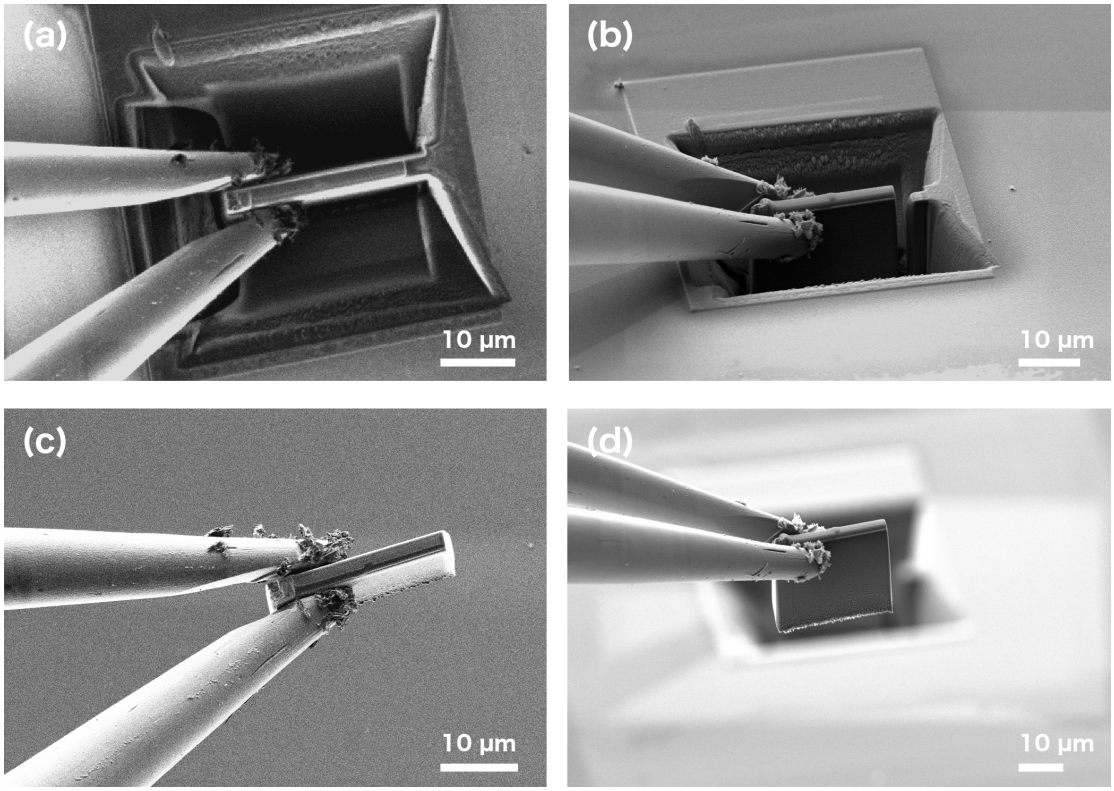

Figure 6-9: (a) Focused Ion Beam (FIB) image of lamella securely gripped, (b) Scanning Electron Microscopy (SEM) image of milling sidewall connecting to bulk sample, (c) and (d) FIB and SEM images respectively, of the positioning of lamella during the thinning process.

Fine thinning of the lamella is critical to enable high resolution imaging in the TEM. Using the rotating microgrippers, the lamella is tilted between 3°– 5° with respect to the FIB. The lamella is milled by adopting a wedge technique as developed by Schaffer *et al*.[6] This technique utilises a range of decreasing ion beam energies, from 30 kV 240 pA - 5 kV 20 pA, see Table 1., to ensure minimal damage and amorphisation of the sample, and also to minimise the loss of the Pt layer as the ion beam energies are reduced. As can be seen from Figure 6-10 (a) and (b), a staggered approach in relation to the top-down profile of the lamella is also employed. The staggered approach isolates parts of the lamella from the ion beam exposure during the thinning process, providing support to the thin regions. This also creates a ledge between the thinned area of interest of the lamella and the MEMS device. This approach elevates the area of interest while maintaining a parallel geometry between the MEMS device window and the lamella surface.

The thickness of the sample can be estimated by Secondary Electron (SE) imaging.[7] As the thickness of the specimen decreases, the SE yield increases. The net result is a significant brightness increase in the SE signal as the specimen thickness is reduced, highlighted region shown in Figure 6-10 (d). While imaging with a 5 kV accelerating voltage, the area of interest is thinned to approximately 70 - 100 nm thickness. The accelerating voltage is reduced to 3 kV and the lamella is polished further until it is approximately 50–70 nm thick, Figure 6-10 (d).

The use of the RoTip microgrippers provides many advantages over conventional methods.[8] The lamella can be milled and polished (front and back) without the obstruction of the MEMS device itself and removes potential damage to the area surrounding the MEMS device window. The microgrippers also ensure there is no sputtering or re-sputtering of Pt due to welding, as no Pt weld is needed.

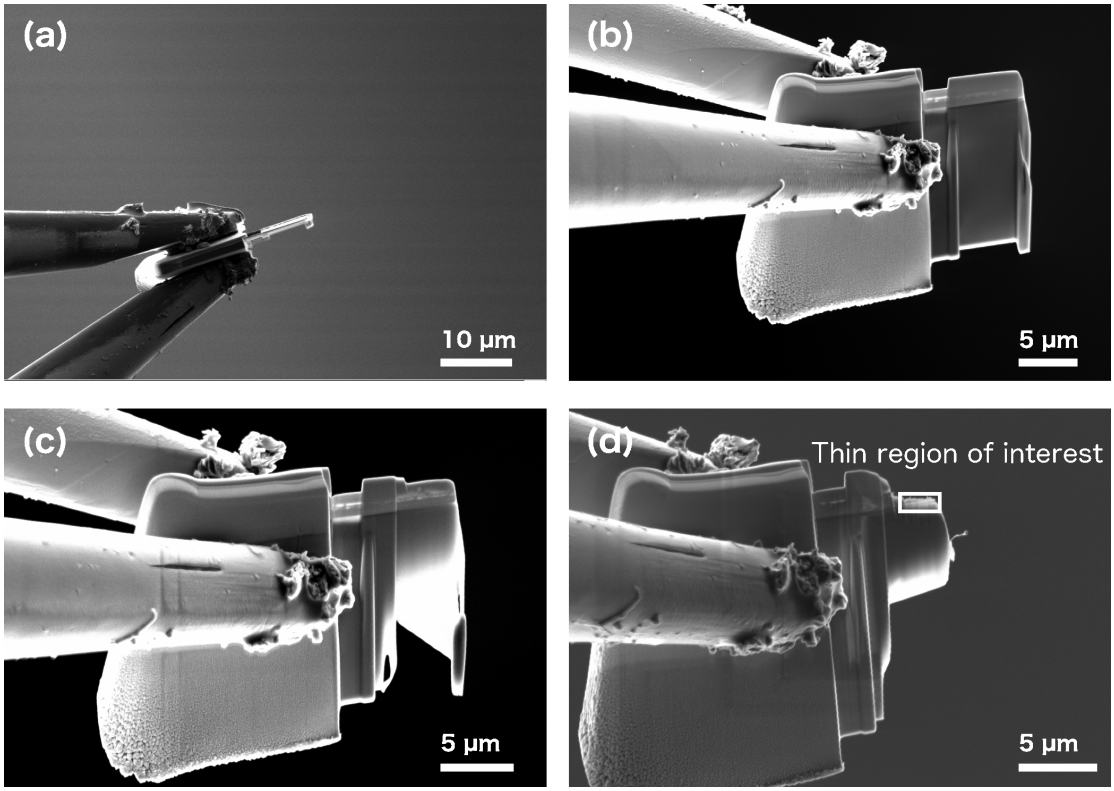

Figure 6-10: (a) and (b) Focused Ion Beam and Scanning Electron Microscopy (SEM) images respectively, showing the staggered approach to the thinning process, allowing the thicker segment to create a ledge between the thinned section of the lamella and the surface of the Micro-Electro-Mechanical Systems (MEMS) device, (c) and (d) SEM images of the final thinning stages 15 kV 200 pA and 5 kV 20 pA respectively with thin region of interest highlighted.

When the lamella is polished to a thickness of ~70 nm, the stage is tilted back to 0° and the MEMS device is brought to the SEM/FIB coincidence point of 5 mm, see Figure 6-11 (a) and (b). Having the stage at 0° tilt ensures the lamella will be in a more favourable position to lie flat over the window of the MEMS device, as the angle between the top of the lamella and the device surface is reduced below 90°, see Figure 6-11 (c) and (d).

To minimise charging between the sample, micrograpper and MEMS device, the SEM accelerating voltage is kept at 3 kV, and the electron beam current reduced to ~ 10 pA. Furthermore, this prevents the SEMGlu from curing/hardening before the lamella is placed over the window.

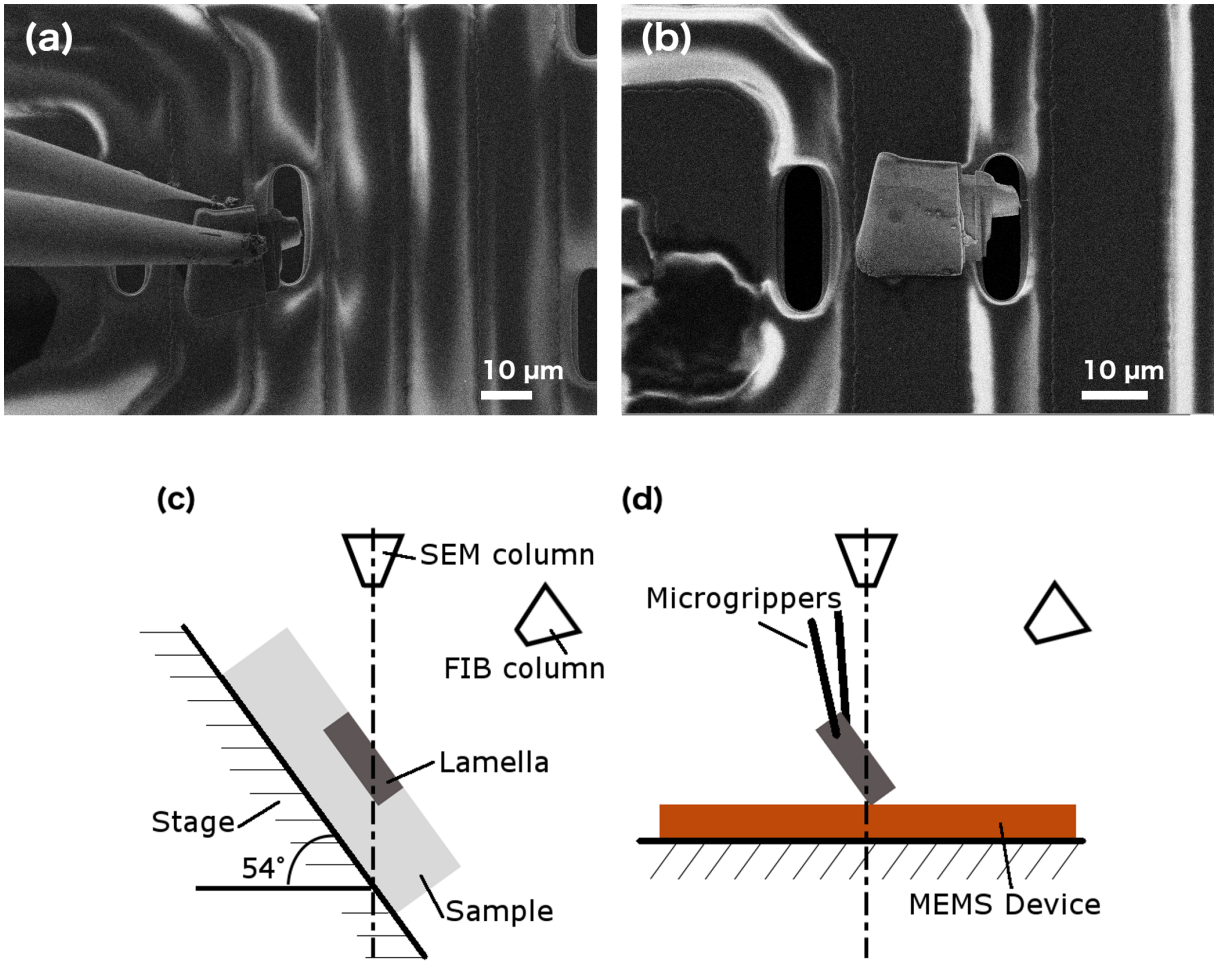

Figure 6-11: Scanning Electron Microscopy (SEM) images of (a) the transfer of the lamella from the grippers to the Micro-Electro-Mechanical Systems (MEMS) device, (b) the high-kV curing of the lamella and SEMGlu, (c) and (d) schematics of lift-out geometry.

The lamella is positioned above a window in the centre of the MEMS device and slowly lowered until the base of the lamella is in contact with the SiN_x surface. It is critical that the lamella is placed in the centre of the device where the temperature measurement is most accurate (the variation from the centre to the edge is ~ 15%).[26] The thick part of the lamella gripped by the microgrippers is placed directly over the SEMGlu, with the thinned area of interest extending over the adjacent through-hole window. To release the lamella, the microgrippers are slowly opened while simultaneously moving them in the x- and y- direction. In the closed position the microgrippers can be used to make minor adjustments to positioning of the lamella, which lies flat over the window. A short video clip demonstrating the complete lift-out and polishing procedure is available in the Appendix A3. The Appendix video was recorded on an FEI Quanta 200 3D.

To secure the lamella in the desired position, electron transparent section in field of view over window, the microgrippers are pressed against the thick side of the lamella away from the window. The SEMGlu beneath the thick section is cured by increasing the acceleration voltage to 30 kV with an electron beam current of ~ 6 nA with a field of view of approximately 100 μm^2 and exposing the area for 30 min. This process results in a securely bound lamella to the MEMS device, providing a robust platform for *in-situ* TEM analysis.

Figure 6-12 shows TEM images of the thinned region extending over the electron transparent window, after sample transfer to the *in-situ* holder and TEM. From a comparison between the SEM image in Figure 6-11 (b) and the TEM image in Figure 6-12 (a), the lamella remains in the desired position with no movement evident. This demonstrates the mechanical robustness of the SEMGlu as well as the vacuum-compatibility within the TEM.

Figure 6-12 (b) shows the high-resolution TEM image of the Si (110) substrate recorded from the thin region of the lamella. From the TEM image and fast Fourier Transform (FFT) it is clear that the sample remains crystalline with no apparent damage after ion-beam polishing. These results are what we expect from lamellae prepared by traditional *in-situ* lift-out techniques, Figure 6-12 (d). It is evident that lamellae prepared using this novel technique maintain the same quality while removing the risk of Pt re-deposition as well as the risk of damaging the MEMS device through milling.

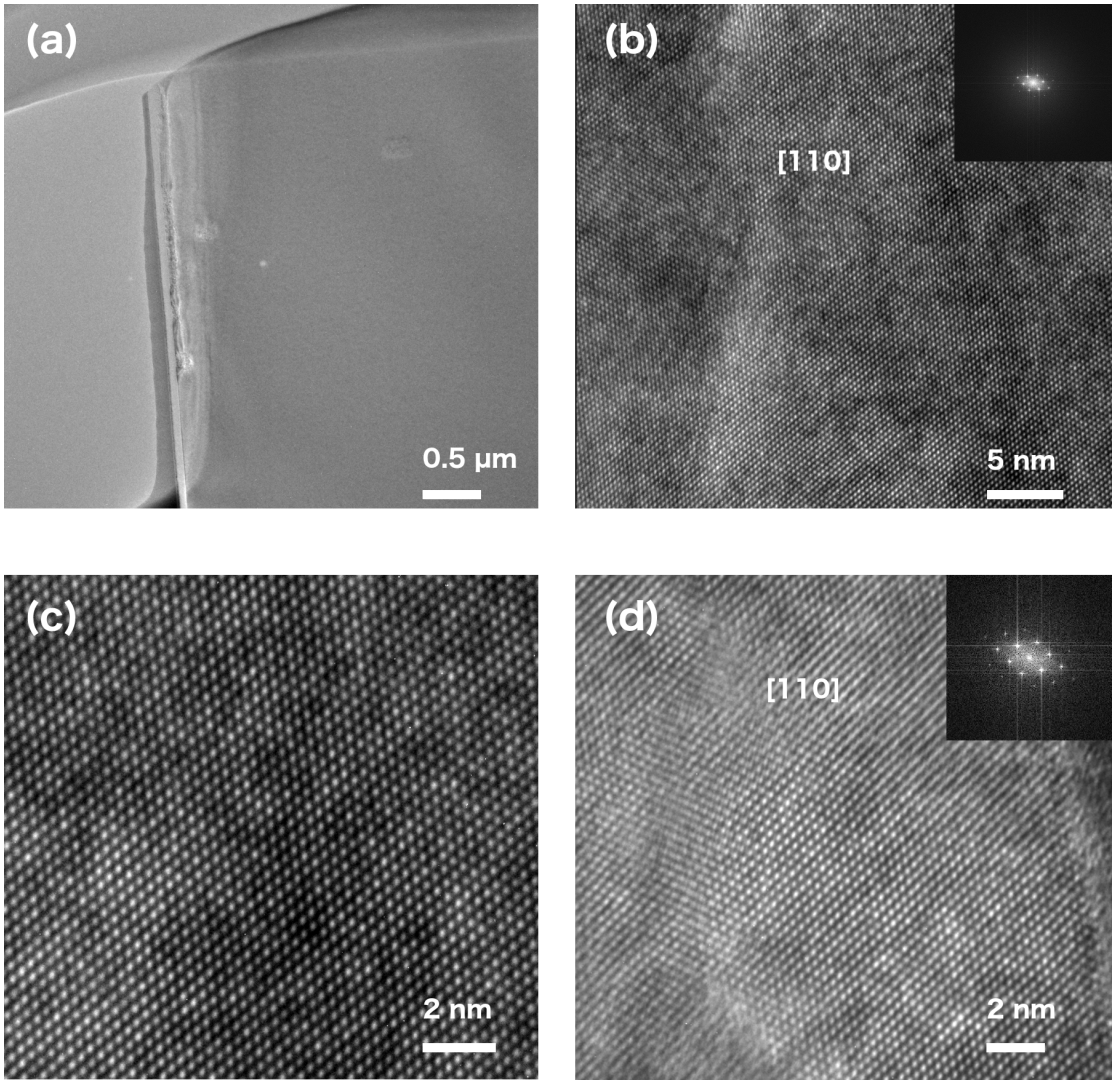

Figure 6-12: (a) Transmission Electron Microscopy (TEM) image of lamella remains in desired position over through-hole window, (b) High-resolution TEM (HRTEM) of silicon (Si) with fast Fourier Transform (FFT) inset, (c) high magnification image of Si and (d) reference HRTEM image of Si substrate prepared using traditional in-situ lift-out technique with platinum (Pt) weld with FFT inset.

6.5 First Applications

To date, three Cu film lamellae have been prepared as well as two Si only lamellae for purposes of developing the technique. Below are the initial results from these Cu lamellae, further heating experiments need to be performed to fully characterise the formation of the precipitates and the behaviour of the Ta liner in real time.

The Cu annealed film lamella cross-section was placed in a double tilt heating DENSsolutions Lightning holder. This lamella was imaged in STEM mode using a 0.5 µm aperture. The lamella

was not at the ideal thickness compared to previous prepared lamellae so it was easier to assess and observe the Ta layer in STEM mode. This lamella was chosen for investigation due to the Cu_3Si precipitate that formed *in-situ* during the annealing procedure. As this process is sporadic and not uniform throughout the film, the likelihood of a precipitate forming and rupturing through the Cu film and Si substrate of a lamella is low. Hence this particular lamella is of a special interest.

The temperature applied to the lamella by the MEMS technology is ramped from room temperature to 50°C, with a 50°C increase until 250°C, at which point the increments are decreased to every 25°C.

Up to 250°C the sample remains similar. Figure 6-13 (a) captured at 250°C shows a slight difference within the Cu grain structure. There appears to be a possible thinning of the Cu structure. Increasing the temperature to 300°C shows a gradual thinning of the Cu film as can be seen in Figure 6-13 (b) and (c), starting from the small area indicated in Figure 6-13 (a).

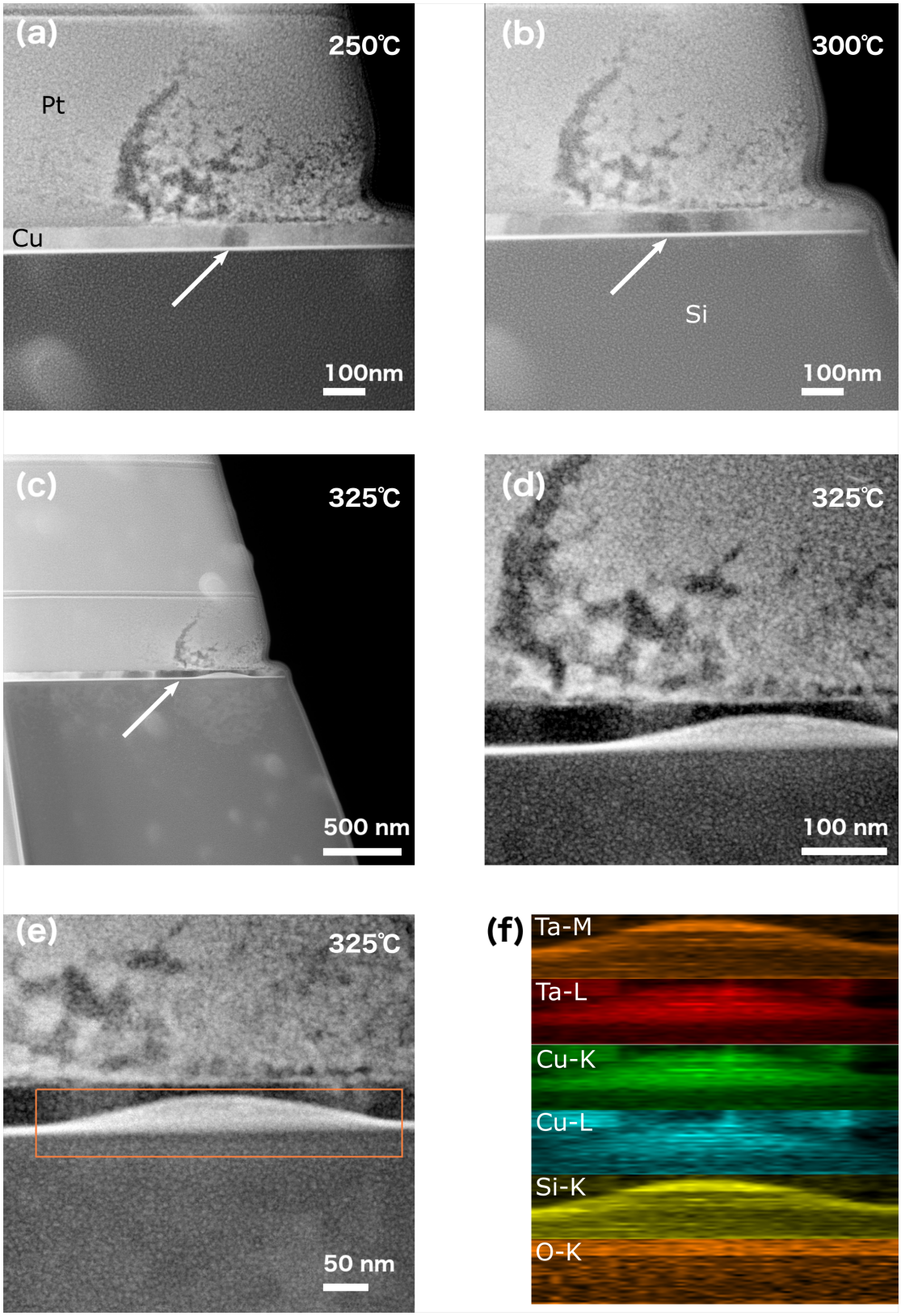

Figure 6-13: (a) Scanning Transmission Electron Microscopy (STEM) image of copper (Cu) film at a temperature of 250°C, (b) STEM image of Cu film at a temperature of 300°C, (c) STEM image of Cu film at 325°C at low magnification, (d) STEM image of Cu film at 325°C at high magnification, (e) Area in which Energy-dispersive X-ray (EDX) map was obtained of mound at temperature of 325°C and (f) extracted individual elemental maps of Cu, tantalum (Ta), silicon (Si) and oxygen (O).

As shown in the video attached in Appendix A4, as the temperature was increased to 325°C, formation of the mound/Cu_3Si precipitate within the Cu film can be observed immediately, starting from the Ta layer. At this point the temperature was left constant at 325°C. At this stage, EDX was acquired of the sample during the heating process, area of interest highlighted in Figure 6-13 (e). This initial EDX data showed movement of the Ta, ballooning to the top of the mound. This is observed by the presence of the Ta-M line along the top of the mound, shown in the elemental maps in Figure 6-13 (f). However, as mentioned earlier, there is an overlap with the Si-K and Ta-M, which is very difficult to decipher. The EDX map also displays the presence of both Si and Cu within the mound, further confirming through qualitative analysis what is expected from the literature. Throughout there is a presence of Pt, this can be due to the fact that the lamella was slightly thicker than previous attempts and the milling angle may have been too aggressive. This would cause a lot of Pt to potentially be pushed further into the sample. However, the Pt-L also overlaps with the Ga-K line, which also could be contributing to intensity profile. There is a clear mound forming within the Cu layer. The Si substrate is also experiencing some potential structural changes. When the temperature was further increased to 335°C, see Figure 6-14 (a), there seemed to be a slight increase in the height of the mound and amorphisation of the Si substrate. There is a non-uniformity in the scan which is visible in Figure 6-13 (f), which should not be misconstrued for an obvious break in the mound/Ta barrier layer. Unfortunately, a continuous scan could not be obtained.

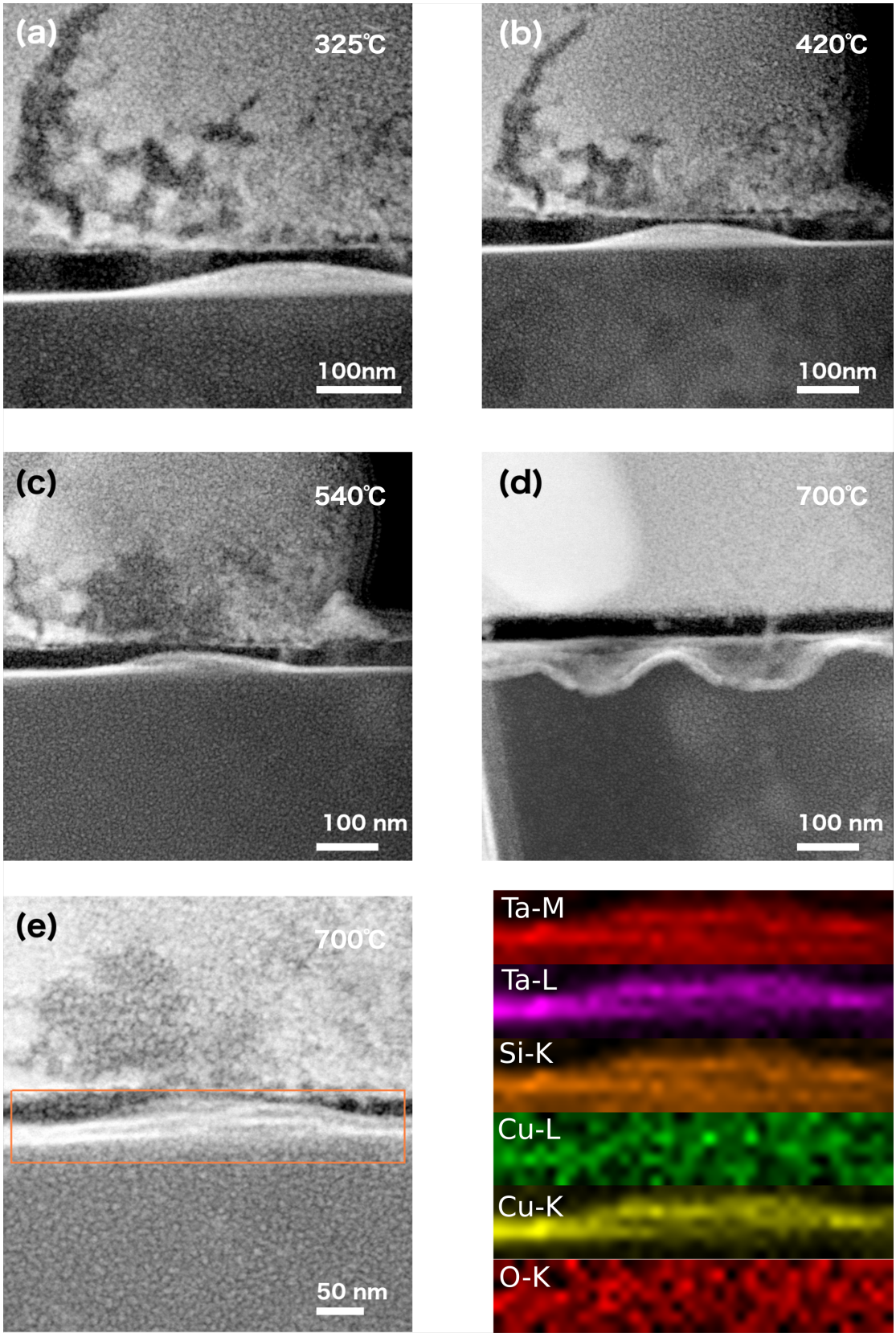

Figure 6-14: (a) Scanning Transmission Electron Microscopy (STEM) image of copper (Cu) film at a temperature of 325°C, (b) STEM image of Cu film at a temperature of 420°C, (c) STEM image of Cu film at 540°C, (d) STEM image of Cu film at 700°C and (e) Area in which Energy-dispersive X-ray (EDX) map of mound was obtained at a temperature of 23°C after

experiencing temperatures of up to 700°C and (f) extracted individual elemental maps Cu, tantalum (Ta), silicon (Si) and oxygen (O).

At ~420°C, Figure 6-14 (b), changes in both the Pt layer and Si substrate were observed. This progressed when temperatures increased to 450°C, which is visible from the video in Appendix A4 of this particular increase in temperature. There is a slow and steady change in possibly the thickness of the Si substrate.

At ~540°C, Figure 6-14 (c) we start to see a change within the mound formed in the Cu film. It is very clear from this image that the remainder of the Cu film surrounding the mound is beginning to possibly delaminate or thin.

The lamella was heated to a final temperature of 700°C. There was significant change within the Cu film, the Si substrate and the precipitate formed. The behaviour and microstructure of the Ta barrier layer was extremely challenging to interpret due to the thickness of the lamella.

At these higher temperatures at ~600-650°C, the Cu_3Si precipitate begins to experience degrading/thinning or possibly mixing of the Cu and Si. Upon closer inspection of the remaining parts of the lamella, more mounds were discovered, this time rupturing internally within the Si substrate, see Figure 6-14 (d). As EDX could not be performed at such high temperatures, the temperature was reduced back down to 23°C and an EDX map was acquired from the area highlighted in Figure 6-14 (e).

From the elemental maps extracted from the EDX data in Figure 6-14 (f), the Cu signal does not appear as strong within the mound. This could be that at these high temperatures the Cu is degrading and being sputtered from the sample. There is still a strong presence of Ta/Si at surface of the precipitate. It is challenging to determine whether the Ta barrier has been structurally compromised due to this annealing process and this is an aspect of the project, which needs further comprehensive investigating.

6.6 Conclusions

It was observed that micron-sized mounds formed on the surface of annealed Cu films after exposure to temperatures of 300 - 400°C. These mounds were successfully cross-sectioned using FIB milling and it was observed that the internal structure, a trapezoidal shape bounded by the Si (111) and Si (100) planes, was similar to that reported in the literature. To confirm whether the mounds formed were an intermixing of Cu and Si forming Cu_3Si, a lamella cross-section for TEM was successfully prepared. HRTEM imaging and EDX analysis were performed, confirming the intermixing of the film and substrate along with the migration of the barrier layer to the mound surface.

An alternative *in-situ* lift-out procedure using FIB milling was developed and optimised for the preparation of lamellae for *in-situ* annealing in the TEM and beyond. This technique combines for the first time the use of rotating microgrippers for lift-out and thinning, and a unique adhesive substance, SEMGlu, during the lift-out procedure, instead of the traditional micromanipulator needle and Pt weld. Lamellae were successfully mounted onto a MEMS device for *in-situ* TEM annealing experiments without damage to the MEMS.

It has been shown that this novel method ensures the ability to employ the wedge technique during the thinning procedure due to the rotation of the microgrippers. The use of the microgrippers also ensured no Pt deposition onto the sample and reduced the risk of damaging the MEMS device during thinning. HRTEM imaging of the polished lamella verifies that this method can produce high quality lamellae comparable with regular *in-situ* lift-out procedures. *In-situ* annealing of the non-annealed Cu film lamella also showed in real-time the forming of the Cu_3Si precipitate and the pushing of the Ta liner upwards towards the mound surface along with the subsequent rupturing of the precipitate within the Si substrate.

Not only is the method successful for *in-situ* annealing, it can also be used and adapted for a number of *in-situ* applications, including fluid and gas phase analysis as well as *in-situ* electrical experimentation and also traditional lamella preparation.

6.7 Bibliography

[1] M. Canavan, D. Daly, A. Rummel, E. K. McCarthy, C. McAuley, and V. Nicolosi, "Novel in-situ lamella fabrication technique for in-situ TEM," *Ultramicroscopy*, vol. 190, pp. 21–29, 2018.

[2] R. M. Langford and M. Rogers, "In situ lift-out: Steps to improve yield and a comparison with other FIB TEM sample preparation techniques," *Micron*, vol. 39, no. 8, pp. 1325–1330, 2008.

[3] D. Tomus and H. P. Ng, "In situ lift-out dedicated techniques using FIB–SEM system for TEM specimen preparation," *Micron*, vol. 44, pp. 115–119, 2013.

[4] R. M. Langford and A. K. Petford-Long, "Preparation of transmission electron microscopy cross-section specimens using focused ion beam milling," *J. Vac. Sci. Technol. A*, vol. 19, no. 5, pp. 2186-2193, 2001.

[5] L. A. Giannuzzi, J. L. Drown, S. R. Brown, R. B. Irwin, and F. A. Stevie, "Focused Ion Beam Milling and Micromanipulation Lift-Out for Site Specific Cross-Section Tem Specimen Preparation," *MRS Proc.*, vol. 480, pp. 19–27, 1997.

[6] M. Schaffer, B. Schaffer, and Q. Ramasse, "Sample preparation for atomic-resolution STEM at low voltages by FIB," *Ultramicroscopy*, vol. 114, pp. 62–71, 2012.

[7] R. M. Langford and C. Clinton, "In situ lift-out using a FIB-SEM system," *Micron*, vol. 35, no. 7, pp. 607–611, 2004.

[8] M. Duchamp, Q. Xu, and R. E. Dunin-Borkowski, "Convenient Preparation of High-Quality Specimens for Annealing Experiments in the Transmission Electron Microscope," *Microsc Microanal*, vol. 20, no. 6, pp. 1638–1645, 2014.

[9] P. J. Ferreira, K. Mitsuishi, and E. A. Stach, "*In Situ* Transmission Electron Microscopy," *MRS Bull.*, vol. 33, no. 2, pp. 1–8, 2008.

[10] R. Dannenberg, E. Stach, J. R. Groza, and B. J. Dresser, "TEM annealing study of normal grain growth in silver thin films," *Thin Solid Films*, vol. 379, no. 1, pp. 133–138, 2000.

[11] R. J. Kamaladasa, A. A. Sharma, Y.-T. Lai, W. Chen, P. A. Salvador, J. A. Bain, M. Skowronski, and Y. N. Picard, "In Situ TEM Imaging of Defect Dynamics under Electrical Bias in Resistive Switching Rutile-TiO_2," *Microsc Microanal*, pp. 1–14, 2015.

[12] K. Tai, Y. Liu, and S. J. Dillon, "In Situ Cryogenic Transmission Electron Microscopy for Characterizing the Evolution of Solidifying Water Ice in Colloidal Systems," *Microsc Microanal*, vol. 20, no. 2, pp. 330–337, 2014.

[13] H. Zheng, S. A. Claridge, A. M. Minor, A. P. Alivisatos, and U. Dahmen, “Nanocrystal Diffusion in a Liquid Thin Film Observed by in Situ Transmission Electron Microscopy,” *Nano Lett.*, vol. 9, no. 6, pp. 2460–2465, 2009.

[14] M. J. Williamson, R. M. Tromp, P. M. Vereecken, R. Hull, and F. M. Ross, “Dynamic microscopy of nanoscale cluster growth at the solid–liquid interface,” *Nat Mater*, vol. 2, no. 8, pp. 532–536, 2003.

[15] J. F. Creemer, S. Helveg, G. H. Hoveling, S. Ullmann, A. M. Molenbroek, P. M. Sarro, and H. W. Zandbergen, “Atomic-scale electron microscopy at ambient pressure,” *Ultramicroscopy*, vol. 108, no. 9, pp. 993–998, 2008.

[16] M. Legros, D. S. Gianola, and K. J. Hemker, “In situ TEM observations of fast grain-boundary motion in stressed nanocrystalline aluminum films,” *Acta Materialia*, vol. 56, no. 14, pp. 3380–3393, 2008.

[17] N. Li, H. Wang, A. Misra, and J. Wang, “In situ Nanoindentation Study of Plastic Co-deformation in Al-TiN Nanocomposites,” *Sci. Rep.*, vol. 4, no. 1, pp. 6538–7, 2014.

[18] J. Y. Huang, H. Choi, D. Takahashi, K. Kono, and E. Kim, “In Situ Observation of the Electrochemical Lithiation of a Single SnO_2 Nanowire Electrode,” *Science*, vol. 330, no. 6010, pp. 1512–1515, 2010.

[19] H. Saka, T. Kamino, S. Arai, and K. Sasaki, “In Situ Heating Transmission Electron Microscopy,” *MRS Bull.*, vol. 33, no. 2, pp. 1–8, 2008.

[20] M. Miyasaka, K. Makihira, T. Asano, E. Polychroniadis, and J. Stoemenos, “In situ observation of nickel metal-induced lateral crystallization of amorphous silicon thin films,” *Appl. Phys. Lett.*, vol. 80, no. 6, pp. 944–946, 2002.

[21] A. Rath, R. R. Juluri, and P. V. Satyam, “Real time nanoscale structural evaluation of gold structures on Si (100) surface using in-situ transmission electron microscopy,” *J. Appl. Phys.*, vol. 115, no. 18, pp. 184303–7, 2014.

[22] R. Dannenberg, E. A. Stach, J. R. Groza, and B. J. Dresser, “In-situ TEM observations of abnormal grain growth, coarsening, and substrate de-wetting in nanocrystalline Ag thin films,” *Thin Solid Films*, vol. 370, no. 1, pp. 54–62, 2000.

[23] L. F. Allard, W. C. Bigelow, M. Jose-Yacaman, D. P. Nackashi, J. Damiano, and S. E. Mick, “A new MEMS-based system for ultra-high-resolution imaging at elevated temperatures,” *Microsc. Res. Tech.*, vol. 72, no. 3, pp. 208–215, 2009.

[24] N. P. Young, M. A. van Huis, H. W. Zandbergen, H. Xu, and A. I. Kirkland, “Transformations of gold nanoparticles investigated using variable temperature high-resolution transmission electron microscopy,” *Ultramicroscopy*, vol. 110, no. 5, pp.

506–516, 2010.

[25] M. A. van Huis, N. P. Young, G. Pandraud, J. F. Creemer, D. Vanmaekelbergh, A. I. Kirkland, and H. W. Zandbergen, “Atomic Imaging of Phase Transitions and Morphology Transformations in Nanocrystals,” *Adv. Mater.*, vol. 21, no. 48, pp. 4992–4995, 2009.

[26] L. Mele, F. Santagata, E. Iervolino, M. Mihailovic, T. Rossi, A. T. Tran, H. Schellevis, J. F. Creemer, and P. M. Sarro, “A molybdenum MEMS microhotplate for high-temperature operation,” *Sensors & Actuators: A. Physical*, vol. 188, pp. 173–180, 2012.

[27] A. Rummel, G. Frayne, A. J. Smith, and S. Kleindiek, “Achieving Fast and Reliable TEM-Sample Lift-out and Transfer Using Novel Materials and Novel in-situ Tools,” *Prakt. Metallogr.*, pp. 1–5, 2009.

[28] K. Holloway and P. M. Fryer, “Tantalum as a diffusion barrier between copper and silicon,” *Appl. Phys. Lett.*, vol. 57, no. 17, pp. 1736–1738, 1990.

[29] K. Holloway, P. M. Fryer, C. Cabral Jr., J. M. E. Harper, P. J. Bailey, and K. H. Kelleher, “Tantalum as a diffusion barrier between copper and silicon: Failure mechanism and effect of nitrogen additions,” *J. Appl. Phys.*, vol. 71, no. 11, pp. 5433–5444, 1992.

[30] T. Laurila, K. Zeng, J. K. Kivilahti, J. Molarius, and I. Suni, “Failure mechanism of Ta diffusion barrier between Cu and Si,” *J. Appl. Phys.*, vol. 88, no. 6, pp. 3377–3384, 2000.

[31] J. S. Chen and J. L. Wang, “Diffusion Barrier Properties of Sputtered TiB_2 Between Cu and Si ,” *J. Electrochem. Soc.*, vol. 147, no. 5, pp. 1940–1944, 2000.

[32] L. A. Clevenger, N. A. Bojarczuk, K. Holloway, J. M. E. Harper, C. Cabral Jr., R. G. Schad, F. Cardone, and L. Stolt, “Comparison of high vacuum and ultra-high-vacuum tantalum diffusion barrier performance against copper penetration,” *J. Appl. Phys.*, vol. 73, no. 1, pp. 300–308, 1993.

[33] C.Y. Yang and J. S. Chen, “Investigation of Copper Agglomeration at Elevated Temperatures,” *J. Electrochem. Soc.*, vol. 150, no. 12, pp. G826–G830, 2003.

[34] C.Y. Yang, J. S. Jeng, and J. S. Chen, “Grain growth, agglomeration and interfacial reaction of copper interconnects,” *Thin Solid Films*, pp. 398–402, 2002.

[35] C. V. Thompson, “Solid-State Dewetting of Thin Films,” *Annu. Rev. Mater. Res.*, vol. 42, no. 1, pp. 399–434, 2012.

[36] H. Kim, T. Koseki, T. Ohba, T. Ohta, Y. Kojima, H. Sato, and Y. Shimogaki, “Cu Wettability and Diffusion Barrier Property of Ru Thin Film for Cu Metallization,” *J.*

Electrochem. Soc., vol. 152, no. 8, pp. G594–G600, 2005.

[37] J. K. Solberg, "The Crystal Structure of Cu3Si Precipitates in Silicon ," *Acta Cryst.*, vol. A, no. 34, pp. 684–698, 1978.

[38] S. J. Jung, T. Lutz, A. P. Bell, E. K. McCarthy, and J. J. Boland, "Free-Standing, Single-Crystal Cu 3Si Nanowires," *Crystal Growth & Design*, vol. 12, no. 6, pp. 3076–3081, 2012.

7. Conclusions and Future Work

Overall this thesis work has shown optimised lamella preparation techniques for high-resolution Scanning/Transmission Electron Microscopy (S/TEM) imaging and analysis of copper (Cu) films and nanowires (NWs). Multiple lamella preparation methods such as plan-view, site-specific and Micro-Electro-Mechanical-Systems (MEMS) device mounted have been developed and optimised for film surface imaging, cross-sectional nanowire imaging and *in-situ* annealing respectively.

Chapter 4 discussed the successful optimisation of the cross-sectional lamella preparation technique for 40 nm Cu film on SiO_2. This was done through an iterative process of combining low kV milling, an extra Pt protective layer along with an exaggerated milling incidence angle, a method developed by Schaffer *et al.* also known as the wedge technique. Successful S/TEM imaging displayed a mixture of grain boundaries including twins and grooved boundaries. Grains also varied between columnar (running depth of film) and not occupying the entirety of the film depth. As the cross-sectional preparation technique improved and thinner lamellae were being produced, it was noted that damage was experienced by the Cu film under the electron beam. This damage was recorded and it was concluded that the evaporated Cu was of poor quality containing grains of non-uniform crystallinity and amorphisation. The successful preparation of cross-sectional lamella of the 40 nm Cu film on SiO_2 was of extreme importance to the project. Both STM and C-AFM proved extremely difficult to obtain any information due to the roughness and oxidation of the film surface. Cross-sectional TEM provided data about the grain and grain boundary structure, which was otherwise not obtainable for this particular film. Finally an alternative 50 nm Cu film on a 7 nm Ta which was sputtered as opposed to evaporated was analysed. This sample proved to be of a better quality and the optimised lamella preparation technique produced high-resolution S/TEM imaging with stable Cu films under the electron beam at 300 kV.

Chapter 5 outlines the aberration-corrected STEM imaging and analysis obtained due to the lamella produced from the cross-sectional preparation. From this it was noted that the film contained complex grain boundaries that were both tilted and twisted but predominantly tilted. The grains were mostly “bamboo” or columnar in nature with approximate widths of 40

– 50 nm. Similar to the Cu film on SiO_2 the 50 nm Cu film on 7 nm Ta contained twin boundaries with particular interest on twin boundaries running parallel to the Cu film. These twin boundaries were discovered to be slightly incoherent with a misalignment of between 1-2°. From complementary STM data, this misalignment could potentially confirm the out-of-plane rotation observed. Using the zero-loss peak obtained by EELS analysis, the absolute thickness of the Cu film was calculated and found to be ~30 nm.

This chapter also detailed the various plan-view lamella preparation techniques successfully executed to obtain high-resolution S/TEM imaging of the 50 nm Cu film surface. The three techniques detailed were side-view mounted, HF dip plan-view and side-view mounted with XeF_2 etch. Each technique successfully produced lamellae suitable for S/TEM imaging and analysis. The most successful technique however, was the side-view mounted with XeF_2. The preparation of plan-view lamellae enabled the analysis of the Cu grain structure through Transmission Kikuchi Diffraction analysis, obtaining data about the percentage of HAGB and LAGB as well as grain size statistics. It was also noted that the dominant grain orientation of the Cu film surface is [111]. This corroborates with the STM results.

Finally fulfilling the ultimate objective of this work, site-specific lamellae were prepared of 100 nm Cu nanowires (NWs) with a depth of ~160 nm. High resolution S/TEM imaging of the Cu NWs was achieved, which is difficult to achieve with the width of the NW and the likelihood of only partially milling the correct NW during the final thinning stages. Similar grain boundary features were discovered within these NWs including twin boundaries. Grains rarely ran the depth of the film with a mixture of grain size and shape evident throughout. Site-specific lamella preparation is extremely important for this type of work and in the future it is vital that specific NWs can be targeted and data from a specific NW can be acquired using a range of different, complementary techniques. There is a high demand for such a correlative approach, integrating several imaging and analysis techniques.

Chapter 6 details the conception and development of a novel *in-situ* lamella fabrication technique for *in-situ* TEM annealing experimentation. This technique combines for the first time the use of rotating microgrippers for lift-out and thinning, and a unique adhesive substance, SEMGlu, during the lift-out procedure, instead of the traditional micromanipulator needle and Pt weld. Lamellae were successfully mounted onto a MEMS device for *in-situ* TEM annealing experiments without damage to the MEMS.

It can be concluded that this novel method ensures the ability to employ the wedge technique during the thinning procedure due to the rotation of the microgrippers. The use of the microgrippers also ensured no Pt deposition onto the sample and reduced the risk of damaging the MEMS device during thinning. HRTEM imaging of the polished lamella verifies that this method can produce high quality lamellae comparable with regular *in-situ* lift-out procedures.

In-situ annealing of the non-annealed Cu film lamella enabled real-time observation of the formation of the Cu_3Si precipitate along with the lifting of the Ta barrier above the mound surface and the subsequent rupturing of the precipitate within the Si substrate.

This technique shows versatility as it can be used and adapted for a number of *in-situ* applications such as liquid, gas, electrical *in-situ* analysis as well as traditional lamella preparation.

7.1 Future Work

The future work going forward with this project work can be categorised into two parts, which can work concurrently with each other: a) the further iterative optimisation of sample preparation techniques and b) the extended advanced analysis and characterisation of the Cu film/NW microstructure.

7.1.1 Further Iterative Optimisation of Sample Preparation Techniques

In terms of sample preparation techniques, there are many alternatives as well as some additional steps/enhancements that could be included to the methodologies developed in this project. Low kV Ar ion milling would most likely be the next step to achieving a more crystalline and uniformly thin lamella. Ar ion milling using beam voltages as low as 500 V, which can be used as a final polishing step. This might provide a cleaner, less damaged and amorphised sample. It may also reduce some of the disadvantages associated with the broader, less controllable beam of 2 kV and even 5 kV in the Focused Ion Beam (FIB), by allowing 30 kV thinning to approximately 400-500 nm and proceeding with Ar ion milling for

the remaining thinning. Later on, it could also be used to ensure larger areas of interest would be thinned to sub-50 nm thickness with minimal damage. Larger areas of interest would be extremely beneficial for the continual analysis of Cu NWs. This Ar ion milling could be employed for final polishing procedure for both cross-sectional and plan-view preparation of Cu films and Cu nanowires.

Another alternative to gallium $(Ga)^+$ FIB milling sample preparation is mechanical preparation combined with Ar milling. This is a commonly used procedure but isn't favoured over the "faster" procedure of FIB milling. This would be an attractive alternative to display comparisons between the ion prepared Cu films and mechanically prepared, to observe any amorphisation, crystal structure differences or grain size difference between both.

7.1.2 Extended Advanced Analysis and Characterisation of the Cu Film/Nanowire Microstructure

The second section of this potential future work would be the continuation of the advanced characterisation of the Cu films' and NWs microstructures. This would involve atomic resolution S/TEM imaging and analysis of the grain boundaries in particular. Currently this is difficult to do with the thickness and current crystallinity of the lamellae. With the slight improvement of the sample preparation mentioned above the high-resolution analysis of the grains and grain boundaries within the Cu films and nanowires would be more readily achieved. By achieving this high resolution, the potential to correlate the STM data of the "zipper" like structures appearing along the ridge and valley grain boundaries would be much greater. The ultimate ambition would be to do a complete grain boundary and interface analysis of varying Cu film thicknesses (30 nm, 20 nm, 10 nm) as well as Cu NW thickness and correlate this with the resistivity measurements obtained through C-AFM. Being able to track a drop or increase in conductivity and correlate that to a specific grain boundary within a particular Cu NW would be the ultimate achievement here.

In terms of the *in-situ* annealing analysis, future work would be centred around the continued imaging of the mound formation. Particular focus would be placed on the Ta layer and the structural changes it undergoes during the annealing process. Again, this also reverts back to the further optimisation of the lamella preparation. The current lamellae were thinned at a final beam voltage of 5 kV, with further optimisation, a 2 kV beam voltage could potentially be used. This would lead to high-resolution imaging of both the Cu film and the Ta barrier layer.

The Ta liner, grain growth and grain boundary changes of the Cu film during the annealing process could be analysed. Again, as with the project described here, these findings would be applicable and useful for a range of *in-situ* TEM techniques including but not limited to liquid, biasing and gas phase applications.

A. Appendix

A.1 Damage Experienced by Electron Beam

Video of damage experienced by 40 nm Cu on SiO_2 taken over the course of 8 minutes in total, attached in USB drive. Each TEM image taken at ~30 second intervals.

A.2 Focused Ion Beam Cross-section of Mounds

Video of 50 nm annealed Cu mound cross-section, imaged by SEM, attached in USB drive. Image slice captured every 20 seconds.

A.3 Novel *in-situ* Lift-out Technique

Video of *in-situ* FIB lift-out performed on a FEI Quanta 200 3D, attached in USB drive.

A.4 Formation of Cu_3Si Mounds *in-situ* TEM

Video of Cu_3Si mound formation during *in-situ* TEM annealing from room temperature to 700°C, attached in USB drive.